UNIVERSITY OF CALIFORNIA
SANTA CRUZ

THE EVOLUTION AND EXPLOSION OF MASSIVE STARS

A dissertation submitted in partial satisfaction of the
requirements for the degree of

Doctor of Philosophy

in

ASTRONOMY & ASTROPHYSICS

by

Tuguldur Sukhbold

September 2016

The Dissertation of Tuguldur Sukhbold
is approved:

Professor Stan Woosley, Chair

Professor Greg Laughlin

Professor Jonathan Fortney

Dean Tyrus Miller
Vice Provost and Dean of Graduate Studies

Table of Contents

List of Figures

List of Tables

Abstract

The Evolution and Explosion of Massive Stars

by

Tuguldur Sukhbold

How a massive star ends its life depends upon how that life has been lived - the rotation, mass and composition it was born with, mass loss and exchange, and the complex convective and nuclear burning episodes it experienced along the way. In the end, the presupernova stellar core has a density structure that can be characterized by its "compactness" - essentially how fast the density declines outside the iron core. The likelihood that a massive star explodes, by any means, is sensitive to this compactness. It turns out, perhaps surprisingly, that the compactness is not a monotonic function of the star's birth mass, and, in some mass regions, whether the star explodes or not is almost random. Here the stellar physics underlying the development of compactness is explored for a fine grid of masses across a broad range of masses (9 - 120 solar masses). Using the model set generated, and with collaborators, the resulting explosions are explored assuming a neutrino-powered mechanism. Full isotopic nucleosynthesis, light curves, and remnant masses are calculated and found to be in good agreement with observations. Neglecting rotation, most stars above 20 $M_{\odot}$ do not explode - though there are exceptions. In a related study, based on the same model set, the upper bound to the most luminous supernovae is explored considering various energy sources. The brightest possible supernova is found to be a rotationally powered explosion of a stripped core.

For my mother Sukhbold Sandag.

Acknowledgments

The past five years have been packed with ups and downs, and on the way I had to overcome various challenges both scientifically and personally. I could not have made this far without the support and guidance of many great people , to whom I feel extremely fortunate to have crossed paths in my life.

First and foremost I thank my adviser and my scientific "father" Prof. Stan Woosley. There is simply not enough space here to express fully the debt I owe to him. Most of my scientific education is due to Stan, and it has been an honour to learn from one of the best. I will be forever grateful to you!

I can't thank enough my family, especially my mother, who despite all of the odds gave her everything for my future. I am deeply indebted to her and my brother for their belief in me and continual support. And to my wife for constant encouragement and for having patience with an all-consuming lifestyle of a grad student.

I have greatly benefited from the association with many great scientists, including Alex Heger, Thomas Janka, Thomas Ertl, Justin Brown, Frank Timmes, Chris Malone, Bill Paxton, Todd Thompson, Chris Kochanek, Iair Arcavi, and Jamie Lombardi. I am thankful for their inspiration and encouragement.

I also owe a debt of gratitude to individuals who have shaped my education prior to UC Santa Cruz. In particular to Casey Meakin, my mentor at the University of Arizona, for launching my interest in massive stars and teaching me the foundations of computational astrophysics.

I deeply appreciate the support and friendship of many fellow students and old friends for helping me to keep my sanity in grad school. Notably my office mate Hassen, fellow students Elizabeth, Justin and Srikar, my jail-mate Manos, and my longtime highschool pal Denar.

Finally, I would like to acknowledge the public support for science in this country. My whole graduate education and research were funded by following grants through my adviser Stan Woosley: National Science Foundation (AST 0909129), NASA (NNX14AH34G, NNX09AK36G) and UC Office of the President (12-LR-237070).

Chapter 1

Introduction

1.1 Overview

Stars are the main baryonic building blocks of the universe. Massive stars, though few in number, play a disproportionally important role in the chemical and dynamical evolution of galaxies. They dominate the evolution of the interstellar medium through their energy output, ionizing radiation, explosions and heavy element production. Their intense luminosities are an important means of exploring various astrophysical environments from our galactic neighbourhood to deep into the early universe. Upon their death, massive stars experience a dynamical instability and perish in the most dramatic way, which signals the birth of neutron stars, black holes, and they are sites of much the nucleosynthesis of heavy elements. Therefore, a better understanding of the evolution and explosion of massive stars is an essential piece of the puzzle in our understanding of the universe.

Despite their central role in a wide range of astrophysical phenomena, more than half

a century of effort has not been enough to build a comprehensive picture detailing all aspects of the evolution and explosion of massive stars. In terms of evolution, the lack of universally agreed upon theories for convective overshoot mixing, semiconvection, mass loss and rotational angular momentum transport, cloud the accuracy of our models, especially those describing the last stages of its life. In terms of the explosion, the underlying mechanism is embedded in a difficult problem that is rich in physics, involving self-gravity, radiation hydrodynamics, complicated equations of state and multi-species neutrino-transport.

Observational constraints provide only an indirect means to probe the problem. A few dozen supernova progenitors have been directly observed, however, those measured surface parameters provide little insight into the final evolution of the core, which evolves separately from the envelope. Modern techniques, such as asteroseismology, are still inadequate to probe the core structure of an evolved massive star. The wealth of information in the form of supernova light curves and spectra are not adequate probe of the mechanism of explosion. Neutrino observations are would be helpful in this regard, but unfortunately their utility is mitigated by the fact that nearby supernovae are extremely rare.

Part of the difficulty with the physical theories mentioned above is that, they are inherently multi-dimensional. There are major ongoing efforts to tackle the problem through large scale multi-dimensional simulations. Though these calculations can capture all of the essential physics, they are expensive and complicated, and currently even with the most powerful computers it is not feasible to perform a comprehensive 3D study of critical problems.

In this thesis, the problem is attacked using a different approach through one-dimensional (1D) simulations of both the evolution and explosion of massive stars - a path that trades some

accuracy with computational expense, but allows one to explore a very wide parameter space. Overall, despite its limitations, this work is one of the most extensive surveys of 1D models to date, and should advance our understanding of a broad range of high-energy astrophysical phenomena. In particular, it sheds a new light on the non-monotonic nature of late stage evolution of massive stars, and corroborates the newly emerging idea that there is no single initial mass, below which stars always explode and above implode. This work also explores the parameter space and systematics of the core-collapse supernova problem, and lays theoretical groundwork for the interpretation of the diverse results expected from next-generation telescopes, such as LSST and Zwicky.

All presupernova progenitor models, explosion results, nucleosynthesis yields and light curves have been publicly released[1][2], which will be a significant service to supernova, chemical evolution and transient communities. Already several researchers are taking advantage of this extensive library, including: Mark Krumholz (ANU) for galactic chemical evolution studies, Austin Harris (LBNL), Evan O'Connor (NCSU), Tomoya Takiwaki (NAO), Brian Metzger (Columbia) for explosion mechanisms, and Iair Arcavi (LCOGT) for light curve studies.

1.2 Brief Basic Background

Stuctural evolution of a massive star. Stars are considered to be massive if their initial mass is bigger than the smallest mass star that can explode as a supernova, i.e. never reach a state where it is fully supported by electron degeneracy. Currently this threshold mass

[1] www.ucolick.org/∼sukhbold
[2] http://doi.org/10.17617/1.b

is believed to be around 8 ± 1 $M_{\odot}$, separating massive super-AGB stars that die as white dwarfs embedded in planetary nebulae from massive stars that die as electron-capture supernovae. On the higher end, for solar-metallicity, theoretically massive stars can reach up to 120-150 $M_{\odot}$, however, there are observational claims that exceed 300 $M_{\odot}$. In the early universe, when the metal enrichment was much lower, even more massive stars could have existed. Furthermore, most massive stars are in binary systems and a significant fraction of these are interacting binaries. Such interactions can lead to spin up, envelope stripping, and merging, thus the evolutionary paths can significantly differ from that of a single star. In general, the topics concerning minimum mass supernova, formation of massive stars and binary evolution are well beyond the scope of this thesis, which is focused on non-rotating solar metallicity single stars between 9-120 $M_{\odot}$.

Like any other star, most of the life of a massive star is characterized by a steady struggle between pressure and gravity. Nuclear reactions evolve the composition along with structure, and provide pressure at the expense of losing energy in radiation and neutrinos. Unlike smaller stars, instead of ending up being supported by electron degeneracy, the center of a massive star evolves to higher temperatures by burning fuels from hydrogen until silicon. An inert iron core forms in the end, and being unable to further generate energy from nuclear burning, the core eventually collapses under its own weight.

Table 1.1 lists all central nuclear burning stages for a solar metallicity non-rotating 15 $M_{\odot}$ model, where numerical values for surface parameters, central temperature and neutrino luminosity are measured when each fuel is nearly depleted in the core. Every fuel source creates main ashes to be ignited later at a higher temperature (except silicon), along with many

other secondary products. The condition for ignition of the new fuel is always attained at the center (or near the center for some fuels of lighter stars), and the energy from burning is almost always transported through convection. In turn, convection keeps replenishing the hot central region with fuel until it eventually runs out, and as a result the major burning episodes create nested regions of ash, whose maximum extents in mass are referred as "cores". In other words, hydrogen burning at the center creates a helium core, helium burning afterwards creates a carbon-oxygen core *within* the helium core, and carbon burning episode creates neon-magnesium-oxygen core within the carbon-oxygen core etc. The 15 $M_{\odot}$ model, at the time of presupernova, has M_{He}=4.35 $M_{\odot}$, M_{CO}= 3.14 $M_{\odot}$, M_{NeMgO}=1.89 $M_{\odot}$, M_{Si}=1.88 $M_{\odot}$, and M_{Fe}= 1.42 $M_{\odot}$.

The boundaries of the cores are chiefly characterized by the compositional difference, i.e. little helium outside and little hydrogen inside the helium core. However, they often correspond to a sharp structural change. The most notable case is a large pressure jump at the boundary of the helium core, separating it from the extended envelope of mostly hydrogen. As the star finishes burning hydrogen at the center, the burning weakens and its core starts to shrink to eventually ignite the next fuel helium. But during this time hydrogen starts to burn in a shell just outside the helium core, forcing the envelope to expand and cool as the star evolves from a main sequence star to a red supergiant. During this phase the outermost part of the extended envelope becomes loosely bound to the star, and most of the mass loss takes place.

The initial mass of the star correlates well with its final to its helium core and carbon-oxygen core masses up until an initial mass of about $\sim$40 $M_{\odot}$, where the entire envelope is lost to winds (for solar metallicity). Above this mass Wolf-Rayet stars form and their powerful wind

can shrink the helium core and expose layers rich in carbon and oxygen. The efficiency of this mass loss is one of the most uncertain parts of modern theory of stellar evolution.

Most of the star's life is spent burning hydrogen in the center, and for each subsequent fuel source the nuclear burning time scale shrinks drastically. Starting with carbon burning in the center, the beginning of the advanced stage burning episodes, neurtino losses begin to play an important role. Note in Table 1.1 that after core helium burning, the outer surface is effectively frozen, i.e. radius and effective temperature don't change until the star's death, and that neutrino luminosities keep increasing by many orders of magnitude. To keep up with this loss of energy through neutrinos, the star has to burn faster. This ever shortening nuclear burning time scale during the advanced stages of evolution forces the core out of thermal equilibrium with the envelope (Kelvin-Helmholtz time scale of the envelope is many thousand years), and therefore in massive stars the carbon-oxygen core evolves separately from the envelope. This is essentially why no one can tell precisely when Betelgeuse will die, except to say that it will within a helium burning timescale.

In general, each burning episode in the center is followed by one or more shell burning episodes. Central hydrogen and helium burning are followed by a single episode of shell burning that last until the star dies, while central burning episodes during the advanced stages, on the other hand, can occur in multiple consecutive shells and follow a rather complicated evolutionary path. As will be discussed extensively in chapter 2, for heavier stars central carbon burning can take the form of a radiative flame, instead of a convective core, and the shell burning episodes of different fuels can merge or split. Uncertainties concerning the physics of convective boundary overshoot and semiconvective mixing play an important role here. The location

and extent of the carbon, oxygen and silicon burning episodes determine the final structure of a presupernova star.

The "Core-Collapse" Problem. Nearing the time of presupernova, an inert iron core forms at the center surrounded by shells that are burning silicon, oxygen, carbon, helium and hydrogen. In massive stars this state continues until iron core mass exceeds the effective Chandrasekhar mass, at which point the pressure from semi-degenerate electrons gives up to gravity and the core starts to collapse. The collapse proceeds in a dynamical timescale (~ 0.1 seconds) and releases energy on the order of the gravitational binding energy of the iron core (a few times 10^{53} erg). Historically it was first suggested that perhaps the dynamical instability from exceeding the Chandrasekhar limit initiated a prompt hydrodynamical explosion. As intuitive as that may have seemed, however, it is now a well established that the bounced outgoing shock stalls after travelling only ~ 100 km, due to neutrino losses and photodisscociation. For a successful explosion to ensue, this stalled shock must be revived by some mechanism, and the favored hypothesis for many decades has been that neutrino energy transport, perhaps augmented by rotation plays a key role.

During the initial phase of the collapse two instabilities suppress the pressure support. First, heavy bound nuclei capture electrons making them more neutron rich and robbing the core of much needed pressure support. Secondly, photodisintegration creates a large abundance of α particles, which reduces the binding energy and limits the gain of thermal energy from contraction. These instabilities efficiently accelerate the collapse and the peak infall velocities approach quarter of the speed of light. Upon reaching the nuclear density (a few times 10^{14} g cm^{-3}) the nuclei start to melt into a nuclear fluid which encounters the hard core repulsive

component of the nuclear force. A powerful sound wave forms near the center and steepens into a shock as the rebounding core supersonically crashes into the infalling material. However, on its way out the shock liberates free protons from infalling heavy nuclei, which in turn creates a massive amount of energy loss, mostly through electron neutrinos. This is the primary reason for the stalling of the bounced shock.

In order to revive this stalled shock, the neutrino-driven mechanism needs to provide enough energy through neutrino interactions, in the region just behind the shock. The gravitational binding energy of the protoneutron star ($\sim 10^{53}$ erg) is almost exclusively released in the form of neutrinos, and since the typical supernova kinetic energies are observed to be near $\sim 10^{51}$ erg, the neutrino-transport model requires only a percent of the energy reservoir to couple with the matter outside the protoneutron star. Because this region is barely optically thin to neutrinos, such calculations require careful solutions to the transport equations for all species of neutrinos. Self-consistent three-dimensional simulations with state-of-the-art neutrino transport have become possible only in the past ~ 5 years, and, as of yet, the community is still lacking consensus.

After the revival of stalled shock, the extended protoneutron star is left to shrink and cool. It contracts from a few dozen km in radius to about 10 km, and in the process liberates a fraction of solar mass worth of gravitational binding energy in neutrinos.

Nucleosynthesis. The element production of a massive star during its main sequence evolution is relatively simple. Hydrogen burning by the C-N-O cycle rearranges the abundances of these light species.

Helium burning is the only case where a major fuel is consumed by two nearly equally

competing reactions - 3α and $^{12}C(\alpha,\gamma)^{16}O$. As will be discussed in chapter 2, carbon is produced more in lighter stars, while oxygen is produced more in heavier stars. The ratio of these two main ashes, which effectively set the initial composition of the carbon-oxygen core, plays an important role in the advanced stage evolution. Beside carbon and oxygen, helium burning also creates a few neutron rich isotopes like ^{18}O and ^{22}Ne, some of which get destroyed and others amplified in abundance later on during the advanced stages.

An important aspect of helium burning in massive stars is that it is responsible for most of the "weak" component of s-process nucleosynthesis. This process refers to the slow capture of neutrons (relative to beta decay) on heavy seed nuclei, and is known to produce isotopes from iron until approximately yttrium (though lighter isotopes down to sulfur are also appreciably created). At the end of helium burning $^{22}Ne(\alpha,n)^{25}Mg$ provides enough neutron density at the right temperature. The "main" component of the s-process, responsible for isotopes between yttrium and lead, operates during helium flashes of AGB stars in a different environment.

Nucleosynthesis during the advanced stages is extremely rich and complicated, largely due to the high temperatures and abundant reactions that release free protons, neutrons and alpha particles. Carbon burning proceeds through a binary fusion reaction chiefly creating isotopes of magnesium, sodium and neon. Some of the secondary products decay and further react to create excess of neutrons in the carbon-oxygen core.

After carbon is gone, the neon burns before oxygen, even though the latter is the isotope with the smallest Coulomb barrier inside oxygen-neon-magnesium core. This is because neon is the most frail of the three with the least amount of α-separation energy, and thus it

gets disintegrated through high energy photons, which then get captured and form magnesium. Since the energy yield from this rearranging reaction is rather small, neon burning has been historically overlooked. However, this period is rich in many nucleosynthetically important secondary reactions.

Like carbon, oxygen also burns through a binary fusion reaction, which mostly creates silicon and sulfur. Appreciable amounts of chlorine, argon and calcium are also created. Similar to previous advanced stage episodes this process is rich in secondary reactions, including many weak interactions that further enrich the neutron excess. During this phase the high temperature also destroys most of the s-process products, carried from previous episodes, back to the seed nuclei of iron group isotopes. A lot of the material formed near the center during this phase will eventually end up inside the iron core and become a compact remnant after the collapse (will not be ejected).

In the last few days before the explosion, silicon burns in a somewhat similar fashion as neon. Through a sequence of photodisintegrating reactions some of the silicon will evaporate off α particles and free nucleons. These are ultimately added on the big quasi-equilibrium group of isotopes all heavier than magnesium, and progressively decrease the abundance of silicon to produce tightly bound species of iron group isotopes.

During the explosion, after the stalled shock gets revived through neutrino-heating, or some other mechanism, on its way out it will manage to reprocess some of the inner parts of the ejecta consisting from heavy isotopes. The critical condition for this explosive burning is that the burning timescale of the fuel needs to be smaller or similar to the dynamic timescale. This process is mostly characterized by the elevated temperature caused by the shock passing, rather

than the initial composition of the fuel.

Silicon and oxygen get reprocessed when the shock heats the region above 4 billion Kelvins. In general, this explosive burning will yield very similar ashes as the burning that took place before the explosion, i.e. iron group nuclei, except that the fuel and products both have nearly equal number of neutrons and protons (the density is too low and the time is too short for appreciable electron capture). However, when the dynamic time gets short, the ejecta will manage and cool off before the α particles had a chance to get added onto the seed nuclei. Therefore the composition "freezes out" with free α particles, which eventually get captured on to produce heavier isotopes until germanium.

If the region gets heated between 2 and 4 billion Kelvins, the carbon and neon can also get reprocessed through the shock. Here again the primary products are similar to the burning during the presupernova evolution, except it manages to produce many rare neutron-rich isotopes until zirconium. Two of these are ^{26}Al and ^{60}Fe, both long lived radioactive isotopes that can be measured through gamma-ray observations and used as a cosmic chronometers.

There are other processes that take place during the explosive nucleosynthesis. Copious amount of neutrinos produced by the contracting proto-neutron star gives rise to ν-process, which synthesizes some light isotopes (chiefly boron, fluorine and lithium), through the inelastic scattering of certain species of neutrinos. The environment for the explosive oxygen and neon burning is also the site for p-process (or γ-process). This process creates heavy proton rich isotopes by photodisintegrating s-process nuclei.

Light Curves. The temporal evolution of energy release by stellar explosions has been one of the main stays of supernova research. Two major sources of power, that are re-

sponsible for most of the common supernova light curves, are the recombination of the shock deposited energy and the decay of unstable species synthesized during the explosion. The former plays a dominant role if the progenitor star had an extended hydrogen envelope, while the latter dominates in supernovae from bare helium or carbon-oxygen cores. For radioactivity, the main supply is ^{56}Ni, a product from the explosive silicon burning. With a half-life of 6.1 days, it decays due to electron capture to ^{56}Co, which has a half-life of 77.3 days and eventually decays to ^{56}Fe. Gamma rays released from radioactivity are down-scattered and thermalized in the supernova ejecta until they emerge as optical photons. Depending on the details of progenitor, explosion and surrounding environment, additional energy inputs also come into play, such as collision with the circumstellar medium and energy injection from compact remnants.

Despite the wide range of possibilities, the light curves of different supernova types are reasonably distinct, and therefore the observational classifications are quite rich. Light curves types that are most relevant for this thesis study are of Type IIP and Type Ib/c. The IIP supernova light curves are characterized by the distinct several month long nearly constant luminosity "plateau" feature, and would emerge from the explosion of a RSG with an extended hydrogen rich envelope. The Ib/c light curves, on the other hand, result in an explosion of a massive star with its helium or carbon-oxygen core exposed, by loosing all of its envelope material in mass loss or through binary interaction.

The IIP light curve is characterized from three segments. First, when the explosion shock wave breaks out from the surface of the star, it will create an extremely bright display for a brief amount of time. For a typical case, the luminosity exceeds 10^{44} erg s^{-1} and lasts about dozen minutes. Luminosity and temperature will decline rapidly from here as the ejecta expands

and the diffusing radiation cools. Once the temperature cools to about 6000 K, the hydrogen in the expanding envelope material begins to recombine and release the shock deposited radiation. This recombination process propagates inward in mass and maintains roughly a constant temperature. For a typical case, the luminosity stays nearly constant and lasts about 100 days, creating the "plateau" phase. Finally, when the recombination wave terminates, the luminosity rapidly declines and the last section of the light curve is purely powered by radioactive decay. After $\sim$100 days since the explosion, most of the energy from the decay of ^{56}Ni will be spent in the ejecta expansion, and thus this final tail section will solely be powered by the decay of ^{56}Co.

The Ib/c light curves are mostly powered by the radioactivity. Since the exposed core is compact, the transient resulting from shock break out will be much fainter and briefer, compared to that of a IIP case. And since there is no envelope material to be ionized and recombined, there is no "plateau". Instead, the light curve simply rises and declines, reaching a peak brightness when the age of the ejecta becomes comparable to its effective diffusion timescale. The types Ib and Ic are separate observational classifications based on the existence of a helium absorption line in the spectra. However, since it is not clear if the lack of this line directly implies an absence of helium in the presupernova star, they are collectively being referred as Ib/c in this work.

1.3 KEPLER code

The one-dimensional (1D) implicit Lagrangian hydrodynamic code KEPLER (Weaver *et al.*, 1978) was employed throughout most of this thesis. The code is capable of performing stellar evolution calculations for full hydrogenic stars, or bare cores, including mass loss, nucleosynthesis and rotation. It also employs a piston scheme for blowing stars up and a single-temperature flux-limited radiative diffusion, and therefore is able of calculating isotropic supernova explosions of all kinds. The input physics and its capabilities have been previously discussed in detail in numerous publications (e.g., Woosley *et al.*, 2002; Rauscher *et al.*, 2002; Heger *et al.*, 2005; Woosley *et al.*, 2007; Sukhbold and Woosley, 2014; Woosley and Heger, 2015b; Sukhbold *et al.*, 2016), thus a brief summary is provided here.

The version of the code used in this thesis employed red-supergiant (RSG) and Wolf-Rayet phase mass loss schemes from Nieuwenhuijzen and de Jager (1990) and Wellstein and Langer (1999) respectively. While these are rather old references, the theory here has advanced very little, and at least for the mass loss during the critical red supergiant phase, it is not superseded. KEPLER uses Ledoux criterion for convection, and includes semiconvective mixing along with overshoot mixing. In general, mass loss and convection physics are some of the biggest uncertainties in modern stellar evolution codes, and due to lack of consensus within the community, various groups often employ different prescriptions.

For the low-temperature opacity, for example in the convective envelopes of RSG the code uses OPAL tables (Iglesias and Rogers, 1996), and for high-temperature the opacity is chiefly due to electron-scattering with corrections due to degeneracy and relativity (Weaver

et al., 1978). A newer version of the code has α-enhanced Type I OPAL tables available (Menon and Heger, 2016). Nuclear energy generation rate uses a standard 19-isotope network until oxygen is depleted in the core, and employs 128-isotope quasi-equilibrium network thereafter. A large "adaptive" network (Rauscher *et al.*, 2002) of up to 2000-isotopes is often carried in parallel with the main structure calculation. This large network carefully follows the temperature and density history generated from the smaller network to calculate nucleosynthesis, also feeding back accurately calculated electron mole number Y_e into the structural calculation.

Though the work presented in this thesis employed mostly non-rotating models, the code has the capability to calculate rotationally induced mixing, mass loss, and magnetic torques (Heger *et al.*, 2000; Heger and Langer, 2000; Heger *et al.*, 2005).

1.4 Structure of this thesis

Following this general overview, this thesis is divided into three main chapters, each presenting material based upon peer-reviewed publications from *The Astrophysical Journal*:

- Sukhbold and Woosley (2014)
- Sukhbold *et al.* (2016)
- Sukhbold and Woosley (2016)

A brief description of the contents along with the contribution from the author of this thesis to each paper are highlighted in the following.

Chapter 2, reports a study of the late stages of massive star evolution. Fine-meshed grids of presupernova models using both `KEPLER` and the open source stellar evolution code

MESA (Paxton *et al.*, 2011, 2013, 2015) are computed. The details of the advanced stage evolution of both hydrogenic full stars and bare CO cores of various initial masses and compositions are explored, considering the uncertainties in the physics of stellar convection, mass loss and nuclear reaction rates. Special emphasis is given to explaining why, and how, the structure of the core changes throughout the evolution, and why the final presupernova core structure is non-monotonic with initial mass.

In this work, the author calculated all presupernova evolution models with MESA and nearly all of models with KEPLER, and performed a significant part of the analysis.

Chapter 3, describes a survey of the explosions and its various outcomes employing a novel approach. Several neutrino light-bulb "engines", that essentially describe the evolution of the inner 1.1 M of the progenitor, were first calibrated using the observational data for SN1987A and SN1054 along with the lessons learned from 3D core-collapse simulations. These engines were placed in each of the 200 KEPLER presupernova models from 9 to 120 $M_{\odot}$ (some compiled from older studies and some newly calculated), and the neutrino transport outside the engine is calculated in an efficient and approximate way using the 1D code Prometheus-HOTB (PHOTB). With this configuration the explosion energy, remnant mass and nucleosynthesis are strongly dependent on the progenitor structure, unlike in previous survey studies where these explosion outcomes were explicitly controlled. Resulting outcomes for several engines were integrated over the initial mass function, and compared to the solar abundances and the observed counts of neutron stars and black holes. All successful explosions were followed for about 230 days using flux-limited diffusion, and the systematics of the resulting type IIp and Ib/c light curves were explored.

The author's contributions in this work included calculation of majority of presupernova models, all of explosion models with KEPLER including both nucleosynthesis yields and light curves, analysis of explosion, bound remnants and light curve systematics.

Chapters 2 and 3 have dealt with common "ordinary" supernovae. Chapter 4 goes on to consider some of the outliers and asks the question "what is the most luminous supernova we can justify with models we know about?". Various energy sources are considered - prompt explosions, pair-instability, collisions of shells, pulsational pair-instability and magnetars - in the context of non-relativistic and isotropic supernovae. Upper limits based on analytic arguments and some numerical models were provided for each scenario.

The author's input in this work included all KEPLER calculations, and the analysis for radioactivity and magnetar powered supernovae.

1.5 Related works not contained in this thesis

Additional work performed while advanced to candidacy at UC Santa Cruz, but not presented in this thesis are worth mentioning. The author had the opportunity to contribute to two published works and is heading two other projects currently in preparation.

In collaboration with Thomas Ertl (MPIA), Thomas Janka (MPIA), Stan Woosley (UCSC) and Marcella Ugliano (MPIA), the predictability of the final fate of a massive star from its presupernova structure was investigated (Ertl *et al.*, 2016). While prior attempts in this direction have failed to find a non-ambiguous single parameter that can separate explosions from implosions, two parameters have been found through this work that can serve as an accurate

criterion. One is the normalized mass enclosing the location where specific entropy s=4, and the other is the Lagrangian mass derivative at this location. The explosion calculations presented in chapter 3 of this thesis were based on this work.

With Ke-Jung Chen (NAOJ) and Stan Woosley (UCSC) the hydrodynamics of magnetar powered supernovae were explored through 2D simulations (Chen *et al.*, 2016). Spherically symmetric studies on this problem have been hindered by the pile up of radiatively accelerated matter due to "snow plowing" effect. In 2D, while the pile up is found to be unstable and fracturing into filamentary structures, the concentration of matter in the hollow shell still persists. Relevance of this characteristic to other situations, where energy is input over an extended period by a centrally concentrated source, such as a pulsar, radioactive decay, a neutrino-powered wind, or colliding shells is discussed.

In collaboration with Casey Meakin (LANL), Hassen Yesuf (UCSC) and Zeyana Musthafa (UCB), the author explored ways of testing overshooting convection physics using detached eclipsing binary systems. Precision stellar parameter measurements are being compared against 1.8 million stellar evolution models that describe various prescriptions for convective core overshooting in the main-sequence evolution of massive stars. Preliminary results do not support the previously suggested weak positive correlation between the step-overshooting parameter α_{ov} and initial mass of the star. Instead the values that describe high precision measurements show a large dispersion across the whole mass range from 2 to 30 $M_{\odot}$, reflecting the missing physics in the simple step overshooting model.

Finally, with Stan Woosley (UCSC) and Jamie Lombardi (Allegheny), the supernova progenitors from stellar mergers are being investigated, with a special emphasis on the case of

Table 1.1: Evolution of 15 $M_\odot$ model

Fuel	Ashes	T_{center} [10^9 K]	log L_ν [erg s^{-1}]	T_{eff} [10^3 K]	Radius [10^{13} cm]	Timescale
H	He	0.05	37.0	26	0.07	10 Myr
He	C,O	0.25	36.8	3.7	4.4	1 Myr
C	Ne, Mg	1.2	41.6	3.5	5.7	1000 yr
Ne	O, Mg	1.6	42.2	3.5	5.7	years
O	Si, S	2.2	43.6	3.5	5.7	months
Si	Fe	3.7	45.4	3.5	5.7	days
presupernova		7.5	49.4	3.5	5.7	...

SN1987A which had a blue supergiant (BSG) compact progenitor. All current progenitor models for SN1987A, including those used in chapter 3, employ stellar evolution of a single star coupled with extreme rotation or semiconvection, in order to achive a BSG structure. While the merger scenario has been studied in the past to explain the ring-structure of SN1987A ejecta, a presupernova BSG model evolved from a merger product has never been calculated. Merger of a massive RSG star with an intermediate mass main sequence star is being explored through `KEPLER` simulations, coupled with sorting algorithms that resemble smooth-particle hydrodynamics calculations.

Chapter 2

The Compactness of Presupernova Stellar Cores

2.1 Introduction

The compactness of its core is an important structural characteristic of a presupernova star that affects whether it will explode as a supernova. A shallow density gradient around the iron core, as typically exists in more massive stars, implies a higher accretion rate and "ram pressure" (Cooperstein *et al.*, 1984) surrounding the iron core during its collapse that must be overcome by neutrino energy deposition or other energy deposition to turn what is initially an implosion into an explosion. The connection between this structure and the likelihood of explosion has been noted many times (Burrows and Lattimer, 1987; Fryer, 1999; O'Connor and Ott, 2011; Ugliano *et al.*, 2012), but little attention has been given to explaining just why the compactness has the values that it does, or why different groups obtain different core structures

for models with similar main sequence mass.

Recently, O'Connor and Ott (2011) quantified this compactness in terms of a parameter,

$$\xi_M = \frac{M/M_\odot}{R(M_{bary} = M)/1000\,km}\Big|_{t_{bounce}}, \tag{2.1}$$

where M=2.5 $M_\odot$ was chosen as the relevant mass for quantifying the density gradient outside of the iron core, which itself typically has a mass in the range 1.4 to 2.0 $M_\odot$. In O'Connor et al's definition, the time, t_{bounce}, chosen for evaluating ξ_M is when the core has collapsed to its maximum (super-nuclear) density. As we shall show (§ 2.2.3), for M = 2.5 $M_\odot$, no substantial accuracy is lost if this parameter is evaluated for the "presupernova model" defined by when the collapse speed first reaches 1000 km s^{-1}. The choice of M = 2.5 $M_\odot$ is justified as being larger than the iron core itself, yet deep enough in the star to sample matter that might accrete, especially in a failed explosion. Since $\xi_{2.5}$ is inversely proportional to the radius of a fiducial mass outside the iron core, it is small when the density around the iron core falls off rapidly with radius and greater when the density gradient is shallow. That is, when $\xi_{2.5}$ is large, one need go only a shorter distance to include more mass. The systematics of neutrino-powered supernova explosions were explored as a function of $\xi_{2.5}$ by O'Connor and Ott (2011) and Ugliano *et al.* (2012), both of whom found that a small value of $\xi_{2.5}$ favored explosion. O'Connor and Ott (2011) plotted $\xi_{2.5}$ as a function of main sequence mass for a variety of surveys due to Woosley *et al.* (2002), Woosley *et al.* (2007) and Limongi and Chieffi (2006b), and a subset of that data is shown in Fig. 2.1. Note especially the distinctly non-monotonic

behaviour in the vicinity of 25 $M_\odot$ and 40 $M_\odot$.

For a polytrope of constant index and composition supported by a constant fraction (β) of ideal gas pressure, the compactness defined by equation 2.1 will actually *decrease* monotonically with increasing mass when evaluated at a constant central temperature and small radius. This is because, for polytropes, the central temperature and density obey a relation (e.g. Woosley *et al.*, 2002)

$$\frac{T_c^3}{\rho_c} \propto M^2 \tag{2.2}$$

For a given T_c the central density thus declines as $1/M^2$ and the radius required to enclose a given mass increases with M. As will be discussed in § 2.3.1, equation 2.2 works reasonably well for massive stars that are burning hydrogen and helium in their centers. The inner regions of such stars are non-degenerate and can be well represented by polytropes of constant index.

As massive stars evolve, however, they develop nested cores with different compositions and entropies. Lighter stars develop more degenerate cores in their late stages, especially during oxygen burning. The large gravitational potential at the edge of these degenerate cores implies a small pressure scale height that results in a steep decline in the local density (Faulkner, 2001, 2005). As a result, in heavier stars, the higher entropy actually leads to more extended configurations and larger values of $\xi_{2.5}$. One does not have to to go out as far in the "envelope" of the compact core to encompass 2.5 $M_\odot$, while in lighter stars that mass is reached farther out. This accounts for a general tendency of the compactness parameter for presupernova stars

to increase with mass, especially for low metallicity stars where mass loss is less important.

Fig. 2.1 also shows that the core compactness has significant non-monotonic behavior above about 20 $M_\odot$, and possibly some fine structure below 20 $M_\odot$. If this behaviour is real and robust, it would have interesting implications for the explosion mechanism(s) for massive stars, the masses of their compact remnants, and stellar nucleosynthesis. To address the "real and robust" issue, it is necessary to understand why this non-monotonic structure exists and its sensitivity to uncertainties and variations in the stellar models.

The present study has several parts, some dealing with the systematics of $\xi_{2.5}$ found in new surveys of massive stars, others with the uncertainties one should assign to those results. In § 2.2, three new surveys of massive stellar evolution are presented for stars of solar metallicity, very low metallicity (10^{-4} solar), and solar metallicity with suppressed mass loss. These new surveys, though using the same physics as in previous works (Woosley *et al.*, 2007), are needed to provide a finer mass grid for examining rapid fluctuations in $\xi_{2.5}$ and to give additional data not archived in previous work. In § 2.3, we address the heart of the matter: why is the compactness a non-monotonic function and, in some places, almost chaotic function of main sequence mass. The timing and location of several carbon and oxygen convective shells are found to play a major role. Because there are multiple episodes of shell burning, the final compactness can be quite complex. In § 2.4 the sensitivity of these results to uncertain assumptions in the physics used in two stellar evolution codes, `KEPLER` and `MESA`, is explored. These uncertainties, especially the treatment of semiconvection and convective overshoot mixing, lead to large variations in the final CO core mass that emerges for a given main sequence mass and account for much of the diversity of published results for presupernova evolution. Since these uncertainties cloud

the interpretation of the compactness plot, a further study is carried out in § 2.5 for bare CO stars using both codes. Provided the carbon mass fractions at carbon ignition are the same as in the full star models, the same trends seen previously for the compactness parameter are also found in these simpler cores, albeit with an offset due to surface boundary pressure in the full star. Thus the non-monotonicity of $\xi_{2.5}$ can be considered robust and the CO core mass is a somewhat better indicator of pre-supernova structure (and to some extent explosion dynamics) than the main sequence mass. Finally, § 2.6 offers some conclusions.

2.2 Surveys of presupernova evolution

The models published in previous surveys (e.g. Woosley *et al.*, 2007) were aimed at sampling supernova nucleosynthesis and light curves for a broad range of non-rotating stars. The resolution in mass necessary for that purpose was not particularly fine, so those studies have been repeated using the same code and physics, but with very fine mass grid.

For all runs, the convective time history was recorded and checkpoints registered at representative points along the evolution including: 1) helium depletion - when helium reached 1% by mass in the stellar center; 2) carbon ignition - when the central temperature was 5×10^8 K; 3) carbon depletion - when the central carbon mass fraction fell below 1%; 4) oxygen ignition - when the central temperature first reached 1.6×10^9 K; 5) oxygen depletion - when the central oxygen abundance declined to 4%; 6) silicon depletion - when silicon mass fraction reached 1% in the center; and 7) presupernova - when any point in the core collapsed faster than 1000 km s^{-1}. Subsequent discussion will refer to these points as representative of the stellar models

at these different times as He.dep., O.ign., preSN., etc.

2.2.1 Solar Metallicity Stars

The new survey (Fig. 2.2) includes non-rotating stars with solar metallicity and masses in the range 15 to 30 $M_\odot$ calculated in increments of 0.1 $M_\odot$using KEPLER (Table 2.1). Altogether, 151 models were simulated using the standard physics (§ 3.3.2, for variations see § 2.4). These models are collectively referred to as the "S series" stars - for "solar".

In addition to confirming the distinct "bump" previously seen around 23 $M_\odot$ the new study (Fig. 2.2) shows other interesting features. Fine scale variation of the compactness parameter persists throughout most of the mass range, but is particularly apparent between 19 and 21 $M_\odot$. These features are further explored in § 2.3.

For this series of models, $\xi_{2.5}$ is small for main sequence stars lighter than 22 $M_\odot$. It then rises rapidly to a peak, but declines again to lower values for main sequence masses between 26 $M_\odot$ and 30 $M_\odot$. Above about 30 $M_\odot$, results for these solar metallicity stars are clouded by the effects of mass loss reducing the helium core mass, but if mass loss is suppressed, the compactness stays large above 40 $M_\odot$ with a slight dip around 50 $M_\odot$ (Fig. 2.1 and § 2.2.2). These features pose a challenge to the conventional notion that the difficulty of exploding a star is a monotonically increasing function of its initial mass and instead imply that models below 22 $M_\odot$ and between 26 $M_\odot$ and 30 $M_\odot$ may be easier to blow-up than other masses. This could alter how we think about the galactic chemical evolution (Brown and Woosley, 2013).

For the assumed mass loss rates (Nieuwenhuijzen and de Jager, 1990), the entire hydrogen envelope is lost for stars with initial masses above 33 $M_\odot$. Heavier stars thus die

as Wolf-Rayet (WR) stars with smaller helium cores than would have existed had mass loss been neglected. For the mass loss rate adopted during the WR-phase (Wellstein and Langer, 1999), the core shrinks to the extent that the final compactness becomes small again, thus the compactness of very heavy massive stars when they die depends upon an uncertain prescription for mass loss.

In order to facilitate the comparison with low metallicity stars where the mass loss rate may be negligible, another series of solar metallicity models was calculated for stars above 30 $M_{\odot}$ in which mass loss was artificially suppressed. These are the "SH models" covering the mass range of 30 - 60 $M_{\odot}$ with varying increments - 31,32,33,35,40,..,60 $M_{\odot}$(Table 2.1). This survey was truncated at 60 $M_{\odot}$ because the effect of the pulsational pair instability became noticeable around 70 - 80 $M_{\odot}$. The 60 $M_{\odot}$ model of the SH-series has a helium core mass of 27.5 $M_{\odot}$ (Fig. 2.4), far greater than that of any of the solar metallicity stars calculated with mass loss.

2.2.2 Low Metallicity Stars

Stars with equal masses on the main sequence, but differing initial metallicity can have different presupernova structure for a variety of reasons. Most importantly, metallicity affects the mass loss. If the amount of mass lost is very low or zero, the presupernova star, including its helium core, is larger, and that has a dramatic effect on the compactness (Fig. 2.1). There are also other less dramatic, but important effects. Low metallicity implies a smaller initial helium mass fraction (and more hydrogen). The final helium core mass is sensitive to this and is reduced. Nitrogen has an abundance just prior to helium ignition that is directly propor-

tional to the initial metallicity and "nitrogen burning" by $^{14}N(\alpha,\gamma)^{18}F(e^{+}\nu)^{18}O$ is an important exoergic, convective phase in the star's life that precedes helium burning. Low metallicity affects the energy generation during hydrogen shell burning by the CNO cycle, and this affects the boundary conditions for the helium core. Low metallicity also affects the opacity, and the combined effects of opacity, energy generation, and mass loss determine if the star is a red supergiant or a blue one when it dies. This is especially true for the non-rotating stars studied here. The more compact radiative structure of a blue supergiant envelope places greater surface boundary pressure on the helium core therein and can affect its evolution.

To illustrate the systematics of compactness in stars of low metallicity, we include here a previously unpublished set of non-rotating presupernova stars by Heger and Woosley with metallicity of 10^{-4} $Z_{\odot}$. These used the same physics as the S series, but had an initial composition of 76% hydrogen and 24% helium with only a trace, 10^{-4} solar, of heavier elements. The masses of these stars were 10 to 95 $M_{\odot}$, though only a subset, 15 - 65 $M_{\odot}$, is considered here. This restricted set, called the U series, contains 86 models with varying mass increments ($0.2M_{\odot}$between 15 - $25M_{\odot}$, $0.5M_{\odot}$between 25-35 $M_{\odot}$, $1M_{\odot}$between 35 - $45M_{\odot}$ and $5M_{\odot}$between 45 - 65 $M_{\odot}$; (Table 2.1). Other details of these models not related to their compactness will be published elsewhere.

The compactness of these low metallicity models is shown, along with those from S and SH series, in Fig. 2.3. Without mass loss, a much larger range of helium and CO-core masses is accessible (Figure 4). One sees a continuation of the overall increase in compactness parameter with increasing mass all the way up to 65 $M_{\odot}$, but with new features. The compactness rises rapidly above 30 $M_{\odot}$ to a broad peak around 40 $M_{\odot}$ and then, following a dip at 50

$M_\odot$, resumes its rise. All of the stars above 30 $M_\odot$, with no mass loss, will probably be very difficult to explode by any solely neutrino-powered mechanism.

Below 30 $M_\odot$, the compactness curve for the U series shows non-monotonic structure with peaks qualitatively similar to those observed for the S series in Figure 2, but with an offset of about a solar mass. The offset is most pronounced in the range 20 - 25 $M_\odot$ where the compactness starts to rise in the U series for a lower value of main sequence mass. The main cause of this shift is the lower mass fraction of carbon produced by helium burning in the U stars (Fig. 2.5). That value, in turn, affects the critical mass where carbon ceases to burn convectively in the star's center (§ 2.3.1), shifting it to lower values, which causes the compactness curve to rise earlier (§ 2.3).

This variable nucleosynthesis of carbon for the S and U stars results from differing amounts of helium being mixed into the convective helium core as it grows during the final stages of helium burning. In fact, the carbon mass fractions for S and U stars in this mass range are very similar half way through helium burning, but as the helium mass fraction declines below 10%, the U stars are more effective at bringing additional helium in from their outer regions. Each helium convected down turns a carbon into an oxygen. The U stars have somewhat higher helium core luminosities at this point and the structure at the outer edge of the helium convection is also influenced by surface boundary pressure from the hydrogen envelope which is different for red and blue supergiants. Below 30 $M_\odot$, the U-series stars are blue supergiants while the S-series stars are red ones (Fig. 2.6). The pressure at the edge of the helium core does not decline as steeply in a blue supergiant and the entropy barriers inhibiting convection in the outer helium core are slightly reduced. This makes the growth of the helium convective core

easier. Convective dredge up in a red supergiant could also possibly reduce the helium core mass, though this effect seems to be small in the present models. With rotation, many of these lighter U-stars would also be red supergiants in the end because of primary nitrogen production at the hydrogen-helium interface, and the effect would be diminished. Above 30 $M_\odot$ the structure of the SH and U stars are very similar because both are red supergiants.

In the past, it has sometimes been assumed that the helium core mass uniquely determines the presupernova structure of a star and hence that structure would be roughly independent of the metallicity for two stars that made the same helium core mass. While this is qualitatively true, the figures here show that this assumption is not very accurate for supernova progenitors below 30 $M_\odot$.

2.2.3 Choice of Fiducial Mass and Time for Evaluating the Compactness

With the new surveys, it is possible to address a point of possible concern - the choice of mass (2.5 $M_\odot$) and time ("preSN model") for evaluating the compactness in equation 2.1. The full evolution of a massive star to the point that its iron core collapses and possibly powers an explosion is being characterized by a single number here. What motivates the choice of this particular point in space and time?

Ugliano *et al.* (2012) explored the effect of evaluating ξ at different fiducial masses and concluded that 1.75 $M_\odot$ might be a better discriminant of explosion characteristics rather than the 2.5 $M_\odot$ chosen here and in O'Connor and Ott (2011). The time of core bounce rather than initial collapse ("preSN") also seemed a more relevant time for its evaluation. Recently, O'Connor and Ott (2013) also examined the choice of 1.75 $M_\odot$, since the early neutrino signal

is more sensitive to the structure around the neutron star. Obviously smaller choices than 1.75 $M_\odot$ would not be sensible since they often lie *within* the collapsing iron core itself, and depend on different physics that occurs after that core has already reached high density, but what about values in between?

To address these questions, the collapse of the S series was continued until the central density reached $\rho_c = 5 \times 10^{11}$g cm^{-3}. This is about 100 times greater than the central density of presupernova S-series stars. Beyond this point, neutrino trapping and, ultimately, the nuclear equation of state, would influence the dynamics (Fig. 2.7). As expected, ξ rises with increasing central density since a smaller radius encloses the same mass. It also rises as the mass chosen for its evaluation decreases, since the average density enclosed by r increases faster than r^{-2}. Running `KEPLER` well beyond 5×10^{11} g cm^{-3} to nuclear density gives values of questionable accuracy, but strongly suggests that very little further evolution will occur in the compactness so long as the sampling mass remains greater than 1.75 $M_\odot$. As the figure shows, the compactness evaluated at 2.5 $M_\odot$ changes very little during the collapse from the presupernova star to high central density. At that larger radius, the hydrodynamical response time is longer than the time for the denser part of the core to collapse.

Substantial variation does occur, however, for smaller sampling masses. Smaller fiducial masses show a non-linear amplification of the structure in the compactness curve with time. Large values get much larger than adjacent smaller ones, suggesting the development of islands of stars that may be hard to blow up. This is due to the tendency of high density regions to collapse faster under the influence of their own gravity and is particularly apparent for stars in the 18 to 22 $M_\odot$ mass range. This may account for some of the variability in outcome seen by

Ugliano *et al.* (2012) for supernovae in this mass range.

The robustness of $\xi_{2.5}$ evaluated at 2.5 $M_\odot$, however, and its strong correlation with the compactness evaluated at smaller masses suggests that we can continue to use our standard choices of time and mass for its evaluation. It should be kept in mind, however, that structures that seem small in some of the plots for presupernova stars may become amplified by the further collapse.

2.3 Physical Basis of the Behaviour of the Compactness Parameter

Surveys of stellar evolution find a complex, non-monotonic behaviour for the compactness parameter as a function of main sequence mass and metallicity. Why is this so? Why doesn't the compactness vary smoothly with mass as it would in a polytrope with a single index?

Four factors drive the development of the compactness profile for massive presupernova stars. One obvious effect is the contraction of the core to higher densities in order to burn heavier fuels. This contraction increases the average density inside 2.5 $M_\odot$ and causes $\xi_{2.5}$ to grow with time. Another is the tendency of lighter stars to have lower entropy cores and be more degenerate. Degeneracy is responsible for the transition between stars that make planetary nebulae and those that make supernovae around 8 $M_\odot$, but the effects of degeneracy on the post-carbon burning evolution continue to be important throughout the entire mass range studied here. Third, as has been noted previously (Barkat, 1994; Timmes *et al.*, 1996), is the disappearance, around, 20 $M_\odot$, of central convective carbon core burning. Above 20 $M_\odot$, carbon fuses away without contributing a large excess of energy generation over what neutrinos

are carrying away in the center of the star.

Fourth and frequently overlooked (though see Barkat (1994)) are the effects of convective carbon and oxygen shell burning. Lighter stars can have three or more carbon burning shells in addition to core carbon burning (Fig. 2.8). As these stars evolve, their central regions become increasingly degenerate, especially after carbon depletion in the star's center, and, by oxygen ignition, the concept of a Chandrasekhar mass has some approximate meaning, especially for stars lighter than 30 $M_\odot$. Shells that burn outside the effective Chandrasekhar mass, roughly 1.7 $M_\odot$ depending on thermal corrections, but inside the point where the compactness is measured at 2.5 $M_\odot$, will considerably modulate the compactness parameter.

2.3.1 Evolution Through Central Carbon Depletion

Fig. 2.9 shows that $\xi_{2.5}$ remains nearly independent of the main sequence mass until after carbon ignites in the core. Prior to this time, the fiducial point at 2.5 $M_\odot$ lies well within a much larger star or helium core that can be characterized by a single polytropic index. The tendency of ρ_c to decrease as M^{-2}, as given by equation 2.2, is offset by the slight increase of the burning temperature with mass, resulting in a nearly flat curve.

By the time carbon has disappeared from the center of the star though, things have started to change. A pronounced dip in $\xi_{2.5}$ develops for the lower mass stars, and the curve shows an abrupt, small rise at 20 $M_\odot$. For current code physics and solar metallicity, 20 $M_\odot$ is the mass below which carbon burns convectively (exoergically) at the stellar center as opposed to radiatively (endoergically). Convection brings additional fuel into the burning region increasing the effective supply by approximately the ratio of the convective mass to the mass of the

burning region. Because of the high temperature sensitivity of the carbon fusion reaction, the energy generating region is small, so the enhancement is significant. During this longer time, neutrino losses carry away both energy and entropy, not only from the carbon convective core, but from the hot, overlying helium-rich layers supported by it. This loss of entropy exacerbates the natural tendency of lighter cores to have greater degeneracy and accelerates the development of a compact, white dwarf-like core structure - a dense degenerate core surrounded by a much less dense extended envelope.

As Fig. 2.10 makes clear, *central* carbon burning, by itself, is not the whole story though. Most of the increase in central degeneracy occurs after carbon has been exhausted in the star's center. It is during the period between central carbon depletion and oxygen depletion that neutrinos cool the core appreciably and, for masses below about 30 $M_{\odot}$, give it a white dwarf-like structure. During this long cooling-off time, contraction of the inner core is frequently held up by two, or even three vigorous carbon burning shells (Fig. 2.11), the first igniting shortly after carbon core depletion typically about 0.5 $M_{\odot}$ from the center. As we shall see, the presence and location of these shells is strongly correlated with how carbon burns in the center, so 20 $M_{\odot}$ remains a critical mass. It is ultimately the timing and location of these carbon convective shells, however, not just central carbon burning, that account for the structure developed during and after oxygen burning.

2.3.2 Carbon Shell Burning

Fig. 2.12 shows the evolution of the compactness parameter for the S series stars from the time carbon is depleted at the center of the star until oxygen is similarly depleted. This is a

critical period when the major features of the compactness emerge (Fig. 2.7).

The typically low values for $\xi_{2.5}$ below 18 $M_\odot$ result from the operation of the first two convective carbon shells (Fig. 2.11). While the star is supported by these shells, its inner regions radiate neutrinos and become cool and degenerate. The rapid variation of $\xi_{2.5}$ in the range 18 to 21 $M_\odot$ reflects the response of these three shells to the disappearance of the convective core. When that happens, *the first carbon burning shell disappears*, and the second and third convective shells move inwards dramatically in response to its loss. These events do not happen simultaneously. The center of the star ceases to be convective at 20.3 $M_\odot$, but the first shell has already gone out at 19.9 $M_\odot$. The second and third shells "migrate" inwards until this mass is reached, and then move outwards for bigger stars. The offsets in these masses and the rapid motion, first in, then out, of shells two and three underlie some of the complex structure in degeneracy and compactness seen around 20 $M_\odot$.

From 21 to 30 $M_\odot$, the compactness is most sensitive to whether, when oxygen core burning ignites, there is, or very recently has been an active carbon convective shell inside of about 2.0 $M_\odot$ (Fig. 2.13). An active shell supports the overlying star and relieves pressure on the oxygen core, allowing it to evolve as if it had a smaller effective mass. Smaller oxygen cores burn longer, emit more neutrinos, cool more effectively, and become more degenerate. The relevant carbon shell can either be the third (for 18 - 20 $M_\odot$) or the second (for 21 - 30 $M_\odot$) shell. If that shell is inside 1.4 $M_\odot$, the oxygen core lacks sufficient mass to ignite (**?**), so the most important mass range for the convective shell is 1.4 to 2.0 $M_\odot$.

The location of the boundaries of these convective carbon shells are given in Fig. 2.11. The third convective shell is given there as a solid curve only for the mass range where it has

a lifetime longer than one year. Shorter lived shells do not greatly affect the evolution prior to oxygen depletion. Based upon this criterion, the third shell only has a major effect in the range 19 to 21 $M_\odot$. For heavier stars, the second shell dominates (note that, for the sake of continuity, we persist in calling it the "second" shell even though the "first" convective shell has been replaced by radiative burning).

This behaviour is illustrated by the convective history during carbon and oxygen burning for stars of four masses: 20.0, 20.5, 23.0 and 28.0 (Fig. 2.13). None of these four stars experience central convective carbon core burning or "first shell" burning (in 20 $M_\odot$ there is a very tiny convective carbon core). The relevant carbon shells are thus "2" and "3", and they are labeled as such in the figure. At oxygen depletion, the 20.5 $M_\odot$ and 28.0$M_\odot$ models have small values of $\xi_{2.5}$ (0.13 and 0.15, respectively), while the 20.0 and 23.0 have larger ones (0.19 and 0.21).

In the 20 $M_\odot$ model, shells 2 and 3 complete their major burning about a year before oxygen ignites in the stellar center. Shell 3 is located at 1.32 $M_\odot$, which is too small to allow oxygen to ignite. Later, following a brief, inconsequential "blip" of convective neon burning, oxygen burning ignites in a core devoid of any nuclear energy sources out to more than 3 $M_\odot$. The entropy is higher and the degeneracy is less at both oxygen ignition and depletion (Fig. 2.10). Oxygen burning ignites late, with less than a year remaining in the star's life. Ultimately the star dies with a relatively large compactness parameter, 0.26.

The 20.5 $M_\odot$ model, though only slightly different in mass, has a very different evolution. The third carbon shell now has its base at 1.62 $M_\odot$ which is sufficiently large for oxygen burning to ignite before carbon shell burning is over. When oxygen does ignite at the center, the

resulting expansion extinguishes the carbon shell, leaving unburned carbon in the region outside 1.62 $M_\odot$. Some neutrino losses have already occurred in the oxygen before it ignited, but over the course of its burning, which commences much earlier than in the 20.0 $M_\odot$ model, more cooling occurs and the core becomes very degenerate. By oxygen depletion, the compactness parameter has a value of 0.13, which declines still further to 0.10 when the star dies.

For 23.0 $M_\odot$, the evolution resembles that of the 20.0 $M_\odot$ model more than it does the 20.5 $M_\odot$ model. By now, the third carbon shell is igniting so late as to be unimportant. Shell 2, burning at 1.33 $M_\odot$, however, again delays oxygen ignition to a late time. The oxygen burns in a core that, at the time has essentially no active burning shell except the helium shell far above it (off-scale). It is easier for the layers above the core to contract since there is a time with no active burning, neither core nor shell. Once it ignites, the oxygen core burns rapidly and at low density, producing a less degenerate silicon core. By oxygen depletion, the compactness parameter is 0.21 which rises to 0.42 in the presupernova star, the largest compactness of any model under 30 $M_\odot$.

For 28.0 $M_\odot$ and nearby masses, the evolution resembles that of the 20.5 $M_\odot$model, but with no third shell. The second shell has now moved out to 1.91 $M_\odot$ which is enough to allow core oxygen burning to ignite. There is always support by an active burning front, reducing the contraction of the outer core. Oxygen burning lasts longer and occurs in a core of smaller effective mass. The compactness at the end of oxygen burning is back down to 0.15, though this rises to 0.28 in the presupernova star.

Beyond 28 $M_\odot$, the second carbon shell continues to move out and the effective core mass when it ignites oxygen grows. When the shell crosses 2.5 $M_\odot$ at 30 $M_\odot$, the compactness

parameter rapidly increases once more. This marks the end of the epoch of carbon shells. All heavier stars will have large compactness parameters (Fig. 2.3) with relatively small variations introduced by the *oxygen* burning shells.

The location and strength of the carbon shells prior to oxygen depletion thus sculpt a highly variable result out of what was a comparatively smooth curve at carbon depletion. In some sense, 20.5 $M_\odot$ and 28 $M_\odot$ stars resemble each other more at death than do 20.5 $M_\odot$ and 20 $M_\odot$ stars. Above 30 $M_\odot$, the carbon shells lose their influence.

2.3.3 From Oxygen Depletion to Silicon Depletion

After oxygen finishes burning in the center, powerful convective *oxygen*-burning shells develop that can also modify the structure either by themselves, or by interacting with existing carbon shells. The continued evolution serves chiefly to amplify the features already present at oxygen ignition (Fig. 2.14). Having developed a degenerate core, further shell burning pushes matter out at 2.5 $M_\odot$ and reduces $\xi_{2.5}$. The location of the first oxygen shell at silicon depletion correlates tightly with $\xi_{2.5}$. Its base is located between 0.8 and 1.2 $M_\odot$ and is set by the extent of the oxygen convective core. Its extent correlates tightly with the location of its base. Similarly, the second oxygen shell, when there is one, sets atop the extent of the first. The farther out these shells and the later their ignition, the more extended the core, which results into a shallower density gradient around the iron core later on (higher $\xi_{2.5}$). The peak in $\xi_{2.5}$ in Fig. 2.14, around 23 to 25 $M_\odot$, is enhanced by the migration outwards in mass of this oxygen burning shell. Unlike the carbon burning shells, however, the outwards movement of the oxygen burning shell is not monotonic in mass, since the extent of the oxygen core varies

due to the effect of previous carbon shells. As it recedes inwards from 24 to 28 $M_\odot$, the $\xi_{2.5}$ curve declines, leading to a pronounced dip at 28 to 30 $M_\odot$. Above 30 $M_\odot$, the oxygen burning shells move out rapidly.

2.3.4 From Silicon Depletion to Presupernova

Fig. 2.15 shows that, while the peak in $\xi_{2.5}$ at 23 $M_\odot$ continues to grow due to core contraction and the operation of the oxygen shells, the principal qualitative change in $\xi_{2.5}$ during this final stage of the star's life is a "chopping up" of the peak that existed at silicon depletion around 20 $M_\odot$ into finer structures. Given that these structures will be amplified in the collapse (Fig. 2.7), they may yet affect the outcome of the explosion.

This rapid variation for a narrow range of masses results from an almost random decision by the star whether to burn oxygen or silicon in a shell first, the decision depending upon fine details of all that happened before. Fig. 2.16 shows the history of the convection following central silicon depletion in two stars of the S series with masses 20.1 and 20.2 $M_\odot$. Note especially the timing of the ignition of silicon shell burning compared with the growing extent of the strong oxygen burning shell with a base at 1.71 $M_\odot$ in the 20.1 $M_\odot$ star and 1.59 $M_\odot$ in the 20.2 $M_\odot$ star. In both stars this convective oxygen shell is very powerful, and eventually grows to include both the carbon and neon burning convective shells in one large aggregate shell shortly before the star dies. The oxygen shell in the 20.1 $M_\odot$ star drives a similar linking of convective layers and creates a large positive energy generation rate, but only *after* the silicon shell has already burned out and the star is close to collapsing. In the 20.2 $M_\odot$ star, on the other hand, the strong oxygen shell ignites *before* silicon shell burning and operates

for a much longer time.

In the 20.1 $M_\odot$ star, oxygen shell burning initially generates, only a limited convection zone that slightly alters the structure of the star before silicon shell burning ignites and slows the contraction. In the 20.2 $M_\odot$ star, the oxygen shell becomes strong first and has already engulfed a large fraction of the CO core before the silicon shell ignites. The 20.1 $M_\odot$ star ends up with a high $\xi_{2.5}$, the 20.2 $M_\odot$ star with a low one. The strong oxygen shell in the latter pushes matter out to larger radii and leaves a less extended structure inside.

This sensitivity of the presupernova compactness to the timing of oxygen and silicon shell burning suggests that a correlation might exist between the time from silicon core depletion to death and $\xi_{2.5}$. This is indeed observed (Fig. 2.17). The longer the strong oxygen shell supports the star after the initial iron core has formed from central silicon burning, the smaller $\xi_{2.5}$ for the presupernova star.

These energetic, merged oxygen, neon and carbon burning shells during the last hours of a massive star's life are a robust feature seen in many models of stars above about 15 - 20 $M_\odot$, both here and in previous studies (Woosley *et al.*, 1995; Tur *et al.*, 2007; Woosley *et al.*, 2007; Rauscher *et al.*, 2002). Their study would be an interesting, though perhaps challenging topic for 3D simulation.

2.3.5 Fine Scale Variations and Convergence

If such small differences in the central structure of the star at silicon core depletion can lead to major changes in presupernova structure, even for stars differing in mass by only 0.1 $M_\odot$, how sensitive might the results be to other "hidden variables", such as the time step criteria

and zoning. Fig. 2.18 shows that, for some masses, a substantial variation in outcome can also be caused by varying these variables. The location of the oxygen shell is a sensitive function of the many convective episodes that went on in the same star during its earlier evolution, and to the physics used to treat that convection.

As previously noted by Rauscher *et al.* (2002), this sensitivity to small changes is especially strong for the stars in the 19 to 21 $M_\odot$ range. To quantify this behavior better, a subset of the S series was calculated using the same code, compiler, and physics, but slightly altered zoning and time step criteria. In each case, the standard calculations were recomputed using 50% finer resolution (i.e., $2/3$ the default zone size), and, in separate calculations, the default time step was multiplied by $1/2$ and 2. Even these relatively small changes in operational parameters were frequently sufficient to provoke the star into two different final states. For comparison, we studied two distinct regions of main sequence masses, 17.1-17.5 $M_\odot$- region "A", and 20.1-20.5 $M_\odot$- region "B". As shown in Figure 2, the observed variations of $\xi_{2.5}$ in these two regions are quite different.

Panels 1A and 2A of Fig. 2.18 show that the solutions in region A are comparatively robust. Decreasing the time step and or changing the zoning does little to alter the final values of $\xi_{2.5}$. Increasing the time step by a factor of 2 does cause some mild variation $\Delta\xi_{2.5} < 0.05$. Panels 1B and 2B of Fig. 2.18, however, show a much more pronounced sensitivity near 20 $M_\odot$. The resulting values of $\xi_{2.5}$ seem to be bimodal. Small variations in mass, zoning, or time step can send the star down one path or the other. Typical models in the surveys used 20,000 time steps to reach the presupernova stage and employed approximately 1000 mass shells of variable thickness. It is certainly feasible to double or even quadruple both the resolution and time steps,

but the values used here are already conservative. To test the effect of finer time steps, the 21 S-series models from 19 to 21 $M_\odot$ were rerun with twice as many time steps. While $\xi_{2.5}$ for some individual stars did change significantly, the overall appearance of the pattern, including its rapid, but bounded variation between $\xi_{2.5} = 0.1$ and 0.25, did not.

2.3.6 Stars Over 30 $M_\odot$

Above 30 $M_\odot$, if mass loss is neglected, the structure of the core becomes much simpler. The carbon shells have moved far out and no longer affect the solution. The oxygen core is larger and the oxygen shells farther out. Because of the larger mass, the degeneracy is reduced and the compactness is always large.

The most notable feature above 30 $M_\odot$ is a pronounced dip in $\xi_{2.5}$ around 50 $M_\odot$. The dip is not large, but is seen in both the U-series and SH-series stars, albeit at slightly different masses (Fig. 2.3). It is also present in the compactness plot for the bare CO cores studied later in § 2.5.

This behaviour can be traced to the presence of a strong, extended convective oxygen burning shell during the post-silicon burning evolution of stars over about 50 $M_\odot$. The lighter stars lack this shell; the heavier ones have it. Starting at 50 $M_\odot$ for the U-series, this shell is present at silicon depletion with a base at 1.8 $M_\odot$. Moving to heavier masses, the shell grows larger and its base moves outwards, reaching 2.5 $M_\odot$ at 65 $M_\odot$. There is a sharp density decline at the base of the shell and because of this migration outside the fiducial point for measuring $\xi_{2.5}$, the compactness parameter rises again as the star mass passes about 60 $M_\odot$.

Whether this shell is present or not depends upon the timing of silicon core ignition

and oxygen shell burning. Recall the key role played by the carbon shell and oxygen ignition for stars in the range 21 - 30 $M_\odot$ (§ 2.3.2). When the carbon shell was situated far enough out, oxygen burning would ignite before carbon shell burning was done with major consequences for the compactness. Here, the oxygen shell plays the role of the former carbon shell. If it burns far enough out, the silicon core can ignite earlier. In this case, however, igniting silicon does not blow out the oxygen shell. It persists until the end.

Fig. 2.19 shows the locations of various silicon and oxygen burning episodes as a function of mass for the SH-series models. Though it lacks the time dimension of a full convective history plot, the figure shows that the size of the oxygen convective core increases monotonically with mass for these heavy stars. Where the oxygen convective shell ignites is pegged to the extent of that convective core. At about 50 $M_\odot$, the extent of the oxygen convective core passes the value needed to ignite silicon core burning. An oxygen shell ignites at the edge of that depleted core at about 1.8 $M_\odot$. This is sufficiently large that silicon core burning also ignites, and after that, silicon shell burning, but both ignite without putting out the oxygen shell. Indeed, the oxygen shell persists until the iron core collapses and forces the compactness parameter down.

Above 50 $M_\odot$, the compactness parameter continues to increase until about 70 $M_\odot$, where the onset of the pulsational pair instability becomes important (Heger and Woosley, 2010).

2.4 Sensitivity to Code Physics

Studies of massive stellar evolution by different groups yield substantially different presupernova structures and nucleosynthesis. A key quantity is the CO core mass. The yield of elements heavier than helium, for an energetic explosion, is the difference between the mass of the collapsed remnant (neutron star or black hole) and the CO core mass. As we shall see, the compactness is also quite sensitive to this quantity. Table 2.2 shows the disparate values for the CO core mass obtained by various groups studying the problem. For example, a 20 $M_{\odot}$ star may end up with a CO core of anywhere from 2.71 to 6.59 $M_{\odot}$ for various choices of convective physics and assumptions about rotation. Even for non-rotating stars the range is 2.71 to 4.99 $M_{\odot}$. Why are the values so different? Might using the CO core mass as a discriminant for the presupernova compactness alleviate some of the sensitivity to uncertain code physics?

The effect of rotation is not surprising. Rotation adds new mixing processes (e.g. Heger *et al.*, 2000) that increase the masses of both the helium and CO core. Shear mixing in differentially rotating stars can also erase some of the sensitivity to the treatment of semi-convection and convective shell boundaries. The large residual range of CO core masses in non-rotating stars reflects these uncertainties in the treatment of convection and warrants discussion.

2.4.1 Sensitivity to Semiconvection and Overshoot Mixing

Uncertainties in the treatment of convection for non-rotating massive stars can be lumped into three categories: a) the use of time-dependent mixing length theory (MLT) to de-

scribe the overall transport; b) uncertainties in semiconvection, i.e., what to do about stellar regions that are unstable to convection by the Schwarzschild criterion, but not the Ledoux criterion; and c) the treatment of convective boundaries (i.e., overshoot and undershoot). A detailed review is beyond the scope of this thesis. Most modern studies use time-dependent MLT, if only for the lack of a viable, implemented alternative. Semiconvection and convective overshoot can sometimes have similar effects since both allow convective regions on their tops and bottoms to grow smoothly when circumstances warrant it, and prevent the unrealistic fracturing of convective regions into multiple concentric shells. Semiconvection additionally slowly mixes regions that, owing to composition barriers, would not have mixed if the Ledoux criterion were strictly applied.

A relevant case in point is the convective helium core. It has been known for some time that the CO core mass is quite sensitive to the efficiency of semiconvection during helium burning (Langer *et al.*, 1989). In situations where semiconvection is very small (or zero), a mathematical instability can develop that leads to the bifurcation of the helium convective core and the production of an unusually small CO core. In an algorithm that looks at the composition to determine convective instability (i.e., Ledoux criterion), a single zone that is marginally unstable might temporarily become flagged as stable due to a trivially small increase in the mean atomic weight (helium plus carbon and oxygen) in the zone beneath. If this zone is flagged as stable against convection, burning during the next time step will increase the atomic weight farther in the region that is still convectively coupled to the burning at the center of the star without raising it in the outer core. This makes convection between the two shells even more difficult. The helium convective core splits permanently into two pieces. In the outer one, helium never

burns to completion and the resulting CO core for the star is small. If enough semiconvective mixing (or rotation) is included though, the splitting of the the convective core does not happen. In fact, considering the real situation in three dimensions, this numerical instability seems unphysical and should be avoided.

Overshoot mixing can also help bridge this artificial segregation. It also leads to an increased growth of the helium convective core at the end of helium burning that affects not only the CO core mass, but the carbon mass fraction when carbon burning ignites. Simulations by Meakin and collaborators (e.g. Meakin and Arnett, 2007; Viallet *et al.*, 2013) confirm that some type of mixing will always take place at convective boundaries defined by either the Ledoux or Schwarzschild criterion, although the exact formulation of this mixing remains uncertain.

The treatment of convective overshoot and semiconvection in KEPLER has been discussed previously (Weaver *et al.*, 1978; Woosley and Weaver, 1988; Woosley *et al.*, 2002). Semiconvection is parametrized by a diffusion coefficient that is manufactured from the local convective diffusion coefficient and the radiative one:

$$D_{SC} = q_r D_r D_c / (D_c + q_r D_r), \tag{2.3}$$

where D_C is the convective diffusion coefficient the zone would have had based upon the Schwarzschild criterion, and q_r is a free parameter that multiplies the radiative diffusion coefficient, D_r. Usually $D_c \gg D_r$ so that D_r dominates the transport. The actual value of q_r is not known, or even that such a simple formula captures the essential features of semiconvection. In past surveys using KEPLER, q_r has usually been taken to be 0.1, and, unless otherwise speci-

fied, that is the value used in this study. In practice, this generally assigns the semiconvective diffusion coefficient a value of near 10% of the radiative one.

Overshoot mixing is presently treated very crudely in KEPLER. Single zones at the top and bottom of regions flagged as unstable to Ledoux convection are slowly mixed with a diffusion coefficient given by equation 2.3. The convective diffusion coefficient is calculated based upon the Schwarzschild criterion:

$$w = \frac{dp}{P} - \frac{\Gamma_2}{1-\Gamma_2}\frac{dT}{T} \tag{2.4}$$

with w assumed to be a parametrized fraction,

$$w = q_{Ov} d\ln(T), \tag{2.5}$$

and with q_{Ov} having a default of 0.01. Typically the convective diffusion coefficient so calculated is much greater than $q_r D_r$ so that the mixing occurs on a time scale given by this quantity. This prescription lacks a physical basis, but at least allows convective zones the liberty of slowly growing into regions where mild entropy gradients would otherwise disallow mixing.

To explore the sensitivity of the compactness and the CO core mass to semiconvection and overshoot mixing, a subset of 16 solar metallicity models in the mass range of 15 to 30 $M_\odot$ was calculated multiple times using various settings for the both semiconvection and convective overshoot mixing multipliers. The masses studied were the integers from 15 to 30 and a total of 176 new models was calculated (Table 2.1 and Table 2.2). In these, the semiconvective multiplier, q_r, was varied from 0.001 to 0.1 (16 models each with q_r = 0.001, 0.0025, 0.005,

0.0075, 0.01, 0.0125, 0.015, 0.0175, 0.02, 0.05, and 0.075 in addition to the standard models with $q_r = 0.1$) and are collectively called SS series. Additionally, a set of 16 models was run with standard semiconvection ($q_r = 0.1$), but zero overshoot mixing (q_{Ov}) = 0 (SO series). All models were generated on the zero age main sequence and run until core collapse. The CO core mass does not change significantly after carbon depletion, however, and presupernova values can safely be compared with other studies that stop at an earlier time.

Fig. 2.20 shows that the compactness exhibits great deal of diversity depending on the efficiency of semiconvection. The mass resolution in these figures is significantly degraded by considering only 16 masses points between 15 and 30 $M_\odot$, but the location of the peak in $\xi_{2.5}$, when one exists, is clear. Reduced values of q_r give smaller CO cores, more than spanning the space of published values. The carbon mass fraction at carbon ignition is also affected by the choice of convection physics, both in response to the altered CO core mass and the mixing of helium at the outer boundary of the helium core that is altered when semiconvection is turned off. Consequently the compactness, which is quite sensitive to both the CO core mass and the carbon mass fraction, vary significantly.

For small reductions in q_r, the peaks found for $\xi_{2.5}$ in the standard runs is robust. Both the locations and amplitudes do not vary much. Though not explored, we expect that small changes upwards of q_r would have given similar results. When q_r declines below 0.02 however, significant changes occur. With smaller q_r, it takes a higher mass main sequence star to give a specific CO core mass, so the peak that was at 23 $M_\odot$ shifts rapidly to higher values, ultimately leaving the grid. By $q_r = 0.01$, the peak is no longer clearly discernible in the mass range examined.

Continued reduction in q_r (bottom panel, Fig. 2.20) results in a compactness curve that loses most of its non-monotonic structure and increases steadily with mass. However, such small values imply a CO core that is small compared with all previous studies in the literature (Table 2.2). For q_r = 0.001, the 15, 16 and 17 $M_\odot$ models closely resembled previous models calculated with KEPLER and other codes for stars with mass near 10 $M_\odot$ (Nomoto, 1987; Poelarends *et al.*, 2008; Wanajo *et al.*, 2009). Oxygen ignition occurs off center in these models and propagates as a convectively bounded flame to the stellar center (e.g. **?**). A similar result was obtained for q_r = 0.0025 for the 15 and 16 $M_\odot$ models. Such stars are known to have a very steep density gradient surrounding the iron core, which might be a boon to those trying to blow up stars in a wider mass range, but contribute almost nothing to the nucleosynthesis of intermediate mass elements. Were the observational limit on the maximum mass supernova to be pegged not far above 18 $M_\odot$ (Brown and Woosley, 2013), models of this sort would be inconsistent with the theory of stellar nucleosynthesis. A model with 12 $M_\odot$ and q_r =0.001 failed even to ignite oxygen burning and would likely become an AGB star with a degenerate neon-oxygen core and not a supernova. Since this would be in contradiction with a large volume of observational data showing that stars down to about 8 $M_\odot$ do explode, we must consider values of q_r much below 0.01 as unrealistic.

Turning off convective overshoot mixing in KEPLER also has a significant effect on the CO core mass and carbon mass fraction, though not so extreme as that caused by large variations in semiconvection (Table 2.2). Fig. 2.21 shows the CO core sizes and final presupernova $\xi_{2.5}$ of the SO-series models compared with those from S series. The elimination of overshoot reduces the CO core sizes (top-panel), and as a consequence, the $\xi_{2.5}$ curve is shifted to higher

masses. For example, central carbon burning shifts to being radiative at a higher mass compared to the S-series models with overshooting.

These results, which imply that the success or failure of exploding a presupernova model of given mass will vary appreciably depending upon who calculated the model and the description they used for convection physics, are troubling. However, semiconvection and overshoot mixing are real physical processes that will eventually be better understood. Some of the very small values for q_r used here may not be physically realistic (e.g. Biello, 2001) and the high threshold mass that they imply for making a supernova is inconsistent with observations. Zeroing overshoot mixing is also unrealistic. Bifurcation of the helium convective core probably does not occur. Real stars rotate, and rotationally induced mixing reduces the sensitivity to semiconvection and overshoot mixing. We believe that our standard choices for q_r and q_{Ov} (0.1 and 0.01) are a good compromise for non-rotating stars since they avoid the unphysical splitting of the convective core, agree reasonably well with the results for rotating models (Table 2.2), and are not presently at odds with any existing physical prediction. Clearly this is an area where more work is needed. See Zaussinger and Spruit (2013) and references therein for some recent insights.

Our results also suggest that $\xi_{2.5}$, and presupernova structure in general, will be more similar for two models having the same helium and CO core masses than for two that simply started with the same main sequence mass. Carrying this to the extreme, the outcome of the explosion of two stars with the same CO core mass will be more similar than for those having the same main sequence mass, but different CO core masses. Fig. 2.22 shows this to be approximately true. The offset in peaks seen in Fig. 2.21 for the stars calculated with and without

overshoot mixing is greatly reduced if $\xi_{2.5}$ is plotted against CO core mass rather than main sequence mass. Similarly, the large discrepancy with the S series found for low values of semi-convection (e.g., $q_r = 0.005$; Fig. 2.20) is significantly improved. Note that the allowed range of CO masses in the figure is much more limited for 15 to 30 $M_\odot$ stars if semiconvection is reduced significantly. Just what constitutes the "CO core mass" inside a massive star is ambiguous however, because there usually is no sharp decline of pressure at its edge (§ 2.5). Here we arbitrarily took the value inside of which the carbon mass fraction rose above 0.20. Differing values of the carbon mass fraction at carbon ignition due to changes in the initial composition or code physics must also be considered.

2.4.2 Survey of Solar Metallicity Stars Using MESA

Even similar physics often has different implementations in various stellar evolution codes, so to further explore the sensitivity of the compactness curve to the way it is calculated, we repeated part of our study using a completely different code. MESA (Paxton *et al.*, 2011; **?**; **?**) is a popular open source code for the study of stellar evolution, which has been successfully applied to a large variety problems in astrophysics, including some calculation of presupernova models (e.g. Paxton *et al.*, 2013; **?**; **?**). This work employed MESA version r4930 compiled with SDK 20120710. The code has been continually evolving and at the time of writing this thesis, it is at version r8118. However, we stress that none of the main findings of this work are affected.

The MESA models used similar nuclear physics to KEPLER for energy generation during hydrogen through oxygen burning and a very similar equation of state and opacity tables.

It can be constrained to use similar mass loss rates. Here the red giant mass loss rates of Nieuwenhuijzen and de Jager (1990) was used in both codes:

$$\log(\dot{M}) = -7.93 + 1.64\log(\frac{L}{L_\odot}) + 0.16\log(\frac{M}{M_\odot}) - 1.61\log(T_{eff}) \tag{2.6}$$

However, the two codes have quite different prescriptions for semiconvection and overshooting. Given the previous discussion, those differences can be expected to cause changes that might be educational. MESA also uses different nuclear physics during silicon burning and iron-core formation that affect the post-oxygen evolution. In particular, MESA continues to use a 19 isotope network to describe the energy generation and changes in composition after oxygen depletion, while KEPLER uses a 125 isotope "quasi-statistical equilibrium" (QSE) network (Weaver *et al.*, 1978). The latter is more stable and less prone to spurious temperature transients and is also able to follow accurately the appreciable changes in electron mole number that happen in these late phases.

Since the major features of the pre-supernova $\xi_{2.5}(M)$ curve, including the existence and location of peaks, have already been imprinted by oxygen depletion, we elected to compare the results of the two codes at that point, not for the pre-supernova star. This way, the post-oxygen burning differences are avoided and also the run time greatly reduced. The stars studied are a subset (Table 2.1) of our S series, that is, non-rotating stars with solar metallicity.

This version of MESA employed Ledoux convection. For the mixing length parameter, $\Lambda \equiv \alpha_{MLT} H_P$, the free parameter α_{MLT} was taken to be 2.0, which is within the range found in the literature. In those zones flagged as semiconvective, the Langer *et al.* (1983) model was

used. This calculates the diffusion coefficient as:

$$D_{SC} = \alpha_{SC} \left(\frac{2acT^3}{9\kappa\rho^2 C_P} \right) \frac{\nabla_T - \nabla_{ad}}{\nabla_L - \nabla_T}, \tag{2.7}$$

where C_P is the specific heat at constant pressure and the efficiency is tuned by the free parameter α_{SC}. We carried out a brief survey varying this parameter between 10^{-5}-10^{2}, and found its effect to be rather complicated. For the masses tested, this range of α_{SC} gave a spread of about $0.5M_\odot$ in the CO core mass, $1M_\odot$ difference in final mass, and a one order of magnitude change in radius. In general, for larger values (≥ 0.5) the MESA results approached that of the pure Schwarzschild case. The very low values, on the other hand, gave results that were very similar to one another, but quite different results were obtained using the larger values. The greatest sensitivity for the CO core size was found to be between 0.01 and 0.5. In our survey α_{SC} was taken to be 0.1 as a "midpoint" between these two extremes, which is also well within the range used in literature (e.g. Yoon *et al.*, 2006). We also note that the work to eliminate or greatly constrain this parameter is underway (Wood *et al.*, 2013; Spruit, 2013).

Overshoot mixing in MESA is accomplished either by fully mixing the zones flagged as overshooting ("step" overshooting) or by applying an exponential cutoff to the diffusion coefficient calculated for convection in zones that are unstable by the Ledoux or Schwarzschild criterion. In our survey we have employed the exponential decay formalism, that is:

$$D = D_{conv.} \exp(-2z/fH_P), \tag{2.8}$$

where $D_{conv.}$ is the diffusion coefficient from MLT, z is the height, and H_P, the pres-

sure scale height. The efficiency is then controlled by the free parameter f (see Herwig (2000), Paxton *et al.* (2011) for further details).

In general, the value of f is quite uncertain as well (Meakin *et al.*, 2011). A value of 0.016 was used by Herwig (2000) for his studies of AGB stars. Since the stellar context here is quite different, we have performed some additional test runs. The effects of five different choices for f ranging from 0 to 0.025 were explored (Table 2.2). In the end, a value of 0.025 was selected for detailed study since it produced very similar CO core sizes to the S-series models calculated using KEPLER (Fig. 2.23). A value as small as Herwig's had little effect and values much bigger than 0.025 resulted in the bump in compactness around 23 $M_{\odot}$ becoming very broadened and shifted to lower masses. Though our understanding of overshoot mixing is not adequate to rule this out, there was no compelling region to use larger values that would have given larger CO core masses for the heavier stars than previously published by others (Table 2.2).

Two sets of MESA models were ultimately calculated - one with overshooting (Mov series) and another without (M series). Each set had 16 models in the mass range of $15-30M_{\odot}$ with $1M_{\odot}$ increments, and both used the Ledoux criterion (Table 2.1). As expected, the results from KEPLER and MESA were nearly identical during hydrogen and helium burning, but started to diverge following helium depletion when the structure became more sensitive to the treatment of semiconvection and overshoot mixing.

As shown in Fig. 2.24, by carbon depletion, the discrepancy had become significant, especially around the critical mass for the extinction of central carbon convection, 20 $M_{\odot}$, and continued to grow during oxygen burning.

Fig. 2.23 and Table 2.2 show the comparison at oxygen depletion between the KEPLER S series and MESA Mov series. The quantity $\xi_{2.5}$ for the Mov series shows a non-monotonic structure similar to that in the S series, but shifted in mass by about 2 $M_\odot$. Since the CO cores are nearly identical for Mov- and S-series models, the difference must result from either a different composition at carbon ignition or a different treatment of convection after carbon ignites, or both.

The carbon mass fractions at carbon ignition are indeed different in the two studies. Mass fractions in the Mov series range from 0.34 to 0.24, declining roughly linearly as the mass rises from 15 to 30 $M_\odot$, while the corresponding limits for the S series are 0.21 to 0.18. The larger carbon abundance probably accounts for most of the shift in the peak of the Mov plot. As we shall see (§ 2.5), however, the treatment of post-carbon burning convection also matters. Even bare CO cores with identical initial compositions often have significantly different compactness when evolved to oxygen depletion in the two codes. The results from the M series are not shown in Fig. 2.23, but Table 2.2 shows that the resulting CO cores are much smaller, and the compactness thus differs appreciably, especially for the lighter stars.

Despite the shift, it is encouraging that the non-monotonic structure of $\xi_{2.5}$ as a function of mass in Fig. 2.23 and, qualitatively, the location of its peak, can be achieved using standard settings for convection physics in two very different codes. The study also highlights the dependence of the outcome on the CO core mass.

2.4.3 Sensitivity to Uncertain Nuclear Physics - $^{12}C(\alpha,\gamma)^{16}O$

Because of the sensitivity of the results to the carbon mass fraction at carbon ignition, outcomes will depend on the rates used for its creation and destruction. Three major reaction rates are involved, each of which has some associated uncertainty: 3α, $^{12}C(\alpha,\gamma)^{16}O$, and ^{12}C+^{12}C.

It is the competition of 3α and $^{12}C(\alpha,\gamma)^{16}O$ that sets the ratio of carbon to oxygen produced by helium burning. Increasing the former raises the carbon yield while increasing the latter makes it smaller. As we have shown, small reductions in carbon mass fraction tends to shift the compactness curve downwards, especially the critical mass, 20 $M_\odot$, above which carbon burns radiatively.

The effects of varying the three uncertain reaction rates on massive stellar evolution, and nucleosynthesis in particular, have been previously explored by Weaver and Woosley (1993), Tur *et al.* (2007), and West *et al.* (2013) for 3α, and $^{12}C(\alpha,\gamma)^{16}$ O and by Pignatari *et al.* (2013); Bennett *et al.* (2012) for ^{12}C+^{12}C, but none of these works explicitly focused on how these rates affect the *structure* of presupernova stars. We will not attempt a survey of all possibilities at the present time, but focus here on just the one rate for $^{12}C(\alpha,\gamma)^{16}O$.

Historically, the large possible range for this reaction rate has been a source, perhaps even *the* major source of nuclear physics uncertainty in massive stellar evolution. Recent developments (e.g. Schürmann *et al.*, 2012) have narrowed the error bar for this rate to less than 20%, which is not so much greater than the uncertainty in 3α (West *et al.*, 2013). For small errors in the rates, it is the ratio of these rates that matters most, so variation of $^{12}C(\alpha,\gamma)^{16}O$

can act, qualitatively, as a surrogate for exploring the uncertainty in 3α.

The standard value used in this study for $^{12}C(\alpha,\gamma)^{16}O$ is 1.2 times Buchmann (1996, 1997) who used S(300 keV) = 146 keV b; that is, our effective S-factor at 300 keV, near the Gamow energy for helium burning, is 175 keV b. Schürmann *et al.* (2012) now report laboratory measurements and analysis that gives S(300 keV) = 161 $\pm$ 19 stat - 2 sys + 8 keV b, or a range 0.9 to 1.3 times the Buchmann value. A subset of our S-series models was thus recalculated with varying multipliers on the Buchmann rate. Thirteen different masses of presupernova star were calculated in the mass range of 19 to 25$M_\odot$ (0.5$M_\odot$ intervals) for each multipliers of 0.7, 0.9, 1.3, 1.5 and 1.9 times the Buchmann rate. These are the SB series (Table 2.1).

Fig. 2.25 and Table 2.2 and Table 2.3 show the results. Decreasing the rate for $^{12}C(\alpha,\gamma)^{16}O$ significantly increases the carbon mass fraction at helium ignition, but affects the mass of the CO core very little. The greater (or smaller) carbon mass fraction shifts the peak in $\xi_{2.5}$, formerly seen at 23 $M_\odot$ for a multiplier of 1.2 to higher (or lower) values. For a multiplier of 1.9, the peak would disappear altogether, and is not plotted for clarity. However, such large values are outside the current experimental range. The current (1 σ) error bar for the rate translates into a multiplier between 0.9 and 1.3, but even this smaller range can shift the explodabilty of massive stars enough to have a dramatic potentially observable effect on presupernova masses and nucleosynthesis. A total uncertainty of less than 10% in the combined error of 3α and $^{12}C(\alpha,\gamma)^{16}O$ may be needed to pin down the mass range of supernovae that explode by the neutrino transport model to an accuracy of less than 2 $M_\odot$.

2.5 Surveys with Bare Carbon-Oxygen Cores

The importance of the CO core mass motivates a separate study of the compactness of presupernova stars evolved from *bare* CO stars of constant mass. It is to be emphasized that there is no direct correspondence between the results of evolving an isolated CO core and those obtained for a complete massive star with the same CO core mass embedded inside a helium core. The lack of a precipitous drop in density and pressure at the edge of a CO core inside a massive star results in an evolution that is qualitatively different. The definition of a CO core there, even by composition, is ambiguous (Hirschi *et al.*, 2004). How does one count a partly burned helium shell (and these are a common case)? Nevertheless, CO cores are simple to evolve and bypass the uncertainties associated with convection during the helium burning phase. If they display the same sort of compactness systematics seen for the full stars, one can have greater confidence in the result.

A total of 380 CO cores were evolved using both `KEPLER` and `MESA` (Table 2.1). `MESA` used $\alpha_{\rm MLT} = 2, \alpha_{\rm SC} = 0.1$ and f = 0.025 and `KEPLER` used $q_r = 0.1$ and $q_{Ov} = 0.01$. The calculations followed the evolution from central carbon ignition until the presupernova stage for the `KEPLER` cores and until the core oxygen depletion stage for `MESA` models. The core masses ranged from 3 to 25$M_\odot$ with varying increments: 0.1 $M_\odot$ increments were used for 3 to 10 $M_\odot$, 0.5 $M_\odot$ was used for 10 to 20 $M_\odot$, and 1 $M_\odot$was used for 20 to 25 $M_\odot$. CO core masses of 3 to 9 $M_\odot$ correspond, approximately, to the main sequence masses of 15 to 30$M_\odot$ studied in the S series. For low metallicity models (U series) or other models with no mass loss (SH series), the maximum CO core mass (at 65 $M_\odot$) was 25 $M_\odot$, and that sets the upper limit. The physics

used to calculate the CO core models was identical to that in the full star calculations.

The different mass fractions of carbon for the S and U stars (Fig. 2.5), however, necessitated separate surveys. Because of convection, the composition of a CO core of given metallicity and mass can be taken as roughly constant. A good fit to the abundances in Fig. 2.5 is

$$\begin{aligned} X(^{12}C) &= -0.037 \times \ln(M_{CO}) + 0.221 \quad \text{(U)} \\ X(^{12}C) &= -0.035 \times \ln(M_{CO}) + 0.253 \quad \text{(S)} \end{aligned} \tag{2.9}$$

The mass fraction of oxygen was $X(^{16}O) = 1 - X(^{12}C)$ in each case. These 4 sets of calculations are denoted as: KS, KU, MS and MU., i.e. - KS stands for `KEPLER` cores with initial composition from solar metallicity full stars (S Series), and MU stands for `MESA` cores with initial composition from low metallicity full stars (U series).

Fig. 2.26 shows $\xi_{2.5}$ at core oxygen depletion point for the 4 series (see also Table 2.1). The same sort of non-monotonic variation in $\xi_{2.5}$ seen previously in the full star models is evident in all cases but, as expected, cores with initial composition from U series (KU and MU), have their first peak at a lower mass than the cores with initial composition from solar metallicity stars (KS and MS). This same sort of offset was also seen in the $\xi_{2.5}$ curve for full stars of different metallicities (Fig. 2.3).

Above CO core masses of 11 $M_\odot$, the differences between runs using `KEPLER` and `MESA` are minimal. Below that, one sees similar structures for KS and MS, for example, but there are differences. The major peak for the KS stars at 7 $M_\odot$, is near 5.5$M_\odot$ for the MS

stars and the peak of KU stars is also shifted down about 1 $M_\odot$ in the MU stars. Even after removing the major dependence on CO core mass by running bare CO cores, there is still some residual difference resulting from the sensitivity of the location of carbon burning shells to convective and semiconvective physics in the two codes. The overall similarity of the patterns is encouraging, however. The compactness is non-monotonic with mass and there are regions of mass that will easier to explode than others.

The KEPLER calculations of CO cores were continued until the presupernova stage, and Fig. 2.27 shows the compactness parameter as a function of core mass for both the KS and KU series at this final stage. A comparison with Fig. 2.3 is interesting. The peaks at 22 and 23 $M_\odot$ in the full star models for the U and S series are reflected well in their equivalent mass CO cores, 5.8 $M_\odot$ and 6.2 $M_\odot$, respectively. The good agreement continues to heavier masses where the dip at 50 $M_\odot$ for the U-series appears as a dip at 18.5 $M_\odot$ in the KU-series. The mass of the CO core in the U-model 50 $M_\odot$ star was indeed 18.5 $M_\odot$. Similarly, although not so precisely, the CO core of the SH-series 55 $M_\odot$ star was 20.6 $M_\odot$, close to the dip at 24 $M_\odot$ seen in the lower panel of Fig. 2.27. The maximum mass CO core in the SH series was 27 $M_\odot$ for the 65 $M_\odot$ model. For the U series, the corresponding CO core mass was 26 $M_\odot$.

2.6 Conclusions

While characterizing the complex structure of a presupernova massive star with a single number is a gross over-simplification, considerable insight can be achieved by studying the systematics of the compactness parameter, $\xi_{2.5}$. The compactness of a given presupernova core

turns out to be sensitive to a variety of inputs, including not only the star's initial mass and composition, but the way convection is handled in the code, the nuclear physics employed, and the code used for the calculation. Stellar modeling, at least of massive stars, is, in a sense, a statistical science. Different groups will almost universally obtain different results for the structure and composition of a non-rotating presupernova star resulting from a given main sequence mass star, even without the complication of mass loss. However, for the same input physics, there should exist a robust pattern of results that can be sampled by running a large set of models. This is a study about one such pattern, the compactness parameter.

Our study confirms the non-monotonic nature of $\xi_{2.5}$ noted in previous works, and explores its causes. Fig. 2.7 shows that the choice of 2.5 $M_\odot$ as a fiducial point for evaluating the compactness, though arbitrary, is a good indicator of the behavior at other locations deep inside the star, but outside the iron core. Whether $\xi_{2.5}$ is evaluated at the "presupernova model ($V_{collapse}$ = 1000 km s^{-1}), or at core bounce matters little at 2.5 $M_\odot$, but for points deeper in, small variations seen in $\xi_{2.5}$ for the presupernova model are amplified during the collapse. Small variations in main sequence mass might therefore result in significant differences in outcome for an explosion model (Ugliano *et al.*, 2012).

Extensive new surveys of presupernova evolution are reported for both solar metallicity and low metallicity (10^{-4} $Z_\odot$) stars (§ 2.2; Table 2.1). While the emphasis here is on presupernova structure and compactness, this is clearly a rich data set for exploring nucleosynthesis and supernova explosion physics, and this will be done elsewhere. Major differences are found in the presupernova compactness for stars of the same initial mass, but different metallicity (§ 2.2.2). The most obvious differences result from the differing degrees of mass loss

expected for the two compositions, but there are subtle secondary effects involving the amount of helium convected into the helium core near central helium depletion. The growth of the helium convection zone results from a different structure at its outer edge which, in turn, is affected by the strength of the hydrogen shell, whether the star is a red or blue supergiant, and how much hydrogenic envelope remains following mass loss (in the solar metallicity stars). Even with mass loss suppressed, a substantial offset remains between presupernova stars of solar and low metallicity. Generally speaking, the low metallicity stars become difficult to blow up at a lower mass (Fig. 2.3) and may make more black holes.

The underlying cause for the non-monotonic behaviour of $\xi_{2.5}$ with initial mass derives from the interaction of carbon-burning and oxygen-burning shells with the carbon-depleted and, later, oxygen depleted core (§ 2.3). As has been noted previously, the end of convective carbon core burning at around 20 $M_\odot$ for standard stellar physics, has a major effect, but not so much due to the entropy decrease during central carbon burning itself as to the effect this has on the ensuing shells. Above 20 $M_\odot$, both central carbon burning and what was the first convective shell switch to radiative transport. Energy generation in excess of pair neutrino losses is unable to support core against further contraction, and the next two carbon convective shells are pulled down. Their gradual migration outwards again causes the rise and decline, and rise again of $\xi_{2.5}$ above 20 $M_\odot$. Above 30 $M_\odot$, $\xi_{2.5}$ rises to large values and, in the absence of mass loss, keeps on rising. There is an appreciable dip at about 50 $M_\odot$, though, due to the outward migration of the oxygen shell which essentially plays the same role as the carbon shells did for lower mass stars.

Broadly speaking, then, the evolution of massive stars separates into four mass inter-

vals characterized by similar values of $\xi_{2.5}$. For a standard choice of physics and solar metallicity these are stars from 8 to 22 $M_\odot$, 22 - 25 $M_\odot$, 25 - 30 $M_\odot$, and above 30 $M_\odot$(e.g., Fig. 2.3). Stars below 22 $M_\odot$ and between 25 and 30 $M_\odot$ have low $\xi_{2.5}$ and might more easily explode. Between 22 and 25 $M_\odot$and above 30 $M_\odot$, it will be more difficult for the traditional neutrino-transport model to succeed. There can be large variations within those ranges and not all stars lighter than 22 $M_\odot$ will be easy to explode (Ugliano *et al.*, 2012), but the distribution of stars that make black holes, for example, or important contributions to nucleosynthesis could be bi-modal. Galactic chemical evolution studies using such non-monotonic yields have yet to be done, but may give quite different results, e.g., for the s-process and oxygen synthesis (Brown and Woosley, 2013).

While the pattern seen in $\xi_{2.5}$ *vs* mass is robust, the locations of its peaks and valleys are sensitive to the treatment of semiconvection and convective overshoot in the code. These cause variations in the mass of the CO core and the carbon mass fraction when carbon burning ignites. Reducing semiconvection or convective overshoot makes the CO core smaller and this is a leading cause of the large variations seen in the literature for many studies of presupernova (Table 2.2). Smaller CO cores can mimic the effect of reducing the main sequence mass in a calculation where the convection physics is held constant and thus make cores with steep surrounding density gradients up to a higher mass. However these cores, while easier to blow up will be essentially nucleosynthetically barren. Extremely small values for semiconvective efficiency and overshoot mixing can lead to a discrepancy between the lightest stars expected to explode as supernovae based upon observations, about 8 $M_\odot$, and that calculated by theory. Caution must be exercised when using the CO core mass as a discriminant, however, because

the outcome is also very sensitive to the carbon mass fraction, and even to the treatment of convection after helium depletion.

Most of the models in this study were calculated using the KEPLER code, but the MESA code was also used to calculate the compactness curve at oxygen deletion where its essential features have already been determined. Reasonable agreement is achieved between the two codes provided that some amount of semiconvection and convective overshoot mixing is used in both. The non-monotonic nature of the compactness plot, in particular, is apparent in the results of both surveys.

The effects of varying the uncertain reaction rate for $^{12}C(\alpha,\gamma)^{16}O$ within its error range were also explored and found to have an appreciable effect. A total error of just 10% in the combined error for 3 α and $^{12}C(\alpha,\gamma)^{16}O$ can shift features in the compactness plot by a solar mass or more. To the extent the compactness is related to the difficulty of exploding a given model using neutrinos, the changes for nucleosynthesis and supernova "cut-off mass" are significant at that level.

Because the CO core mass plays such a major role in determining $\xi_{2.5}$, we explored its systematics using a grid of "bare" CO-cores. These differ from the CO cores of massive stars which are defined by composition changes and do not have sharp declines in density and pressure at their edges. Nevertheless, the same non-monotonic compactness curve results. This both confirms the robustness of the $\xi_{2.5}$ relation found in the other surveys and suggests that, for a given presupernova model, its final CO core mass, not its main sequence mass might be a more accurate structural indicator. The same behavior was found for CO cores studied using MESA. Picking the CO core mass circumvents some, though certainly not all of the uncertainty

introduced by ambiguous treatments of semiconvection and convective overshoot mixing during core helium burning. For WR stars and other stars that have experienced severe mass loss, the presupernova CO core mass will be the best indicator of presupernova structure. Even for bare CO cores, however, the mass fraction of carbon at carbon ignition remains an important "hidden variable" that will be sensitive to both the code physics and the metallicity of the star.

While this study has emphasized the relation between compactness of the core and its explodability in terms of the neutrino transport model, the results are actually more general. Fig. 2.28 shows the binding energy of the matter outside of the iron core of the presupernova star as a function of its compactness. Stars with larger values of $\xi_{2.5}$ will be more difficult to explode by *any* mechanism, both because of the higher ram pressure immediately after collapse and the larger energy needed to eject the matter outside the iron core.

Table 2.1: Calculations

Code	series	evolution	mass-range	# of models	comments
KEPLER	S	ZAMS-5 $\times 10^{11}$gcc	15-30	151	default
$\cdots$	SH	ZAMS-preSN	30-60	9	no mass-loss
$\cdots$	U	ZAMS-preSN	15-65	86	$10^{-4}Z_{\odot}$, no mass-loss
$\cdots$	SS	ZAMS-preSN	15-30	176	weak semiconvection
$\cdots$	SO	ZAMS-preSN	15-30	16	no overshooting
$\cdots$	SB	ZAMS-preSN	19-25	65	varied $^{12}C(\alpha,\gamma)^{16}O$
$\cdots$	KS	C.ign-preSN	3-25	95	CO core with S composition
$\cdots$	KU	C.ign-preSN	3-25	95	CO core with U composition
MESA	M	ZAMS-O.dep	15-30	16	default

Table 2.1 (cont'd): Calculations

Code	series	evolution	mass-range	# of models	comments
···	Mov	ZAMS-O.dep	15-30	16	with overshooting
···	MS	C.ign-O.dep	3-25	95	CO core with S composition
···	MU	C.ign-O.dep	3-25	95	CO core with U composition

Table 2.2: He Core and CO Core Sizes

$15M_\odot$		$20M_\odot$		$25M_\odot$		boundary criteria		comments	References
M_α	M_{CO}	M_α	M_{CO}	M_α	M_{CO}	M_α	M_{CO}		
4.84	2.97	7.17	4.94	9.65	7.20	$X_H = 0.01$	$X_{He} = 0.01$ (?)	$\alpha_{ov} = 0.2$	Maeder (1992)
4.0[1]	2.02	6.0[1]	3.70	8.0[1]	5.75	$max(\epsilon_{nuc})$ in shells		$\alpha_{ov} = 0.0$	Thielemann *et al.* (1996)
4.21	2.44	6.27	4.13	8.50	6.27	$X_{He} = 0.75$	$X_{He} = 0.01$	$\alpha_{ov} = 0.1$	Hirschi *et al.* (2004)
5.68	3.76	8.65	6.59	10.0	8.63	$X_{He} = 0.75$	$X_{He} = 0.01$	and rotation	Hirschi *et al.* (2004)
3.85	2.19	5.70[2]	3.54	5.18	7.73	$X_H = 0.001$	$X_{He} = 0.001$		El Eid *et al.* (2004)
4.97	2.56	7.31	3.83	9.80	5.48	$max(\epsilon_{nuc})$ in shells		$\alpha_{ov} = 0.2, \alpha_{sc} = 0.02$	Chieffi and Limongi (2013)
5.37	3.59	WR[3]	5.53	WR[3]	6.63	$max(\epsilon_{nuc})$ in shells		and rotation	Chieffi and Limongi (2013)
4.35	3.14	6.21	4.93	8.25	6.95	$X_H = 0.2$	$X_{He} = 0.2$	$q_r = 0.1, q_{ov} = 0.01$	KEPLER,S
4.44	3.14	7.18	5.61	9.07	7.35	$X_H = 0.2$	$X_{He} = 0.2$	and rotation	KEPLER

Table 2.2 (cont'd): He Core and CO Core Sizes

$15M_\odot$		$20M_\odot$		$25M_\odot$		boundary criteria		comments	References
M_α	M_{CO}	M_α	M_{CO}	M_α	M_{CO}	M_α	M_{CO}		
4.29	3.08	6.27	4.99	8.50	7.18	$X_H = 0.2$	$X_{He} = 0.2$	$q_r = 0.05, q_{ov} = 0.01$	KEPLER, SS
4.15	2.93	6.22	4.59	8.40	6.39	$X_H = 0.2$	$X_{He} = 0.2$	$q_r = 0.015, q_{ov} = 0.01$	KEPLER, SS
4.09	1.96	6.00	2.95	8.30	4.40	$X_H = 0.2$	$X_{He} = 0.2$	$q_r = 0.005, q_{ov} = 0.01$	KEPLER, SS
3.98	1.63	6.08	2.71	8.42	4.11	$X_H = 0.2$	$X_{He} = 0.2$	$q_r = 0.001, q_{ov} = 0.01$	KEPLER, SS
-	-	6.22	4.96	8.28	7.00	$X_H = 0.2$	$X_{He} = 0.2$	$1.5\times$Buchmann	KEPLER, SB
-	-	6.21	4.90	8.26	6.98	$X_H = 0.2$	$X_{He} = 0.2$	$1.3\times$Buchmann	KEPLER, SB
-	-	6.17	4.96	8.23	6.99	$X_H = 0.2$	$X_{He} = 0.2$	$0.9\times$Buchmann	KEPLER, SB
-	-	6.16	4.94	8.21	6.99	$X_H = 0.2$	$X_{He} = 0.2$	$0.7\times$Buchmann	KEPLER, SB
4.19	2.70	6.11	4.38	8.14	6.27	$X_H = 0.2$	$X_{He} = 0.2$	$q_r = 0.1, q_{ov} = 0.0$	KEPLER, SO

Table 2.2 (cont'd): He Core and CO Core Sizes

$15M_\odot$		$20M_\odot$		$25M_\odot$		boundary criteria		comments	References
M_α	M_{CO}	M_α	M_{CO}	M_α	M_{CO}	M_α	M_{CO}		
3.77	1.96	5.81	3.47	7.31	3.91	$X_H = 0.2$	$X_{He} = 0.2$	$f = 0.001$	MESA, M
4.01	2.21	-	-	7.80	5.16	$X_H = 0.2$	$X_{He} = 0.2$	$f = 0.005$	MESA
4.20	2.39	-	-	8.06	5.47	$X_H = 0.2$	$X_{He} = 0.2$	$f = 0.01$	MESA
4.41	2.61	-	-	8.34	5.81	$X_H = 0.2$	$X_{He} = 0.2$	$f = 0.015$	MESA
4.85	3.05	6.92	4.77	9.28	6.84	$X_H = 0.2$	$X_{He} = 0.2$	$f = 0.025$	MESA, Mov

Note. — q_r-eq. (2.3); q_{Ov}-eq. (2.5); α_{sc}-eq. (2.7); f-eq. (2.8); α_{ov} - is the multiplier on the pressure scale height.

[1]Calculations for bare helium cores.

[2]Averaged from 5 different values with varying reaction rates and convection physics for the $25M_\odot$ model.

[3]Lost all of its hydrogenic envelope.

Table 2.3: X(^{12}C) and $^{12}C(\alpha,\gamma)^{16}O$

Multiplier[1]	19 $M_\odot$	22 $M_\odot$	25 $M_\odot$
1.9	0.132	0.120	0.110
1.5	0.183	0.171	0.161
1.3	0.212	0.200	0.193
1.2	0.229	0.218	0.209
0.9	0.286	0.276	0.270
0.7	0.335	0.325	0.320

Note. — Evaluated at central helium depletion for the KEPLER SB series.

[1]Multipliers times the Buchmann (1996, 1997) rate.

Table 2.4: Critical Masses for Central Carbon Burning

Series	ZAMS Mass [$M_\odot$]	CO Core Mass [$M_\odot$]
S (KEPLER)	20.3	5.03
U (KEPLER)	18.6	4.27
Mov (MESA)	23.0	5.47
M (MESA)	28.5	4.86
KS (KEPLER)		5.3
KU (KEPLER)		4.6
MS (MESA)		4.6
MU (MESA)		3.9

Note. — The CO core boundary is defined as location where ^{4}He drops below 0.2 in mass fraction.

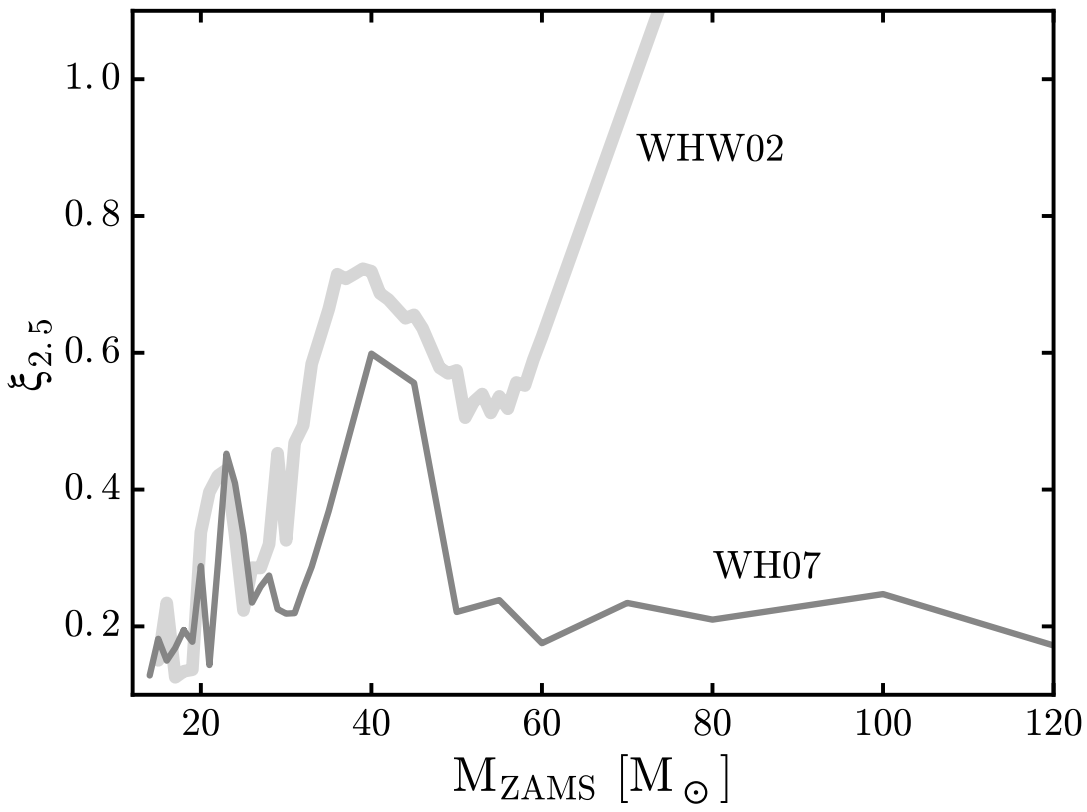

Figure 2.1: The compactness parameter as a function of mass for the very low metallicity (10^{-4} $Z_\odot$) models from Woosley *et al.* (2002) (light gray) and for the solar metallicity models from Woosley *et al.* (2007) (dark gray). See also Fig. 2.9 of O'Connor and Ott (2011). Note the non-monotonic behavior in both sets of models around 25 $M_\odot$and 40 $M_\odot$. Since the mass loss was ignored in the low metallicity models, the mass of the CO core and the compactness continues to increase for those models at very high masses.

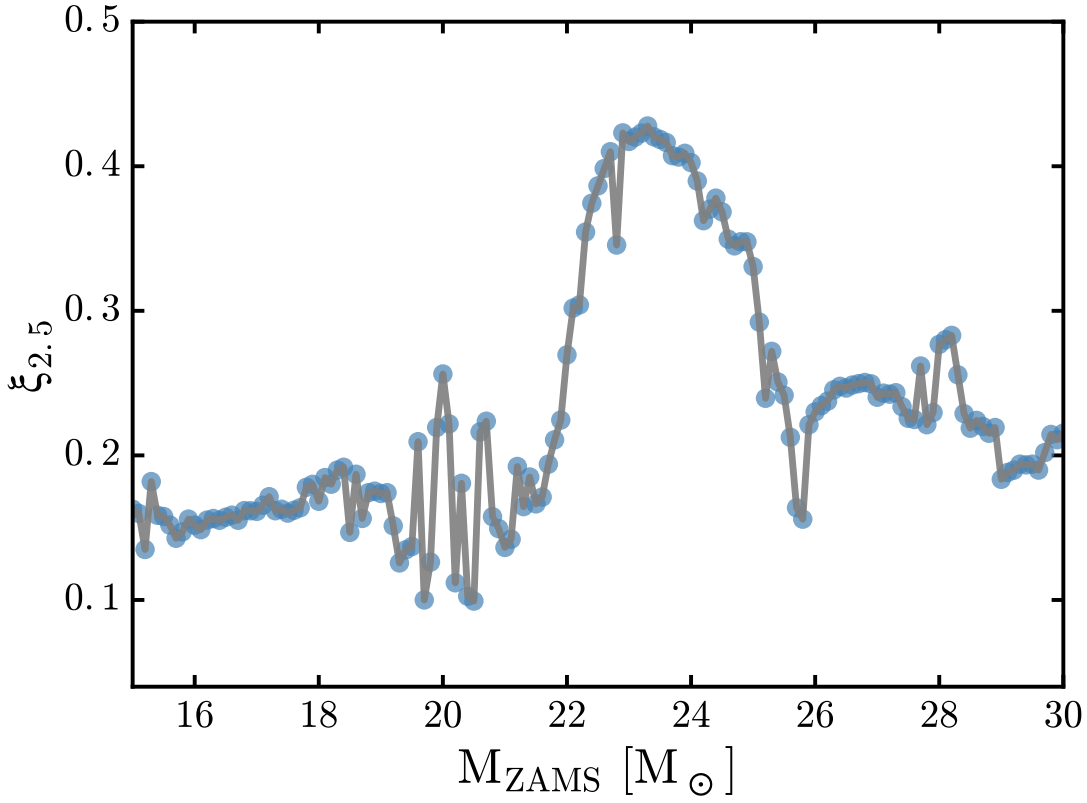

Figure 2.2: The core compactness determined for 151 KEPLER presupernova models (blue circles) derived from solar metallicity stars of the given masses (the "S series"). $\xi_{2.5}$ is evaluated when the collapse speed anywhere in the iron core first reaches 1000 km s^{-1} (see Fig. 2.7 for other choices). Notice especially the low values of $\xi_{2.5}$ for stars lighter than 22 $M_\odot$, the irregular variations from 18 to 22 $M_\odot$, and the subsequent rise to a maximum at 23 - 24 $M_\odot$ followed by a decline. For heavier stars additional structure, including a second rise, is found at higher masses (Fig. 2.3).

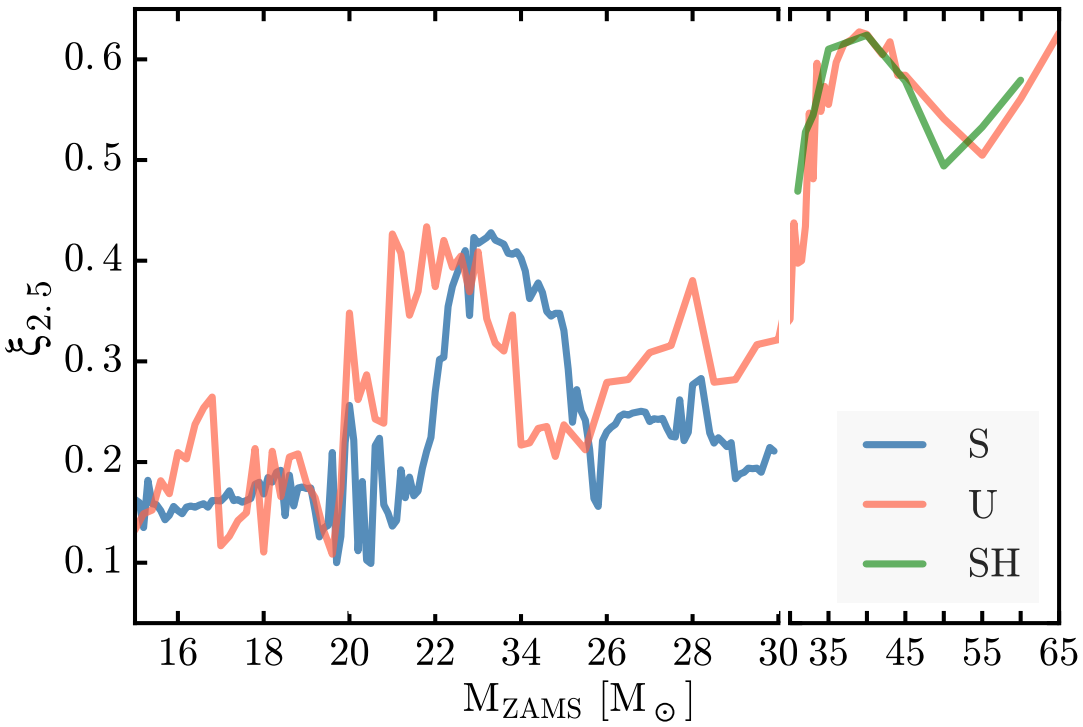

Figure 2.3: The final core compactness parameters evaluated at 2.5$M_\odot$ are shown for the S-series (solar metallicity; blue) and U-series (10^{-4} solar metallicity; red) and SH-series (solar metallicity, no mas sloss; green) models. For masses less than 30 $M_\odot$, notice a slight shift of $\xi_{2.5}$ near the first "bump" between S- and U-series.

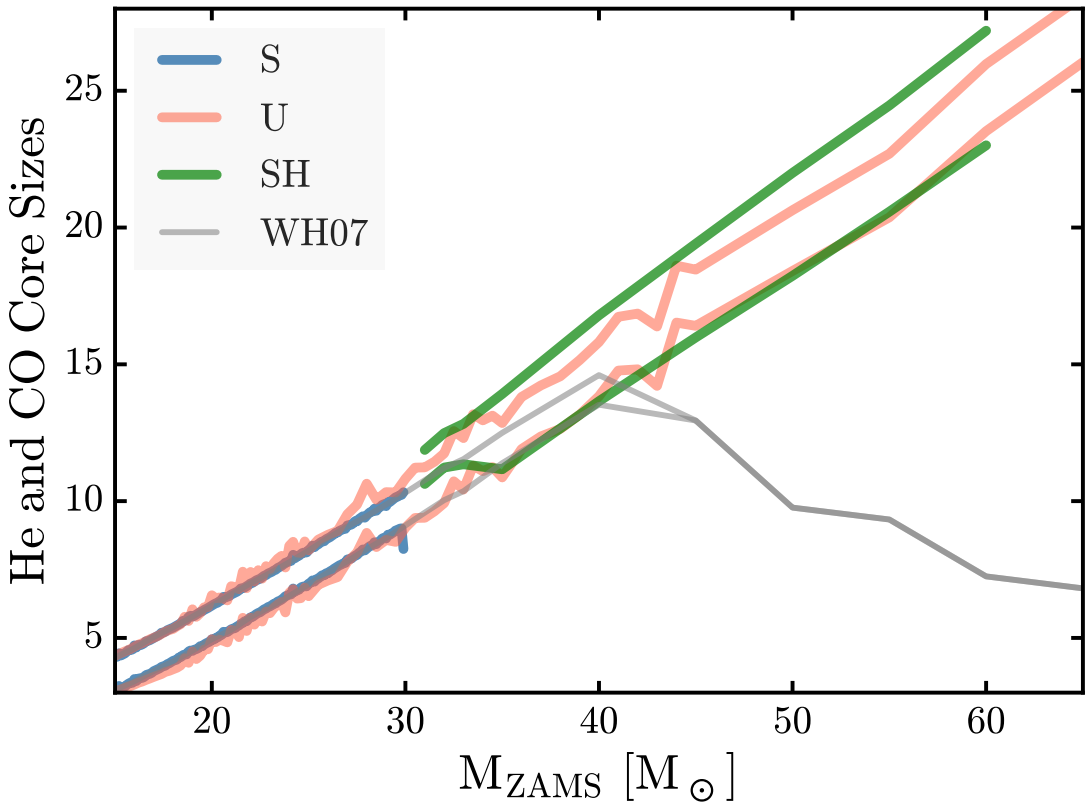

Figure 2.4: Core masses are shown as a function of initial mass for the new surveys in comparison with solar metallicity survey of WH07. Below 35 $M_{\odot}$, the core masses are not very sensitive to metallicity and since the input physics are identical for S and WH07, all curves look indistinguishable. Above 35 $M_{\odot}$, U and SH models diverge from WH07 due to reduced mass loss in the former, and the small variation of helium core masses between U and SH models suggest that core masses are not very sensitive to metallicity. Also the helium core is somewhat larger for the higher metallicity stars reflecting a more active hydrogen-burning shell during helium burning.

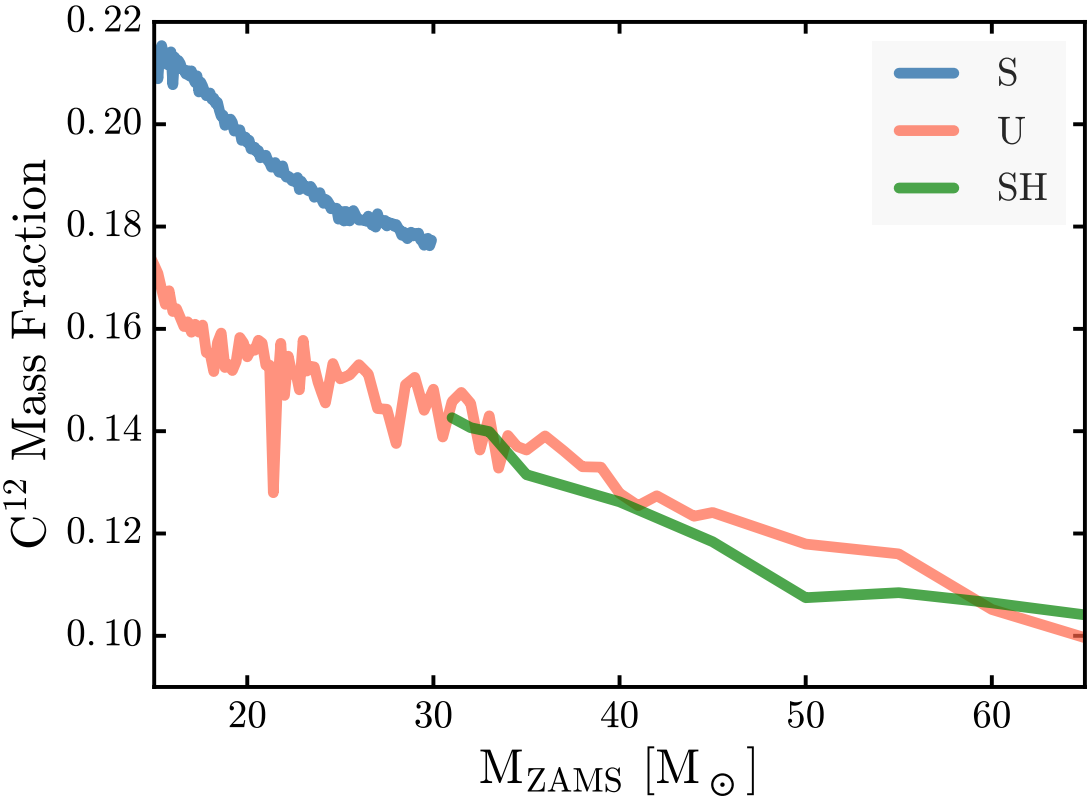

Figure 2.5: The ^{12}C mass fraction at the time of core carbon ignition is shown for S (blue), SH (green) and U (red) stars. Note that the carbon mass fraction is smaller in stars that ignore mass loss and that the SH series tracks the U series very well.

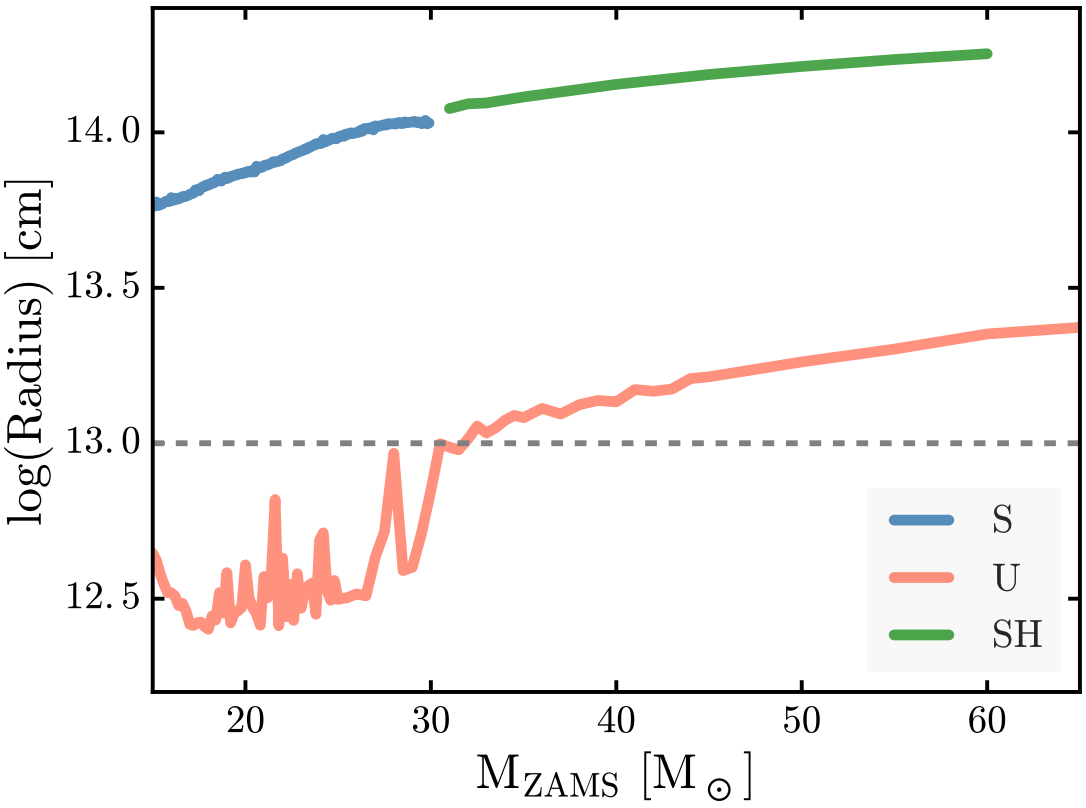

Figure 2.6: Final radii of the presupernova stars are shown from different surveys - S (blue), SH (green) and U (red). The dashed horizontal line marks the approximate size limit of a red supergiant, thus U-stars below about 30 $M_{\odot}$ are ending their lives as blue supergiants.

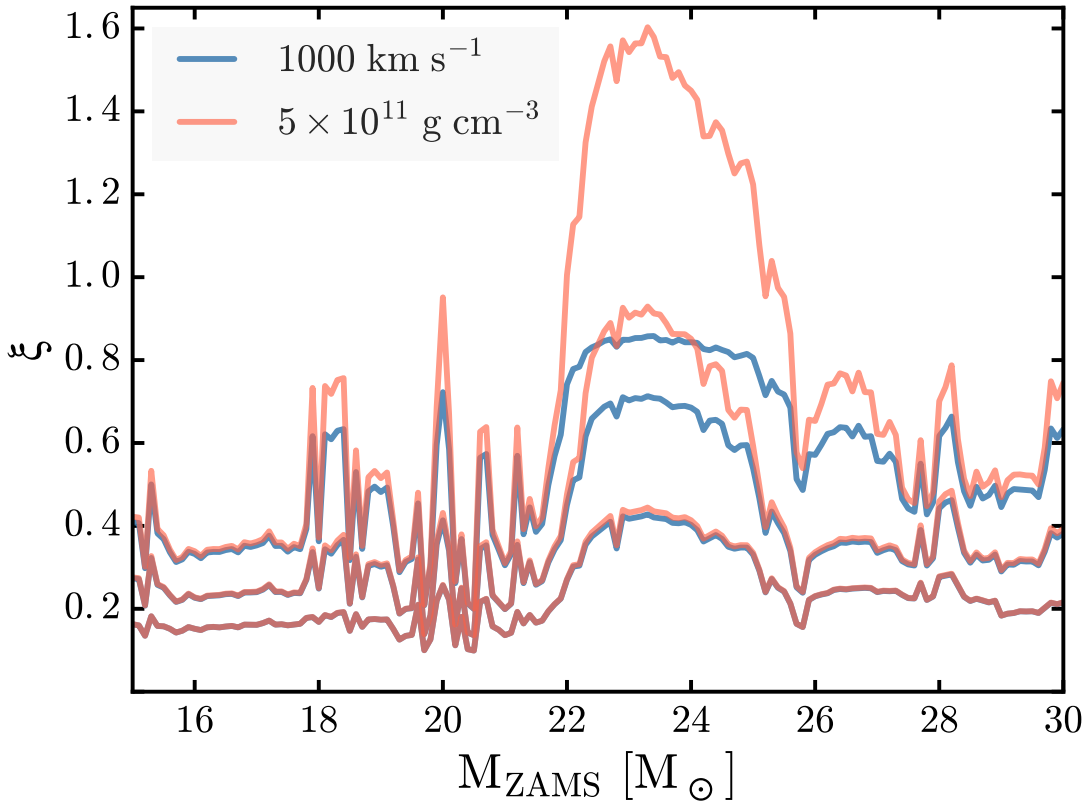

Figure 2.7: Presupernova compactness for the S-series models evaluated when the infall speed reaches 1000 kms^{-1} (blue), and later when the central density reaches 5×10^{11} g cm^{-3} (red). Each pair of curves represent ξ evaluated at the same time in evolution, but at different points in fiducial mass: 1.75 $M_\odot$(top), 2.0 $M_\odot$ (middle) and the default 2.5 $M_\odot$ (bottom). Little evolution occurs during the collapse from about 5.5×10^9 g cm^{-3} to 5×10^{11} g cm^{-3} if the compactness is evaluated at 2.5 $M_\odot$, but for smaller fiducial masses the contrasts seen at 2.5 $M_\odot$ are significantly amplified with time.

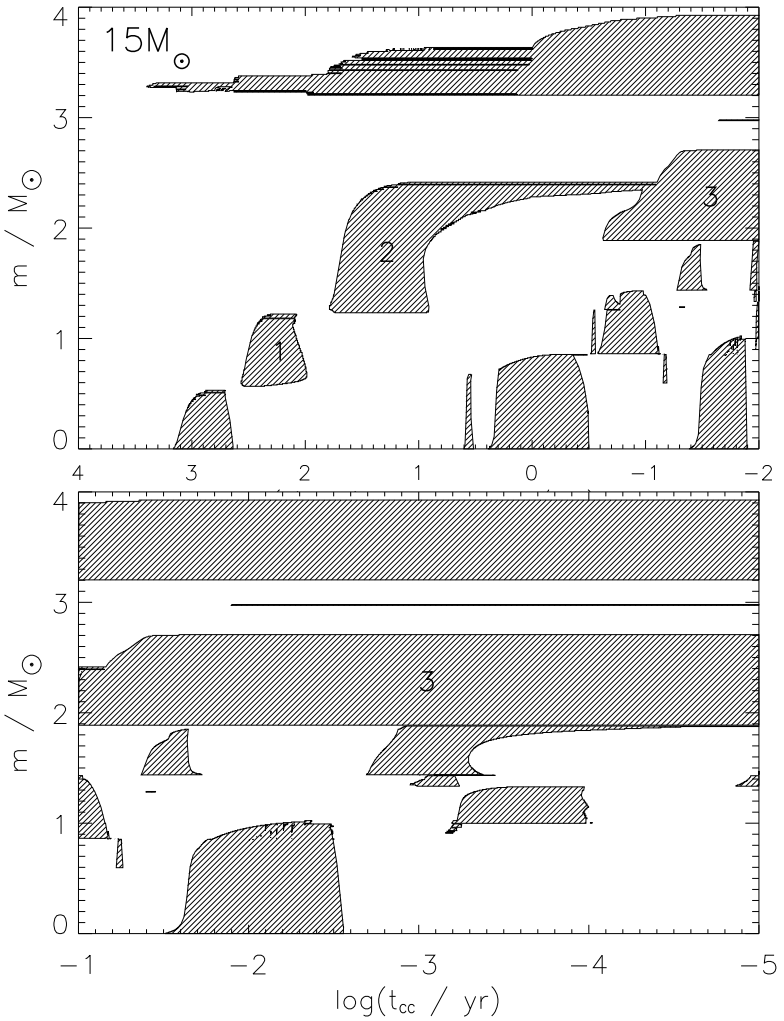

Figure 2.8: Convective history of a 15 $M_\odot$ model, a typical supernova mass, (top:) from carbon burning until silicon shell ignition, and (bottom:) from the end of first oxygen shell burning until 5 minutes before collapse. Only the inner 4 $M_\odot$ is plotted and the time axis is plotted as the logarithm of time until iron core collapse (t_{cc}) measured in years. Cross hatched regions indicate convection and integer numbers annotate convective carbon burning shell episodes. The convective carbon core burning starts about 1000 years before death and is followed by three episode of carbon shell burning. Oxygen burning starts about two years before death and is preceded by a brief stage of neon burning. Silicon burning is the last convective episode in the center. At silicon depletion, no oxygen shell is active, only a carbon shell at about 1.9 $M_\odot$. Shortly afterwards though, the third oxygen shell ignites in the incompletely burned ashes of the second shell. This final vigorous shell merges with the carbon and some neon burning shells shortly before the star dies. The operation of these shells, especially the ones between 1.5 and 2.5 $M_\odot$, affects the compactness parameter.

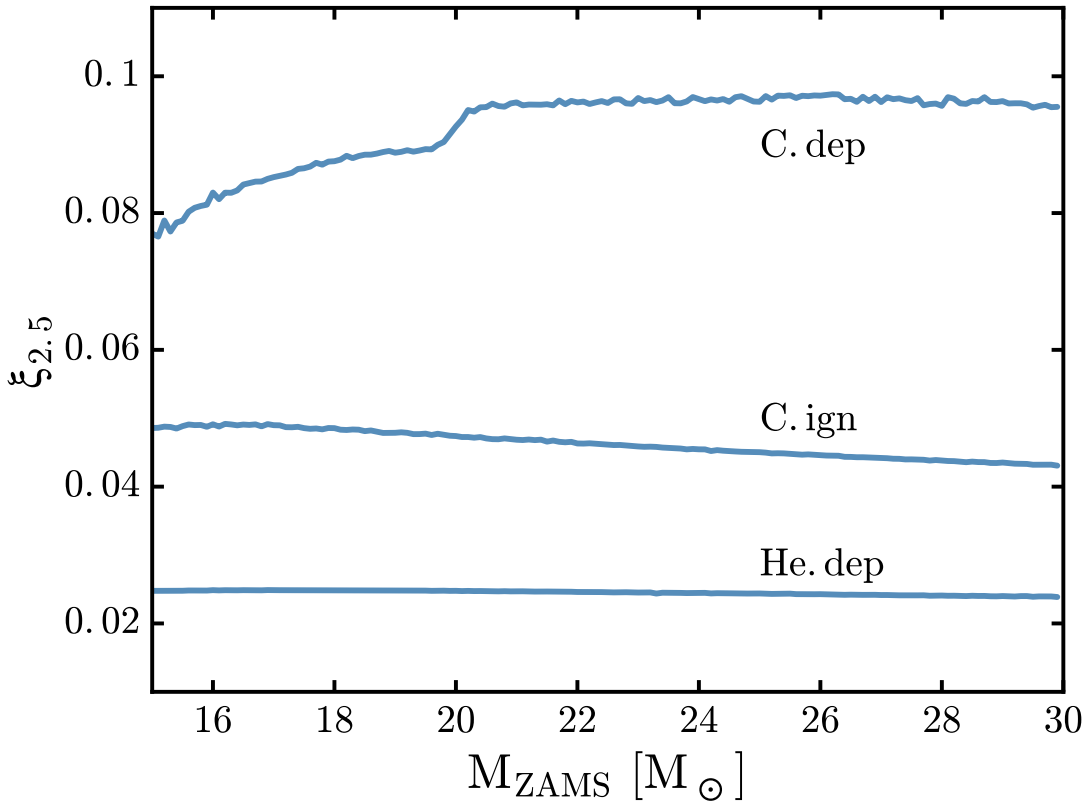

Figure 2.9: The evolution of $\xi_{2.5}$ as a function of main sequence mass for the S series models up to the point when the carbon mass fraction decreases below 1% in the center of the star ("C.dep"). At each successive stage, the star has contracted to higher density and the average curve for $\xi_{2.5}$ rises. Below about 20 $M_\odot$ carbon burns convectively in the core and this reduces $\xi_{2.5}$.

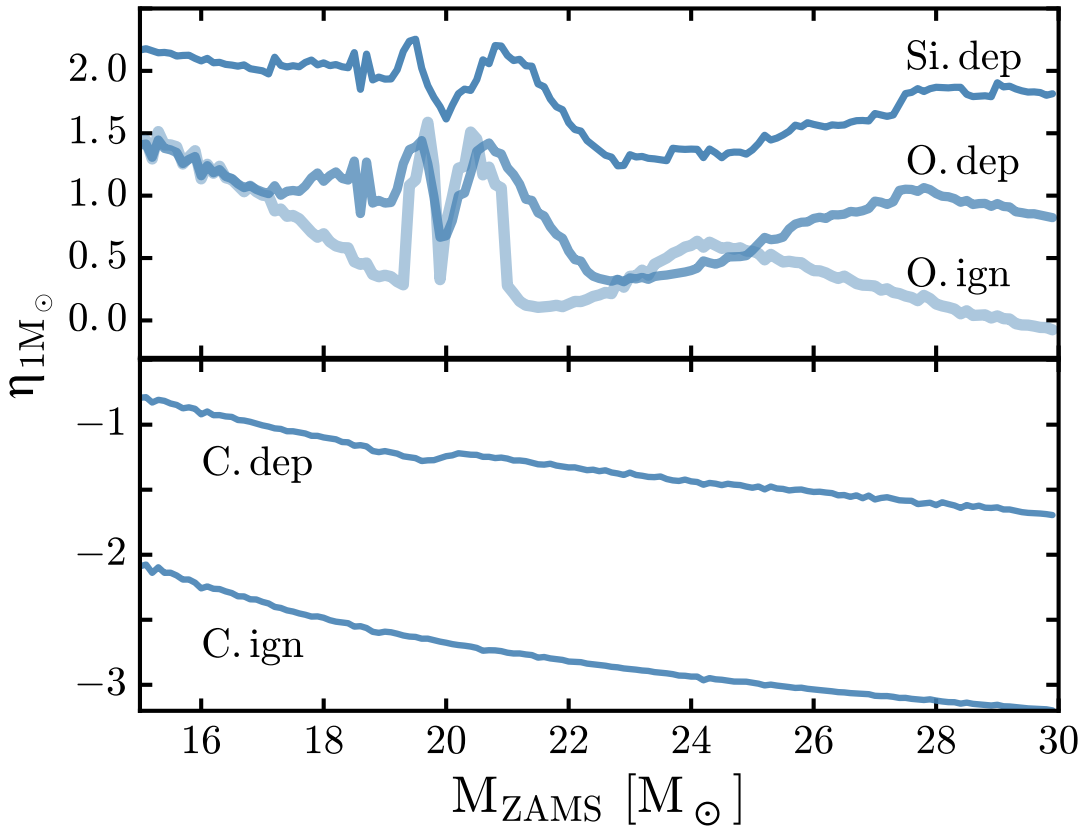

Figure 2.10: The degeneracy parameter, $\eta \equiv \mu/kT$, averaged over the inner 1 $M_\odot$ of the star is shown as a function of initial mass at the times of (bottom:) carbon ignition and core carbon depletion, (top:) oxygen ignition, oxygen depletion and silicon depletion. Very negative values of η correspond to a non-degenerate gas and large positive values imply degeneracy. The cores of the lower mass models grow much more degenerate due to neutrino losses between carbon depletion and oxygen ignition. The structure around 20 $M_\odot$ in the curve for oxygen ignition reflects the brief appearance of strong, deeply-sited carbon convective shells in this mass range (§ 2.3.2 and Fig. 2.11). These degeneracy curves at oxygen ignition and depletion are nearly mirror images of the $\xi_{2.5}$ curves at these times (Fig. 2.13) showing the key role played by degeneracy in determining the compactness.

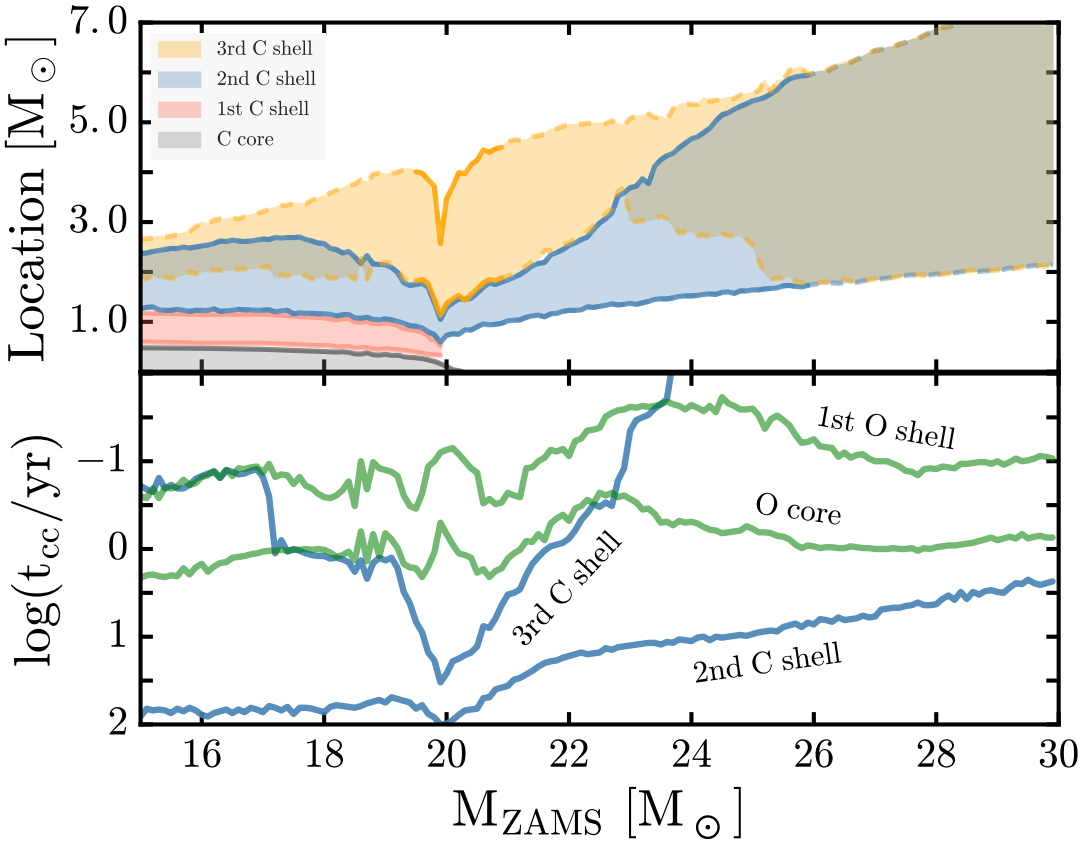

Figure 2.11: (top:) The history of the carbon burning core and as many as three shells above it for the S-series models. Different color shades show the boundaries of each convective shell: core - gray, first shell - red; second shell - blue; third shell - orange. The outermost shell boundaries are plotted as a dashed line. The transition from convective carbon core burning to radiative burning near the center at around 20 $M_\odot$ greatly affects the location and extent of all three convective shells. Right before that mass, the first convective shell (red) disappears. After that mass carbon burns from the center radiatively out to the base of the former second shell. Above 26$M_\odot$ the former second and third shells at lower mass model, burng effectively as a single shell. The location of the third shell is drawn as a dashed line when it that shell exists for less than a year at the end of the life of the star, or equivalently when it is the outermost one. (bottom:) difference between starting times and core collapse for various convective episodes (oxygen burning - green and carbon burning - blue) as a function of initial mass.

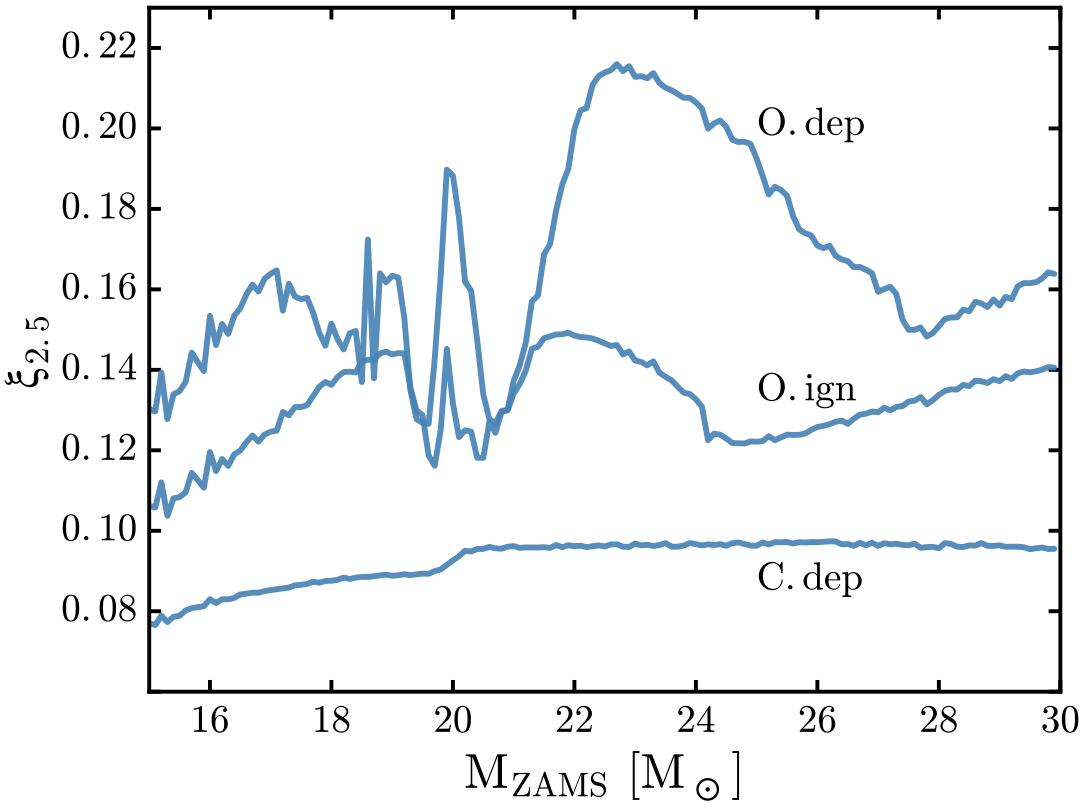

Figure 2.12: The compactness parameter, $\xi_{2.5}$, as a function of initial mass at the time of central carbon depletion (lower curve; see also Fig. 2.9; oxygen ignition (central temperature equals 1.6 GK); and oxygen depletion (central oxygen mass fraction equals 0.04; top curve). Non-monotonic behavior caused by carbon burning shells is clearly evident above 18 $M_\odot$ by the time oxygen ignites, and a broad peak in $\xi_{2.5}$ is emerging around 18 - 24 $M_\odot$ with a "notch" between 19 and 21 $M_\odot$. Note the strong anti-correlation of $\xi_{2.5}$ with degeneracy below 22 $M_\odot$ (Fig. 2.10) especially around 20 $M_\odot$.

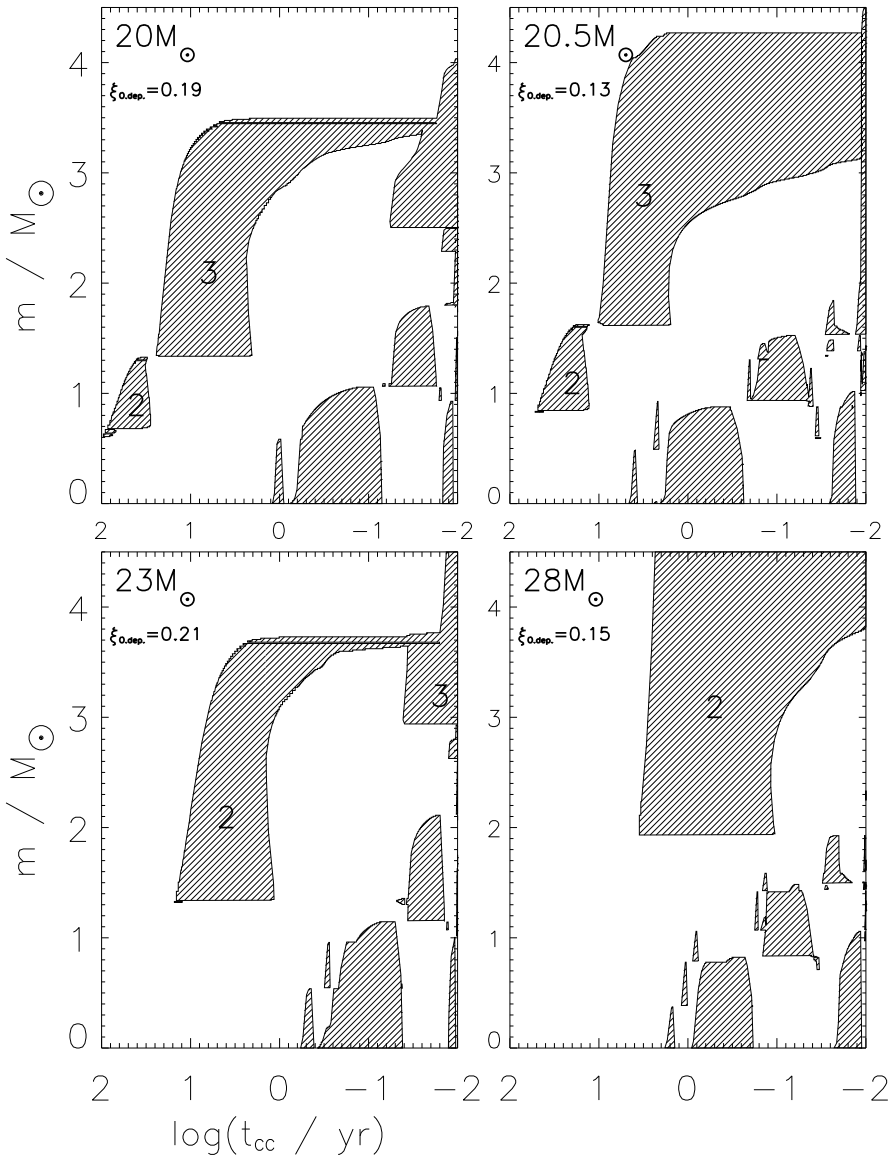

Figure 2.13: Convective history of four models showing the major changes in the evolution until silicon burning. Only the inner 4.5 $M_\odot$ is plotted in each case and the format is similar to Fig. 2.8, but here all stars, except the 20$M_\odot$ model (which has a very tiny convective core), burn carbon radiatively in their centers. Prominent in all figures is a powerful carbon burning shell igniting roughly 10 years before the star dies. Note the migration outwards of the base of this shell as the mass increases. The shell that ignites farther out supports the star while the inner core emits neutrinos and becomes increasingly degenerate. The shorter Kelvin-Helmholtz time for the larger carbon-depleted core in the heavier star also leads to oxygen ignition at a substantially earlier time. The 20$M_\odot$ and 23 $M_\odot$ models end up with a large value of $\xi_{2.5}$, while 20.5$M_\odot$ and 28 $M_\odot$ models give a smaller value. See also Fig. 2.13.

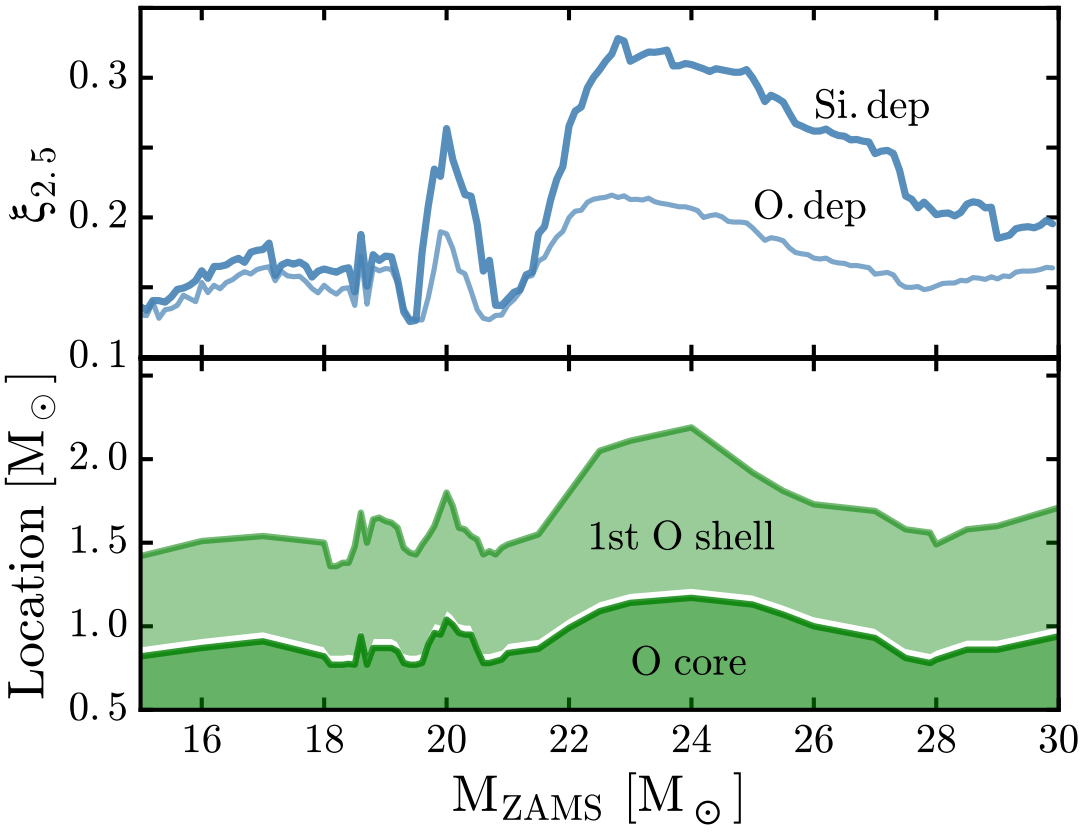

Figure 2.14: Top: The compactness parameter as a function of initial mass at the times of oxygen depletion (lower curve; see also Fig. 2.13) and silicon depletion. The tendency of existing features to be amplified by the contraction, as seen previously in Fig. 2.13, continues. Bottom: The range of the convective oxygen core, of which the extent is also the base of the first oxygen shell is given as the lower darker band labeled "O core", while the range of the first oxygen shell is the lighter band labeled "1st O shell". Note the correlation between shell locations and the compactness.

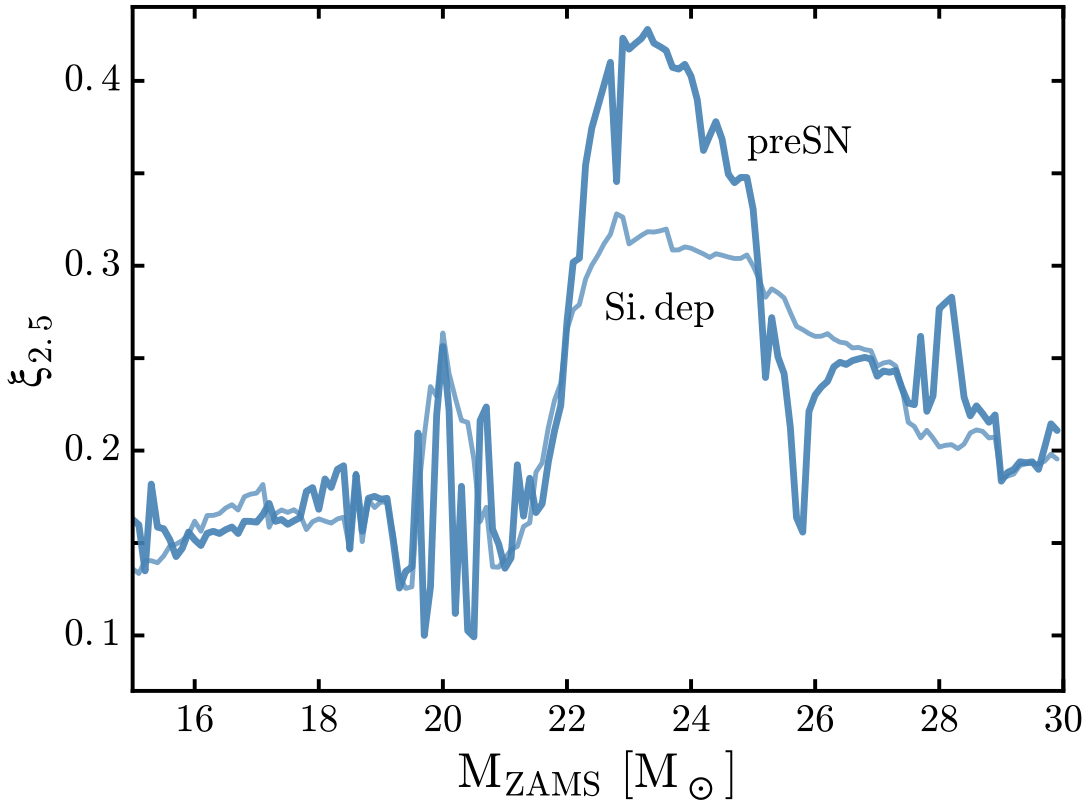

Figure 2.15: The compactness parameter, $\xi_{2.5}$, as a function of initial mass at silicon depletion and for the presupernova star. The peak at 24 $M_\odot$ grows due to core contraction and fine structure is imprinted between 19 and 22 $M_\odot$ by a strong oxygen burning shells in the last few days of it's life.

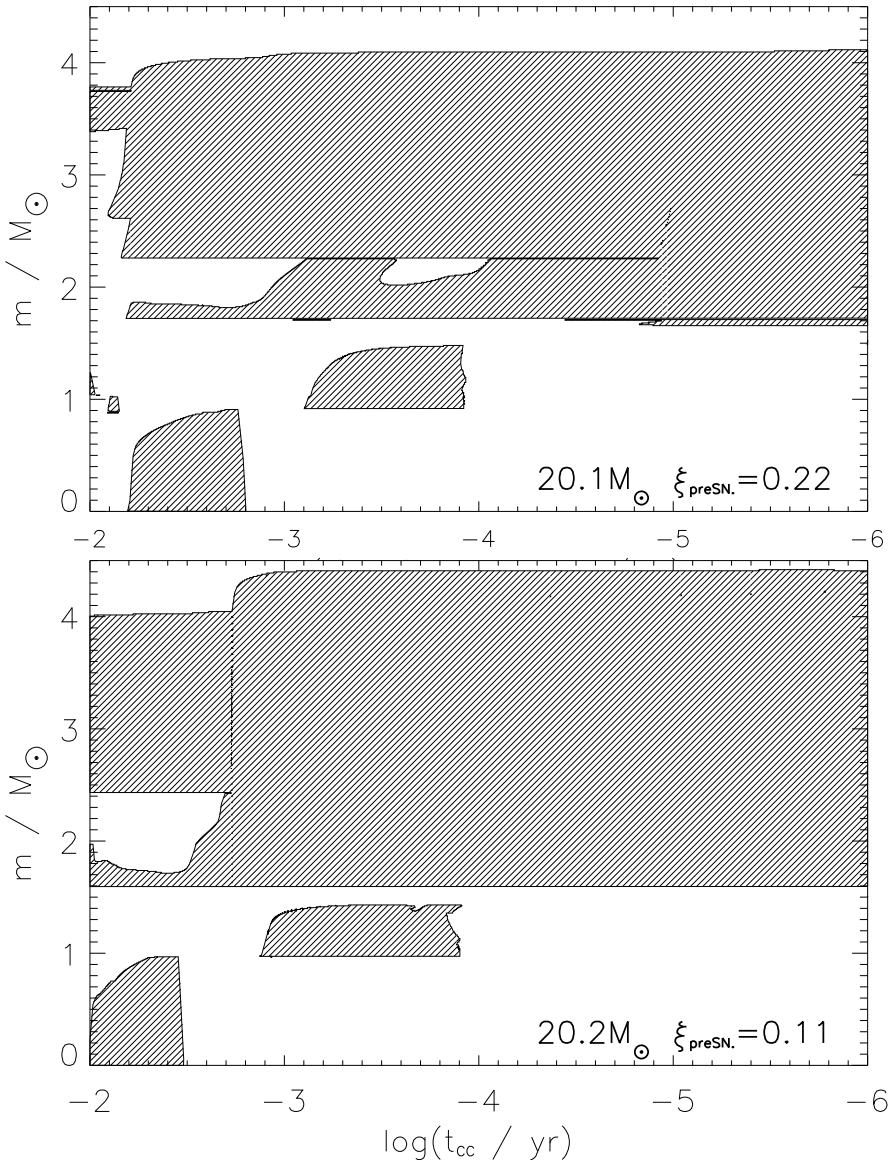

Figure 2.16: Convection plots for the 20.1 $M_\odot$ (top) and 20.2 $M_\odot$ (bottom) stars of S series. Each plot shows the evolution inside inner 4.5 $M_\odot$ during the -2 to -6 in the log of time until collapse. This last few days of evolution roughly corresponds to the time-evolution from the start of Silicon ignition in the core until the presupernova stage. Shaded regions describe convection. Notice in 20.2$M_\odot$, where the $\xi_{2.5}$(measured at presupernova) is low, the Silicon ignites int the core earlier and the shell C-O burning is very different.

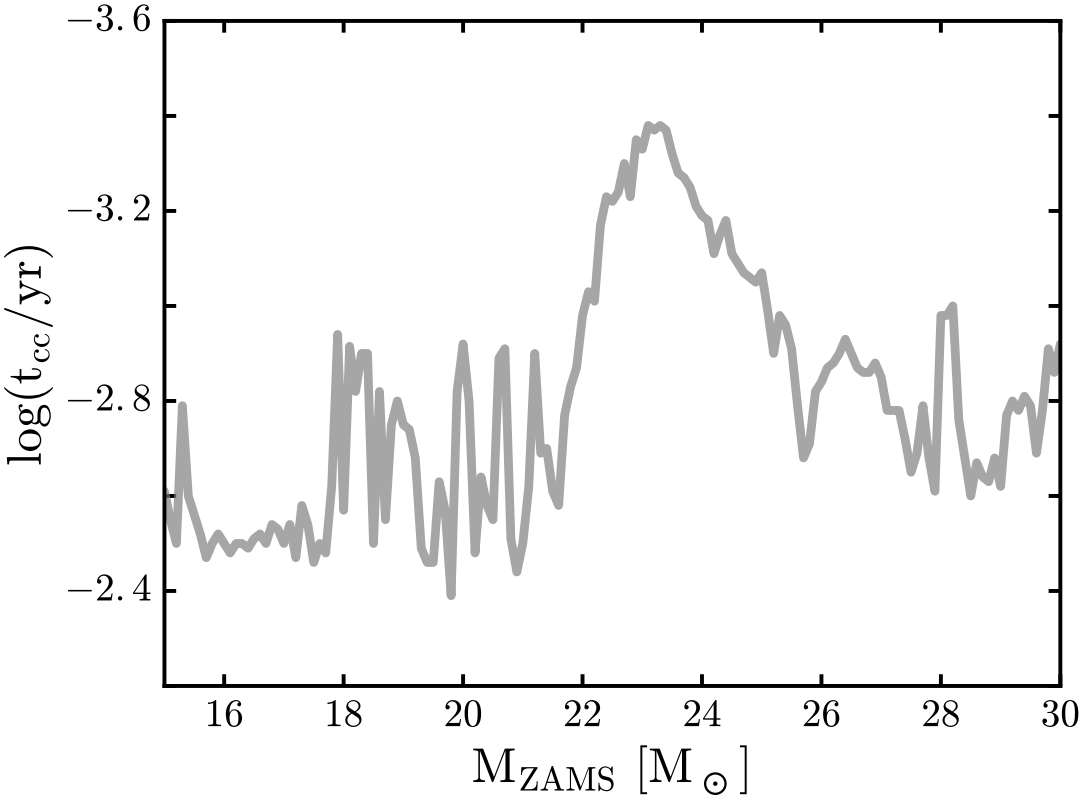

Figure 2.17: Log of the time from the core Si depletion until the iron-core collapse as a function of the initial mass for S series models. A striking correlation is evident with the variation of the compactness shown in Fig. 2.2.

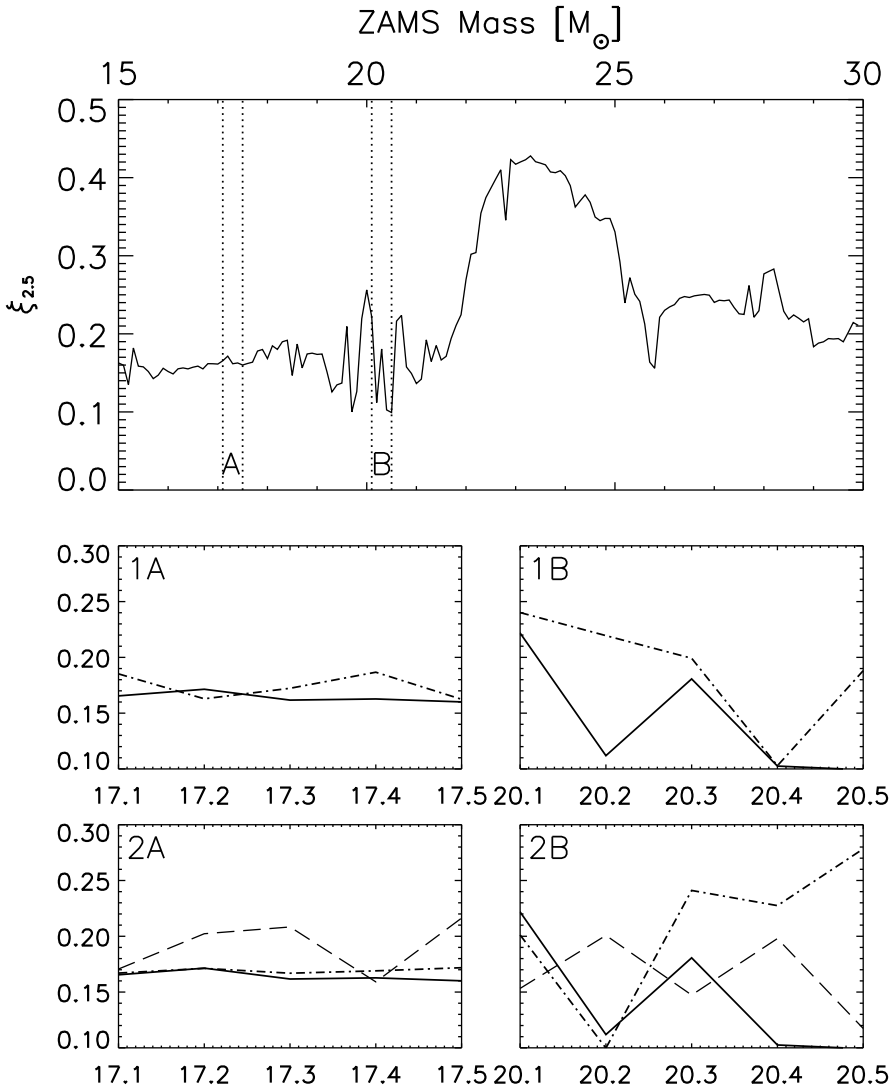

Figure 2.18: The effect of various zoning and time step criteria on the final core compactness in two different regions - A: 17.1 - 17.5 $M_\odot$ and B: 20.1 - 20.5 $M_\odot$. 1A,B - different zoning: default (thick) and $2/3$ of default (dot-dash). 2A,B - time step: default (thick), half (dot-dash) and double (thick-dashed).

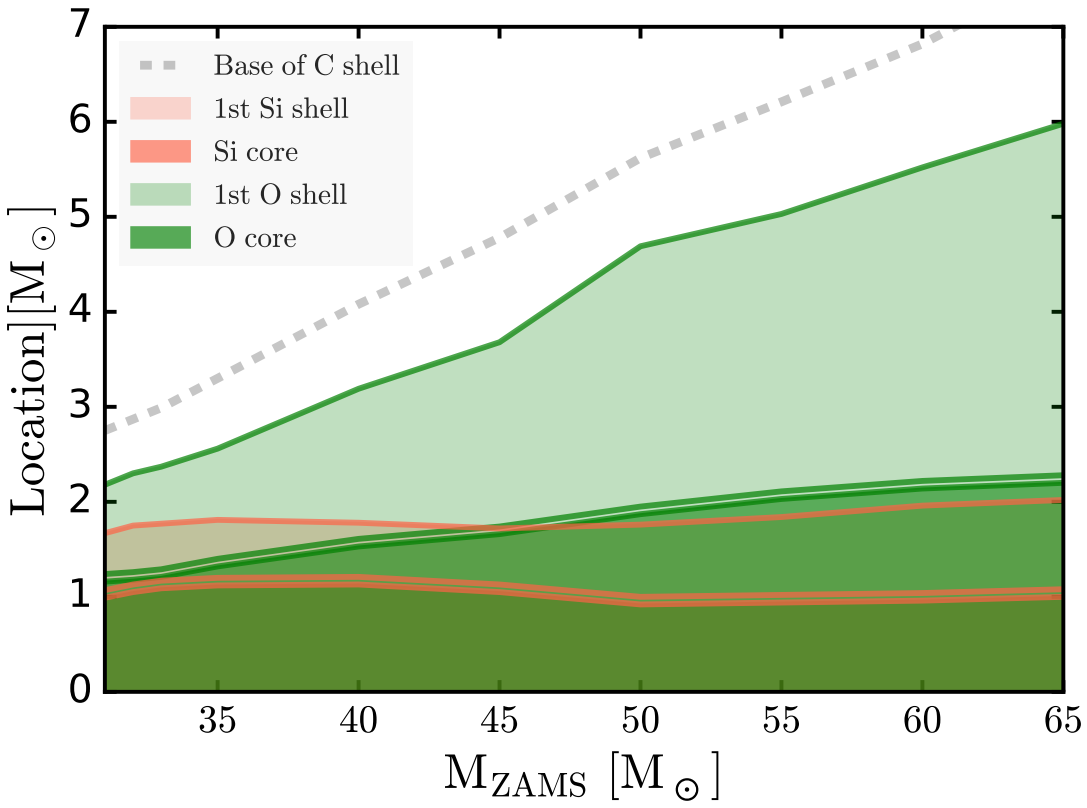

Figure 2.19: The extents of the oxygen and silicon burning convective cores and 1st shells are plotted against the initial mass of the model for SH stars. The base of the single remaining carbon convective shell (gray dashed) is also shown, but lies well outside 2.5 $M_\odot$ and has little effect on $\xi_{2.5}$ in this mass range. Notice, how the silicon core size responds as the oxygen core overgrows the silicon shell near 45-50 $M_\odot$.

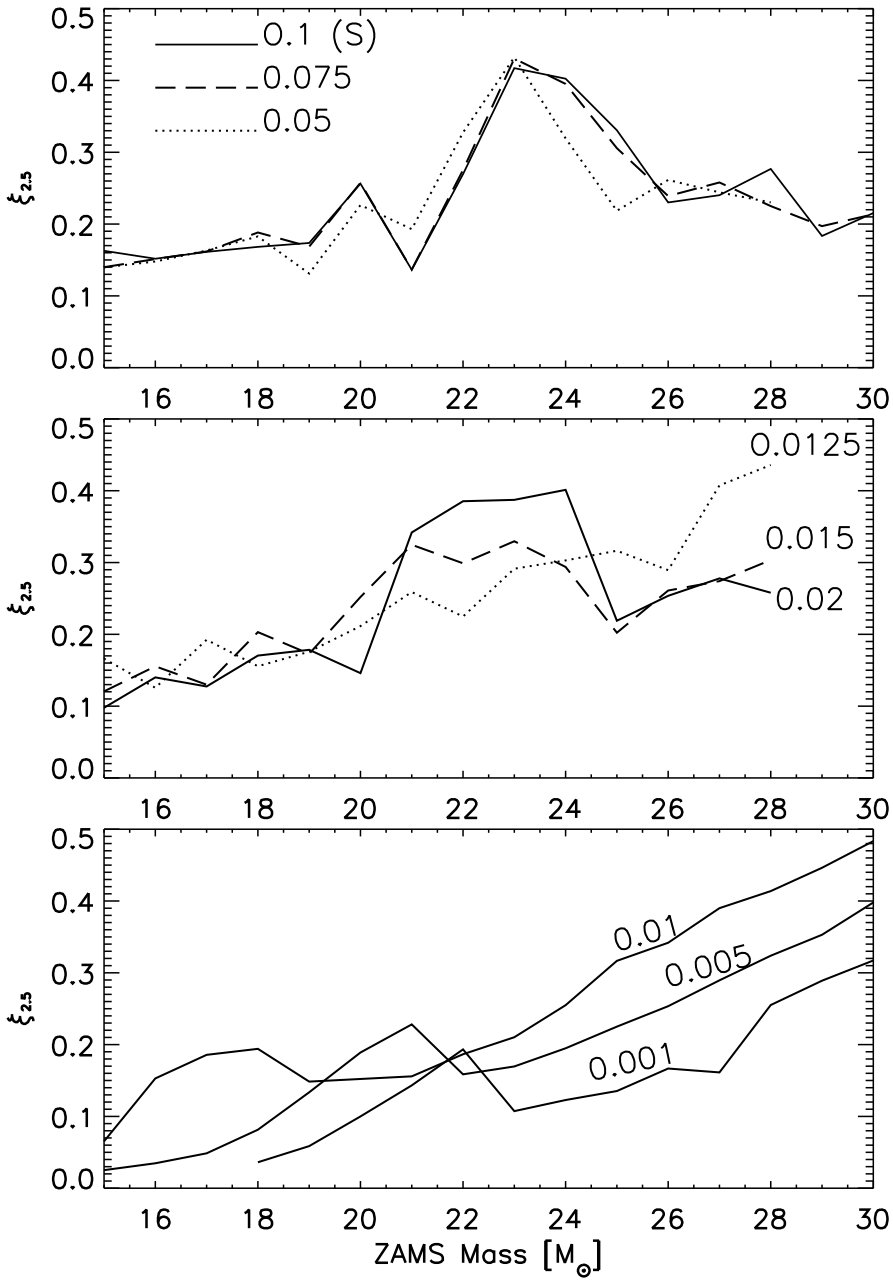

Figure 2.20: The core compactness curve as a function of initial mass sensitively depends on the semiconvection efficiency. Several sets of SS series KEPLER models of low semiconvective efficiency (down to $q_r = 0.001$) are shown in comparison with the S series models (top panel) with $q_r = 0.1$. The S series is plotted with the same $1M_\odot$ increments as was used in SS series calculations.

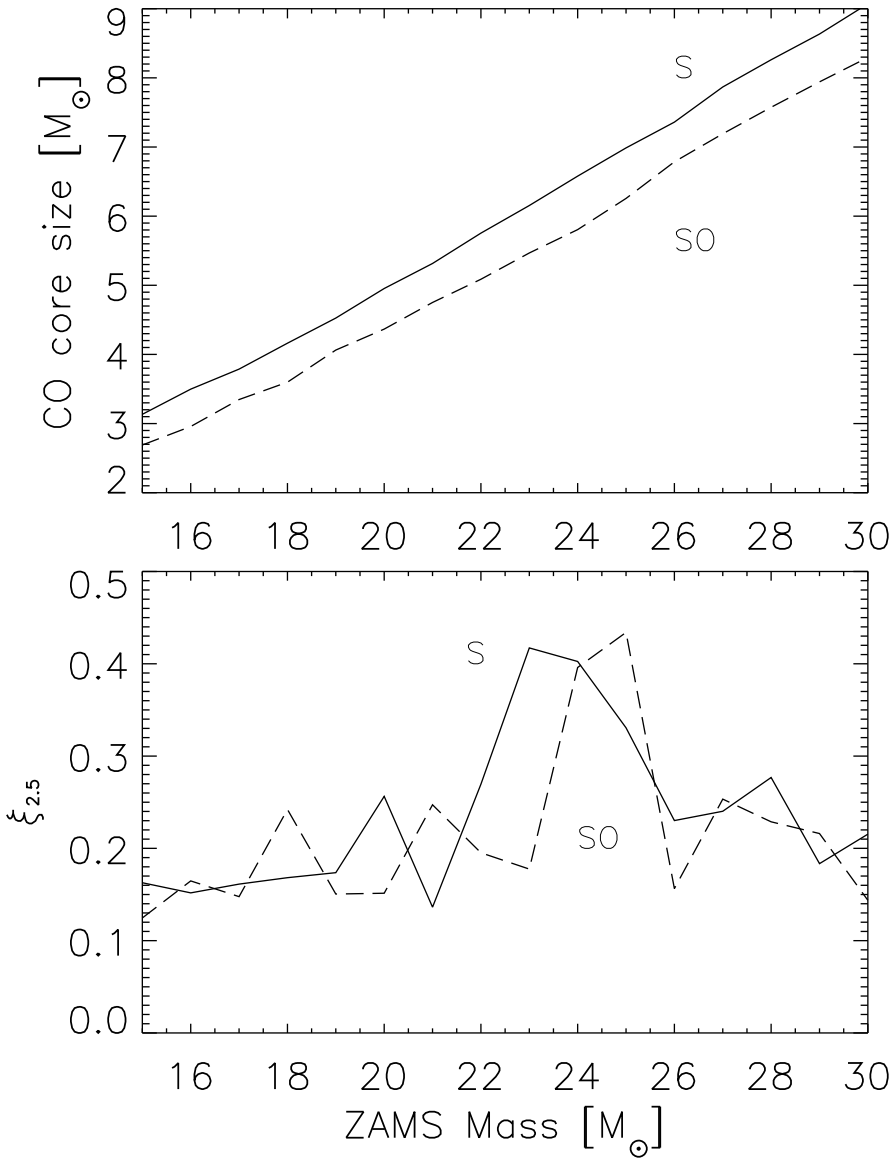

Figure 2.21: The effects of overshoot mixing on the S-series models. The "SO-series" of models includes no overshoot mixing. (top:) CO core mass as a function of main sequence mass. Without overshoot mixing, helium burning extends to a smaller mass when burning convectively in the center of the star resulting in CO core masses that are systematically smaller. (bottom:) The smaller CO cores for a given main sequence mass result in a shift upwards for the compactness parameter plot of 1 to 2 $M_{\odot}$.

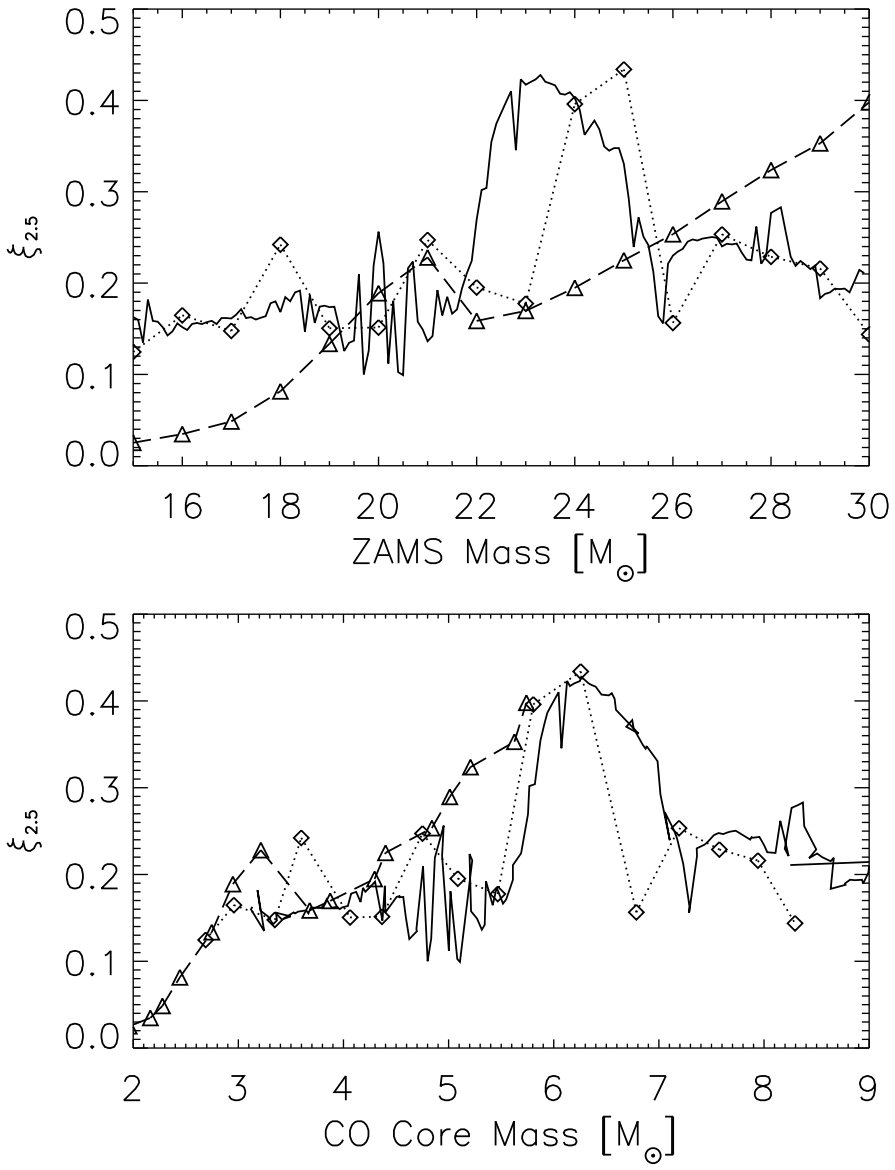

Figure 2.22: Final $\xi_{2.5}$ as a function of initial main sequence mass (top) and final CO core mass (bottom) for the S-series models (continuous), a subset of SS-series models with $q_r = 0.005$ (triangles) and SO-series models (diamonds). Though the definition of boundary of the CO core inside a massive star is ambiguous, its mass can be a better discriminant of $\xi_{2.5}$ than the initial mass in most cases.

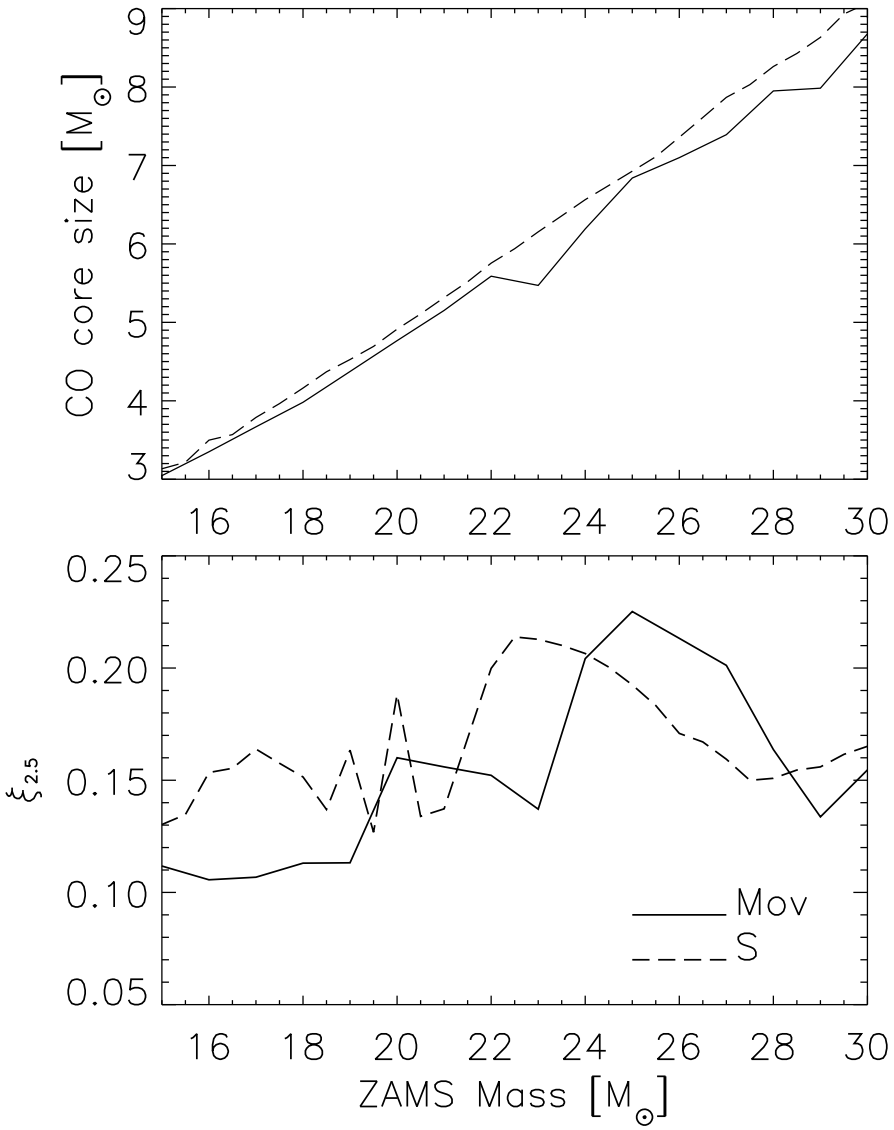

Figure 2.23: The MESA Mov series (with overshooting) is shown in comparison with the KEPLER S series. (top:) CO core mass as a function of main sequence mass. The overshooting configuration in Mov produces quite similar CO core sizes as the S series (bottom:) The compactness parameter, $\xi_{2.5}$, as a function of initial mass curves at oxygen depletion in the core for each series.

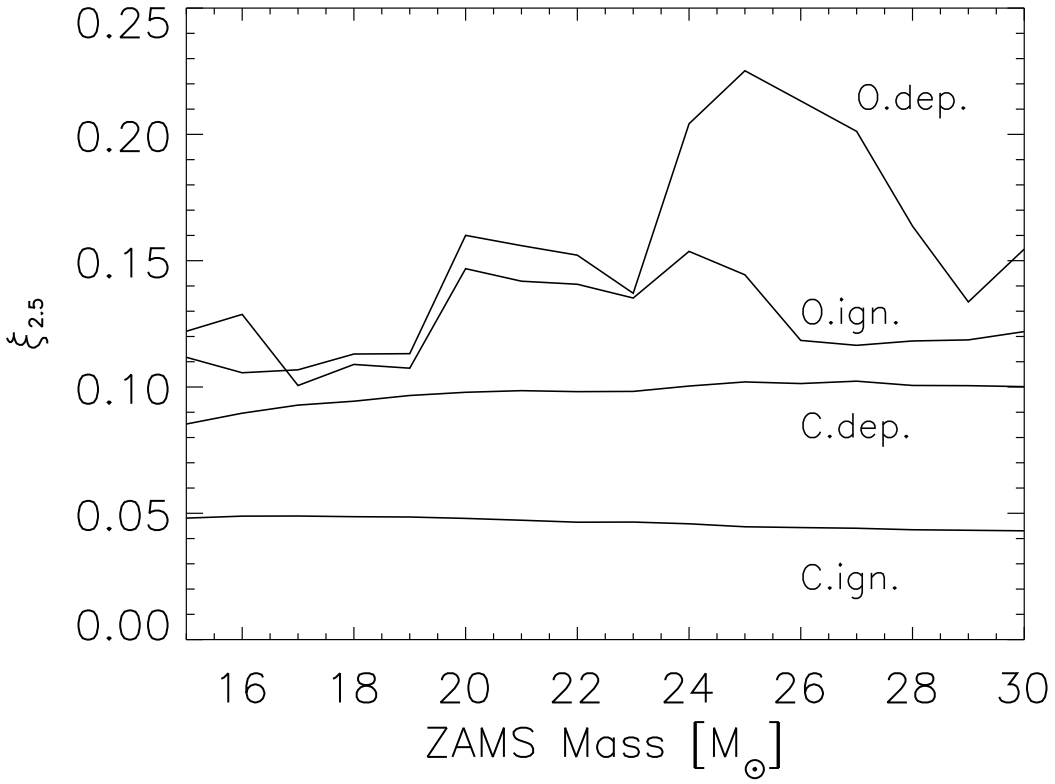

Figure 2.24: Evolution of the compactness parameter in the MESA models of Mov series. Shown is the compactness parameter, $\xi_{2.5}$, evaluated at carbon ignition, carbon depletion, oxygen ignition and oxygen depletion. Compare with Fig. 2.9 and Fig. 2.13 for the equivalent runs using KEPLER.

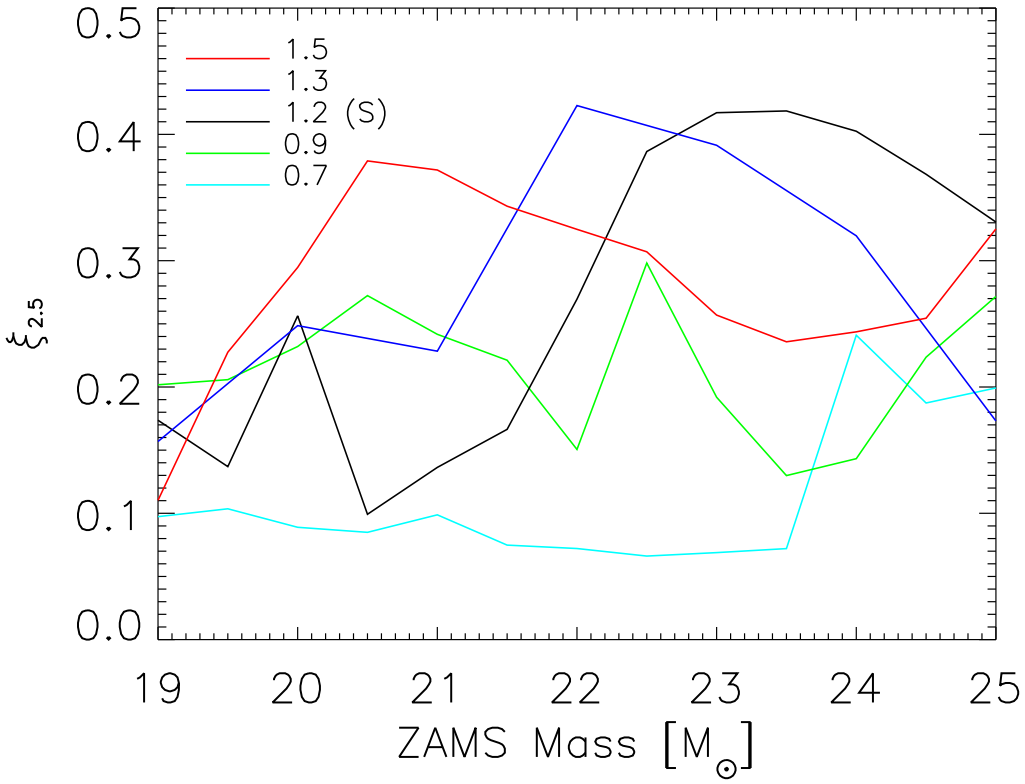

Figure 2.25: The compactness parameter as a function of main sequence mass for non-rotating, solar metallicity stars using variable rates for the $^{12}C(\alpha,\gamma)^{16}O$ reaction rate. Curves are labeled by a multiplier times the rate of Buchmann (1996, 1997). A value of 1.2 was used in the rest of the paper. The current 1σ range is approximately 0.9 to 1.3.

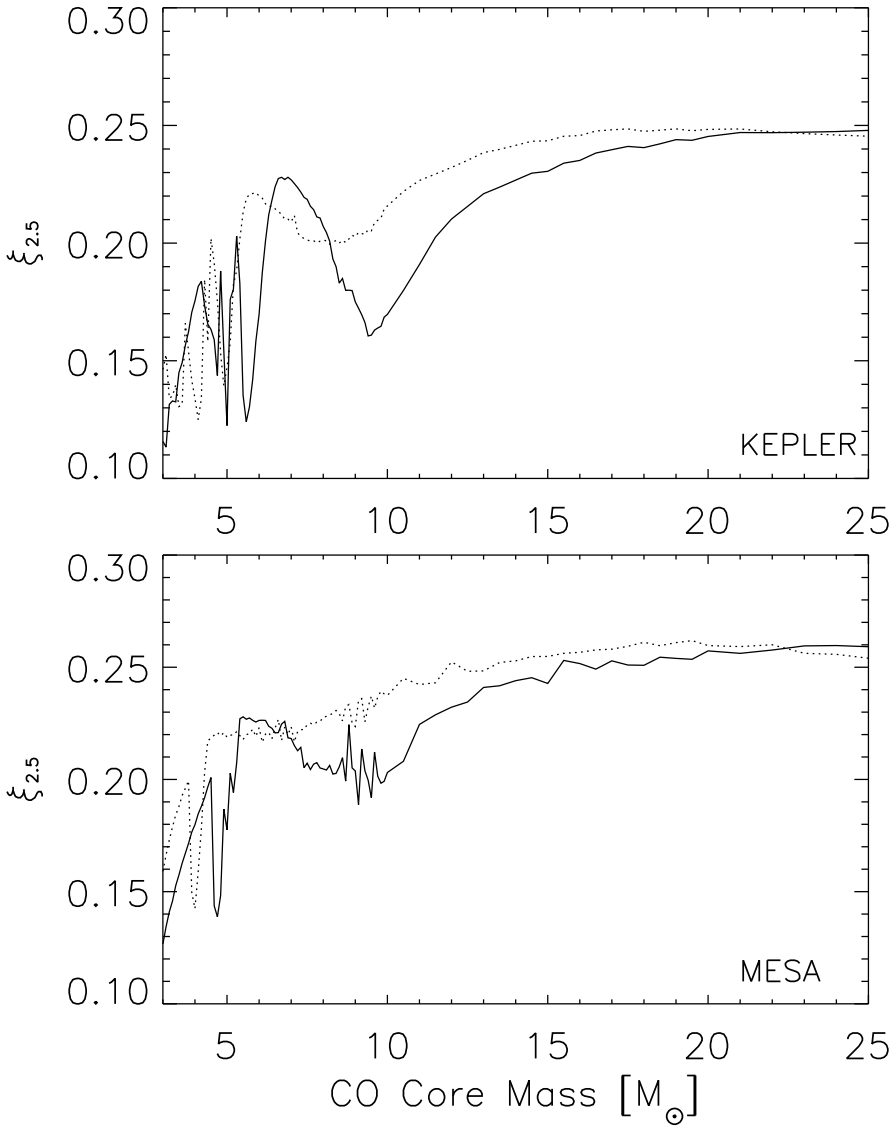

Figure 2.26: $\xi_{2.5}$ as a function of mass at central oxygen depletion for bare CO stars studied with KEPLER and MESA. Top: KS (solid) and KU (dotted); bottom: MS(solid) and MU(dotted).

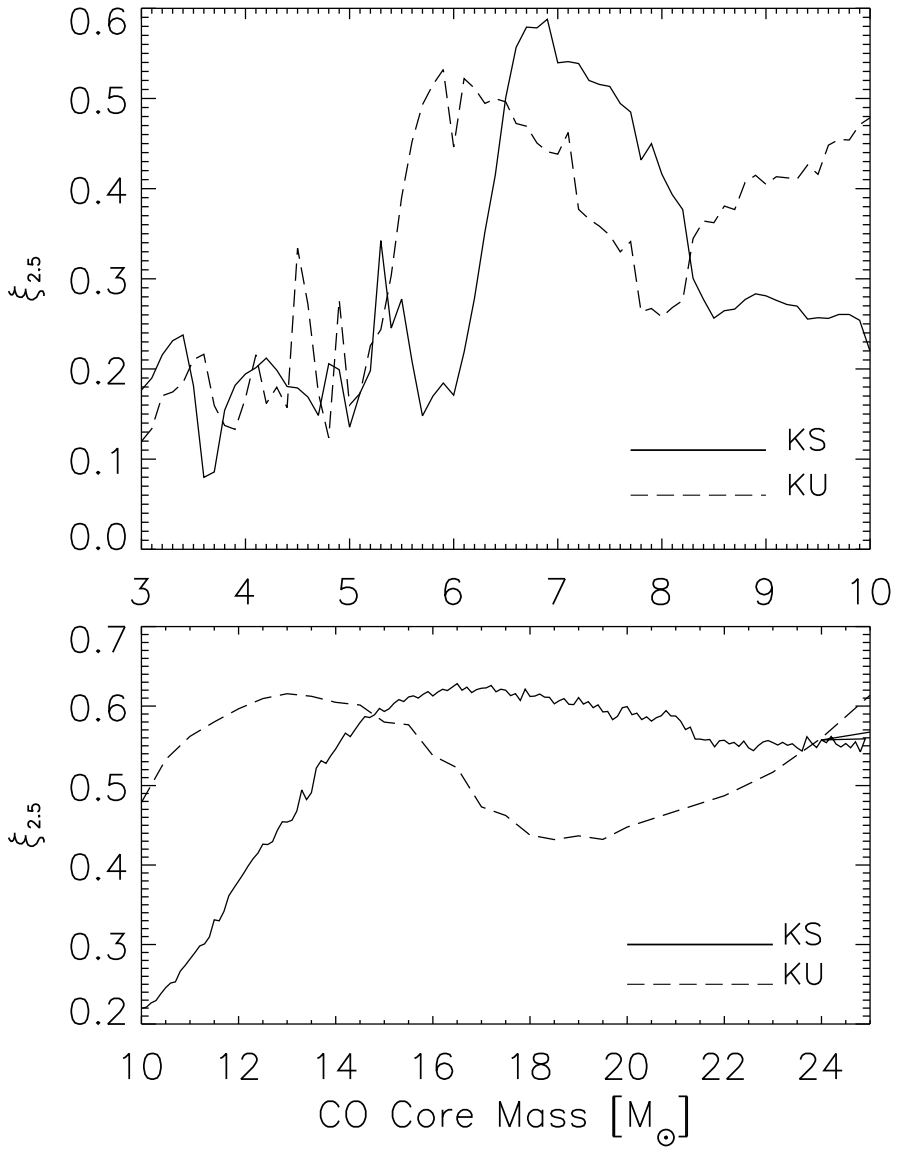

Figure 2.27: Final $\xi_{2.5}$ for presupernova stars derived from bare CO cores of a given mass and composition. (Top:) For the mass range 3 to 12 $M_\odot$, corresponding to main sequence masses from about 15 $M_\odot$ to 30 $M_\odot$. Note the large bump near 6 $M_\odot$ corresponding to the similar peak for main sequence masses 22 to 24 $M_\odot$shown in Fig. 2.3. The offset between solar (KS; green) and low metallicity (KU; red) is also similar. (Bottom:) A similar plot for the heavier CO cores. The agreement with Fig. 2.3 is striking.

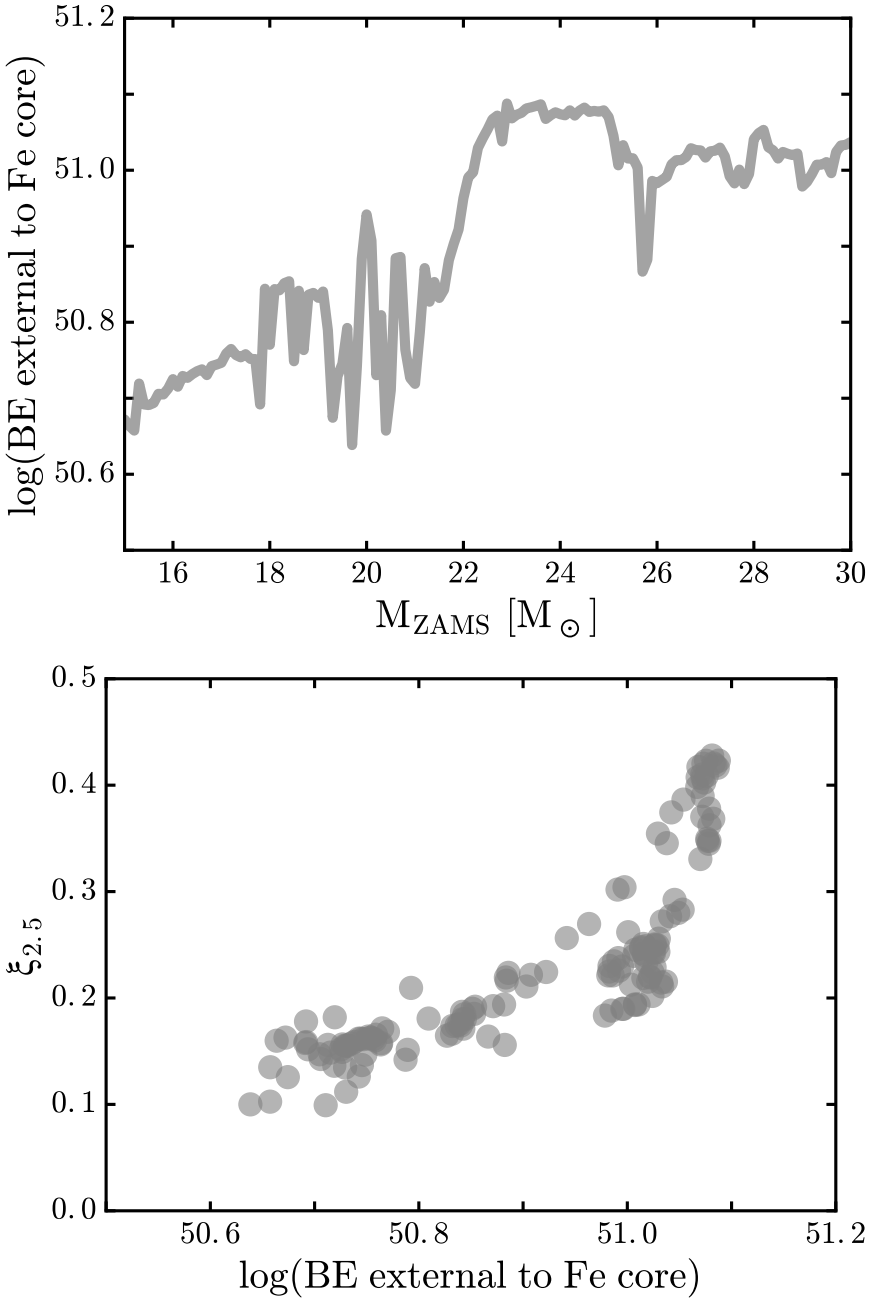

Figure 2.28: Final $\xi_{2.5}$ and binding energies for presupernova stars of the S series (Top:) The binding energy above the iron core shown as a function of initial mass. Despite the general increasing baseline trend, the relative variations closely follow that of $\xi_{2.5}$. (Bottom:) The final value of $\xi_{2.5}$ is plotted against the binding energy outside of the iron core.

Chapter 3

Core-Collapse Supernovae from 9 to 120 $M_\odot$ based on Neutrino-Powered Explosions

3.1 Introduction

The study of nucleosynthesis in massive stars has a rich history (e.g. Burbidge *et al.*, 1957; Woosley *et al.*, 1995; Thielemann *et al.*, 1996; Woosley *et al.*, 2002; Nomoto *et al.*, 2013). These studies have frequently taken the form of a detailed analysis for individual events, e.g., SN 1987A (87A), or surveys for stars of just a few different masses. In some cases where broader surveys were done, the nucleosynthesis was calculated separately from any consideration of the explosion physics, and the central engine was linked in as a parametrized inner boundary condition for a calculation that included only the matter outside of the collapsing core. The explosion was parametrized either by dumping a prescribed amount of energy into inner zones, or by the motion of a piston, generally constrained to give a fixed value of kinetic energy for

the final supernova. Sometimes this energy was varied over a limited range and the sensitivity of outcomes determined.

Here we report the results of a different approach. The starting point is an ensemble of 200 presupernova models that together span the range of masses expected for common supernovae (9.0 - 120 $M_{\odot}$). For the most part, these models or very similar ones have been published before (Woosley *et al.*, 2007; Sukhbold and Woosley, 2014; Woosley and Heger, 2015b). All have solar metallicity. Each was calculated using the KEPLER code and identical stellar physics. The major innovation here is the treatment of the explosion mechanism. Two sorts of calculations of the explosion are carried out for each mass. Iron-core collapse and bounce, neutrino transport, and the propagation of the outgoing shock are followed in one simulation until sufficiently late that the final mass cut and explosion energy have been well determined. This calculation, which includes a high density equation of state and neutrino transport that captures the essential effects of neutrinos, also gives an estimate of nucleosynthesis, especially for ^{56}Ni. The second calculation tracks the results of the first in a study of detailed nucleosynthesis and radiation transport that gives the bolometric light curve. A consistent mapping between the two codes gives, for each presupernova star, very nearly the same remnant mass, kinetic energy at infinity, and ^{56}Ni mass. Nucleosynthesis is calculated for all isotopes from hydrogen through lead, except that the nucleosynthesis in the neutrino wind is not included.

Both calculations are one-dimensional (1D). While the actual physics of neutrino-powered supernovae cannot be fully represented in a such a limited study (Janka, 2012; Burrows, 2013; Foglizzo *et al.*, 2015), multi-dimensional models are expensive, scarce, and often lack community consensus. Of necessity, an expedient track is adopted that should capture

many characteristics of a real explosion. The 1D core-collapse code is used to calculate the explosion of five different progenitors for SN 1987A (Ertl *et al.*, 2016) and one progenitor for SN 1054 (the "Crab"; § 3.2.2.2). Adjustable parameters in the central engine model are varied to give the well-determined ^{56}Ni mass, kinetic energy and neutrino burst time scale for SN 1987A, and the kinetic energy of the Crab. Based upon the systematics of presupernova core structure (§ 3.3.1.2), supernovae below 12.0 $M_{\odot}$ are deemed to be "Crab-like", while heavier stars are "87A-like". Further partition of the mass space might be practical given more observational constraints, especially supernovae with well-determined masses, but was not attempted here.

These central engines are then used to explore the outcomes when placed in the 200 presupernova stars. The use of these "calibrated central engines", which are really just standardized descriptions of the inner 1.1 $M_{\odot}$ of the proto-neutron star, allows a calculation of the neutrino and accretion physics outside the inner core that depends sensitively upon the structure of individual presupernova stars. For some models, the standard central engine is unable to provide enough energy for explosion and a black hole forms. For others, the star explodes with a variable amount of kinetic energy. For the stars that do explode, the resulting patterns of supernova energetics, nucleosynthesis, remnant masses, and light curves are reasonable for four out of five of the calibrations for SN 1987A. One set of calculations that used a model for SN 1987A that exploded too easily, gave explosions that, on the average, were deemed too weak. In this case an inadequate number of stars exploded to make the abundances we see in the sun (§ 3.4). Thus nucleosynthesis was not studied in detail using this model as a basis.

We are particularly interested in how the "explodability" of the presupernova models and their observable properties correlate with their "compactness" (Fig. 3.1; eq. (2.1)) and other

measures of presupernova core structure (§ 3.3.1.2;Ertl *et al.* (2016)). Using a standard central engine in presupernova models of variable compactness, a significant correlation in outcome is found (§ 3.4). As previously suggested, the resulting mass spectrum of successful supernovae is not simply connected (O'Connor and Ott, 2011; Ugliano *et al.*, 2012; Sukhbold and Woosley, 2014). That is, there is no single mass above which stars make black holes and below which they explode. Rather there are mass ranges that "tend" to explode, albeit with significant variations, even in narrow ranges. The model stars below 15 $M_{\odot}$ always explode easily, while those from 22 - 25 and 27 -30 $M_{\odot}$, rarely explode. The outcome for other masses is either variable (15 - 22 $M_{\odot}$ and 25 - 27 $M_{\odot}$), or sensitive to the treatment of mass loss ($M > 30\ M_{\odot}$).

The input physics and the systematics for all of the progenitors, including the models used for the explosion calibrations have been discussed in previous publications, but are summarized in § 3.2. Details of the explosion modelling for both the `PHOTB` code, which is used to study core collapse, and the `KEPLER` code, which is used to calculate nucleosynthesis and light curves, and how agreement is enforced between the two codes are discussed in § 3.3. The properties of the explosions in relation to the progenitor compactness parameter, especially their explosion energies and ^{56}Ni masses, are addressed in § 3.4, and the mass distributions of neutron stars and black holes from the explosions are discussed in § 3.5. The resulting nucleosynthesis from different mass ranges and the integrated yields for different element groups are examined in § 3.6, and the light curves of various types emerging from the explosions and their systematics are analysed in § 3.7. In § 3.8, we offer some conclusions.

3.2 Presupernova Models

3.2.1 Stellar Physics

All presupernova models, both the ones used for the explosion and its calibration, were calculated using the KEPLER code (§ 3.3.2). All stars, except one model used for the calibration of 87A, were non-rotating. Except two calibrations models, each had an initially solar (Lodders, 2003) composition. All were evolved from the main sequence until the onset of iron-core collapse. The lower bound to the survey, 9.0 $M_\odot$, is set by the lightest star to experience iron-core collapse in the KEPLER code (Woosley and Heger, 2015b). The evolution of still lighter stars in the 7 to 9 $M_\odot$ range was not calculated. Some uncertain fraction of these will evolve to electron-capture supernovae and contribute to the supernova rate and remnant distribution. Those contributions are neglected here. Their contribution to nucleosynthesis, other than the r- and s-processes is likely to be small, however. All were evolved from the main sequence until the onset of iron-core collapse.

Most of the models, or very similar ones, have been published previously (Woosley *et al.*, 2007; Sukhbold and Woosley, 2014; Woosley and Heger, 2015b). The nuclear physics varied (though not the individual reaction rates). For stars 13.0 $M_\odot$ and heavier, including the models for 87A, the evolution up to core oxygen depletion was followed using a 19 isotope approximation network and, after central oxygen decreased to below 4% by mass, using a 128 isotope quasi-equilibrium network (Weaver *et al.*, 1978). Those calculations were "co-processed" using an adaptive network (Rauscher *et al.*, 2002) that, near the end included, typically, 1500 isotopes and sometimes over 2000. In addition to following the nucleosynthesis zone by zone

and step by step, the evolution of the (slowly evolving) electron mole number, Y_e, calculated by the large network was fed back into the structure calculation. Energy generation within an iterative loop, however, came from the 19 isotope network or the quasi-equilibrium network.

For stars lighter than 13 $M_\odot$, the tracking of off-center burning and convectively bounded flames requires a more careful treatment of the nuclear physics (Woosley and Heger, 2015b). For these stars, the large network and all neutrino losses from weak reactions on individual nuclei, was coupled directly to the structure calculation. The 19 isotope network and quasi-equilibrium networks were not employed. Several stars in the 12 to 13 $M_\odot$ range were computed using both the direct coupling of the big network and co-processing. The results were nearly identical.

Formally, only single stars were included. The key quantity for nucleosynthesis and remnant masses is the mass of the core of helium and heavy elements at the time of the explosion. To the extent that the Salpeter IMF properly reflects this distribution of helium core masses, our results would not be changed if a substantial fraction of the stars were in binary systems. If mass exchange proceeds so far as to appreciably reduce the mass of the helium core from what it would have been for a single star, including radiatively-driven mass loss, then the answer will change. For example, it seems most likely that common SN Ib and Ic result from binary systems containing stars whose presupernova mass is only 3 or 4 $M_\odot$ (Dessart *et al.*, 2012; Ensman and Woosley, 1988). Many of these may come from 12 to 15 $M_\odot$ main sequence stars that lost their envelopes and little else to a companion. Treating these as single stars does not greatly distort the nucleosynthetic outcome, though it obviously changes the rate of Type Ib and Ic supernovae a lot. If the progenitors in binaries were much heavier, some of their nucle-

osynthesis, especially in the helium shell, might have been lost to a companion and it becomes an issue whether *that* star blows up returning what it accreted to the interstellar medium. If more massive stars in binaries are involved in making SN Ic, then our results would be altered. The explosion of stripped down 4 $M_\odot$ cores of oxygen and heavy elements is different from the explosion of a 4 $M_\odot$ helium core, both in mechanism and consequence (Woosley *et al.*, 1993). However, such supernovae are relatively rare and we do not expect substantial changes from what we report here. Including the contributions of SN Ib and Ic models explicitly would be a worthwhile project for the future.

3.2.2 Explosion Calibration Models

3.2.2.1 SN 1987A

The presupernova evolution of Sk -69^o 202 and its explosion as SN 1987A have been studied extensively for almost 30 years (e.g. Arnett *et al.*, 1989; Utrobin *et al.*, 2015, and references therein), yet a comprehensive, self-consistent model for the progenitor star, its ring structure, and the explosion is still lacking. The observational constraints are tighter, though, than for any other supernova, so it is worthwhile to try to use SN 1987A as a calibration point.

It is known that the progenitor star was a Type B3-I blue supergiant, Sk -69^o 202 (Walborn *et al.*, 1987), with an effective temperature 14,000 - 17,000 K (Humphreys and McElroy, 1984; Crowther *et al.*, 2006; Smith, 2007), a luminosity $3-6\times10^{38}$ erg s^{-1} (Humphreys and McElroy, 1984; Arnett *et al.*, 1989), and thus a radius $2-4\times10^{12}$ cm. Since the presupernova luminosity is determined chiefly by the helium core mass, a core mass of 6 ± 1 $M_\odot$ has been inferred theoretically (e.g. Woosley, 1988). Based upon analysis of the supernova light curve,

this core was surrounded by about 10 $M_\odot$ of envelope in which helium and nitrogen were enriched, but hydrogen was still a major constituent (Woosley, 1988; Shigeyama *et al.*, 1988). The star had been a red supergiant before dying as a blue one in order to produce the colliding wind structure seen shortly after the explosion. Spectral analysis, as well as the light curve, give an explosion energy near 1.5×10^{51} erg (Arnett *et al.*, 1989; Utrobin *et al.*, 2015), and the late time light curve shows unambiguously that the explosion produced 0.07 $M_\odot$ of ^{56} Ni (Bouchet *et al.*, 1991; Suntzeff *et al.*, 1992). The explosion also ejected approximately 1.4 ± 0.7 $M_\odot$ of oxygen (Fransson and Kozma, 2002).

Numerous attempts have been made to model the presupernova evolution of Sk -69^o 202. The final stages are complicated by the widespread belief that SN 1987A may have been a merger event (**??**), though see Smith (2007). In any case, the star that exploded was single at the time, in hydrostatic and, given the necessary timescale for the red-to-blue transition, probably in approximate thermal equilibrium. Its helium core mass is thus constrained by the presupernova luminosity and so single star models are relevant.

Five principal models for SN 1987A are considered here, the ones above the blank line in Table 3.1, and span the space of possible helium and heavy element core structures (Fig. 3.2). The 3D explosion and observable properties of four of them have been explored previously (Utrobin *et al.*, 2015) and agree well with experimental data. These models are N20, W15, W18, and W20.

Model N20 (**?**Nomoto and Hashimoto, 1988; Saio *et al.*, 1988), a historical model, was "prepared" by artificially combining the presupernova structure of an evolved 6 $M_\odot$ helium core from one calculation with the hydrogen envelope from another. This model was

thus defined to satisfy observational constraints on helium core mass, hydrogen envelope mass, radius, and luminosity, but lacks the physical basis of a presupernova model evolved intact from the main sequence onwards. Since the helium core of Model N20 was evolved using the Schwarzschild criterion for convection (Nomoto and Hashimoto, 1988), its carbon-oxygen (CO) core is large compared with some of the other models (Table 3.1), which used restricted semiconvection in order to produce a blue supergiant progenitor. It is not clear that, had the 6 $M_{\odot}$ core been included in a self-consistent calculation with an envelope always in place, a blue supergiant would have resulted rather than a red one.

Model W15 (Woosley and Weaver, 1988), another early model calculated shortly after SN 1987A occurred, was produced by evolving a single 15 $M_{\odot}$ star from beginning to end, but relied upon opacities that are now outdated, reduced metallicity, and greatly restricted semiconvection to produce a blue supergiant. Mass loss was not included. The small ratio (less than about 0.6) of the CO core mass to helium core mass in W15 is characteristic of all models in Table 3.1 that produce blue supergiant progenitors. So far as we know, this is a hallmark of all solutions that use Ledoux convection or restricted semiconvection to achieve this goal. The helium core mass and luminosity of W15 are too small compared with more accurate observations of Sk -69^{o} 202. Still W15 is included here because it has been studied in the literature and it brackets, on the low side, the observed luminosity and helium core mass of Sk -69 ^{o} 202 (Fig. 3.2).

Model W20 (**?**) used more modern opacities (**?**Iglesias and Rogers, 1996) and included mass loss. Its luminosity, radius, and helium core mass agree well with observations of Sk -69^{o} 202 (Fig. 3.2). Its presupernova oxygen mass, 0.68 $M_{\odot}$, is on the small side compared

with observations Fransson and Kozma (2002), especially when allowance is made for the processing of some oxygen into heavier elements during the explosion. The envelope is also not enriched in helium. The surface mass fraction of helium is 0.26.

Model W18 is a more recent unpublished model that is presented in greater detail in §2.2.1.2 of Sukhbold *et al.* (2016). It achieves the desired goals of making a blue supergiant progenitor, producing a relatively large mass of oxygen, and displaying large enhancements in surface helium and nitrogen abundances, by invoking reduced metallicity, restricted semiconvection, and a substantial amount of rotation. Rotation makes the helium core larger and also stirs more helium into the envelope, raising the mean atomic weight there, and reducing the opacity. A larger helium core implies a larger luminosity, somewhat above the observed limit for SN 1987A (Fig. 3.2), but the increased helium fraction in the envelope facilitates a blue solution (Saio *et al.*, 1988; Langer, 1992). In general, W18 is the heaviest possible blue supergiant model for SN 1987A in terms of its helium core mass. While a bit overluminous, it fits many other observed characteristics of the supernova well, especially the oxygen mass synthesized, and its central core structure is similar to other lighter models, W16 and W17. Table 1 of Ertl *et al.* (2016) shows that, at least in terms of compactness, W18 is quite similar to W20, N20, and S19.8.

Three other models similar to W18 are also given in Table 3.1 and Fig. 3.2 to illustrate some sensitivities, but were not used in the remainder of the chapter. W16 and W17 are identical to W18 except for their different masses and rotation rates. The angular momentum on the zero age main sequence for Models W16, W17, and W18 was $J_{\rm ZAMS}$ = 2.7, 2.9 and 3.1 $\times 10^{52}$ erg s. The presupernova core properties for W16 and W17 are similar to W18 and one would

expect similar results were they to be employed as standard central engines. W18x on the other hand is slightly different in input physics, yet quite different in outcome. Like W18, W18x includes rotation, but the total angular momentum on the main sequence was reduced by ∼25% to $J_{ZAMS} = 2.3 \times 10^{52}$ erg s. This small reduction in J resulted in a dramatic decrease in the helium core mass and presupernova luminosity (Table 3.1; Fig. 3.2). Another model, not shown, with an angular momentum 50% of W18 gave almost identical results to W18x, showing that W18 itself was on the verge of becoming a chemically homogeneous model (Maeder, 1987; Langer, 1992; Woosley and Heger, 2006). Nevertheless, we chose to use Model W18 itself as one of our standard models because it gave reasonable agreement with the observed properties of Sk -69^o 202, had a core structure similar to the non-rotating, solar metallicity stars in the present survey, was available a few years ago when this study began, and had been previously studied in the literature (Utrobin *et al.*, 2015; Ertl *et al.*, 2016).

In addition to the above models with restricted semi-convection and low metallicity, a non-rotating, solar metallicity red supergiant progenitor was also examined. "S19.8" (Woosley *et al.*, 2002), was not considered by Utrobin et al., but has a similar helium core structure to W18 and N20 (Table 3.1). Because the surface boundary pressure is small in both cases, the structure of the helium core is insensitive to whether the envelope is that of a blue or red supergiant. Despite its vintage, Model S19.8 was calculated using essentially the same initial composition and stellar physics as in the present survey - including opacities, mass loss, semiconvection, and metallicity. The luminosity, helium core mass, and hydrogen envelope mass of presupernova Model S19.8 are all what one would want for SN 1987A, but the presupernova star was a red supergiant. Also given in Table 3.1 is an 18 $M_\odot$ presupernova model from the present survey.

The luminosity is very similar to Sk -69^o 202 and the structure similar to S19.8.

The point of these calculations was not to generate the best possible model for SN 1987A itself, but to use its well studied properties to bracket and calibrate a central engine capable of exploding helium cores with similar characteristics. It was important to study a range of models to test the sensitivity of the results to the choice of a model for SN 1987A (see § 3.4 for results).

3.2.2.2 SN 1054 - The Crab

While the Crab supernova was not studied spectroscopically, modern observations of its remnant suggest that the kinetic energy was much lower than that of SN 1987A and other common supernovae from more massive stars (Arnett *et al.*, 1989; Kasen and Woosley, 2009; Yang and Chevalier, 2015). The event has been successfully and repeatedly modelled as the explosion of a star near 10 $M_\odot$ (Nomoto *et al.*, 1982; Nomoto, 1987; Smith, 2013; Tominaga *et al.*, 2013). Such stars are known to have compact structures that explode easily by the neutrino-heating mechanism, even in spherical symmetry (Kitaura *et al.*, 2006; Fischer *et al.*, 2010; Melson *et al.*, 2015). Use of an 87A-like central engine in stars of this sort thus overestimates the power of the supernova and gives an unphysically large kinetic energy (§ 3.3.1.2). Systematics of the presupernova core structure, to be discussed later, suggest that, for KEPLER models, this low energy branch of supernovae should characterize events from 9.0 (or less) to 12.0 $M_\odot$.

The fiducial model employed to represent the core physics in this low mass range was a 9.6 $M_\odot$ zero-metallicity model (Z9.6) provided by A. Heger (2012, private communication).

This star was also calculated using the KEPLER code using physics described in Heger and Woosley (2010) and, while a star of zero metallicity, it has a very similar core structure to the lightest solar metallicity models employed here (Fig. 3.3). The model has the merit of having been successfully exploded in 1D and multi-dimensional calculations (Janka *et al.*, 2012; Melson *et al.*, 2015), developing an explosion dynamically similar to collapsing O-Ne-Mg core progenitors (Kitaura *et al.*, 2006; Janka *et al.*, 2008). It also gives similar nucleosynthesis to the electron-capture supernovae (Wanajo *et al.*, 2016) often mentioned as candidates for the Crab (Wanajo *et al.*, 2011b; Jerkstrand *et al.*, 2015), but has the advantage of being an iron-core collapse supernova similar to the ones we are presently modelling.

3.2.3 Presupernova Models used for this Study

The presupernova models into which these calibrated central engines are placed are all the outcomes of non-rotating stars with initially solar metallicity. Mass loss was included in all calculations. Qualitatively, the models reflect four partitions of expected behaviour (e.g. Woosley and Heger, 2015b):

- 9 – 12 $M_\odot$: these are stars with degenerate compact cores, essentially tightly bound white dwarf-like cores inside loosely bound envelopes. They are easy to explode. Starting at 9 $M_\odot$, an iron core is produced before the star dies. Slightly below 9 $M_\odot$, an electron-capture supernova results or an oxygen-neon white dwarf is made. The presence of an active oxygen burning shell at the edge of the effective Chandrasekhar mass in the pre-supernova star causes a rapid fall off in density near the edge of a dense central core for models below 12 $M_\odot$.

- 12 – 20 $M_\odot$: starting at about 10.5 $M_\odot$, all fuels ignite in the center of the star (Woosley and Heger, 2015b). The compactness parameter, eq. (2.1), which is a measure of the core's density structure, increases rapidly from 12 to 15 $M_\odot$ and then remains roughly constant (Fig. 3.1). Carbon ignites exoergically and powers convection in all stars up to about 20 $M_\odot$, and models near the transition to radiative central carbon burning end up creating highly variable presupernova core structures (Sukhbold and Woosley, 2014). The central core is degenerate and is surrounded by helium and heavy element shells of increasing thickness. Most of these stars are also relatively easy to explode.

- 20 – 30 $M_\odot$: these stars ignite central carbon burning endoergically and are thus not convective during a critical phase when excess entropy might have been radiated by neutrinos. Thick shells of oxygen, neon and carbon contribute appreciably to nucleosynthesis, but, depending upon the location of carbon and oxygen burning shells during the later stages of evolution, lead to a greater compactness parameter. These stars may be difficult to explode (Sukhbold and Woosley, 2014).

- Above 30 $M_\odot$presupernova stars have increasingly thick shells of heavy elements and shallow density gradients around large iron cores making them difficult to explode with neutrinos. Mass loss plays a very important role. For the assumed prescription, the presupernova mass actually decreases with increasing initial mass above 23.5 $M_\odot$. The maximum presupernova mass there is $\sim$ 16.5 $M_\odot$. Rotation may be increasingly important to the explosion mechanism of stars in this mass range (Heger *et al.*, 2005). If mass loss succeeds in removing the entire hydrogen envelope, as it did here for main sequence

stars above 40 $M_\odot$, these stars may explode as a Type Ib or Ic supernova.

Because of their different characteristics, these mass ranges are often modelled separately. Our models for 9 – 13 $M_\odot$ stars, 13 – 30 $M_\odot$ stars, and 30 – 120 $M_\odot$ stars come from different studies, but all were calculated using the KEPLER code. All presupernova models, along with data from § 3.3, § 3.6 and § 3.7, are available at the MPA-Garching archive[2].

3.2.3.1 9 to 13 $M_\odot$

The 17 models in this mass range, 9.0 - 13.0 $M_\odot$, in intervals of 0.25 $M_\odot$, are based on the recent study of Woosley and Heger (2015b). They use the same stellar physics, especially for the propagation of convectively- bounded oxygen and silicon-burning flames, as in that work (see also **?**), but differ by carrying a much larger network throughout the whole evolution. They are new models.

Stars from 9.0 to 10.25 $M_\odot$ ignite silicon in a strong flash that, for the 10.0 and 10.25 $M_\odot$ models, could be violent enough to eject the hydrogen envelope and helium shell prior to iron-core collapse. What actually happens is uncertain though, and depends upon how much silicon burns in the flash (Woosley and Heger, 2015b). For the present study, silicon burning in the flash was constrained to be small by using a small convective transport coefficient, and envelope ejection did not occur. For models 10.5 $M_\odot$and heavier, all fuels ignited stably in the center of the star.

The nuclear reaction network used was complete up to Bi (Z = 93) and contained roughly 1000 isotopes during helium burning and over 1200 during oxygen and silicon burning. Presupernova stars contained approximately 1900 isotopes. Woosley and Heger (2015b), who

were interested chiefly in stellar structure and not nucleosynthesis, truncated their network at Ge. The extra nuclei included here allowed a better representation of the s-process in the presupernova star and its modification during the explosion, but did not greatly alter the structure.

3.2.3.2 13.1 to 30 $M_\odot$

Models in this mass range were calculated using the same nuclear and stellar physics as in Woosley *et al.* (2007). The survey includes 151 models from 15 to 30 $M_\odot$ taken from the "S-series" in Sukhbold and Woosley (2014), and 19 additional models from 13.1 to 14.9 $M_\odot$ calculated the same way. In order to demonstrate the agreement among models from two different surveys, several additional models from 12 to 13 $M_\odot$ were calculated for comparison with models from § 3.2.3.1, but were not used in the survey. The presupernova structures of stars calculated both ways were in good agreement, having e.g., nearly identical values of the mass enclosed by inner 3000 km (Fig. 3.4). The mesh of stellar masses was relatively fine, 0.1 $M_\odot$, as is necessary to calculate the rich variation of stellar structure in this mass range.

3.2.3.3 31 to 120 $M_\odot$

A total of 13 models with varying mass increments were studied in this range - 31, 32, 33, 35, 40, 45, 50, 55, 60, 70, 80, 100, 120 $M_\odot$ - all coming from Woosley *et al.* (2007). Starting at about 40 $M_\odot$, these models lost their entire envelopes and ended their lives as Wolf-Rayet stars. The final masses are thus sensitive to the treatment of mass loss both for red supergiant stars and stripped cores. The final presupernova masses for the 60, 70, 80, 100, and 120 $M_\odot$ stars were 7.29, 6.41, 6.37, 6.04 and 6.16 $M_\odot$ respectively.

3.3 Explosion Modelling

The presupernova models were exploded using two different one- dimensional hydrodynamics codes, Prometheus-Hot Bubble (henceforth PHOTB Janka and Mueller 1996; **?**) and KEPLERḞor central engines Z9.6, W18, and N20, all models were exploded using both codes. For W15, W20, and S19.8, models were exploded only with PHOTB.

PHOTB includes the necessary neutrino and high-density physics to follow iron-core collapse and neutrino energy and lepton-number transport. It also carries a small reaction network with 14 alpha nuclei (Mueller, 1986), which is capable of tracking bulk nucleosynthesis (Ugliano *et al.*, 2012; Ertl *et al.*, 2016). The neutrino transport is approximated by a fast, gray scheme that solves the coupled set of neutrino number and energy equations for all flavours as described in Scheck *et al.* (2006). The implementation of gravity, including general relativistic corrections, has been detailed in Arcones *et al.* (2007), and the choice of the boundary conditions for hydrodynamics and transport applied in our present work follows Ugliano *et al.* (2012) and Ertl *et al.* (2016). Extending the code used by Ugliano *et al.* (2012), Ertl *et al.* (2016) added a simple deleptonization scheme (Liebendörfer, 2005) for a fast treatment of the core-collapse phase until shortly after core bounce. They also improved the microphysics treatment in several respects, e.g., by implementing a high-density equation of state (EoS) and consistently coupling the burning network with the low-density EoS and hydrodynamics.

KEPLER does not include neutrino transport and its equation of state becomes unreliable above about 10^{11} g cm^{-3}, but it does carry a much larger nuclear reaction network of roughly 1500 isotopes, capable of calculating detailed nucleosynthesis, and includes flux-

limited radiative diffusion so that bolometric light curves can be determined. For cases where both codes were used, the procedure that was followed was to first calculate the explosion using PHOTB, continued to a sufficiently late time to determine the remnant mass, and then to post-process the explosion using KEPLER.

3.3.1 Explosion Simulations with PHOTB

A detailed discussion of our methodology for neutrino-driven explosions for large sets of progenitor models can be found in Ertl *et al.* (2016), and more technical information is also given in Ugliano *et al.* (2012). Here we summarize the essential characteristics.

The calculations with PHOTB assume spherical symmetry and are 1D. They follow the evolution from the onset of stellar collapse as determined by the KEPLER code, when the collapse speed anywhere in the core first exceeds 1000 km s^{-1}, through core bounce and post-bounce accretion to either black-hole (BH) formation or successful explosion. The fall back of matter that does not become gravitationally unbound in the explosion is determined by running the calculation for days to weeks. Proto-neutron star (PNS) cooling and neutrino emission are followed for typically 15 s, at which time the shock has crossed $\sim 10^{10}$ cm and is outside of the CO core. By that time the power of the neutrino-driven wind, which pushes the dense ejecta shell enclosed by the expanding supernova shock and the wind-termination shock, has decayed to a dynamically insignificant level. The models are then mapped to a grid extending to larger radii, and the inner boundary is moved from below the neutrinosphere to 10^9 cm in order to ease the numerical time-step constraint.

Spherically symmetric, first-principles simulations do not yield explosions by the

neutrino-driven mechanism except for low mass progenitors with oxygen-neon-magnesium cores (Kitaura *et al.*, 2006; Janka *et al.*, 2008) or small iron cores (Melson *et al.*, 2015). These stars are characterized by an extremely dilute circum-core density and small compactness values, ξ_M for $M \geq 1.5$. Ignoring the beneficial effects of hydrodynamic instabilities in initiating the revival of the stalled bounce shock, explosions require a suitable tuning of the neutrino source to revive the shock by neutrino heating.

In order to do so, we exclude the inner 1.1 $M_\odot$ of the high-density core of the PNS at densities significantly above the neutrinospheric region from the hydrodynamical modelling, and replace them by an inner grid boundary that is contracted to mimic the shrinking of the core. At this domain boundary, time-dependent neutrino luminosities and mean energies (Scheck *et al.*, 2006; Arcones *et al.*, 2007; Ugliano *et al.*, 2012) are imposed. Outside of this boundary (between neutrino optical depths below $\sim$10, initially, and up to several 1000 after seconds of PNS cooling), the lepton number and energy transport of all species of neutrinos is solved using a fast, analytical, gray transport approximation (Scheck *et al.*, 2006). The time-dependent neutrino emission from PNS accretion, which is determined by the progenitor structure of the collapsing star and by the dynamics of the shock front, is thus included in our models, and ensures that corresponding feedback effects are taken into account, at least as far as they can be represented in spherical symmetry.

The excised PNS core is represented as a time-dependent neutrino source using a simple one-zone model whose behaviour is determined by applying fundamental physics relations (Ugliano *et al.*, 2012). The free parameters of this core model are calibrated by comparing the results of explosion simulations for suitable progenitor models to observations of well-studied

supernovae. For this purpose we consider important diagnostic parameters of the explosion, i.e., the explosion energy and the mass of ^{56}Ni produced, as well as important properties of the PNS as a neutrino source, i.e., the total release of neutrino energy and the time scale of this neutrino emission. For the neutrino properties, the detected neutrino signal from SN 1987A is used as a benchmark, but we also make sure that the neutrino-energy loss of our PNS models is consistent with binding energies of neutron stars based on microphysical equations of state.

Excluding the high-density core of the PNS from direct modelling can be justified by the still incomplete knowledge of the equation of state in the supernuclear regime and significant uncertainties in the neutrino opacities in dense, correlated nuclear matter, which overshadow all fully self-consistent modelling. Of course, modelling supernova explosions in spherical symmetry can only be an intermediate step, and ultimately three-dimensional simulations will be needed. Below we will argue that 1D simulations in the case of tuned explosions exhibit some aspects that are more similar to current 3D models than 2D simulations. According to current multi-dimensional calculations the onset of the explosion differs between 2D and 3D with the former favouring earlier explosions because of differences in the behaviour of turbulence in the post-shock region (e.g., Couch 2013; Hanke *et al.* 2012). Moreover, the imposed constraint of axisymmetry in 2D leads to artificial explosion geometries with pronounced axis features. Also the long-time phase of simultaneous accretion and ejection of neutrino-heated matter seems to differ considerably between 2D and 3D (Müller, 2015), which can lead to more energetic explosions in 3D (Melson *et al.*, 2015; Müller, 2015).

In the following, we present essential information on how the PNS is described as neutrino source in our simulations and how the calibration of this neutrino source is done by

referring to observational data. Since results of nearly the same set of presupernova models using PHOTB have been recently discussed by Ertl *et al.* (2016), our description here can be terse and focused mainly on newly introduced aspects.

3.3.1.1 The PNS as Neutrino Source

The central 1.1 $M_\odot$ core of the PNS resulting from the collapse of each presupernova star is excised from the computational volume and replaced by a contracting inner grid boundary a few milliseconds after core bounce, shortly after the expanding shock has converted to a stalled accretion shock at an enclosed mass of more than 1.1 $M_\odot$. For the hydrodynamics we apply the conditions that are needed to maintain hydrostatic equilibrium at this Lagrangian grid boundary (Janka and Mueller, 1996). The shrinking of the cooling and deleptonizing PNS is mimicked by the contraction of the inner grid boundary, R_{ib}, which is described by an exponential function (Eq. 1 in Arcones *et al.* 2007) with the parameter values given in Sect. 2 of Ugliano *et al.* (2012). In order to avoid too severe time-step restrictions that could hamper the tracking of the combined evolution of PNS and ejecta over more than 20 s, we choose the case of "standard" instead of "rapid" contraction shown in Fig. 1 of Scheck *et al.* (2006). This may lead to an underestimation of the accretion luminosity and of the gradual hardening of the radiated neutrino spectra compared to self-consistent supernova simulations, but in our approach this can well be compensated by a corresponding adjustment of the calibration of the inner core as neutrino source. Since the accretion luminosity computed by the transport adds to core luminosity imposed at the inner grid boundary, the calibration sets constraints to the combined value of these two contributions.

As detailed in Ugliano *et al.* (2012), we describe the high-density PNS core of mass $M_c = 1.1 M_\odot$ by a simple one-zone model under the constraints of energy conservation and the Virial theorem including the effects associated with the growing pressure of the accretion layer, whose accumulation around the PNS core is followed by our hydrodynamic simulations. The one-zone core model provides a time-dependent total core-neutrino luminosity, $L_{\nu,c}(t)$, which determines the boundary luminosity imposed at the inner grid boundary (at R_{ib}) of the computational grid, suitably split between ν_e, $\bar{\nu}_e$, and heavy-lepton neutrinos (see Ugliano *et al.* 2012 and Scheck *et al.* 2006). Besides the luminosities of the different neutrino species also the mean energies (or spectral temperatures) of the inflowing neutrinos are prescribed at R_{ib} (cf. Ugliano *et al.* 2012).

The total core-neutrino luminosity $L_{\nu,c}(t)$ is determined by the core mass, M_c, the core radius, $R_c(t)$, the rate of contraction of this radius, $\dot{R}_c(t)$, the mass of the PNS accretion mantle around the core, m_{acc} (taken to be the mass between the inner grid boundary and a lower density of $10^{10}\,\mathrm{g\,cm^{-3}}$), and the mass-accretion rate of the PNS, $\dot{m}_{acc}$, as computed in our hydrodynamical runs. Equation (4) of Ugliano *et al.* (2012) for the core luminosity can be rewritten as

$$L_{\nu,c}(t) = \frac{1}{3(\Gamma-1)} \left[(3\Gamma - 4)(E_g + S) \frac{\dot{R}_c}{R_c} + S \frac{\dot{m}_{acc}}{m_{acc}} \right] , \tag{3.1}$$

with the factors

$$E_g + S = -\frac{2}{5}\frac{GM_c}{R_c}\left(M_c + \frac{5}{2}\zeta\, m_{acc}\right), \tag{3.2}$$

$$S = -\zeta\frac{GM_c m_{acc}}{R_c}, \tag{3.3}$$

and with the adiabatic index Γ and coefficient ζ ($= \mathcal{O}(1)$) being free parameters of the model. We note that through the S-dependent terms the PNS-core luminosity depends on the structure (e.g., compactness) of the progenitor star, which determines the mass-accretion rate $\dot{m}_{acc}$ and thus the mass m_{acc} of the accretion mantle of the PNS. The core radius as function of time is prescribed by

$$R_c(t) = R_{c,f} + \frac{R_{c,i} - R_{c,f}}{(1+t)^n}, \tag{3.4}$$

where the time t is measured in seconds. The initial PNS core radius, $R_{c,i}$, is set equal to the initial radius of the inner boundary of the hydrodynamic grid, R^i_{ib}, and the final PNS core radius, $R_{c,f}$, as well as the exponent n are also free parameters of our model. Note that R_c should be considered as a representative radius of the high-density core. Since we grossly simplify the radial structure of the PNS core by a one-zone description, the numerical value of R_c has no exact physical meaning except that is represents a rough measure of the size of the PNS core. However, neither its time evolution nor its final value need to be equal to the inner boundary radius of the hydrodynamic grid or to the radius of the 1.1 $M_\odot$ core of a self-consistently computed PNS model using a nuclear EoS. Nevertheless, with a suitably chosen

(calibrated) time dependence of R_c, our model is able to reproduce basic features of the neutrino emission of cooling PNSs, and the choice of n and $R_{c,f}$ can be guided by the temporal behaviour of $R_c(t)$ in sophisticated PNS cooling calculations (see below).

Since both of the expressions of Eqs. (3.2) and (3.3) are negative and $\dot{R}_c < 0$ and $\dot{m}_{acc} > 0$ for the contracting and accreting PNS, the first term in the brackets on the r.h.s. of Eq. (3.1) is positive while the second term is negative. The former term represents the gravitational binding energy release as a consequence of the PNS-core settling in the gravitational potential including the compressional work delivered by the surrounding accretion layer. In contrast, the latter (negative) term accounts for the additional internal energy (and pressure) of the core that is needed for gravitational stability when the overlying mantle grows in mass. This second term thus reduces the energy that can be radiated in neutrinos.

3.3.1.2 Calibration to SN 1987A and SN 1054

The four free parameters of the PNS-core model, Γ, ζ, n, and $R_{c,f}$, determine the core-neutrino emission as given by Eq. (3.1) and thus the solution to a given supernova explosion. The observational cases that serve our needs for calibrating these free parameters are SN 1987A for high-mass stars and the Crab supernova, SN 1054, for low-mass stars. The progenitors and explosion properties of these supernovae are distinctly different and require different values for our model parameters as we shall argue below. For both SN 1987A and SN 1054 the explosion energy and ^{56}Ni mass are fairly well determined and reasonably good guesses for the progenitors exist.

For the SN 1987A progenitor, Ertl *et al.* (2016) considered five different 15–20 $M_\odot$

models, W18, N20, S19.8, W15, and W20. The parameter values that were found to approximately reproduce the known explosion energy and ^{56}Ni production of SN1987A, 1.3–1.5×10^{51} erg and 0.0723–0.0772 $M_\odot$, respectively (Utrobin, 2005; Utrobin and Chugai, 2011; Utrobin *et al.*, 2015), are given in Table 3.2. In the table, E_{51} is the explosion energy in units of 10^{51} erg=1 B=1 bethe, and M(^{56}Ni + 1/2 Tr) is the mass of shock- produced ^{56}Ni plus one-half of the iron group species in the neutrino-powered wind. Because Y_e in the wind is not precisely determined, the actual ^{56}Ni synthesis is between M(^{56}Ni) and M(^{56}Ni + Tr) (Ertl *et al.*, 2016). In practice, Γ, and for most cases $R_{c,f}$, are held constant ($\Gamma = 3$ and $R_{c,f} = 6.0$ km), while n and ζ are adjusted in an iterative process.

Once the parameter values of the PNS core-model are determined for a given SN 1987A progenitor, that same core history is used in all the other presupernova stars of different masses. In this way a set of supernovae calibrated to a given SN 1987A progenitor is generated. This set of explosions is named according to the calibration model, so we have the "W18 series", the "N20 series", etc. In this study we mainly focus on the sets of explosions for the W18 and N20 calibrations.

A problematic point in the results of Ugliano *et al.* (2012) was an overestimation of the explosion energies for lower-mass supernovae. Because of the calibration of the PNS-core parameters with SN 1987A models, a high core-neutrino luminosity caused a strong neutrino-driven wind for low-mass neutron stars. This led to explosion energies in excess of 1.5 B for most stars between 10 $M_\odot$ and 15 $M_\odot$. In particular for progenitors below $\sim$12 $M_\odot$ such high energies are, on the one hand, not compatible with recent self-consistent 2D and 3D models of the explosion, which obtain much lower explosion energies in the range of $\lesssim$0.1 B to at

most a few 0.1 B for progenitors from ~ 8.8 $M_\odot$ to $\sim$12 $M_\odot$ with oxygen-neon-magnesium or iron cores (Kitaura *et al.*, 2006; Janka *et al.*, 2008, 2012; Melson *et al.*, 2015; Müller, 2015). Given the relatively dilute layers and steep density gradients that surround the cores of these progenitors, the hydrodynamic explosion models also suggest that it will be very difficult to reach higher energies by the neutrino-driven mechanism and our present knowledge of the involved physics. On the other hand, high explosion energies for low-mass progenitors are also disfavoured by observations, which seem to suggest some correlation between the progenitor (or ejecta) mass and the explosion energy (e.g., Poznanski 2013; Chugai and Utrobin 2014), although the correlation appears weakened in the light of a more detailed statistical analysis (Pejcha and Thompson, 2015).

Ertl *et al.* (2016) applied a "quick fix" to cure the problem of over- energetic low-mass explosions by using a linear scaling of the compression parameter ζ of the PNS core model, coupled to the decreasing compactness $\xi_{1.75}$ for progenitors with $M \leq 13.5$ $M_\odot$. Here, we elaborate on the background of this measure and introduce an alternative, similarly effective but physics-wise more transparent approach than the ζ modification.

Figure 3.5 displays the mass inside of a radius of 3000 km for all considered progenitor stars up to 30 $M_\odot$ at the onset of core collapse. For most appropriate comparison we evolved all models until they had contracted to the same central density of 3×10^{10} g cm^{-3}. The low-mass stars with $M \leq 12.0$ $M_\odot$ are clearly separated from the more massive progenitors by smaller enclosed masses $M_{3000} = m(r \leq 3000\,\mathrm{km})$. Since the Crab remnant is thought to have originated from the explosion of a star in the $\sim$9–10 $M_\odot$ range (e.g., Nomoto *et al.* 1982; Nomoto 1987; Smith 2013; Tominaga *et al.* 2013), we call the models with small M_{3000} "Crab-

like", whereas we consider the progenitors with $M > 12.0\ M_\odot$ and considerably larger values of M_{3000} as "SN1987A-like". Our calibration models for SN 1987A possess M_{3000} cores that join with the SN 1987A-like cases (see in Fig. 3.5 the purple star and blue diamond for the W18 and N20 progenitors, respectively, and the colored symbols for the other calibration models).

Since the value of M_{3000} provides the mass that is located within 3000 km from the center, it correlates with the mass of the PNS that forms in the collapse of the stellar core. It is important to realize that the contraction behaviour and final radius of the innermost 1.1 $M_\odot$ (which we describe here by our analytic one-zone model) depend in a microphysical model on the mass of the newly formed NS.

Because the simple one-zone core model does not allow to just adopt the core-radius evolution from a self-consistent simulation, we calibrate the "Crab-like" explosions by reproducing the observationally inferred explosion energy of SN 1054 ($\sim$0.05–0.15 B; Tominaga *et al.* 2013; Smith 2013; Yang and Chevalier 2015) and ^{56}Ni mass ($\lesssim 10^{-2} M_\odot$; Tominaga *et al.* 2013; Smith 2013) with a suitable progenitor model.

Table 3.2 lists the parameter values obtained in our Crab calibration of the Z9.6 model. We again use $\Gamma = 3.0$ and $\zeta = 0.65$ as in the W18 series, but now employ a reduced value of $n = 1.55$ and a larger value of $R_{c,f} = 7$ km, because these values describe a slower contraction of the PNS core to a larger final radius (cf. Eq. 3.4) as found for a low-mass PNS in the self-consistent PNS cooling simulation.

Since model Z9.6 for the Crab progenitor is in the extreme corner of the Crab-like sample in terms of mass and M_{3000} (see the blue circle in Fig. 3.5) and the PNS masses in this sample vary considerably, we determine the values of n and $R_{c,f}$ for the other Crab-like

progenitors (with masses M) by interpolating as function of M_{3000} between the Crab model and the SN1987-like progenitor with the smallest value of M_{3000}, which is the case at 15.2 $M_\odot$ in Fig. 3.5, model SW14-15.2. On the SN 1987A-like side we use here the SN 1987A calibration values of n and $R_{c,f}$ for the W18 series. Our interpolation functions for $y \equiv n$, $R_{c,f}$ therefore are:

$$y(x) = y_0 + \frac{y_1 - y_0}{x_1 - x_0}(x - x_0), \tag{3.5}$$

with $x = M_{3000}(M)$, $x_0 = M_{3000}(Z9.6)$, $x_1 = M_{3000}(SW14\text{-}15.2)$, $y(x) = X[M_{3000}(M)]$, $y_0 = X[M_{3000}(Z9.6)]$, and $y_1 = X[M_{3000}(SW14\text{-}15.2)]$. For all SN1987A-like progenitors, we still apply the same values of the model parameters as obtained for the SN 1987A calibration of each series and listed in Table 3.2.

For the 9.0 $M_\odot$ progenitor, which has a lower mass M_{3000} than Z9.6, we use the same values of all core-model parameters as for the 9.6 $M_\odot$ case. Although we employ Z9.6 as our template case for Crab and can also refer to a recent 3D explosion simulation of this model (Melson *et al.*, 2015) for its parameter calibration, our 9.0 $M_\odot$ explosion is equally well compatible with Crab. The computed properties of this explosion (energy around 0.1 B and ^{56}Ni mass below 0.01 $M_\odot$; see following section) turn out to be fully consistent with the observational limits for Crab.

3.3.2 Simulating Explosions with KEPLER

Linking the successful explosions back into the KEPLER code required care in order to preserve the energetics, remnant masses, and bulk nucleosynthesis determined in the more

accurate simulation with neutrino physics. KEPLER is an implicit Lagrangian hydrodynamics code, and thus it can take longer time steps and carry a reaction network of arbitrary size. Since the presupernova models used for the neutrino transport calculation were calculated using the KEPLER code, it was most natural to make the link at that time. Within the Lagrangian code, one then has two options for simulating the explosion - dumping a prescribed amount of energy in one or several zones, or moving a specified inner boundary, a "piston", along a specified trajectory, radius as a function of time.

Here the piston approach was adopted, but considerable experimentation was devoted to determining the optimal trajectory. Major recoding would have been necessary to include neutrino energy transport in KEPLER, so one requirement was that the piston trajectory be located outside of the radius where, even at bounce, neutrino heating and modification of the composition were negligible. On the other hand, the piston needed to be deep enough in the star to give an accurate estimate of the explosion energy and iron synthesis. Experience showed that a piston situated too deep in the star accreted too much matter while waiting for neutrinos to reverse the accretion. The sudden outward motion of the large artificially accreted mass resulted in an overly powerful explosion and too much ^{56}Ni production. Similarly, a piston situated too far out experienced an inadequate peak temperature to make iron. The density also was too low to acquire enough momentum to make a strong shock unless the piston was moved for a very long time.

After some experimentation with various trajectories, the "special trajectories" were chosen (Fig. 3.6). These are Lagrangian mass coordinates that, in the neutrino transport calculation, bounce between 80 and 140 km (most between 120 and 140 km). They mark the first

mass shell to be accelerated outwards when the stalled shock revives. Several such trajectories were followed in KEPLER and gave reasonably good agreement, typically within 20%, with the results from PHOTB for both supernova energy and iron-group synthesis. Better agreement could be obtained, however, if the significant stagnation at small radius for the "special trajectory" used by KEPLER was shortened. The procedure that was eventually adopted used a piston with following velocity evolution for inward ($t < t_{min}$) and outward ($t > t_{min}$) motions, where t_{min} is the time when the piston reaches its smallest radius, r_{min}:

$$\begin{aligned} v_{in} &= (r_{min} - r_z - v_z t_{min}) t / t_{min}^2 + v_z \quad \text{for } t < t_{min} \\ v_{out} &= \sqrt{\frac{2G\alpha m_z (r_{max} - r)}{(r_{max} r)}} \qquad \text{for } t > t_{max} \end{aligned} \tag{3.6}$$

here subscript z denotes the initial piston location in the presupernova model according to the special trajectory from the PHOTB calculation, i.e. m_z, r_z, v_z are the initial Lagrangian location of the trajectory, the corresponding initial radius and collapse velocity. The inward path of the piston follows a parabola that connects this initial location to r_{min} at t_{min}. The outward path from r_{min} to r_{max} (taken as 10^9cm), is determined by the time-dependent velocity that is equal in speed with the free fall velocity that corresponds to the gravitational potential from the piston mass m_z times the multiplier α (Fig. 3.7).

For the stars that exploded in PHOTB, the desired kinetic energy at infinity in KEPLER is obtained by iterating on α. This required an earlier, more rapid motion outwards for the adopted piston. By design, the two explosion models thus agreed almost exactly in explosion energy and piston mass. They also agreed to typically better than 10% in the mass of iron-group

nuclei that were synthesized. Here the total iron in PHOTB calculation is taken as the amount outside the final fallback mass.

To make the agreement in ^{56}Ni mass even better, first, for few models the starting location in mass of the special trajectory, m_z, was slightly varied, usually by ~ 0.01 $M_\odot$, so that the KEPLER total iron mass lies roughly in between the special and fallback trajectories (Fig. 3.8). Then using the innermost zone abundances, most models were scaled up slightly until the fallback trajectory value, so that the final disagreement of iron-group synthesis was a few percent at most.

In the remainder of the chapter, the baryonic remnant masses, the kinetic energies at infinity of the ejecta, and the total iron-group synthesis are based upon the 1D neutrino-powered explosions using PHOTB. Only the isotopic nucleosynthesis (of all elements including presupernova mass loss) and the light curves are taken from KEPLER.

3.4 Explosion Properties

Inserting the standard "central engines" described in § 3.3 in the various presupernova stars resulted in a wide variety of outcomes depending upon the properties of each progenitor, especially its mass and compactness, and the choice of 87A model used for the engine's calibration (Fig. 3.9). Generally speaking, weaker central engines like W20 gave fewer supernova than stronger engines like N20.

This is an interesting point that warrants elaboration. Not every model for 87A will give equivalent, or even necessarily valid results when its central engine is inserted in other

stars. SN 1987A was a blue supergiant in a galaxy with lower metallicity than the sun. All presupernova models considered here, except those that lost their envelopes before exploding, are red supergiants with an initially solar composition. The SN 1987A models, at least those that made blue supergiant progenitors (Table 3.1), also used a different value for semi-convective mixing that affected the size of the carbon-oxygen core for that mass (made the core smaller). One of the models, W18, included rotation while the present survey does not. Our calculations are 1D not 3D. Finally, one expects significant variations in presupernova core structure even for two stars of very similar initial mass and presupernova luminosity (Sukhbold and Woosley, 2014).

The very similar results for "explodability" for models N20, W18, W15 and S19.8 are thus welcome and suggest a robustness to the answer than might not necessarily have existed. They also justify the neglect of model set W20 in the surveys of nucleosynthesis carried out in § 3.6. Use of such a weak engine would grossly underproduce the heavy elements, especially the light s-process (Brown and Woosley, 2013). A much larger supernova rate would be required to make even abundant elements like silicon and oxygen. The results obtained here for solar metallicity stars are also very similar to those of Pejcha and Thompson (2015, their figure 12), who used a very different approach. Qualitatively, the outcome seems more influenced by presupernova structure than details of the central engine, provided that engine is sufficiently powerful to explode many stars.

Models are normalized to SN 1987A here because it was a well studied event with precise determinations for its explosion energy and ^{56} Ni mass as well as its progenitor properties. One could take a different tack and use an even more powerful central engine than N20 in

order to achieve optimal agreement with the solar abundances. That was not done here.

Also given in Fig. 3.10 is the fraction of successful supernovae above a certain main sequence mass, but below 30 $M_{\odot}$. Since heavier stars either fail to explode or explode after losing their hydrogen envelopes, this would be the fraction of Type IIp supernovae.

3.4.1 Relation to Core Compactness

The distribution of successful explosions in Fig. 3.9 is not a simply connected set. The compactness parameter as originally defined in O'Connor and Ott (2011) was innovative for its emphasis on the non-monotonic outcome expected for the deaths of stars of different masses, but is by no means a unique descriptor. Any parameter that samples the density gradient outside the iron core will correlate with explodability. Other measures could be for example, the free fall time from a particular mass shell, the mass enclosed by a fiducial radius, binding energy outside a fiducial mass, d(BE)/dr, the mass where the dimensionless entropy equals 4, etc. Recently Ertl *et al.* (2016) have shown that a physically based two-parameter description of "compactness" can predict explodability for the present set of models presented with almost 100% accuracy (see Figure 6 of that paper). No known single parameter criterion works as well. A less accurate, but perhaps more physically intuitive predictor of explosion is the mass derivative of the binding energy at $\sim$2$M_{\odot}$, shown in Fig. 3.11.

As expected, the successful explosions are, by whatever measure, the outcome of core collapse in stars with steep density gradients around their iron cores. As shown in Fig. 3.1, $\xi_{2.5}$ has a very small value for stars below 12.5 $M_{\odot}$ and it slowly increases to about 0.2 until 15$M_{\odot}$. All of these small models are particularly easy to explode because they are essentially degener-

ate cores inside of loosely bound hydrogenic envelopes, especially at the lower mass end. All versions of the central engine explode stars lighter than this limit. Between 15 and 22 $M_\odot$ stars become more difficult to explode and the outcome can be highly variable for even small changes in the initial mass, especially near $20M_\odot$, where central carbon burning transitions from convective to radiative. From 22 to 25 $M_\odot$, very few or no successful explosions were found for all central engines. There then comes an island around 25 to 27 $M_\odot$ that, once again explodes. The non-monotonic nature of compactness is due to the migration of the location of carbon and oxygen-burning shells with changing mass (Sukhbold and Woosley, 2014). From 30 $M_\odot$ on up to about 60 $M_\odot$, nothing explodes, except for the strongest engines. Eventually however, the large mass loss appropriate for such large solar metallicity stars removes the hydrogen envelope and whittles away at the helium core making it once again compact and easier to explode, at least for the stronger engines. The results are therefore sensitive to the mass loss prescription employed.

3.4.2 Systematics of Explosion Energy and ^{56}Ni Mass

On general principles, one expects correlations to exist among the explosion energy, ^{56}Ni production, and compactness parameter in successful explosions. The compactness parameter is a surrogate for the density gradient outside of the iron core. The larger $\xi_{2.5}$ (Fig. 3.1), the shallower the density gradient and the greater the mass closer to the origin where high temperature is attained in the shock. A frequently used approximation that takes advantage of the fact that, during the epoch of nucleosynthesis, most of the energy behind the shock is in the form of nearly isothermal radiation is (Weaver and Woosley, 1980)

$$E \approx \frac{4}{3}\pi a T_s^4 R_s^3, \tag{3.7}$$

where E is the total internal energy in the shocked region, T_s, the temperature at the shock, and R_s, its radius. After a short time, this internal energy converts into kinetic energy and becomes nearly equal to the final kinetic energy of the supernova. A shock temperature in excess of about 5×10^9 K is required for the production of ^{56}Ni, so for an explosion energy of 10^{51} erg, most of the matter between the final mass cut and a point located at 3600 km in the presupernova star will end up as ^{56}Ni. This is provided, of course, that the 3600 km point does not move a lot closer to the origin as the explosion develops, and the final mass cut lies inside of the initial 3600 km mass coordinate. Both assumptions are generally valid, although fall back can occasionally reduce ^{56}Ni synthesis to zero.

One expects then, for stars of similar initial compactness and final remnant mass, a weak positive correlation between explosion energy and ^{56}Ni production. A greater explosion energy increases $R_s(5 \times 10^9 \mathrm{K})$, and this larger radius encompasses a greater mass. This correlation can be obscured, or at least rendered "noisy" by variations in the compactness, remnant masses and explosion energies. In particular, the compactness of presupernova stars below 12 $M_\odot$ is very small, i.e., the density gradients at the edges of their iron cores are very steep. These stars are also easy to explode and have substantially lower final energies than the heavier stars. The radius that reaches 5×10^9 K is small and the density gradient is also steep there. Thus, as has been known for some time, stars below 12 $M_\odot$ are not prolific sources of iron. These low mass supernovae, in fact, separate rather cleanly, in theory at least, into a separate class with

low energy and low ^{56}Ni yield - and as we shall see in § 3.7, shorter, fainter light curves.

A correlation is also expected between explosion energy and compactness, but which way does it go? Stars with more compact cores (low values of $\xi_{2.5}$) are easier to explode and thus explode with lower energy, but the stars with extended cores (larger values of $\xi_{2.5}$) might also have lower final energy simply because they are harder to explode. The neutrinos have to do more work against infall and the explosion may be delayed. The mantle has greater binding energy that must be subtracted, but the additional accretion might increase the neutrino luminosity and may give a larger explosion energy.

Fig. 3.12 shows the ^{56}Ni mass vs. compactness parameter for the model series Z9.6 and N20. The clustering of points around $\xi_{2.5} = 0$ with low ^{56}Ni and energy is expected, as is a transition region to higher values of both. Over most of the compactness parameter range, however, the explosion energy is roughly constant with some small variation due to the effects just mentioned. With a constant explosion energy, the ^{56}Ni synthesis is slightly greater for the stars with shallower density gradients, i.e., larger $\xi_{2.5}$.

It is also interesting to compare the correlation between ^{56}Ni production and the explosion energy, especially since both can potentially be measured. Two classes of events are expected - the stars above and below 12 $M_\odot$ and above - and a slight positive correlation of ^{56}Ni with explosion energy is also expected in the more massive stars. Fig. 3.13 supports these expectations, but shows that the variation of ^{56}Ni production in stars above 13 $M_\odot$ is really quite small. While it may be tempting to draw a straight line through the full data set, this obscures what is really two different sorts of behaviour. It is important to note that about half of all observable supernovae in the current survey have masses below 12 $M_\odot$ (Table 3.3).

A similar correlation between ^{56}Ni and kinetic energy has been discussed by Pejcha and Thompson (2015) and compared with observational data (their figure 20). The observations (Hamuy, 2003; Spiro *et al.*, 2014) show a particularly strong correlation of plateau luminosity with the inferred mass of ^{56}Ni, extending all the way down to 10^{-3} $M_\odot$ for the latter. Our lowest ^{56}Ni synthesis, in a successful supernova that left a neutron star remnant, was 0.003 $M_\odot$ for the 1.4×10^{50} erg explosion calculated with KEPLER for the 9.25 $M_\odot$ model using the Z9.6 central engine. The ^{56}Ni synthesis in the 9.0 to 9.5 $M_\odot$ models using PHOTB were substantially different and the discrepancy highlights some uncertain physics that warrants discussion. Because the shock-produced ^{56}Ni is very small in these low mass stars, the neutrino wind contribution is non-negligible. For the 9.25 $M_\odot$ model, PHOTB calculates that 0.00659 $M_\odot$ of ^{56}Ni is ejected, but about half of this is made inside the "special trajectory" (Fig. 3.6) used by KEPLER to represent the mass cut (§ 3.3.2), and most of this comes from the approximately-simulated wind in PHOTB. In that calculation all iron-group and trans-iron species in the neutrino-powered wind are represented by ^{56}Ni if neutrino interactions lead to $Y_e \geq 0.49$. Otherwise, ^{56}Ni is replaced by a "tracer nucleus" for neutron-rich species. The network employed does not therefore track the composition in detail.

For heavier stars that make most of the elements, this small difference is negligible, but for these very light stars it is not. The actual ^{56} Ni synthesis in these very light stars is probably between the KEPLER and PHOTB values. Indeed, KEPLER was taken to be "converged" when its ^{56}Ni synthesis lay between these two values - the actual ejected value in PHOTB and the value outside of the "special trajectory". This means that the very low values of ^{56}Ni synthesis calculated for the 9.0 to 9.5 $M_\odot$ models by KEPLER are more uncertain than for other

masses and possibly a lower bound to the actual value. For nucleosynthesis purposes (§ 3.6), the KEPLER iron-group synthesis was renormalized to agree exactly with the full PHOTB value. It is also possible to get still smaller values for ^{56} Ni in heavier stars that experience appreciable fallback.

We note in passing that the ^{56}Ni produced by electron-capture supernovae is mostly made in their neutrino-powered winds. Wanajo *et al.* (2011b), using 1D and 2D explosion models that incorporated realistic neutrino transport, obtained about 0.003 $M_\odot$ of ^{56}Ni for an electron-capture supernova, which is very similar to the wind component predicted with PHOTB for the present explosions of our low-mass progenitors.

On the upper end, one might be tempted to extend this correlation of ^{56}Ni production and kinetic energy to still more energetic events, including gamma-ray bursts and ultra-luminous supernovae (Kushnir, 2015), but these other events likely have other explosion mechanisms, and the study here is focused on non-rotating, neutrino-powered models.

3.5 Bound Remnants

3.5.1 Neutron Stars

The PHOTB calculations continue to sufficiently late times ($\sim 10^6$ s) to include most fallback and accurately determine the baryonic mass that collapses to a neutron star. They also give an estimate of the gravitational mass based upon the neutrino loss of the neutron-star cooling model employed in the simulations. These results are in very good agreement with a simple, radius-dependent correction (Lattimer and Prakash, 2001) that gives the neutron star's

gravitational mass, M_g, from its calculated baryonic mass, M_b:

$$\beta = \frac{GM_g}{c^2 12\text{km}}, \tag{3.8}$$

$$\frac{M_b - M_g}{M_g} = 0.6\frac{\beta}{1-0.5\beta}, \tag{3.9}$$

where G is the gravitational constant and c the speed of light.

A distribution of gravitational masses can then be constructed by weighting the occurrence of each of our successful models according to a Salpeter IMF. The resulting frequencies are plotted as a function of neutron star mass in Fig. 3.14 and are seen to be in reasonably good agreement with the observed values compiled by Özel *et al.* (2012) and Ozel and Freire (2016) in terms of overall spread and mean value. Our maximum neutron star mass for the W18 series is 1.68 $M_\odot$ and the minimum is 1.23 $M_\odot$. Use of 10 km for the neutron star radius reduces these numbers to 1.64 $M_\odot$ and 1.21 $M_\odot$, and reduces the average mass by about 0.02 $M_\odot$. Here we note that, due to the complications of evolutionary effects, we did not build a PDF from the observed measurements, that reflects proper weights of different populations. Instead, the aim here is purely to provide a visual guide to the currently known measurements.

Different mass neutron stars, for the most part, come from different ranges of main sequence mass with lower-mass progenitors producing low-mass neutron stars. There is some overlap however. Remnants from stars between 15 and 18 solar masses have slightly lower masses than some below 15 solar masses. Stars above 18 $M_\odot$ contribute little to the distribution, but do so over a broad range of neutron star masses. This reflects both the variable mass

of the very massive stars at death, due to extensive mass loss, and inherent variability in their compactness. While we have not carried out a statistical analysis, Fig. 3.14 does suggest some bimodality in the distribution, with a separate peak around 1.25 $M_\odot$ (see also Schwab *et al.*, 2010). It is interesting to note that these low mass neutron stars are produced without invoking electron-capture supernovae (e.g., Schwab *et al.*, 2010), none of which are in our sample. Indeed, heavier stars that experience iron-core collapse supernovae are capable, in principle, of producing lighter neutron stars than electron-capture supernovae since the values of Y_e in the cores of the latter are close to 0.5 at the onset of collapse, while they are substantially less after oxygen and silicon burning in the former. In quite heavy stars, this destabilizing effect is more than compensated for by the high entropy and mild degeneracy, but in lighter 9 - 11 $M_\odot$stars, Y_e becomes a major determinant for the onset of core collapse.

An average neutron star mass can also be generated from a IMF-weighted sampling of the successful explosions. The results for four different calibrations of the central engine for SN 1987A, each including the normalization to the Crab for stars below 13 $M_\odot$, are given for a Salpeter IMF in Table 3.3. These values are not very sensitive to the central engine used for SN 1987A, but are determined more by presupernova properties. All lie close to the (error-weighted) observational means given by Lattimer (2012) of 1.368 $M_\odot$ for x-ray and optical binaries, 1.402 $M_\odot$ for neutron star binaries, and 1.369 $M_\odot$ for neutron star - white dwarf binaries. They are not far from the average neutron star mass found by Schwab *et al.* (2010), $1.325 \pm 0.056 M_\odot$. These new theoretical values are closer to the observations than the results from Brown and Woosley (2013).

Table 3.3 also gives the average baryonic mass of the remnants of successful ex-

plosions, $\bar{M}_b$, the average supernova kinetic energy at infinity, $\bar{E}$, and the range of average ^{56}Ni masses, all as calculated in PHOTB. The lower bound ignores the contribution from the neutrino-powered wind while the upper bound assumes all of the wind not in the form of α-particles is ^{56} Ni. Based on post-processing with KEPLER this may be an overestimate of the actual ^{56}Ni production by 10 to 20%. The column labelled SN% is the IMF-weighted fraction of all stars studied that blew up and left neutron star remnants. One minus this fraction is the percentage that became black holes. The last column gives the numerical fraction of all successful explosions that have main sequence masses above 12 $M_\odot$, 20 $M_\odot$, and 30 $M_\odot$. The small value above 20 $M_\odot$ compares much better than past surveys with the results of Smartt (2009, 2015), who place an upper limit on observational supernovae of about 18 $M_\odot$. The successful explosions above 30 $M_\odot$ are all Type Ib or Ic.

3.5.2 Black Holes

Stellar collapses that fail to create a strong outward moving shock after 3–15 s in PHOTB (with variations due to the progenitor-dependent mass-accretion rate) are assumed to form black holes. In the absence of substantial rotation, it is assumed that the rest of the core of helium and heavy elements collapses into that hole. The fate of the hydrogen envelope is less clear. In the more massive stars, above about 30 $M_\odot$, the envelope will already have been lost to a wind. In the lighter stars, all of which are red supergiants, the envelope is very tenuously bound. Typical net binding energies are $\sim 10^{47}$erg. Any small core disturbance prior to explosion (Shiode and Quataert, 2014) or envelope instability (Smith and Arnett, 2014) could lead to its ejection in many cases. Even if the envelope is still in place when the iron core

collapses, the sudden loss of mass from the core as neutrinos can lead to the unbinding of the envelope (Nadezhin, 1980; Lovegrove and Woosley, 2013).

Fig. 3.15 shows the masses ejected and neutron star remnant masses for the successful explosions using the Z9.6 and N20 central engines. For those stars that made black holes, the helium core and envelope masses are indicated and, for all stars, the mass loss to winds before star death is indicated. A few stars made black holes by fallback and are also shown. Fig. 3.16 shows the distribution of black hole masses under two assumptions: a) that only the helium core accretes, and b) that the entire presupernova star falls into the black hole. A distribution of IMF-weighted black hole frequency, calculated just as it was for neutron stars, is given in Table 3.3. No subtraction has been made for the mass lost to neutrinos, that is the gravitational mass has been taken equal to the baryonic mass. It is expected that a proto-neutron star will form in all cases and radiate neutrinos until collapsing inside its event horizon. The amount of emission before trapped surface formation is uncertain, but unlikely to exceed the binding energy of the maximum mass neutron star, about 0.3 $M_\odot$ (O'Connor and Ott, 2011; Steiner *et al.*, 2013).

Assuming the entire collapse of any black-hole forming star, including its hydrogen envelope, gives an upper bound to the mass of the black hole formed. This limiting case is not in good agreement with the existing measurements (Wiktorowicz *et al.*, 2014) [1], in terms of range and frequency of observed masses. The helium core mass seems a better indicator (Zhang *et al.*, 2008; Kochanek, 2014, 2015).

In addition to their production by stars that fail to launch a successful outgoing shock, black holes can also be made in successful explosions that experience a large amount of fallback.

[1] http://stellarcollapse.org/bhmasses; retrieved 6 Sep. 2015

Only a few cases of this were found in the present survey, and the resulting black hole masses were always significantly less than the helium core mass. They were made in some of the most massive stars that exploded. The weakest central engine, W20, did not produce any black holes by fallback. Cases that might have had large fallback failed to explode in the first place. The W15 series yielded only one black hole with a mass of 4.7 $M_\odot$ produced in a star that on the main sequence was 60 $M_\odot$. Series W18 produced black holes by fallback at 27.2 and 27.3 $M_\odot$ with masses of 3.2 and 6.2 $M_\odot$. The strongest two engines S19.8 and N20 gave a few such cases at a slightly higher mass, resulting into black holes in the range 4.1 to 7.3 $M_\odot$. In all cases, the black hole mass was substantially less than the helium core mass, which ranged from 9.2 to 10.2 $M_\odot$.

This tendency of neutrino-powered models to either explode robustly or not at all has been noted previously, and naturally accounts for a substantial mass gap between the heaviest neutron stars and the typical black hole mass (Ugliano *et al.*, 2012). In any successful explosion of a quite massive star (i.e., above 12 $M_\odot$), a few hundredths of a solar mass of photodisintegrated matter reassembles yielding a lower bound to the explosion energy of a few $\times 10^{50}$ erg (e.g., Scheck *et al.*, 2006). On the other hand, the ejection of the hydrogen envelope and collapse of the entire helium core requires that the final kinetic energy at infinity be less than about 10^{50} erg (Lovegrove and Woosley, 2015). Given that the observations favor the implosion of the helium core, but not of the entire star (Fig. 3.16), it seems that another mechanism is at work. One natural explanation is that the hydrogen envelope is ejected during the collapse of these massive "failures" by the Nadyozhin-Lovegrove effect (Nadezhin, 1980; Lovegrove and Woosley, 2013). The loss in binding energy due to neutrino emission of the proto-neutron star

launches a weak shock that ejects the loosely bound envelope. If so, faint, red supernovae may be a diagnostic of typical black hole formation in massive stars (Lovegrove and Woosley, 2013; Kochanek, 2014; Lovegrove and Woosley, 2015).

3.6 Nucleosynthesis

Detailed isotopic nucleosynthesis, from hydrogen to bismuth, was calculated using the KEPLER code for all the models presented in § 3.2.3. During the explosion, all shock-induced transformations were followed as well as nucleosynthesis by the neutrino-process (Woosley *et al.*, 1990; Heger *et al.*, 2005). The r-, s-, and γ-processes were all followed in matter outside the iron core, but nucleosynthesis in the neutrino-powered wind was not followed in any detail.

Rather than discuss the yields of individual stars, however, this section gives and discusses a summary of the nucleosynthesis for the two main explosion series, N20 and W18, averaged over an initial mass function. To give an indication of the variation with mass, separate results are given for three mass ranges: 9 – 12 $M_\odot$; 12 – 30 $M_\odot$; and 30 – 120 $M_\odot$. These ranges are chosen to represent the qualitatively different nature (§ 3.2.3) of supernova progenitors with very compact core structures (first group); supernovae that have actually made most of the elements (second group); and events where mass loss or an uncertain initial mass function plays a key role (third group). At the end, we also summarize the total nucleosynthesis (9 – 120 $M_\odot$) and consider the effect of adding a SN Ia component to pick up deficiencies in iron-group and intermediate-mass element production (§ 3.6.5).

To proceed, the yields of each star, M_i, are separated into two categories: those species

produced in the winds of the star during its presupernova evolution, and those ejected during the supernova itself (only wind for the imploded stars). For each star, these yields, in solar masses, are multiplied by the fractional area under a Salpeter (Salpeter, 1955) initial mass function (IMF) that describes the number of stars in each bin between M_i and M_{i+1}. The area has been normalized so that the total area under the IMF curve from 9 to 120 $M_\odot$is 1. Summing the results across a mass range provides the average ejecta, in solar masses per massive star within that range.

A characteristic mass fraction is then computed which is the ratio of the IMF-weighted ejected mass of a given element (or isotope) produced in a mass range divided by the total mass of all species ejected. The computation may or may not include the wind; both cases are considered. The production factor is then the ratio of this mass fraction to the corresponding mass fraction in the sun (Lodders, 2003).

Defined in this way, a production factor of 1 implies no change in the mass fraction of an isotope from the star or mass range considered compared to the presupernova progenitor. What came in is what goes out. The net production of a given species is proportional to 1 - P. There is also a change in all species since some mass stays behind in the bound remnant and is lost. This is not accounted for in the definition used here for P. If half of the mass of the star is lost to the remnant, but the mass ejected from the star is all of exactly solar composition, the production factor by our definition is still 1, but the *net* production would be this factor times $(M_{ZAMS} - M_{rem})/M_{rem} = 1/2$. As presently designed, the production factor can only be less than 1 if the species is destroyed by nuclear reactions (e.g., deuterium, beryllium).

For purposes of presentation, all production factors are divided by that of ^{16}O so that

the production factor of ^{16}O, an abundant element known to be produced in massive stars, is one. To retain information about the unnormalized production factor, a line is given in each figure at the reciprocal of the unnormalized production factor of ^{16}O. Points lying on this line have no net production, i.e, have an unnormalized production factor of 1.

In order to demonstrate the dependence on uncertain mass loss rates, especially in the heavier stars, some yields are presented with and without mass loss. The "without mass loss results" are an artificial construct because we have not carried out a self-consistent evolution and explosion of constant mass stars. The explosion of such stars would be quite different. For example, the more massive stars would all make black holes. The less massive ones might explode and eject the same matter the wind would have removed. Here, the mass lost in the wind is simply discarded. The effect of removing it shows its importance.

In those calculations that include the wind, the mass loss of all stars has been added, including those that end up making black holes. All stars have winds; only those that explode have supernova ejecta. The tricky issue of how to treat the hydrogen envelope of stars that form black holes, but are presumed (not calculated) to eject their residual envelopes is deferred to a later section (§ 3.6.4.5).

Because of the lower bound on the mass, 9 $M_{\odot}$, no contribution from lighter stars is included here, so it is to be expected that species like the heavy s-process, ^{13}C, ^{14}N etc. which are known to be efficiently produced in AGB stars, will be under-represented. Any r-process from merging neutron stars or the neutrino wind is also missing, as are the products of cosmic ray spallation.

Some interesting statistics relevant to nucleosynthesis are given in Table 3.4. For

the W18 and N20 series, the typical supernova mass, based only upon those stars that actually exploded, is given along with the fraction of the total ejecta that come from each mass range.

3.6.1 9-12 $M_{\odot}$

While roughly half of all observed supernovae lie within this range, (Table 3.3), their contribution to the overall stellar nucleosynthesis is relatively small. Fig. 3.17 shows reasonably good agreement with solar system elemental abundances for elements heavier than beryllium (Z = 4) all the way through the iron group, but this can be misleading since a lot of the yield was in the star to begin with in solar proportions. The actual production factor for oxygen, before renormalization, is 2.37, so a value of 1./2.37 = 0.422 in the figure indicates no net change in the abundance due to stellar nucleosynthesis. This is apparent for the heaviest elements plotted, around Z = 40. To the extent that other elements have the same production factor as oxygen, their abundance is also about 2.37 times greater than what the star had, external to its final gravitationally bound remnant, at birth.

Fig. 3.17 reveals some interesting systematics for low mass supernovae though. First, the abundances *are* roughly solar, even for the iron group. Some elements, Co, Ni, and Cu are even overproduced. This is surprising given that only a minor fraction of iron-group elements is expected to come from massive stars (e.g. Timmes *et al.*, 1995b; Cayrel *et al.*, 2004). More should come from Type Ia supernovae (SN Ia). Their apparent large production here really just reflects the fact that these stars make very little oxygen. As we shall see later, massive stars altogether make only about one-quarter of solar iron. Still it is an interesting prediction that iron to oxygen in the remnants of low mass supernova remnants may be roughly solar.

By the same token, the productions of carbon and nitrogen is not generally attributed to massive stars, but they do have slightly super-solar proportions to oxygen in this mass range. Nitrogen, which is made in the hydrogen envelope by the CNO cycle operating in a large mass on primordial C and O, seems large here because oxygen, made by helium burning in a relatively thin shell is small. Overall, we shall find that nitrogen, at least nowadays, is probably not a massive star product, though the component coming from massive stars is appreciable. The case of carbon is less clear and depends on mass loss rates and the initial mass function.

Also quite abundant in Fig. 3.17 are lithium, boron, and fluorine. ^{7}Li and ^{11}B are made by the neutrino process (Woosley *et al.*, 1990). The assumed temperature of the μ and τ neutrinos here was 6 MeV. The large production of ^{11}B reflects the large carbon abundance in these lower mass stars, and the proximity of the carbon shell to the collapsing iron core which emits the neutrinos. ^{7}Li is made by the spallation of ^{4}He by μ- and τ-neutrinos by the reaction sequence ^{4}He(ν,ν'n)^{3}He$(\alpha,\gamma)^{7}$Be. Its large production (again compared with a small oxygen abundance) reflects the proximity of the helium shell to the core and the importance of the alpha-rich freeze out in the bottom-most layers ejected. Fluorine is made by a combination of the neutrino irradiation of neon and helium burning (Meynet and Arnould, 1993; Woosley *et al.*, 1995), with the former making most of the ^{19}F above 15 $M_{\odot}$, but the latter dominating for lower mass supernovae (see also Sieverding *et al.*, 2015), and slightly dominant overall. The synthesis of ^{19}F by neutrinos is primary, however, since the target is ^{20}Ne, while the synthesis by helium burning depends upon the abundance of ^{14}N and neutrons and is therefore secondary. The production of fluorine by helium burning will thus be reduced in lower metallicity stars.

The low production of Be reflects its destruction in massive stars, ^{9}Be and ^{10}B are

thought to be produced by cosmic ray spallation.

3.6.2 12-30 $M_\odot$

Stars from 12 to 30 $M_\odot$ are responsible for most of the nucleosynthesis that happens in supernovae. Fig. 3.18 shows the production factors for this range. The intermediate mass elements are made in roughly solar relative proportions compared with oxygen, though the low yield of calcium is a concern That the iron-peak elements are deficient is not surprising. Most of iron comes from SN Ia. Some species in the iron group, especially Co, Ni, and Cu, are produced here in roughly solar proportions. All are made in the alpha-rich freeze out: ^{58}Ni as itself, and ^{59}Co and ^{63,65}Cu as ^{59}Cu, ^{63}Ga, and ^{65}Ge respectively. Production of these species is sensitive to the treatment of the inner boundary and the neutrino reactions that might go on there changing the value of Y_e. The calculated production here is thus more uncertain than for other species.

The production of Li, B, C, N, and F have all declined greatly from the large values seen for the lower mass supernovae. This is mostly to do with the larger oxygen production to which these yields are now normalized, but also to the lower carbon abundance and larger radii of the carbon and helium shells.

Of particular note in this mass range is a significant underproduction of s-process elements, especially Sc and the elements just above the iron group. This problem will persist in the final integrated nucleosynthesis from all masses and is a challenge for the present models and approach. Part of this deficiency may be due to an uncertain reaction rate for ^{22}Ne(α,n)^{25}Mg (§ 3.6.4.4).

3.6.3 30-120 $M_\odot$

Most stars above 30 $M_\odot$ in the present study become black holes, and their remnants absorb most of the core-processed elements. Their winds will escape prior to collapse however, and contribute to nucleosynthesis, especially of the lighter elements like CNO. For the assumed mass loss rates, some of the heaviest stars in this range (i.e. from 60 $M_\odot$ upward) also explode, but only because winds have stripped the core of the star down to a manageable size. Such stars, having carbon-oxygen cores comparable to stars in the 12 – 39 $M_\odot$ range will contribute similar ucleosynthesis, but more enhanced in the products of helium burning.

Fig. 3.19 shows that the winds contain excesses of ^{4}He, both from the envelopes of these massive stars that have been enriched by hydrogen burning and convective dredge up, and from the winds of Wolf-Rayet stars that have lost their envelopes altogether. This production significantly augments the primordial helium in the original star from the Big Bang and previous generations of stars. The nuclei ^{12,13}C, ^{14}N, and ^{16,18}O are also significantly enriched, but ^{15}N and ^{17}O are not. ^{22}Ne is greatly enhanced owing to Wolf-Rayet winds. This nucleus comes from two alpha captures on ^{14}N and is abundant in the helium shell from convective helium burning. The s-process up to Rb is also produced in the winds of these very massive stars, but its production is still inadequate to explain its abundance in the sun when the lighter stars are folded in. Intermediate mass elements are underproduced compared with the large oxygen synthesis in the winds.

3.6.4 Integrated Yields

The integrated production factors from massive stars of all masses above 9 $M_\odot$ are shown in Fig. 3.20 summed over isotopes. The individual isotopic abundances are given in Fig. 3.21. The integrated production factor is calculated from a combined weighting of the three mass ranges just discussed. If P_{low} is the production factor for stars 9 – 12 $M_\odot$; P_{mid}, for stars 12 – 30 $M_\odot$; and P_{high}, for stars 30 – 120 $M_\odot$, the total production factor, P_{tot} is

$$P_{tot} = f_1 P_{low} + f_2 P_{mid} + f_3 P_{high} \tag{3.10}$$

where f_i is given in Table 3.4. Because P_{low} is generally low and P_{high} is low except for species produced in the winds like CNO, the total production for most elements is dominated by P_{mid}.

The probable nucleosynthetic sites for producing the various isotopes heavier than lithium have been summarized in Table III of Woosley *et al.* (2002) and our discussion follows that general delineation and omits references given there. We also include the full integrated yield of the N20 series in Fig. 3.22. The primary difference is that the N20 model produces a bit more ^{16}O, which can be seen by comparing the baseline solar abundance of the heavy isotopes.

Additionally, one could vary the power of the initial mass function. Lowering the power from that of a Salpeter IMF of −2.35 to a value as low as −2.7 affects the results in a similar way to a reduction in the contributions of mass loss rates. The value of −2.7 was chosen as being a low value within the known uncertainties (e.g. Scalo, 1986; Chabrier, 2003). The results in Fig. 3.23 show that a steeper IMF acts in the same way as reducing the contributions

from the winds of very heavy stars, but with a smaller effect.

3.6.4.1 Light elements - lithium through aluminum

While perhaps not widely recognized, massive stars can make an important, though not dominant contribution to the abundance of ^{7}Li (though not ^{6}Li). The ^{7}Li is made mostly by the neutrino process, which spalls helium in the deeper layers to make ^{3}He which combines with ^{4}He to make ^{7}Li (after a decay). Some ^{3}He is also made in the hydrogenic envelope. The total contribution to each is about 20% of their solar value. ^{6}Li, ^{9}Be, and ^{10}B must be made elsewhere, perhaps by cosmic ray spallation.

^{11}B, on the other hand, is abundantly produced by the neutrino process. Spallation of carbon by μ and τ-neutrinos produces the isotope in the carbon shell. Without neutrinos, ^{11}B would be greatly underproduced. Its abundance in the sun thus provides a useful thermometer for measuring the typical temperature of the neutrinos (though their spectrum is varies significantly from thermal). The assumed temperature of the neutrinos here was 6 MeV. A slightly smaller value would have sufficed, but larger values are ruled out.

Carbon, perhaps surprisingly is adequately produced in massive stars, but the yield is very sensitive to the treatment of mass loss and, to a lesser extent, the IMF (Fig. 3.23). Too much carbon is made for the mass loss rates assumed here (see also Maeder, 1992), but a mass loss rate half as large is certainly allowed and would produce carbon nicely. In the unrealistic case of no mass loss, only about one-third of carbon would be made in massive stars. Care should be taken though because folding the yields from a population of solar metallicity stars with an IMF is very approximate compared with a full model for galactic chemical evolution.

Lower metallicity massive stars would presumably have diminished winds and would make less carbon. The isotope ^{13}C is always underproduced in massive stars and is presumably made in the winds and planetary nebulae of lower mass stars.

Nitrogen too is underproduced and needs to be mostly made elsewhere. Presumably ^{14}N is made by the CNO cycle in lower mass stars and ^{15}N is made in classical novae by the hot CNO cycle.

Oxygen is the normalization point and both ^{16}O and ^{18}O are copiously produced, both by helium burning. The yield of ^{18}O is sensitive to the metallicity, but that of ^{16}O is not directly, though it is sensitive by way of the mass loss. ^{17}O is not made due to its efficient destruction by ^{17}O(p,α)^{14}N. Perhaps it too is made in classical novae.

Fluorine is somewhat underproduced in the overall ensemble, despite having a very substantial production by the neutrino process and helium burning in low mass stars.

The abundance of neon is uncertain in the sun, but ^{20}Ne and ^{21}Ne are well produced and ^{22}Ne is overproduced. The synthesis of ^{22}Ne depends on the initial metallicity of the star, however, since CNO is converted into ^{22}Ne during helium burning. Lower metal stars would make less and the abundance of ^{22}Ne might come down in a full study of galactic chemical evolution. The yield of ^{22}Ne is also sensitive to mass loss, more so than ^{20}Ne and ^{21}Ne, and lower metallicity would imply lower mass loss.

All isotopes of sodium, magnesium, and aluminium are produced reasonably well by carbon and neon burning. Magnesium and aluminium are a little deficient, however, and this is the beginning of a trend that persists through the intermediate mass elements. It could reflect a systematic underestimate of the CO core size due to the neglect of rotation or inadequate

overshoot mixing, since these isotopes will be produced in greater abundances in larger CO cores, but increasing the core size might make the stars harder to blow up. Or it may indicate an incompleteness in the present approach. Many of the stars that made black holes here would have contributed to the intermediate mass elements. Perhaps rotation or other multi-dimensional effects on the explosion play a role?

3.6.4.2 Intermediate-mass elements - silicon through scandium

The major isotopes of the intermediate-mass elements from silicon through calcium are consistently co-produced in solar proportions. The total mass of these, however, is about 12% of that of ^{16}O, which is only half the solar value of 22%. A similar underproduction was seen by Woosley *et al.* (2007) (their Fig 8), so it is not solely a consequence of the new approach. Part of the difference might be picked up by SN Ia which, aside from being prolific sources of iron, can also produce a significant amount of intermediate-mass elements (Iwamoto *et al.*, 1999, and § 3.6.5). Still the systematic underproduction of so many species generally attributed to massive stars is troubling. Better agreement between intermediate mass element and oxygen productions existed in earlier studies (Timmes *et al.*, 1995b; Woosley *et al.*, 2002) which used a larger solar abundance for ^{16}O.

Several isotopes with particularly anomalous production in this mass range warrant mention. ^{40}K is greatly overproduced compared even with the abundance in the zero age sun. The difference presumably reflects the lengthy time in which decay occurred between the last typical supernova and the sun's birth. ^{44}Ca is underproduced in massive stars. Presumably it is made by sub-Chandrasekhar mass models for SN Ia (§ 3.6.5). ^{48}Ca along with several neutron-

rich iron-group nuclei like ^{50}Ti and ^{54}Cr, is presumably made in a neutron-rich nuclear statistic equilibrium as might exist in a rare variety of Type Ia supernova igniting at high density. ^{45}Sc is due to the s-process and its underproduction is a portent of problems to come (§ 3.6.4.4).

3.6.4.3 The Iron Group

The iron yields here were calibrated to be the maximum calculated in PHOTB, where it was assumed that the neutrino wind makes an appreciable contribution. This was one of the agreements forced upon the KEPLER recalculation (Fig. 3.8).

As expected, even taking this upper bound, the iron group is severely underproduced in massive stars, since most of the iron in the sun has been made by SN Ia. In the next section, we shall consider the consequences of combining both varieties of supernovae. The ratio of the mass of new iron made here as ^{56}Ni to new oxygen (neglecting the initial iron and oxygen in the star because it had solar metallicity) is proportional to the ratio of (P-1) for the two species, where P here is the unnormalized production factor (§ 3.6). When normalized to the solar mass fractions, the fraction of solar iron made in core-collapse supernovae is

$$F_{Fe} = \frac{P_{Fe} - 1}{P_{Ox} - 1}. \tag{3.11}$$

For the series W18 P_{Fe} = 2.17 and P_{Ox} = 7.16; for the N20 series P_{Fe} = 3.09 and P_{Ox} = 8.38. Both sets of numbers include the low mass contributions from the Z9.6 series. In both cases the implied iron production is 28%. Given the way this was calculated, using yields normalized to the maximum production in Table 3.3, this is probably an upper bound, though

not by much.

While SN Ia make most of the iron, it is noteworthy that massive stars do contribute appreciably to many species in the iron group. ^{50}V is well produced by carbon burning and ^{58}Fe by the s-process. Cobalt, copper and the nickel isotopes are well produced and, in the case of ^{62}Ni, actually overproduced. All three elements are made mostly by the α-rich freeze out (as ^{58}Ni, ^{59}Cu, and ^{60,61,62}Zn) and are thus most sensitive to the treatment of the inner boundary in KEPLER and the explosion itself of PHOTB. The abundances of ^{58}Ni and ^{62}Zn, which makes ^{62}Ni, are sensitive to the neutron excess in the innermost zones. In KEPLER, appreciable electron capture occurs as these zones fall to very high density and are heated to high temperature by the shock. In PHOTB the neutron excess in these deepest zones can be changed by the neutrinos flowing through, but this has been treated approximately. As a result, the composition of the neutrino-powered wind has not been accurately determined in either code. A higher value of Y_e in those zones would reduce the synthesis of both ^{58}Ni and ^{62}Ni, so their production here must be regarded as uncertain. An appreciable, though lesser, contribution to ^{62}Ni also comes from the s-process in the helium shell

Also noteworthy is the underproduction of ^{55}Mn in massive stars. This species is made mostly as ^{55}Co in a normal (α-deficient) freeze out from nuclear statistical equilibrium, and its synthesis is not so uncertain as that of nickel which is made deeper in.

3.6.4.4 Heavier elements

In contrast to previous studies (e.g. Woosley *et al.*, 2007), the production of species above the iron group falls off rapidly. This is problematic given that the synthesis of s-process

isotopes up to about A = 90 is often attributed to massive stars (Käppeler *et al.*, 2011). The problem is exacerbated by the fact that these are secondary elements and so are expected to be even more underproduced in stars of lower metallicity. If anything, one would like to produce an excess of isotopes in this metallicity range compared with solar values.

Fig. 3.20 shows that production in the mass range A = 65 – 90 is 20 - 50% of what is needed. Previous studies (Woosley *et al.*, 2002, 2007) using the same code and stellar and nuclear physics showed a slight overproduction in the same mass range. The change is a direct consequence of fewer massive stars exploding (Brown and Woosley, 2013). A larger value for the ^{22}Ne(α,n)^{25}Mg reaction rate might help here. For calibration, the present study used reaction rates at 3×10^8 K of 2.58×10^{-11} Mole^{-1} s^{-1} for ^{22}Ne(α,n)^{25}Mg and 8.13×10^{-12} Mole^{-1}s^{-1} for ^{22}Ne(α,γ)^{26}Mg, the same as used for the last 15 years. Longland *et al.* (2012) recently suggested a best value of 3.36×10^{-11} Mole^{-1} s^{-1} (range 2.74 to 4.15 $\times 10^{-11}$ for ^{22}Ne(α,n)^{25}Mg and 1.13×10^{-11} Mole^{-1} s^{-1} (range 0.932 to 1.38×10^{-11}) for ^{22}Ne(α,γ)^{26}Mg. Use of more modern rates would thus improve the agreement slightly, but would probably not eliminate the discrepancy. An improved treatment of overshoot mixing might also make a difference (Costa *et al.*, 2006). Future studies to further study this discrepancy are planned. For the time being, we take the deficient production of the light s-process as the strongest indicator yet that something may be awry in our present 1D modelling. The possibility that a substantial fraction of heavy element production occurs in stars that blow up because of rotation or other multi-dimensional effects must be considered.

Accompanying the underproduction of light s-process elements is a notable under-production of the heavy p-process, again compared with past results. Some have suggested that

the light p-process could also be made in the neutrino-powered wind (Hoffman *et al.*, 1996; Fröhlich *et al.*, 2006; Wanajo *et al.*, 2011a,c).

3.6.4.5 ^{26}Al and ^{60}Fe

The synthesis processes and sites of the long-lived radioactivities ^{26}Al and ^{60}Fe and their importance to gamma-line astronomy has been extensively discussed in the literature (Timmes *et al.*, 1995a; Limongi and Chieffi, 2006b,a). Here, using the W18 calibration, the IMF-averaged ejection masses for ^{26}Al and ^{60}Fe are, respectively, 2.80×10^{-5} and 2.70×10^{-5} solar masses per typical massive star. Using the N20 calibration instead gives 3.63×10^{-5} and 3.20×10^{-5} solar masses per star. Gamma-ray line observations (Wang *et al.*, 2007) imply a number ratio of ^{60}Fe to ^{26}Al in the interstellar medium of 0.148, which implies a mass ratio of 0.34. The ratios of 0.97 and 0.88 from our two calibrations thus exceed observations almost by a factor of three. Still, this is an improvement from Woosley *et al.* (2007) where the ratio, using the same nuclear physics as here, was 1.8. This factor-of-two decrease reflects both the trapping of substantial ^{60}Fe in stars that no longer explode and weaker typical explosion energies. Limongi and Chieffi (2006b) have discussed other uncertainties that might bring the models and observations into better agreement, including a modified initial mass function, mass loss, modified cross sections, and overshoot mixing.

As in Woosley *et al.* (2007), we also note that alternate, equally justifiable choices for key nuclear reaction rates, especially for ^{26}Al(n,p)^{26}Mg, ^{26}Al(n,α)^{23}Na, and ^{59,60}Fe(n,γ)^{60,61}Fe, might bring this ratio in our models down by an additional factor of two, hence within observational errors. This possibility will be explored in a future work. Interestingly the production

ratio for ^{60}Fe to ^{26}Al is sensitive to stellar mass. Averaging over just the explosions from 9 to 12 $M_{\odot}$, the ratio of masses ejected is close to 2.6 for both the W18 and N20 calibrations, while for heavier stars it is 0.65 (Table 3.5).

We have also examined the potential effect of ejecting the ^{26}Al that resides in the envelopes of the stars that implode to become black holes. While not lost to winds, even weak explosions may eject these loosely bound envelopes while allowing the helium core to collapse to a singularity (Nadezhin, 1980; Lovegrove and Woosley, 2013). For these, we summed the total mass of ^{26}Al still in the hydrogen envelopes of the stars that collapsed and added these to the yields of the stars prior to the integration. We find only a very minor improvement to the total integrated yield of aluminium, of about 7%. This helps to reduce the underproduction of ^{26}Al, but not appreciably.

Additional information on ^{60}Fe production is available from the ^{60}Fe/^{56}Fe ratio observed in cosmic rays (Israel *et al.*, 2015). There the ratio is thought to reflect chiefly the synthesis of both species in massive stars, diluted with some fraction of unprocessed material prior to acceleration. Observations of cosmic rays near the earth give a mass ratio that, when propagated back to the source, is ^{60}Fe /^{56}Fe = $0.80 \pm 0.30 \times 10^{-4}$ by mass. Our IMF average of the mass ratio for ^{60}Fe/^{56}Fe ejected in both sets of explosions and winds is near 7×10^{-4}. Assuming a standard dilution factor of 4 to one for normal ISM to massive star ejecta (Higdon and Lingenfelter, 2003; Israel *et al.*, 2015) gives an expected ratio in the local cosmic rays of 1.4×10^{-4}, in reasonable agreement with the observations. Again though, a reduction of a factor of about 2 in ^{60}Fe would be desirable. This ratio too is sensitive to the mass range of supernovae that are sampled (Table 3.5) and is larger in lower mass stars and somewhat smaller in heavier

ones. Note that the iron in Table 3.5 is expressed in solar masses per massive star death, while that in Table 3.3 is per supernova.

3.6.5 Type Ia Supernova Contribution

3.6.5.1 Nucleosynthesis

The correct model or models for Type Ia supernovae is currently under much debate. In terms of nucleosynthesis, however, the models segregate into two general categories: explosions near the Chandrasekhar mass by a combination of deflagration and detonation, and prompt detonations in sub-Chandrasekhar mass white dwarfs. The requirement that any successful model makes $\sim$0.6 $M_\odot$ of ^{56}Ni in order to explain the light curve and $\sim$0.2 $M_\odot$ of intermediate mass elements to explain the spectrum determines the acceptable bulk nucleosynthesis, so that the models differ only in detail. Here, as a representative example of the Chandrasekhar mass model we use the nucleosynthesis from Nomoto's highly successful "W7" model (Iwamoto *et al.*, 1999). For the sub-Chandrasekhar mass model we use Model 10HC of Woosley and Kasen (2011). This detonation of a 1.0 $M_\odot$ carbon-oxygen white dwarf capped by 0.0445 $M_\odot$ of accreted helium produced 0.636 $M_\odot$ of ^{56}Ni in an explosion with final kinetic energy 1.2×10^{51} erg. The contribution from each SN Ia model was normalized so as to produce a solar proportion of ^{56}Fe/^{16}O when combined with the integrated yield of massive stars from 9 to 120 $M_\odot$.

The combined nucleosynthesis is given in Fig. 3.24 for a sub-Chandrasekhar white dwarf and in Fig. 3.25 for the Chandrasekhar mass model. Most of the intermediate mass elements are unchanged, though some of these isotopes do change. Not surprisingly, the in-

troduction of Type Ia supernovae improves the overall fit especially for the iron group. The sub-Chandrasekhar mass model greatly improves the production of ^{44}Ca (made by helium detonation as ^{44}Ti) and seems to be required if only because of that unique contribution. The Chandrasekhar mass model, on the other hand, does a much better job of producing manganese, suggesting that this component may also be needed (see also Seitenzahl *et al.*, 2013a; Yamaguchi *et al.*, 2015). The Chandrasekhar mass model overproduces nickel however. This is a known deficiency of Model W7 having to do with excess electron capture at high density. It might be circumvented in more modern multi-dimensional models (e.g. Seitenzahl *et al.*, 2013b) especially if the white dwarf expands appreciably during the deflagration stage prior to detonating.

3.6.5.2 Implications for Supernova Rates

As noted previously (§ 3.6.4.3), our massive star models are responsible for producing about 28% of the iron in the sun. The average SN Ia makes very nearly 0.6 $M_{\odot}$. That being the case, and assuming that the typical successful core collapse supernova (mostly SN IIp in the present study) makes 0.04 to 0.05 $M_{\odot}$ of new iron (Table 3.3), the implied ratio of SN Ia event rates to SN IIp is 1/6 to 1/5. If core-collapse supernovae made a little less iron, as seems likely, then the SN Ia rate would need to be a bit bigger. This ratio is consistent with observations for spiral galaxies similar to the Milky Way (Li *et al.*, 2011).

We can also use these abundances, particularly the fact that each massive star above 9 $M_{\odot}$ produces an average of 0.57 $M_{\odot}$ of ^{16}O, to infer a rate of Type II supernova (assuming stars below 9 $M_{\odot}$produce little oxygen in their evolution). From the solar abundance of ^{16}O of

6.6×10^{-3} (Lodders, 2003), we find that there must have been 0.012 massive stars per solar mass of Population I material. Assuming that 66% of these stars become supernovae, as we found in our models, we find that integrated over galactic time, there must be 0.0076 core collapse supernovae (visible or invisible) per solar mass of Pop I material in order to explain the present solar abundance. This seems a reasonable, albeit very approximate number, especially if the supernova rate was different in the past.

3.7 Light Curves

The KEPLER code incorporates flux-limited radiative diffusion and thus is capable of calculating approximate bolometric light curves for supernovae of all types. The light curve calculation includes both contributions from the diffusion of energy deposited by the shock wave and from the decay of radioactive ^{56}Ni and ^{56}Co. Light curves were calculated as described in Woosley *et al.* (2007) using a full Saha-solver for 19 elements, hydrogen to nickel, to obtain the electron density, and adopting a lower bound to the opacity of 10^{-5} cm ^{2} g^{-1}. The full model set corresponding to the successful explosions using the central engines Z9.6, W18 and N20 was post-processed to obtain the luminosity evolution until about 230 days, which was well past the plateau and peak for all models. For the mass loss prescription used, explosions below 40 $M_\odot$, i.e., most successful explosions, produced Type IIp supernovae with a distinct plateau phase. The heavier stars gave rise to Type Ib or Ic supernovae. Fig. 4.2 illustrates the diversity of outcomes from the full model set. In this section, we discuss the systematics of these results and how they compare with simple analytic scalings in the literature. Some scalings of particular

interest to observers are summarized in § 3.4.2.

Since the light curve results from W18 and N20 engines are qualitatively similar, in the following analysis, only the N20 series is considered, supplemented by Z9.6 below 12 $M_\odot$.

3.7.1 Type IIP

Since all of the models that retained their hydrogen envelope were, at death, red supergiants, most of the supernovae modeled here were of Type IIp. A wide diversity of durations and luminosities on the plateau is expected observationally (**?**), and was found owing to the variable presupernova radius, explosion energy, envelope mass, ^{56}Ni ejected, and mixing. Luminosities on the plateau ranged across at least a decade in luminosity ($10^{41.5}$ - 10^{43} erg s^{-1}), with the most luminous events coming from the energetic explosions of stars with exceptionally large radii, touching 10^{14} cm. The ^{56}Ni yields range from 0.003 to 0.15 $M_\odot$, and the envelope masses, for common events, are typically 7 – 10 $M_\odot$ and 3 – 8 $\times 10^{13}$ cm. The explosion energy varied from 0.1 to 2 $\times 10^{51}$ erg (see Fig. 3.12), with a typical value around 0.7×10^{51} erg (Table 3.3).

Approximate analytic scaling rules have been derived for both the luminosity on the plateau and its duration by Popov (1993) and Kasen and Woosley (2009). An important issue is how to measure these quantities, both observationally and for the models. A variety of definitions is used in the literature. The luminosity is not really constant on the "plateau", and the plateau's onset might be counted as beginning at shock breakout; the cooling and recombination of hydrogen in the outermost zone; or the time when the effective temperature first falls below some value. Even more uncertain, the end of the plateau might be measured as when

the envelope first combines; when the whole ejecta first becomes optically transparent; or the beginning of the radioactive tail, if there is one. Here, it is assumed that the bolometric luminosity is evaluated 50 days after shock breakout and that shock breakout defines the beginning of the plateau. This is clearly a lower bound to the actual commencement. For most models, recombination begins about 3 days later, which is short compared with the approximate 100 day duration of the plateau. All SN IIp light curve plateaus were substantially longer than 50 days.

Two measures are used to bracket the end of the plateau. One is when the photospheric radius recedes to less than one-half of its maximum value. Empirically, this corresponds roughly to when the recombination front reaches the base of the hydrogen envelope (or the density increase associated with that former boundary, if the composition has been mixed). This is an operational lower bound to the duration of the plateau. Later, after the internal energy of the helium and heavy element core has diffused out, the whole star recombines and the photosphere shrinks inside 10^{14} cm. It is at this point that any radioactive contribution reaches steady state with the supernova luminosity and the "tail" of the light curve begins. For the observer, these two limits thus correspond to the first strong downward inflection of the light curve, and the onset of the characteristic exponential decay on the tail.

All of our models are artificially mixed after explosive nucleosynthesis has ended, in order to account empirically for both the turbulent convection that goes on behind the shock during the explosion and the Rayleigh-Taylor mixing following the reverse shock. The mixing is calibrated, crudely, to SN 1987A (Woosley, 1988; Kasen and Woosley, 2009). Because most of our models experienced little fall back, mixing is not very important to the nucleosynthesis calculated here.

3.7.1.1 Analytical Scalings

The scalings of Popov (1993), to which our luminosities and plateau durations are compared, are:

$$\begin{aligned} L &\propto E^{5/6} M^{-1/2} R^{2/3} \kappa^{-1/3} T_i^{4/3}, \\ t &\propto E^{-1/6} M^{1/2} R^{1/6} \kappa^{1/6} T_i^{-2/3}, \end{aligned} \tag{3.12}$$

where E is the explosion energy; M, the envelope mass; R, the progenitor radius; κ, the opacity; and T_i, the ionization temperature, which is the effective emission temperature divided by $2^{1/4}$. Adopting, from our models on the plateau, a typical effective temperature of 6300 K (Popov used 6000 K), and retaining his opacity of 0.34 cm^2 g^{-1}, one has the analytic results:

$$\begin{aligned} L_{50} &= C_L \, E_{51}^{5/6} M_{10}^{-1/2} R_{0,500}^{2/3} \quad \text{ergs s}^{-1}, \\ t_{p,0} &= C_t \, E_{51}^{-1/6} M_{10}^{1/2} R_{0,500}^{1/6} \quad \text{days}, \end{aligned} \tag{3.13}$$

where C_L and C_t are 1.82×10^{42} erg s^{-1} and 96 days, respectively. L_{50} is the bolometric luminosity 50 days after shock breakout; $t_{p,0}$, the plateau duration without any radioactive contribution; E_{51}, the final kinetic energy of the explosion in 10^{51} erg units; $R_{0,500}$, the radius of the presupernova star in units of 500 $R_\odot$; and M_{10}, the mass of the presupernova hydrogen envelope in units of 10 $M_\odot$.

For the bolometric luminosity, calibrated to our entire set of 181 type IIp models, 50 days after core collapse we find:

$$L_{50} \;=\; 1.85 \times 10^{42}\, E_{51}^{5/6} M_{10}^{-1/2} R_{0,500}^{2/3} \text{ ergs s}^{-1}. \tag{3.14}$$

This agrees extremely well with Popov's predicted scaling and is our recommended value for this survey. The agreement with all the supernova models is excellent, as shown in Fig. 3.27.

Kasen and Woosley (2009) gave similar scalings to eq. (3.13), and calibrated them to a small set of numerical models that used similar physics to the present work:

$$\begin{aligned} L_{50} &= 1.26 \times 10^{42}\, E_{51}^{5/6} M_{10}^{-1/2} R_{0,500}^{2/3} X_{\mathrm{He},0.33}^{1} \quad \text{ergs s}^{-1}, \\ t_{p,0} &= 122\, E_{51}^{-1/4} M_{10}^{1/2} R_{0,500}^{1/6} X_{\mathrm{He},0.33}^{-1/2} \quad \text{days}, \end{aligned} \tag{3.15}$$

where X_{He} is the helium mass fraction in the envelope. Two typographical errors are fixed here in Eq.(11) of Kasen and Woosley (2009): (1) X_{He} is normalized to 0.33, and (2) $t_{p,0} \propto X_{He,0.33}^{-1/2}$. In comparison to eq. (3.12) and eq. (3.13), this formula assumes scaling with X_{He}, which ranged from 0.30 to 0.53 in the models. Given that the helium mass fraction is typically greater than 0.33, Kasen and Woosley's formula for the luminosity is similar to Popov's, though slightly fainter. Their formula for the plateau duration has been empirically adjusted to models (hence $E^{-1/4}$ instead of $E^{-1/6}$) and is a bit longer, possibly due to differing definitions of what constitutes the plateau.

3.7.1.2 Plateau Duration and Recombination Timescale

As alluded to earlier, the duration of the plateau is more ambiguously defined than the luminosity on a particular day. It is also more sensitive to corrections for mixing and radioactivity. The original scalings of Popov (1993) accounted for neither. To compare with eq. (3.13) and determine our own estimate of $t_{p,0}$, the plateau duration without radioactivity, the light curves of 26 models from the Z9.6 and N20 series with masses from 9 $M_\odot$ to 27 $M_\odot$ were recalculated by assuming no ^{56}Ni was produced in the explosion. Two possible durations of the plateau were estimated for each corresponding to the time between shock breakout and when the photospheric radius shrinks to a) 50% of its maximum and b) 10^{14} cm. The top panel of Fig. 3.28 compares this range from the models with Popov's expression - eq. (3.13).

The range between upper and lower bounds (shaded gray) is mostly due to the energy that continues to diffuse out of the helium core before the whole star recombines. Compared to this range, eq. (3.13) overestimates the duration by about 10%. Reducing the normalization constant, C_t in eq. (3.13) to 88 days gives a better fit to our models. Thus for light curves with no radioactive contribution, we recommend:

$$t_{p,0} = 88 E_{51}^{-1/6} M_{10}^{1/2} R_{0,500}^{1/6} \text{ days.} \tag{3.16}$$

As pointed out by Kasen and Woosley (2009), the presence of radioactivity does not substantially influence the luminosity during most of the plateau because the diffusion time out of the core is long compared with the recombination time. There are exceptions if the star makes more than about 0.1 $M_\odot$ of ^{56}Ni, or if the progenitor is not a red supergiant (e.g., SN 1987A).

The duration of the plateau is another matter, however. Even 0.01 $M_\odot$ of ^{56}Ni can appreciably lengthen it. Radioactivity affects t_p both by contributing to the energy budget and by keeping the gas ionized longer so that its opacity and diffusion time remain high.

Fig. 3.29 shows light curves due to various amounts of nickel masses for the lightest supernova studied, 9 $M_\odot$, and a more 'typical' model of 15.2 $M_\odot$. For the lower mass model, ^{56}Ni masses over 0.01 $M_\odot$ are not physical, and the results shown are purely for comparison. For a realistic amount of ^{56}Ni, the plateau of the 9.0 $M_\odot$ is not appreciably lengthened, but the 15.2 $M_\odot$ model is. Note also a bump at the end of the plateau for both zero ^{56}Ni models, but especially for the larger mass star. This is the energy diffusing out of the helium core after the hydrogen envelope has recombined. This effect is weaker in the smaller model since the helium core is much smaller.

Following Kasen and Woosley (2009), we adopt a correction factor to the internal energy due to the decay of ^{56}Co:

$$f_{rad} = 1 + 24 \frac{M_{Ni}}{E_{51}} \frac{t_{Co}}{t_e} \tag{3.17}$$

where M_{Ni} is the mass of ^{56}Ni produced in the explosion in units of $M_\odot$; t_{Co} is the mean life of ^{56}Co, 113 days; t_e is a characteristic expansion time given by the initial radius of the star divided by a typical speed, $v = (2E/M_{env})^{1/2}$. Two things worth noting in the derivation are that the decay of ^{56}Ni itself has no effect on t_p (this just increases the expansion kinetic energy by a small amount and is neglected), only ^{56}Co does. Second, the derivation implicitly assumes complete mixing, that is the ^{56}Co is distributed homogeneously in the star.

In the derivation of the scaling shown in eq. (3.16) two energies appear that are taken, within a constant multiplier, to be the same, the internal thermal energy, E_T, and the kinetic energy, E_K. The scaling actually depends on $(E_T/E_K^2)^{1/6}$ or $E^{-1/6}$ if, e.g., $E_T = E_K = E$. Since f_{rad} is assumed to only multiply the internal energy, the correction factor enters in as the positive one-sixth power. That is

$$\begin{aligned} t_p &= t_{p,0} \times f_{rad}^{1/6} \\ &= t_{p,0} \times (1 + C_f\, M_{Ni} E_{51}^{-1/2} M_{10}^{-1/2} R_{0,500}^{-1})^{1/6} \end{aligned} \tag{3.18}$$

where $C_f \sim 21$. This is similar to eq. (13) of Kasen and Woosley (2009), but corrects two typographical errors: (1) the constant $C_f \approx 21$ and (2) M is raised to the -1/2 power.

The bottom panel of Fig. 3.28 shows the effect of this correction factor on the plateau duration of models with radioactivity. The same set of 26 models as used in the zero radioactivity case were compared with those in which the calculated amount of radioactivity was turned on. Additional models multiplied the energy generation from radioactivity by two. For progenitor masses above about 12 $M_\odot$, the model results agree well with eq. (3.18), though there are substantial differences at lower masses. Better agreement with our models is obtained if $C_f \sim 50$ and that is our suggested value.

The breakdown below 12 $M_\odot$ is not particularly surprising. These low mass supernovae have low energy ($\sim 10^{50}$ erg), but also low ^{56}Ni mass ($< 0.01 M_\odot$). The combination $M_{Ni} E^{-1/2}$ is still appreciable even though the mass of radioactivity itself is very small. If the mass fraction of ^{56}Ni in a given zone, after mixing, is less than about 0.001, the decay energy, 6.4×10^{16} erg g^{-1} of ^{56}Co, will, after time t_{Co}, be only a small fraction of the internal energy

at recombination, $\sim 10^{15} E_{51}$ erg g^{-1}, and recombination will not be greatly affected. For the very low mass explosions and mixing prescription assumed, the cobalt abundance is below this limiting value in all zones except at the very base of the hydrogen envelope. In any case the correction factor is small, less than 10%, in these low energy explosions.

Combining our best fit to the no-radioactivity models with this best fit correction factor results in good agreement with the full set of models with radioactivity included (Fig. 3.30). As expected, most of the large deviations are for the lightest and heaviest stars. For small stars, the scaling relation overestimates the plateau duration because the correction term, f_{rad}, is too big. At high mass, there are cases with a large amount of fallback (Fig. 3.9), and therefore no ^{56}Ni production. Indeed, such short plateaus in massive stars with normal luminosities (Fig. 3.27) may be an observable signature of black hole formation.

3.7.1.3 Systematics

Given the generally good agreement of our SN IIp model characteristics with analytic expressions, it is worth exploring whether these systematics can be exploited to obtain insights into the masses and energies of observed events. Another interesting question is whether SN IIp, or some subset, can be used as standard candles.

Neglecting the radioactive correction, eq. (3.18), the luminosity and plateau duration are proportional to powers of the explosion energy, presupernova radius, and envelope mass. These are not independent variables. The radius of the presupernova star increases monotonically with its main sequence mass, M_{ZAMS} and, to good approximation in the mass range where most SN IIp occur (9 – 20 $M_\odot$), $R_0 \propto M_{ZAMS}^{3/4}$ (Fig. 3.31). Above 20 $M_\odot$, the hydrogen enve-

lope mass of the presupernova star declines with M_{ZAMS} due to mass loss, but below 20 $M_\odot$, it too has a monotonic scaling, $M_{env} \propto M_{ZAMS}^{2/3}$. The explosion energy also tends to increase with mass because of the greater efficiency of neutrino absorption in heavier stars and the larger neutrino luminosity from accretion, but owing to the non-monotonic behaviour of compactness, this is not as well-defined a correlation. The compactness parameter does generally increase with mass though, especially at low mass (Fig. 3.1), and the explosion energy there is correlated with compactness (Fig. 3.12). Given these correlations, one can derive some simple relations among the luminosity, energy, duration, and main sequence mass.

First, consider the width-luminosity relation for SN IIp. Fig. 3.32 shows L_{50} vs t_p with t_p measured from breakout until the onset of the radioactive tail. The results have been segregated by mass groups, and the explosions used the Z9.6 and N20 central engines. The scaling relations in eq. (3.13) predict $L_{50} t_p^3 \propto E_{51}^{1/3} M_{10} R_{0,500}^{7/6}$. From 12.25 $M_\odot$ to 20 $M_\odot$, roughly half of all supernovae, the energy and envelope mass change only a little and the radius increases by only 30%, so crudely one expects $L_{50} \propto t_p^{-3}$, which is approximately what the figure shows. For stars with t_p near 110 days, most supernovae have a standard bolometric luminosity between log L = 42.45 and 42.58.

Unfortunately, the low mass supernovae, with their unusually low energy explosions, contaminate an otherwise nice relation. These might be selected against on the basis of their low photospheric speeds or even by their colors, but that lies beyond the scope of the present work. Our large model set will be available[2] and represents a resource from which information on dilution factors and spectral velocities, for example, could be extracted. These could be useful for the expanding photosphere method for distance determination (e.g. Eastman *et al.*,

1996; Vinkó *et al.*, 2012).

Next consider the kinetic energy of the explosion. Can it be determined just from observations of the light curve? Fig. 3.33 shows a well-defined relation between the bolometric luminosity on day 50 (after shock breakout) and the kinetic energy of the supernova. This is expected on the basis of eq. (3.14) which shows the luminosity scaling as $E_{51}^{5/6} M_{10}^{-1/2} R_{0,500}^{2/3}$. From 9 to 20 $M_\odot$, which includes about 95% of successful SN IIp explosions, the hydrogen envelope mass varies between 7 and 10 $M_\odot$, and is usually 8 or 9 $M_\odot$. The radius varies about a factor of 3, but enters as a 2/3 power. Moreover, the radius scales as $R \propto M^{3/4}$, and bigger mass stars tend to have bigger explosion energies. Thus the fact that the luminosity scales roughly as the explosion energy is not surprising.

The figure shows though that just by measuring the bolometric luminosity on the plateau one gets a good estimate of the total explosion energy. Models above 22 $M_\odot$ lie off the main curve, but there are very few such explosions. These plots include only the contributions of radioactivity and a point explosion, and not any contribution from a magnetar or circumstellar interaction. An inferred explosion energy above 2×10^{51} erg would be suggestive of a breakdown in this assumption.

Also shown in Fig. 3.33 is the quantity $L_{50} t_p / E$ vs progenitor initial mass. This is the ratio of the total power emitted by the supernova on its plateau to the kinetic energy of the explosion and is expected to scale as $E_{51}^{-1/3} R_{0,500}^{5/6}$. Since E_{51} generally increases with mass and therefore with radius, the figure shows $L_{50} t_p / E$ is roughly constant. The total radiated energy in light for most neutrino-powered supernovas is roughly 1/35 of the kinetic energy of the explosion. The full range of this ratio between 9 and 20 $M_\odot$ is 0.02 to .04. This gives

another way of estimating the energy of a neutrino-powered supernova from observables, L_{50} and t_p.

Finally we consider whether the mass of the zero-age main sequence (ZAMS) star can be determined from the supernova light curve. Fig. 3.34 shows quantity $(L_{50}t_p)^{12/7}/E$, which should scale as $R^{10/7}$, plotted against M_{ZAMS}. Since $R \propto M_{ZAMS}^{3/4}$, this implies that $(L_{50}t_p)^{12/7}/E$ should scale as $M_{ZAMS}^{15/14}$ which is consistent with Fig. 3.34. If one observes L_{50} and t_p and determines the explosion energy from Fig. 3.33, the ZAMS mass of a supernova in our data set is roughly determined.

3.7.2 Type Ib/c

With the adopted mass loss prescription, stars with initial mass greater than about 35 $M_\odot$ lose all of their hydrogen envelope before dying. Successful explosions will then produce supernovae of Type Ib and Ic. Models heavier than $\geq$45 $M_\odot$ have lost most of their helium envelope and all have surface ^{4}He mass fractions less than 0.2, however, the exact distinction between Ib and Ic is as much dependent on mixing as on mass loss (Dessart *et al.*, 2011), and we shall not attempt to separate the two classes in this work. Use of the N20 engine resulted in the explosion of the 60, 80, 100, 120 $M_\odot$ progenitors, while the W18 engine exploded only the 60 and 120$M_\odot$ progenitors. The resulting light curves are shown in the lower panel of Fig. 4.2.

These are not common Ib's or Ic's. Their light curves are too broad and faint. Presumably common Type Ib and Ic supernovae come from mass-exchanging binary star systems and lower mass progenitors (Dessart *et al.*, 2011; Eldridge *et al.*, 2013). The supernovae here are bigger and more slowly expanding, but should exist in nature and might be sought as a

separate subclass of Type Ibc. Since the neutrino mechanism appears inadequate to produce an explosion energy greater than about 2×10^{51} erg (Ugliano *et al.*, 2012; Ertl *et al.*, 2016), these would be fainter and broader than e.g., SN 2009ff (Valenti *et al.*, 2011). Conversely, events with much greater energy than 2×10^{51} erg would not be powered exclusively by neutrinos.

These Type Ibc light curves have peak luminosities larger than predicted by 'Arnett's rule' (Arnett, 1982), which states that $L_{peak} = L_{decay}(t_{peak})$. Consequently, the nickel mass content cannot be accurately inferred in the same way as for Type Ia supernovae. Dessart *et al.* (2015) studied similar light curves and found that the energy-conservation-based arguments of Katz *et al.* (2013) gave better agreement. Their argument follows from the first law of thermodynamics and the assumption that the ejecta are freely coasting, radiation dominated, and powered only by radioactivity. Then

$$tE(t) - t_0E(t_0) = \int_{t_0}^{t} t' L_{dec.}(t')dt' - \int_{t_0}^{t} t' L_{rad.}(t')dt' \tag{3.19}$$

where $L_{rad.}$ is the radiated luminosity, and E is the internal energy of the ejecta. In the special case where $t_0 = 0$, t is sufficiently large such that $E(t) \approx 0$, and $L_{rad.} = L_{bolometric}$, the argument reduces to a connection between an observable (bolometric luminosity) and a physical quantity (^{56}Ni).

Fig. 3.35 illustrates this method applied to one of our models. The approximation works until about 60 days post-explosion (black curve), after which the leakage of gamma rays becomes significant. If one assumes full trapping, eq. (3.19) will hold as long as the radiation dominates the internal energy. Some deviation is expected because the internal energy is not all

in the form of radiation; an appreciable fraction is in the electrons.

In the special case when $t_0 = 0$ and E(t) = 0, eq. (3.19) expresses the equality between the two integrals. At around 70 days the nickel mass inferred from this relation peaks and reaches its closest point with respect to that in the actual model (blue dashed line). After the peak, it goes down again due to leakage, but it doesn't quite reach the 'true' value because the internal energy is not small enough at that time. At 70 days the internal energy is roughly 2×10^{47} ergs, only about 3 times less than its value at 3 days. Though it underestimates the nickel mass, this method is more accurate than 'Arnett's rule' for all of our Ib and Ic models.

3.7.3 Type IIL

None of the exploded models from the Z9.6, W18 and N20 engines showed a clearly linear decline after the shock breakout. All of the explosions from progenitors smaller than 30 $M_\odot$ showed a plateau of roughly constant luminosity. The shortest plateau, as measured by the lower bound, was 79 days for the 12.25 $M_\odot$ model with a 7.8 $M_\odot$ envelope. And the exploded model with the least amount of envelope mass, 29.6 $M_\odot$ model of N20 engine with 3.9 $M_\odot$ envelope, yielded 84 days long plateau. Given that Type IIL should come from at l east some stars in the 9 to 120 $M_\odot$ range, their absence warrants an explanation.

There are several possibilities. We may just have missed them because of sparse mass sampling above 35 $M_\odot$. This is unlikely. Type IIL is expected to come from a star that has lost most of its hydrogen envelope, but retains a large radius and, possibly, makes a lot of ^{56}Ni. Our model set indeed had 5 $M_\odot$ spacing from 35 to 60 $M_\odot$, but none of those stars blew up.

Second, their absence may reflect a deficiency in presupernova modelling. This is

quite possible. Over the years, one of us has noted a chronic problem calculating *ab initio* models of very massive stars with envelope masses below 1 $M_\odot$ using KEPLER. The envelopes expand to such large radii (over 10^{14} cm) that they begin to recombine. Density and even pressure inversions develop near the surface and the calculation cannot be carried further. Such was the case with the 35 $M_\odot$ model studied here and in Woosley *et al.* (2007). At central helium depletion this star had an extended low density envelope of about 1 $M_\odot$ with a radius of 8.3×10^{13} cm and a luminosity of 1.35×10^{39} erg s^{-1}, only slightly below the Eddington limit for its remaining mass, 15 $M_\odot$. As the star attempted to adjust its structure and ignite carbon, its luminosity increased above 1.6×10^{39} erg s^{-1}, and the envelope become unstable. It is quite possible that at this point, the envelope comes off. The central temperature was over 5×10^8 K and it would not have been long before the star died. Fortunately perhaps, there is no way neutrinos would blow up this model, so this behaviour is not an issue for the present study, but a similar fate might befall a lower mass star in a binary system, or the KEPLER calculation may just be wrong. More study is clearly needed.

Finally, it should be noted that the mass range where Type IIL might have occurred, 30 - 40 $M_\odot$, is also a mass range where the effects of rotation are expected to be important to the death of the star (Heger *et al.*, 2005).

Type IIL supernovae could thus be a consequence of collisions with recently ejected envelopes, binary systems, jets, magnetars, stellar evolution still to be done properly, or all five, and that makes them interesting.

3.8 Conclusions

The deaths of massive stars from 9.0 to 120 $M_\odot$ as supernovae have been surveyed using an improved depiction of the explosion physics. Models are one-dimensional, of a single metallicity - solar, and do not include any effects of rotation. Nevertheless, they capture many essential aspects of a general solution neglected in past studies, including the explosion effects of a non-monotonic variation of the presupernova compactness (Fig. 3.1) with mass. The explosions are calibrated to reproduce the characteristics of two well-studied supernovae: the Crab and SN 1987A. The Crab is believed to have been a low mass supernova, near 10 $M_\odot$, with a low explosion energy, $\sim 10^{50}$ erg that made very little iron. SN 1987A was a star near 18 $M_\odot$ that exploded with 1.3×10^{51} erg and made 0.07 $M_\odot$ of ^{56}Ni. These two calibration points anchor our survey. Multiple models for the central engine for 87A were employed and one for the Crab.

Calibrating to these two events, and using lessons learned from previous 3D modelling efforts of core collapse, results in fiducial "central engines" that describe the evolution of only the inner 1.1 $M_\odot$ of the collapsing iron core (§ 3.3.1). These central engines, or inner boundary conditions are characterized by just a few physically descriptive parameters (Table 3.2). These inner core evolution prescriptions are then used to follow the evolution of 200 presupernova stars (§ 3.2.3) in the mass range 9.0 – 120 $M_\odot$. Outside 1.1 $M_\odot$, neutrino transport was followed in an approximate, efficient way for each stellar model, thus assuring a physical representation of the explosion that was sensitive to the structure of individual presupernova stars. Above 12 $M_\odot$, five central engines for various SN 1987A models were employed, two

of them extensively. From 9.0 to 12 $M_\odot$, the properties of the central engine were interpolated between Crab-like and 87A-like behaviour. The Crab model itself was based on a 9.6 $M_\odot$ star whose explosion has been previously studied in 3D.

As a result of these simulations, a large diversity of successful and failed explosions was generated. Kinetic energies at infinity varied from 0.11 to 2.03 $\times 10^{51}$ erg. The outcome of each calculation depended upon the structure of the presupernova star and central engine employed. All stars below 12 $M_\odot$ exploded, albeit weakly. Despite their small compactness parameters and ease of explosion, their final energies were low because a smaller fraction of the neutrino power radiated by the proto-neutron star was converted into kinetic energy of expansion. The steep density gradient outside the iron core reduced the absorption. Conversely, larger stars trapped a larger proportion of the neutrino radiation and had a bigger neutrino luminosity from accretion, but also had a larger binding energy and ram pressure to overcome. Some exploded with variable energy up to 2×10^{51} erg; some not at all.

There was no single mass below which all stars exploded and above which black holes formed, but rather there were islands of "explodability" in a sea of black hole formation (Fig. 3.9). A similar result was found by Pejcha and Thompson (2015) suggesting that the outcome of supernova explosions is more influenced by presupernova structure than details of the central engine, provided that engine is sufficiently powerful to explode many stars. Stars above 35 $M_\odot$ lost their envelopes and a few that experienced severe mass loss as Wolf-Rayet stars exploded as Type Ibc supernovae, but most became black holes. Typically 95% of the stars that did explode were SN IIp with masses less than 20 $M_\odot$ (Table 3.3). The median supernova mass, neglecting any explosions below 9 $M_\odot$, was 12 $M_\odot$. Half were heavier and half lighter.

The heavier half accounted for most of the nucleosynthesis.

From the baryonic masses of the remnants, it was possible to create a distribution of neutron star masses and an average. Both agreed very well with observations (Table 3.3 and Fig. 3.14) with typical neutron star gravitational masses near 1.40 $M_\odot$. The heaviest neutron star made was 1.77 $M_\odot$ and the lightest, 1.23 $M_\odot$. While electron capture supernovae were not computed here, their neutron stars should result from the collapse of Chandrasekhar mass cores with Y_e still close to 0.50. The neutron stars resulting from our 9 and 10 $M_\odot$ models, which have experienced appreciable electron capture during oxygen and silicon burning prior to collapse, can actually be lighter.

For those stars that made black holes, which were most, but not all of the stars above 20 $M_\odot$ and some below 20 $M_\odot$, only a few produced their black holes by fallback. Stars that in past surveys produced black holes by fallback more frequently did not explode at all in the present study.

The present calculations with `PHOTB` also included a contribution to the explosion energy from the neutrino-powered wind and from recombination, of order 10^{49} to 10^{50} erg, that gave an extra push to the inner zones during the first second or so after the shock was launched. This helped to prevent their reimplosion. Usually black hole production involved the collapse of the full star, including its hydrogen envelope. Other mechanisms are necessary and were invoked to explain envelope ejection during black hole formation. If the full presupernova star always collapsed the average black hole mass (IMF weighted) was 13.3 – 13.8 $M_\odot$; if only the helium core collapsed, it was 7.7 – 9.2 $M_\odot$ (Table 3.3). The latter is in better agreement with observations and suggests that black hole formation is accompanied by weak explosions that

eject only the hydrogen envelope. These weak supernovae would have distinctive light curves and colors. The gap between neutron stars and black hole masses from $\sim$2 to $\sim$4 $M_\odot$ suggested by observations was naturally obtained because of the lack of fallback supernovae that could fill this mass interval.

One important result of this study is the nucleosynthesis expected from massive stars calculated using the more realistic depiction of explosion. This was calculated using the KEPLER code and an amply large nuclear reaction network complete up to the element bismuth. A trajectory near the final mass cut in PHOTB was taken as the inner boundary for the KEPLER calculation, and the infall and time of reversal were nearly the same. The velocity of the piston in KEPLER was varied however, to give near perfect agreement in explosion energy with the PHOTB calculations and to reproduce the iron synthesis to better than 10% in most cases. In a few cases the latter required a slight adjustment of the piston mass. Neutrino interactions, except for the neutrino process of nucleosynthesis, were neglected in the KEPLER studies and the neutrino-powered wind was not carried. In practice this meant the neglect of a possible r-process or νp-process component and some uncertainty in the nucleosynthesis of nickel, copper and zinc.

The contributions from various mass stars were then determined as well as their overall IMF-weighted production factors. The lighter supernovae below 12 $M_\odot$, half of all supernovae numerically, make a relatively small contribution to the overall nucleosynthesis, but are important for some elements. Carbon, nitrogen, lithium, boron, and fluorine as well as numerous species in the iron group were produced in solar or super-solar proportions to oxygen (Fig. 3.17). Besides their contribution to Pop I nucleosynthesis in nature, these abundances are

also of interest for the large fraction of supernova remnants they would characterize. The iron to oxygen ratio was nearly normal, despite the fact that overall, the massive stars only account for a minor fraction of the iron in the sun (§ 3.6.4.3 and **???**). Boron was unusually high owing to the operation of the neutrino process in a shell close to the neutron star with a large abundance of carbon.

Explosions from 12 to 30 $M_{\odot}$ are responsible for most of the nucleosynthesis. The elemental production pattern (Fig. 3.18) is consistently solar from boron to copper with the expected deficiency in the iron group due to SN Ia production. Carbon, nitrogen, and fluorine are also greatly reduced compared with the low mass supernovae. In general, there is a tendency to slightly underproduce the intermediate mass elements, Si, S, Ar, and Ca with respect to oxygen. This may indicate a smaller than optimal abundance for oxygen in the sun, or the lack of some other component, e.g., SN Ia. The s-process production, from Cu to Zr is less than in previous works (e.g., Woosley *et al.*, 2007) and is problematic.

Above 30 $M_{\odot}$, there were few explosions, but even stars that make black holes still contribute their winds (Fig. 3.19). Because mass loss rates are uncertain, the nucleosynthesis of these stars must be treated with caution. For standard assumptions, carbon and oxygen are substantially produced in the winds of massive Wolf-Rayet stars, and nitrogen, neon, and sodium also have important components. Indeed the abundances of these light elements are so great that stars in this mass range make little else when the other productions are normalized to them.

Integrating over the entire full range from 9 to 120 $M_{\odot}$, and examining isotopes as well as elements, the nucleosynthesis bears strong resemblance both to the solar pattern and

to the earlier survey by Woosley *et al.* (2007), but with notable exceptions. ^{12}C and ^{22}Ne are slightly overproduced. This might be an indication that the mass loss rates used here are high by about a factor of two, but the ^{22}Ne yield would also be reduced in stars with less than solar metallicity, because of the smaller neutron excess. C and O production in the winds of low metallicity stars would also be reduced. The excesses would instead end up in black holes. A full galactic chemical evolution model would need to be done to see if these overproductions are problematic. Fluorine is underproduced by a factor of two, suggesting a possible contribution from lower mass stars. Radioactive ^{40}K is greatly overproduced, but this is not a problem since a large uncertain fraction of the radioactive species would decay before the sun was born. The iron group retains the underproduction seen in the mid-mass explosions, but some copper and nickel are slightly overproduced, possibly due to the neglect of neutrino interactions at the base of the ejecta. Also notable are the deficient productions of ^{44}Ca and ^{55}Mn and of the s- and p-processes.

In fact, above the iron group, the fit to solar abundances is substantially poorer than in Woosley *et al.* (2007) which used essentially the same stellar physics, but an inferior model for the explosion. The underproductions are a consequence of many massive stars that were once prolific sources of the s-process now imploding to black holes. To a lesser extent, it also reflects the use of a rate for the ^{22}Ne(α,n)^{25}Mg reaction that is about $\sim$50% smaller than a recent reanalysis of experimental data. Given the critical role of the light s-process as a diagnostic here, our calculations should be repeated with a variable value for this rate to test the sensitivity of the outcome. The heavy p-process is also underproduced both compared with the sun and with the results from Woosley *et al.* (2007). This again reflects a deficiency of massive star

explosions with thick layers that experience explosive neon burning. The origin of the light p-process below A = 130 and specifically of the nucleus ^{92}Mo continues to be a mystery. In total, the nucleosynthesis would be improved if more massive stars blew up (Brown and Woosley, 2013).

More ^{26}Al is produced relative to ^{60}Fe than in the 2007 survey because some of the major producers of ^{60}Fe now make black holes. This is good news, but should be treated cautiously because the same changes necessary to increase light s-process production might also increase the yield of ^{60}Fe. The production ratio from the present survey for ^{60}Fe/^{26}Al, averaged over a Salpeter IMF, is, by mass, $\sim$0.90. The observed value is 0.35 $\pm$ 0.1. The Woosley *et al.* (2007) survey gave 1.8. Part of the remaining discrepancy probably has to do with uncertain reaction rates.

As is well known, the underproduction of iron in massive stars is actually desirable since most of iron comes from SN Ia. Here we find 28% of the solar abundance relative to oxygen is made in massive stars. Since both are primary elements whose synthesis is independent of neutron excess, the same ratio would probably characterize low metallicity stars. If the SN Ia rate is at least 1/6 to 1/5 of the SN IIp rate then iron is made in solar proportions. Roughly comparable contributions from both sub-Chandrasekhar mass models and the traditional Chandrasekhar mass model are needed, however, to produce both ^{44}Ca and ^{55}Mn. The sub-Chandrasekhar model also helps boost the deficient production of the alpha-nuclei from silicon through calcium.

The excellent agreement of ^{11}B/^{16}O in the integrated sample provides an accurate measure of the μ- and τ- neutrino temperature during proto-neutron star evolution.

A total of 194 supernova light curves were calculated. The vast majority of these were SN IIp but the successful explosions over 30 $M_\odot$ made a variety of SN Ibc. These are not the common SN Ibc though, because they are too faint and broad. Presumably the common events come from lower mass explosions stripped of their envelopes in binary systems. The massive faint variety should exist in nature though, and should be sought.

The 181 SN IIp models are a community resource that is freely available[2], and they offer a rich opportunity for modelling the spectrum and colors of a large comprehensive sample with standard identical physics. Here we analysed (§ 3.7.1.1) the bolometric light curves using semi-analytic approximations from Popov (1993) and Kasen and Woosley (2009). While the range in plateau luminosities spans one and a half orders of magnitude, its systematics are amazingly well represented by the analytic formulae (Fig. 3.27). This shows that the systematics are well understood and encapsulated in simple scaling relations, lending confidence to the proposition that, with additional constraints from the spectrum, colors, dilution factor, etc., SN IIp may be useful cosmological yardsticks.

Fig. 3.33 shows a tight correlation between SN IIp luminosity on the plateau and its total explosion energy. This is well worth checking with an observational sample with spectroscopically determined kinetic energies. It also gives a useful tool for finding "unusual" supernovae. None of our explosions exceeded 2.03×10^{51} erg and none were brighter than $10^{42.7}$ erg s^{-1}. A SN IIp brighter than this, say 10^{43} erg s^{-1}, then is not powered by neutrinos. This gives a physical basis for discerning "superluminous" supernovae of type IIp. Fig. 3.33 also shows that the fraction of kinetic energy that comes out as light in a neutrino powered SN IIp is roughly constant, $\sim 3 \pm 1\%$ for the 95% of SN IIp lighter than 21 $M_\odot$.

While the width luminosity relation for SN IIp is not nearly so tight or "calibratable" as for SN Ia, typical SN IIp of a given plateau duration have the same luminosity at day 50 to about $\pm 25\%$ (Fig. 3.32). This is not true, however, for a substantial sample of low energy supernovae below 12 $M_{\odot}$. These would need to be spectroscopically distinguished on the basis of their low photospheric speed.

With less precision, the mass of the supernova progenitor can also be determined from measurements of the total radiated light (to good approximation $L_{50}t_{p}$) and estimates of the explosion energy (Fig. 3.34). The figure is especially useful for distinguishing low mass supernovae but loses utility in separating supernovae in the mass range 13 to 21 $M_{\odot}$ because of the much slower variation of integrated light in this range. In practice, the need to determine the explosion energy accurately may limit the application.

The success of the present approach in fitting many observational constraints, including neutron star masses, black hole masses, supernova kinetic energies, light curves, and nucleosynthesis is gratifying, and gives hope that it may be more broadly applied in the future. The existence of a large set of models with controlled, well understood physics will be useful for the statistical analysis of large data sets in the future. There is surely room for improvement, though. Nuclear reaction rates need updating and the effect of varying the mass loss should be explored. Rotation can be included in the presupernova models, and approximated in the explosion. A broader range of metallicities can be explored. The core physics, currently 1D and calibrated using just two observed events can be improved by calibrating to a greater range of 3D simulations and observations. The survey can be done in 2D to capture essential aspects of the mixing, and the neutrino wind included in the yields. Given the vast amount of data

expected in the near future from large dedicated transient surveys, the effort is worth it and it will happen.

Table 3.1: SN 1987A Models

model	$M_{preSN}/M_{\odot}$	$M_{He}/M_{\odot}$	$M_{CO}/M_{\odot}$	$L/10^{38}$ erg s^{-1}	T_{eff}/K	$\xi_{2.5}$	$Z/Z_{\odot}$	Rotation
W18	16.93	7.39	3.06	8.04	18000	0.10	1/3	Yes
N20	16.3	6	3.76	5.0	15500	0.12	low	No
S19.8	15.85	6.09	4.49	5.65	3520	0.13	1	No
W15	15	4.15	2.02	2.0	15300	-	1/4	No
W20	19.38	5.78	2.32	5.16	13800	0.059	1/3	No
W17	16.27	7.04	2.82	7.31	20900	0.11	1/3	Yes
W18x	17.56	5.12	2.12	4.11	19000	0.10	1/3	Yes
S18	14.82	5.39	3.87	4.83	3520	0.19	1	No

Table 3.2: pns core-model parameters in PHOTB

Model	$R_{c,f}$ [km]	Γ	ζ	n	E_{51}	M(^{56}Ni+ 1/2 Tr)
Z9.6	7.0	3.0	0.65	1.55	0.16	0.0087
S19.8	6.5	3.0	0.90	2.96	1.30	0.089
W15	6.0	3.0	0.60	3.10	1.41	0.068
W18	6.0	3.0	0.65	3.06	1.25	0.074
W20	6.0	3.0	0.70	2.84	1.24	0.076
N20	6.0	3.0	0.60	3.23	1.49	0.062

Table 3.3: Integrated Statistics (see § 3.6.4 for descriptions; all masses in $M_\odot$)

Cal.	$\overline{E}$ (erg)	$\overline{M_b}$	$\overline{M_g}$	Low $\overline{M_{\rm BH}}$	Up $\overline{M_{\rm BH}}$	$\overline{M_{{\rm Ni},l}}$	$\overline{M_{{\rm Ni},u}}$	SN%	(>12)	(>20)	(>30)
W15.0	0.68×10^{51}	1.55	1.40	8.40	13.3	0.040	0.049	66	47	8	2
W18.0	0.72×10^{51}	1.56	1.40	9.05	13.6	0.043	0.053	67	48	9	2
W20.0	0.65×10^{51}	1.54	1.38	7.69	13.2	0.036	0.044	55	37	3	0
N20.0	0.81×10^{51}	1.56	1.41	9.23	13.8	0.047	0.062	74	52	13	5

Table 3.4: Supernova Mass Statistics

Mass Range	Engine(s)	$\overline{M_{SN}}$	f (no wind)
$\leq$12	Z9.6+W18	10.25	0.19 (0.40)
12-30	-	14.5	0.37 (0.54)
30-120	-	60.0	0.44 (0.010)
9-120	-	12.0	1
$\leq$12	Z9.6+N20	10.25	0.18 (0.40)
12-30	-	15.2	0.39 (0.58)
30-120	-	80.0	0.43 (0.026)
9-120	-	12.25	1

Table 3.5: Selected Isotopes Production in $M_{\odot}$

Mass Range	Engine(s)	$^{26}Al/10^{-5}$	$^{60}Fe/10^{-5}$	^{56}Fe
9-120	Z9.6+W18	2.80	2.70	0.038
9-120	Z9.6+N20	3.63	3.20	0.052
$\leq$12	Z9.6	1.36	2.73	0.026
$>$12	W18	3.17	2.66	0.053
$>$12	N20	4.22	3.28	0.066

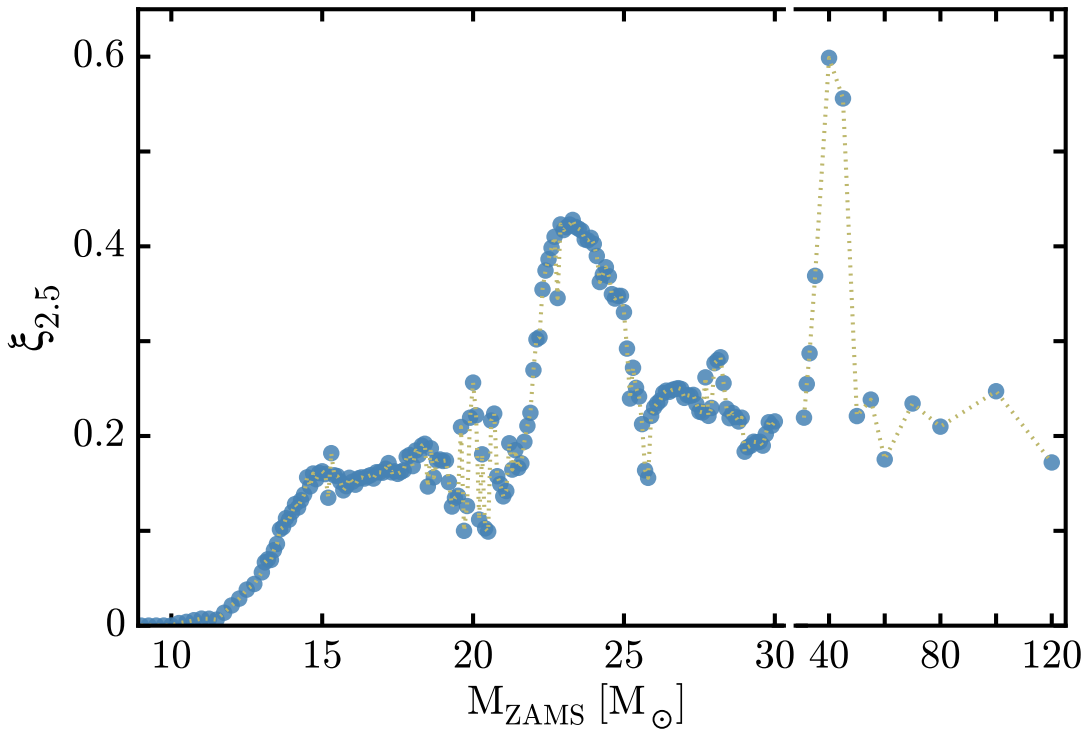

Figure 3.1: The compactness parameter, $\xi_{2.5}$, (eq. (2.1); O'Connor and Ott, 2011) characterizing the inner 2.5 $M_\odot$ of the presupernova star is shown as a function of zero-age main sequence (ZAMS) mass for all 200 models between 9.0 and 120 $M_\odot$. The compactness was evaluated when the collapse speed anywhere in the core first exceeded 1000 km s^{-1}. Studies have shown little difference for $\xi_{2.5}$ evaluated at this time and at core bounce (Sukhbold and Woosley, 2014). Note the scale break at 32 $M_\odot$. Above about 40 $M_\odot$ the compactness parameter declines to a nearly constant value due to the reduction of the helium core by mass loss. Stars below 12 $M_\odot$ have an especially dilute density structure around the iron core, due to the lingering effects of degeneracy on the late stages of evolution. Stars below 15 $M_\odot$ (helium core mass below 4 $M_\odot$) explode comparatively easily, while stars from 22 to 26 $M_\odot$ are hard to explode.

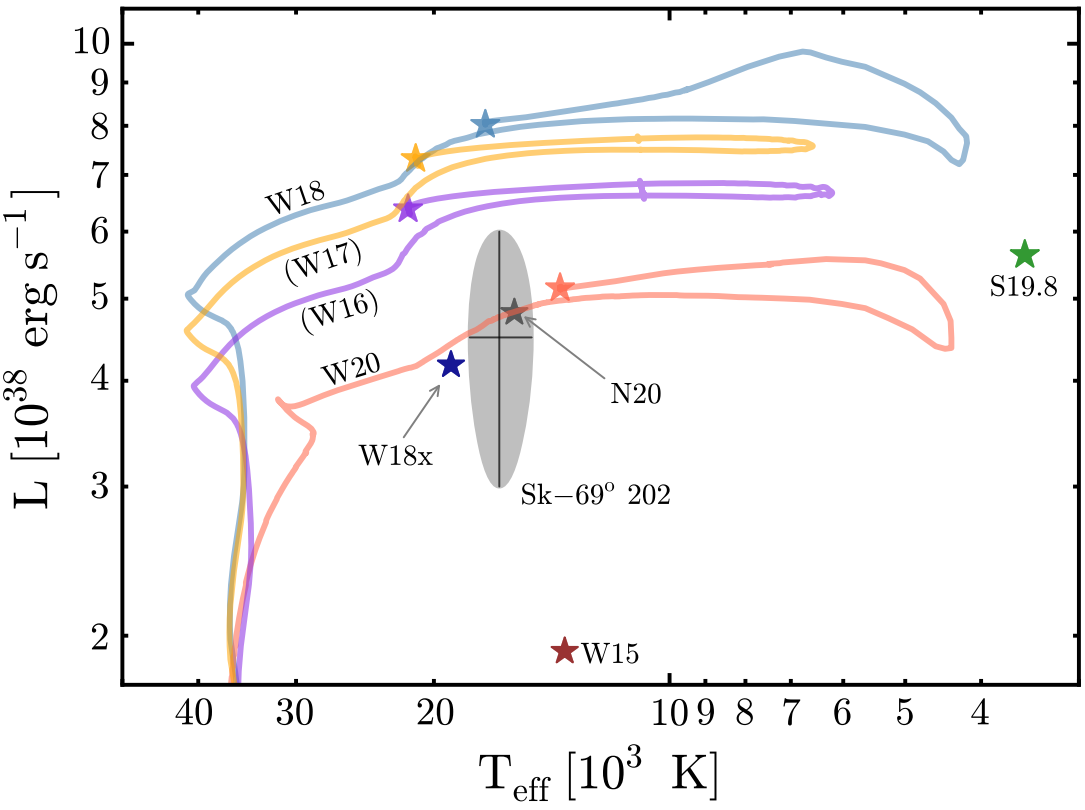

Figure 3.2: Hertzsprung-Russell diagram for the SN 1987A progenitors used in this study. The shaded region shows the observed properties of Sk -69^o 202 (see text). Model S19.8 produced a red supergiant; all the rest gave blue supergiants at the time of core collapse, but were preceded by a phase as a red supergiant. Models W16, W17, W18, and W18x included rotation; the rest were non-rotating. Model N20 was a construct obtained by joining 6 $M_\odot$ helium star to an envelope. All models beginning with a "W" were calculated using the KEPLER code assuming reduced metallicity and restricted semiconvection. Model W18x had 3/4 the angular momentum of Model W18, but was otherwise identical. See also Table 3.1.

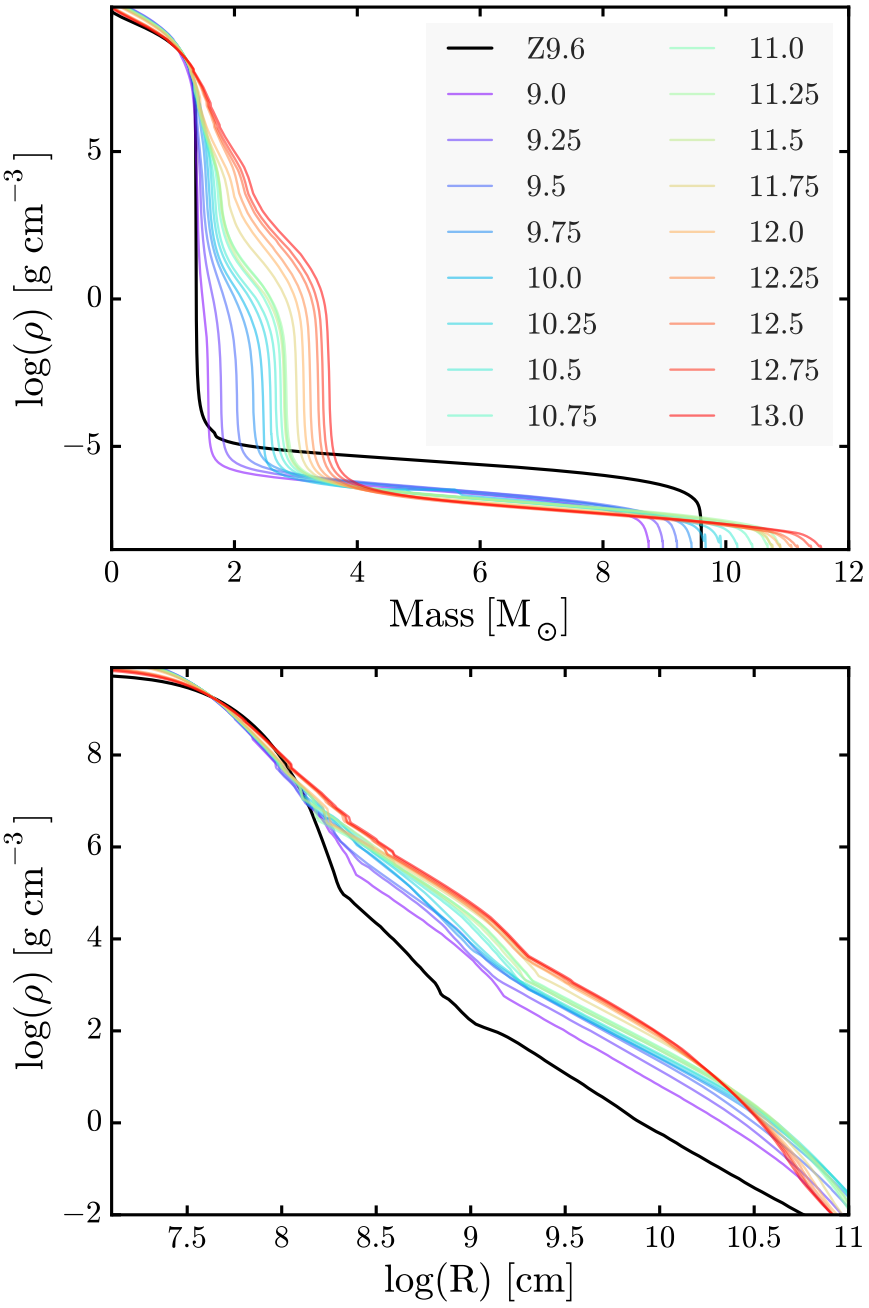

Figure 3.3: Density profiles for the 17 new presupernova models used for stars from 9.0 to 13.0 $M_\odot$. These have a high degree of central concentration and are relatively easy to explode. Also shown for comparison is the zero metallicity calibration model used for Crab, Z9.6, which is similar in structure to the 9.0 $M_\odot$ solar metallicity models studied here.

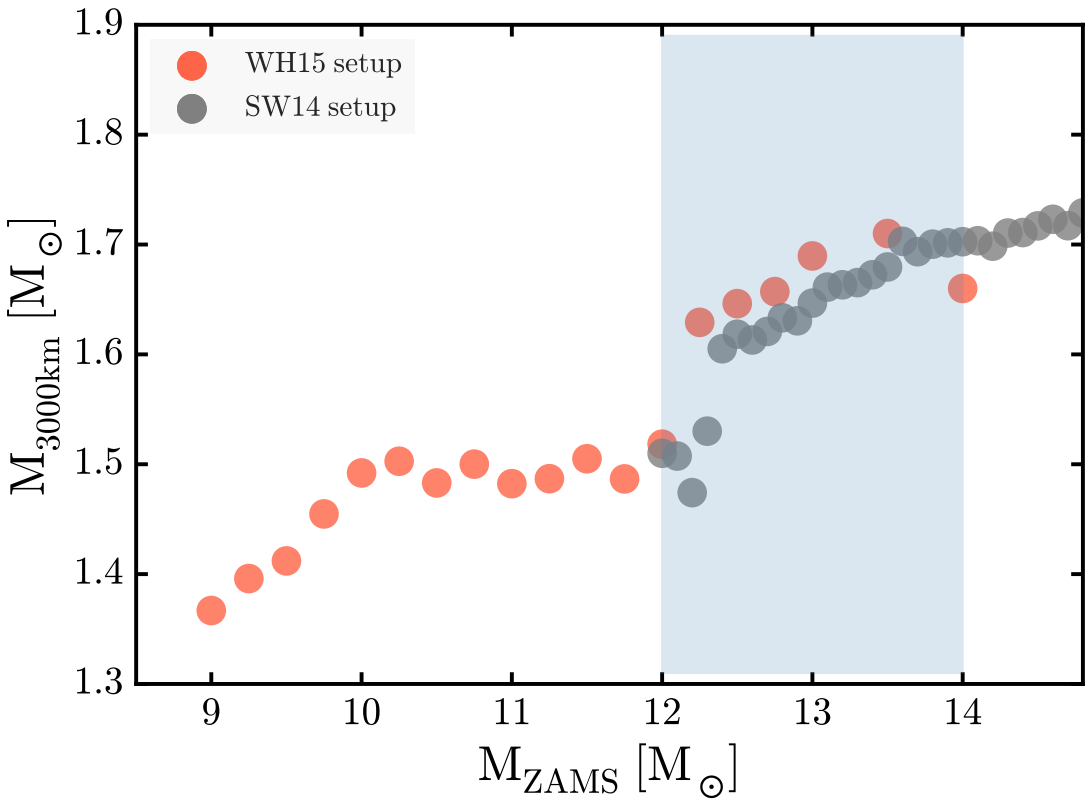

Figure 3.4: The presupernova core mass inside of 3000 km is shown for the 17 new models (see also **?**) up to 13.0 $M_\odot$, along with the 19 new models down to 13.1 $M_\odot$ calculated with the same input physics as in Sukhbold and Woosley (2014). Though the models come from different studies, they are in good agreement. Several models between 12 and 14 $M_\odot$ were calculated both ways to highlight the agreement (gray region).

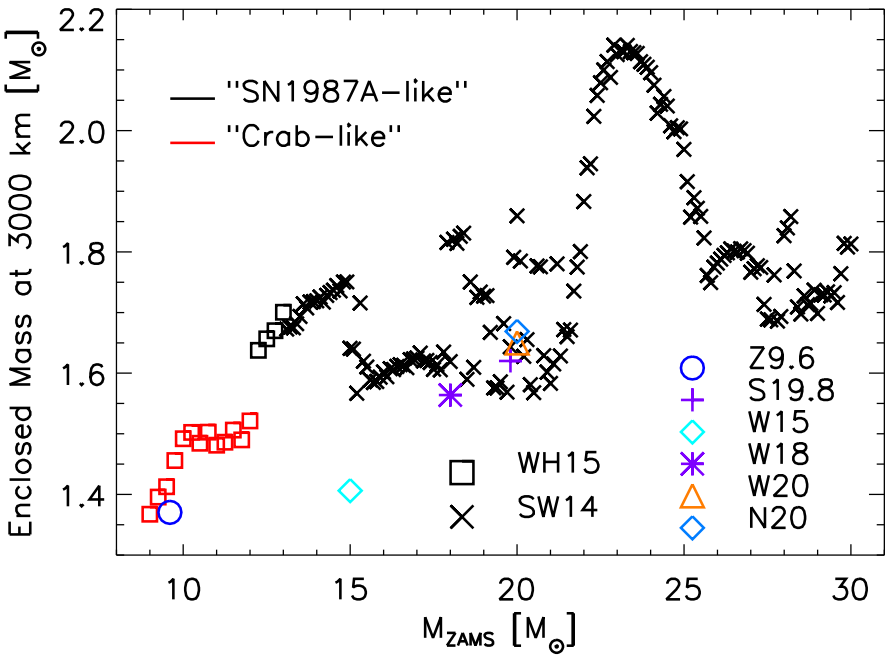

Figure 3.5: Mass inside a radius of 3000 km for all progenitors up to 30 $M_\odot$ at the time when the central density reaches the same value of 3×10^{10} g cm^{-3}. The black crosses and squares mark indicate "SN1987-like" cases; the red squares, "Crab-like" ones. Squares are models similar to Woosley and Heger (2015b); crosses, those of the Sukhbold and Woosley (2014) progenitor set. The locations of the calibration models are indicated by colored symbols as indicated in the figure legend. While N20, W20, and S19.8 cluster closely, W15 lies far off because this model has a very small compactness, $\xi_{2.5}$ (see Ertl *et al.* 2016).

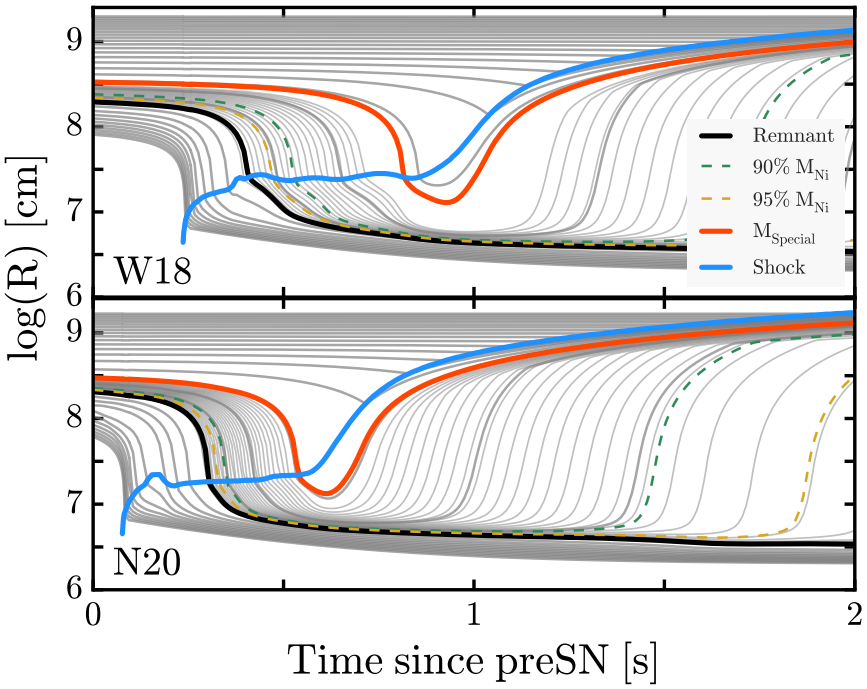

Figure 3.6: Evolution of baryonic mass shells from the explosion of two calibration models, W18 and N20. Thick gray lines are contours of constant enclosed masses in steps of 0.04 $M_\odot$ starting at 1.1 $M_\odot$. The thin gray lines are mass shells in steps of 0.004 $M_\odot$ resolving the neutrino-driven wind, which is defined as the difference between the proto-neutron star mass at the onset of the explosion and its mass after $\sim$15 s. The solid blue line shows the shock radius and solid black curve shows the mass-shell of the final mass cut. The solid red line shows the "special trajectory" used in the KEPLER code. Dashed yellow and green lines show the location of mass shells internal to the initial ejection of 95% and 90% of the iron-group elements in the PHOTB calculations.

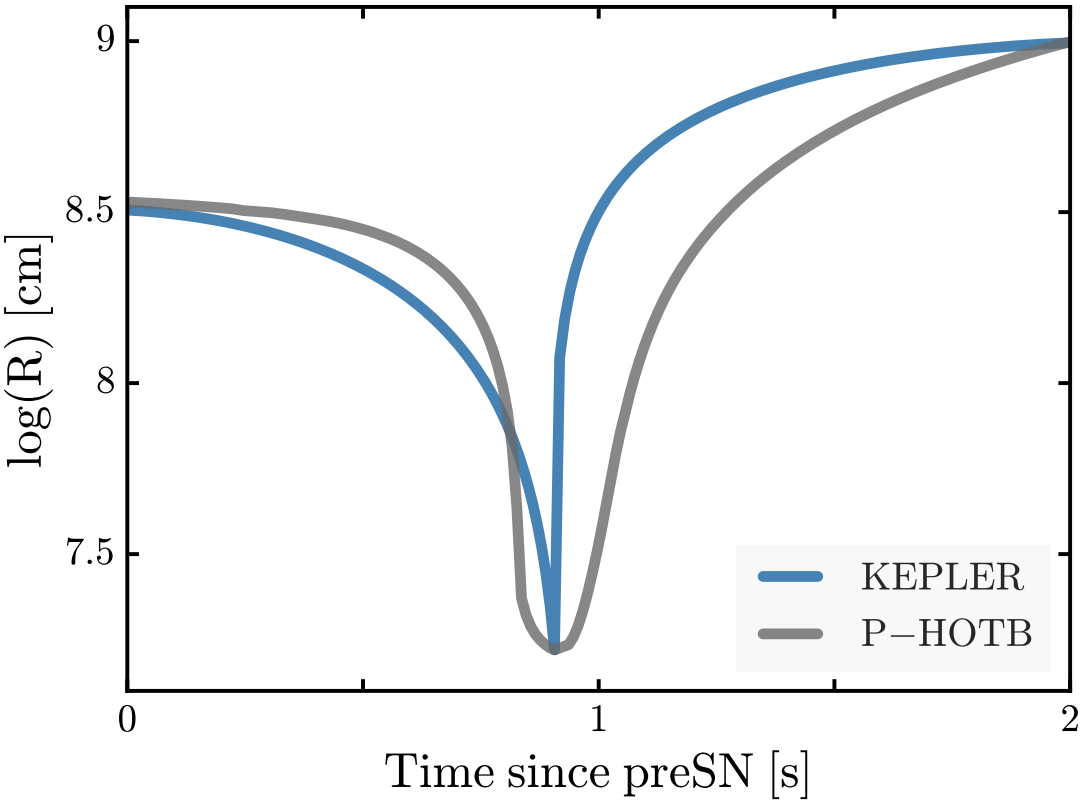

Figure 3.7: The trajectory from the neutrino-driven explosion with PHOTB (gray) is compared against the corresponding trajectory from KEPLER (blue) for the explosion of the W18 engine itself. In all cases, the trajectories from the two codes have a common starting radius and time and the same minimum radius and time.

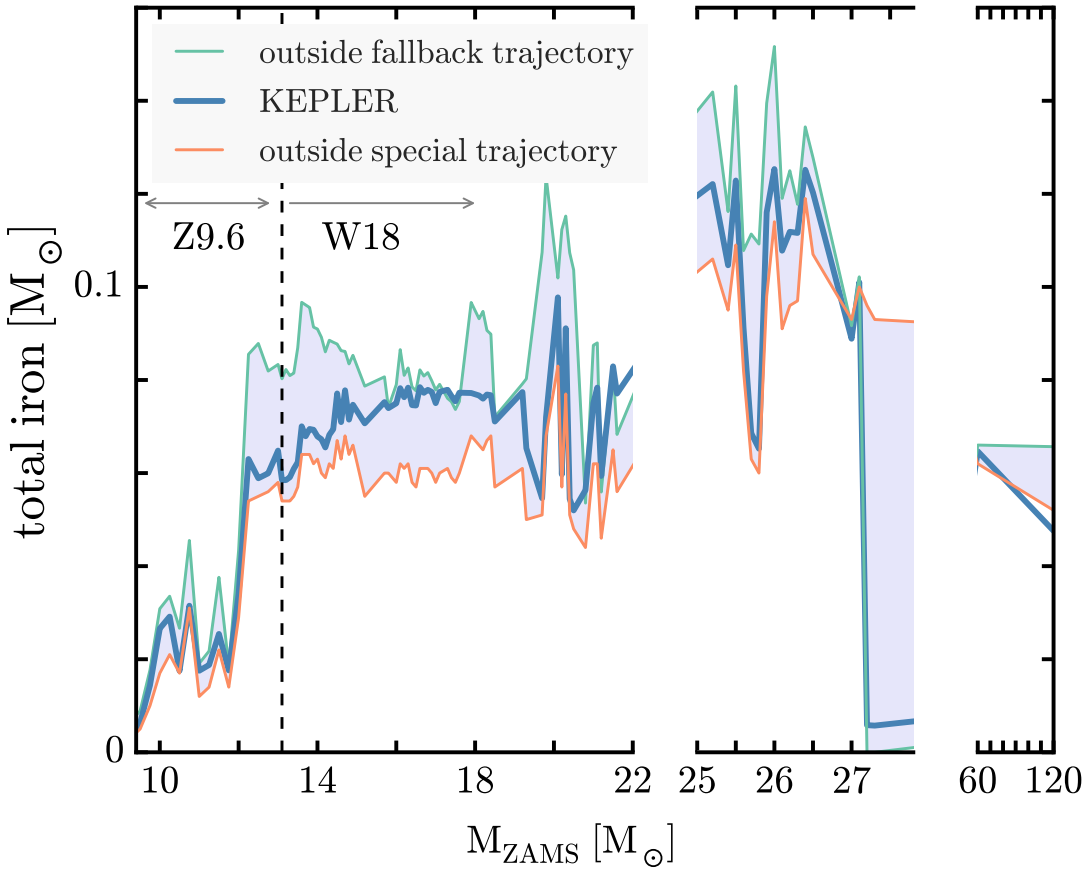

Figure 3.8: Iron production is compared between the KEPLER and PHOTB calculations for all models that exploded using the Z9.6 and W18 engines. The shaded gray region is bounded on the bottom by the total iron produced by PHOTB outside the 'special' trajectory (orange), and on the top by the total iron ejected (green). The thick blue curve represents total iron production in the converged KEPLER explosions.

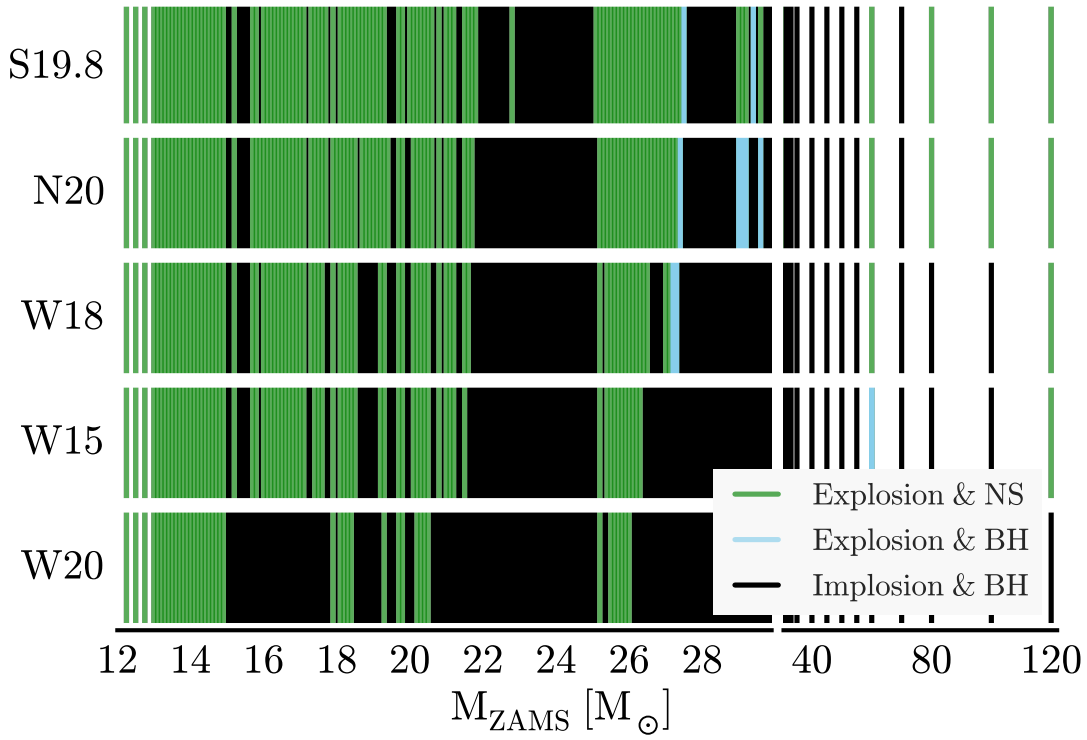

Figure 3.9: The explosion outcomes from the five different central engines for SN 1987A (Table 3.1 and Table 3.2) are shown in comparison. Successful explosions that make neutron stars are green, the explosions that make black holes through fall back are light blue, and the failures, which make black holes, are black lines. The calibrators are listed by the engine strength, weakest at the bottom. Models heavier than $12.25 M_{\odot}$ were covered by these five engines, all lighter models produced successful explosions by the Z9.6 engine calibrated to Crab supernova.

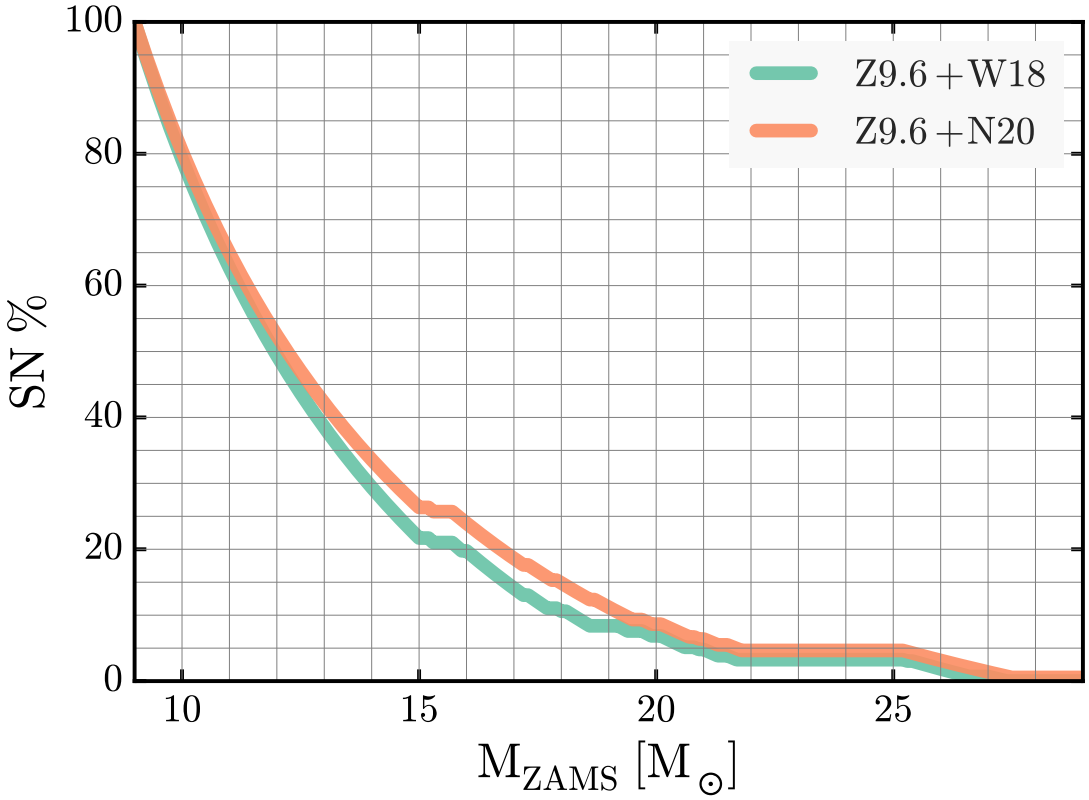

Figure 3.10: The percentage of Type II supernovae above a given main sequence mass for explosions using the Z9.6 and W18 or N20 engines. A Salpeter IMF has been assumed. Successful explosions above 30 $M_\odot$ do not make Type II supernovae.

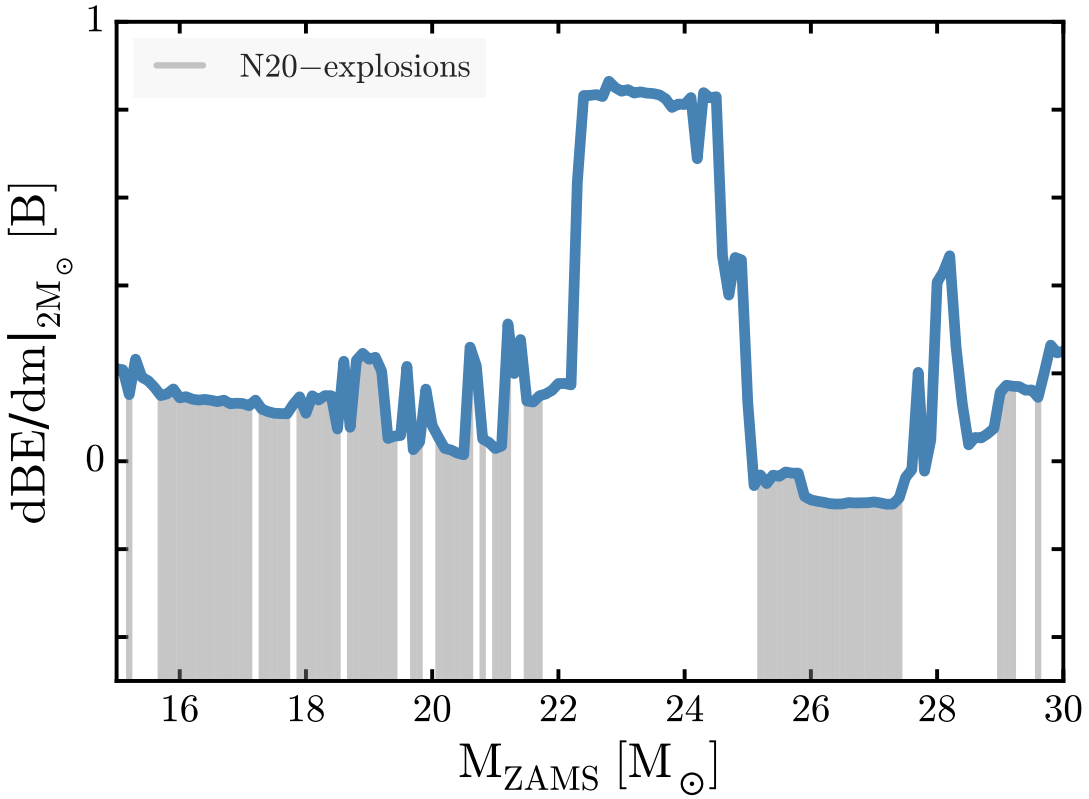

Figure 3.11: The mass derivative of the binding energy (1 Bethe = 10^{51} erg) outside $2M_{\odot}$ as a function of ZAMS mass is compared against the explosion outcome for the N20 engine. The successful explosions are noted with gray vertical lines. Though this doesn't work as well as the 2-parameter method of Ertl *et al.* (2016), it is one of the better single-parameter criteria for an explosion.

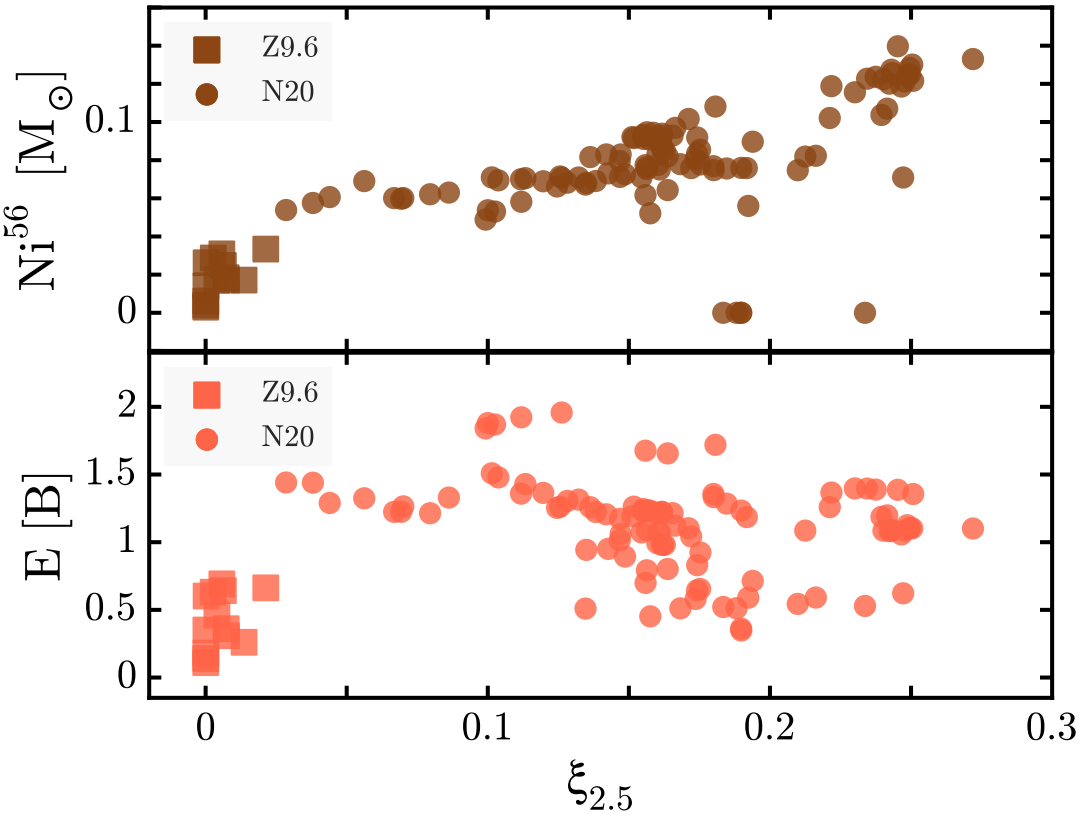

Figure 3.12: The amount of nickel and explosion energies resulting from use of the Z9.6 and N20 engines are shown as functions of the compactness parameter (eq. (2.1)). The top panel shows a positive correlation of ^{56}Ni production with compactness. More matter is heated by the supernova shock for models with high $\xi_{2.5}$. The explosion energy is low for stars with very small compactness parameter because their thin shells are inefficient at trapping neutrino energy and there is very little luminosity from accreting matter. These effects saturate, however, around 10^{51} ergs, since the energy provided by the neutrino source is limited and the the binding energy of the overlying shells is harder to overcome. The results for the W18 engine are not plotted, but closely follow the N20 points plotted here.

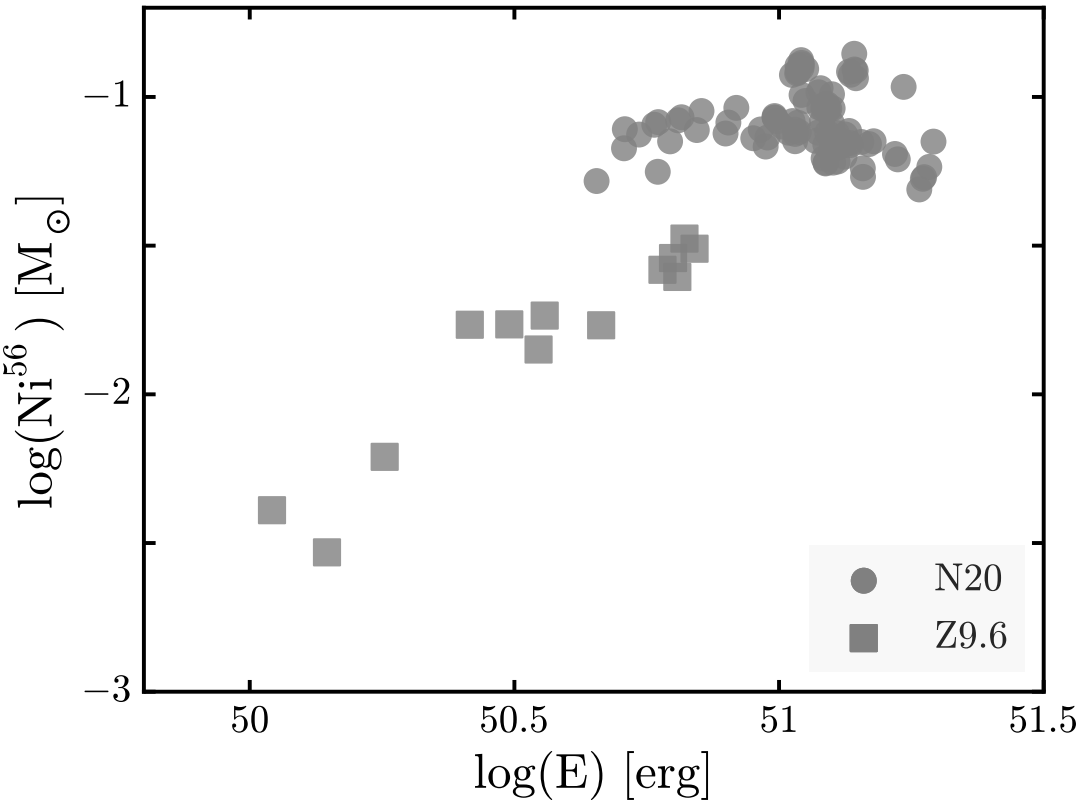

Figure 3.13: The amount of ^{56}Ni nucleosynthesis versus the logarithm of the final kinetic energy of the explosion in units of 10^{51} erg for the Z9.6 (squares) and N20 (circles) series. Models below an initial mass of 12 $M_\odot$ (half of all supernovae) explode easily and produce small amounts of nickel that correlate with their explosion energy. Larger mass models on the other hand, produce a nearly constant 0.07 $M_\odot$ nickel, except for a few cases with large fallback. The results for the W18 engine, though not plotted here for clarity, look very similar to those of N20.

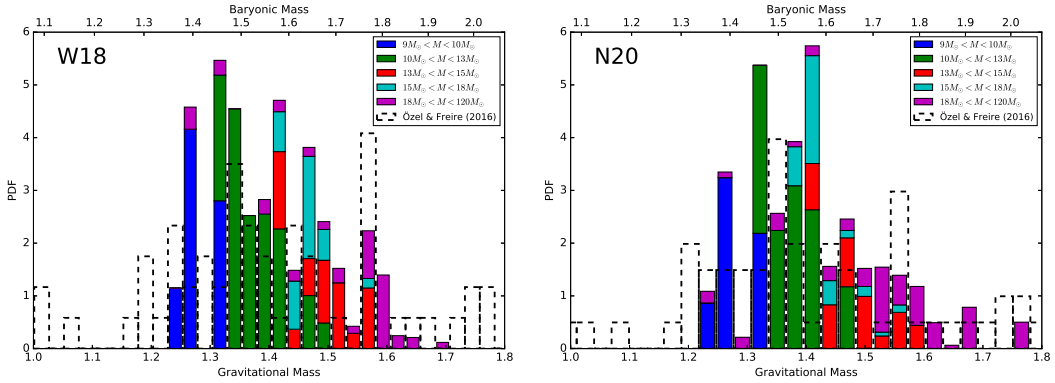

Figure 3.14: Distributions of neutron star masses for the explosions calculated using PHOTB compared with the observational data from Özel *et al.* (2012) and Ozel and Freire (2016). Several neutron stars with masses greater than the maximum mass plotted here have been observed and the lightest observational masses have large error bars. In the top figure, the W18 calibration is used, and in the bottom, the N20. Both distributions show some weak evidence for bimodality around 1.25 and 1.4 $M_{\odot}$. Results have been color coded to show the main sequence masses contributing to each neutron star mass bin. Note that this is not a direct comparison to the observations, as the measured values may already include accretion (i.e., not birth masses) and have not been properly weighted based on their measurement uncertainties and the relative contributions of different classes of neutron stars to the total population.

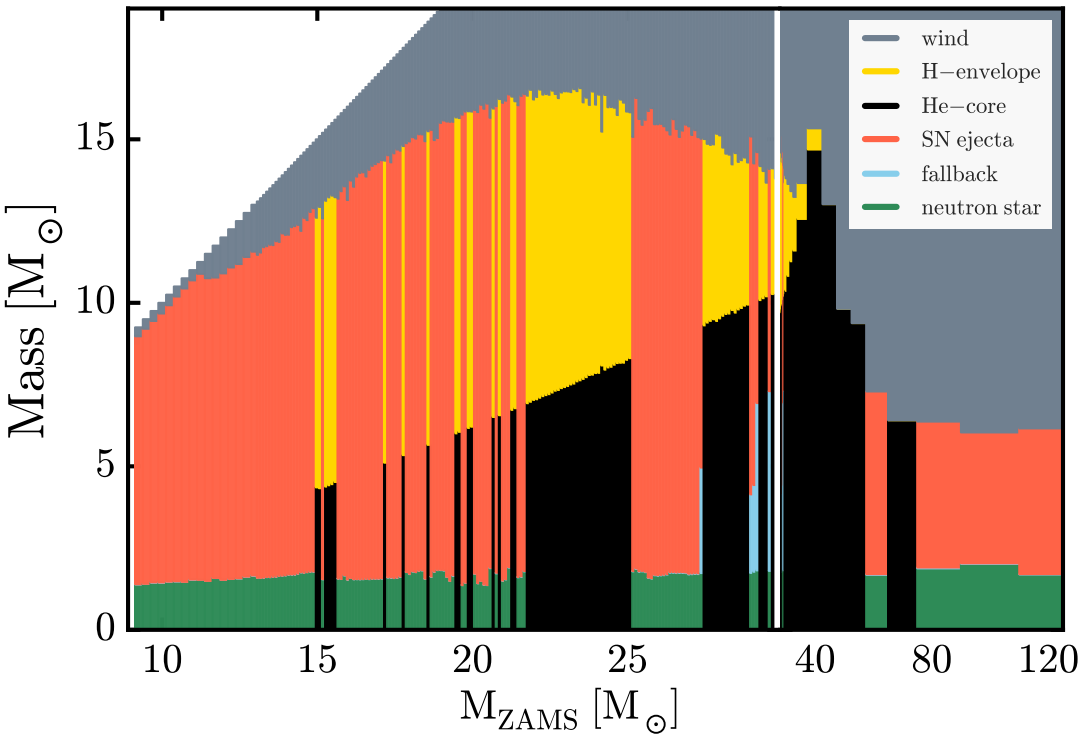

Figure 3.15: The mass 'budget' for each star based on results using the Z9.6 and N20 engines. Grey shows mass lost to winds. For the successfully exploded models, the compact remnant mass is shown in green. For a few models that experienced fallback, the fallback mass is shown in blue. Except near 30 $M_{\odot}$, fallback is negligible. The helium-cores and the hydrogen-envelopes of the "failed" explosions are shown in black and yellow respectively. The resulting black hole mass from an implosion will most likely include the full presupernova star (black plus yellow), or just the helium core (black). Results using the W18 engine are qualitatively similar, with fewer explosions and fewer cases with significant fallback.

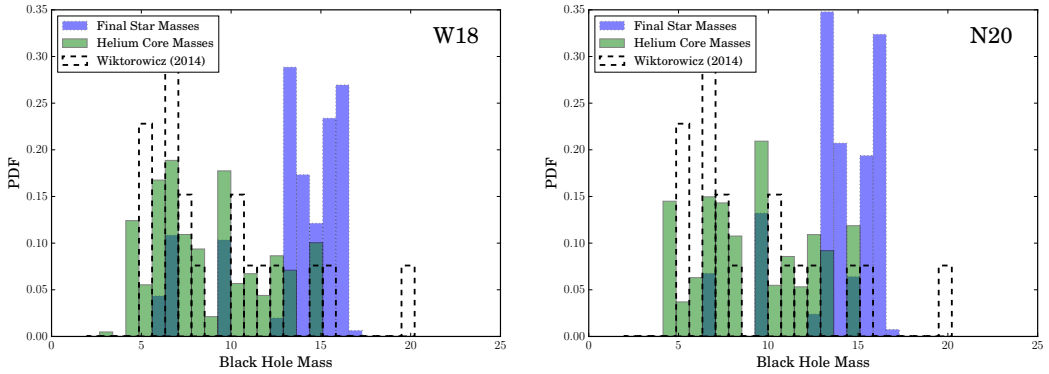

Figure 3.16: Distributions of black hole masses for the explosions calculated using PHOTB compared with the observational data from Wiktorowicz *et al.* (2014)[1] in gray. Theoretical results are shown based on two assumptions: 1) that only the helium core implodes (green); or 2) that the whole presupernova star implodes (blue). Observations are more consistent with just the helium core imploding. As in Fig. 3.14, this is not a direct comparison to the observations.

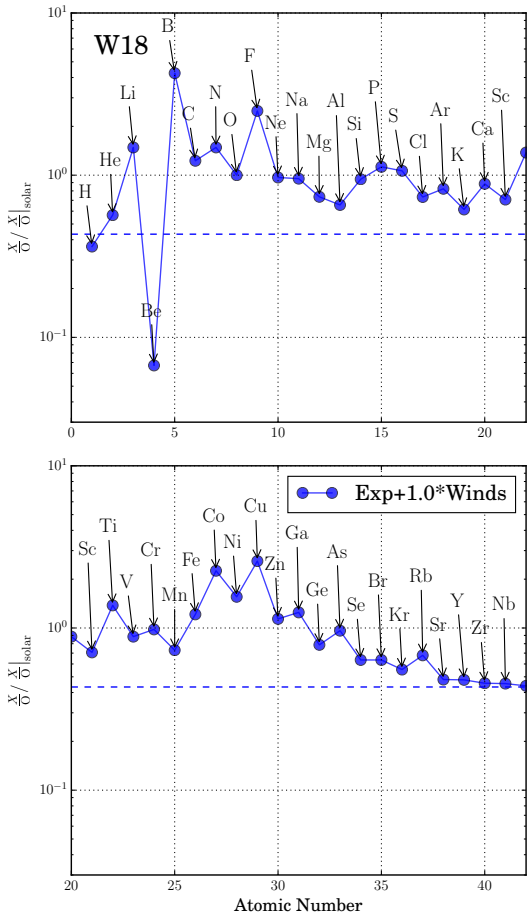

Figure 3.17: Nucleosynthesis in low mass supernovae. The IMF-averaged yields of just the explosions from 9 –12 $M_{\odot}$ are given for the elements from hydrogen through niobium. The calculations actually included elements up to bismuth (Z = 83), but no appreciable production occurred for the heavier elements. Production factors (defined in the text) have been normalized to that of ^{16}O, which is 2.37, by dividing them all by this factor, making the oxygen production unity. The dashed line at $(2.37)^{-1}$ = 0.43 is thus a line of no net change. Elements below the dashed line are destroyed in the star; those above it experience net production. The relative large yields of iron group elements, which are nearly solar compared to oxygen, is a consequence of the low oxygen yield in these light supernovae, and does not characterize heavier stars where more nucleosynthesis happens. The *s*-process just above the iron group is significantly underproduced. Note, however, the large yields of Li and B produced by the neutrino process. Fluorine is also overproduced by a combination of neutrinos and helium burning. Stellar winds of all models have been included.

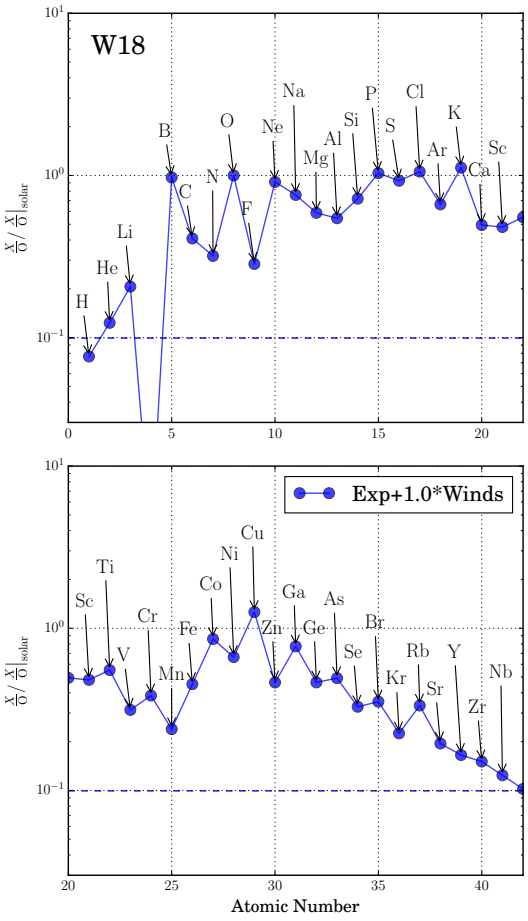

Figure 3.18: Similar to Fig. 3.17, the IMF-averaged production of elements in supernovae from 12 to 30 $M_\odot$ is shown using the W18 calibration for the central engine. This is the range of masses where most supernova nucleosynthesis occurs. The production factor of oxygen before normalization was 10. Production factors above the dashed line at 0.10 thus indicate net nucleosynthesis in the stars considered. The production of iron-group elements is substantially lower than in Fig. 3.17, but will be supplemented by SN Ia. The production of light *s*-process elements is substantially greater, but still inadequate to explain their solar abundances. Production of Li and B by the neutrino process is diminished, but still significant, especially for B. Contributions to nucleosynthesis by the winds of all stars, including those that became black holes is included.

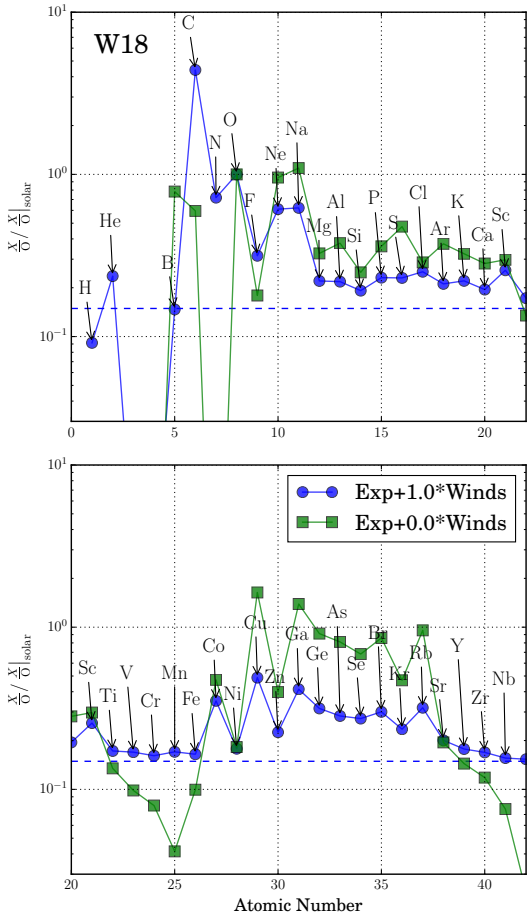

Figure 3.19: Similar to Fig. 3.17, the IMF-averaged production of the elements is shown for stars from 30 to 120 $M_{\odot}$, using the W18 calibration for the central engine. Most, though not all stars in this very massive range become black holes, so their nucleosynthesis is dominated by the winds that they eject before dying. Production factors are normalized to oxygen. If winds are included, net production of an element occurs in this mass range if its average production factor is above 0.15 (blue dashed line). Also shown are the production factors if the wind is discarded. Since oxygen was being appreciably synthesized in the winds, neglecting them results in an overall renormalization of all production factors. The cut-off for the net production without winds falls to 0.010, off the scale of the plot. Including winds, these stars make so much carbon, nitrogen and oxygen that they can be responsible for little else.

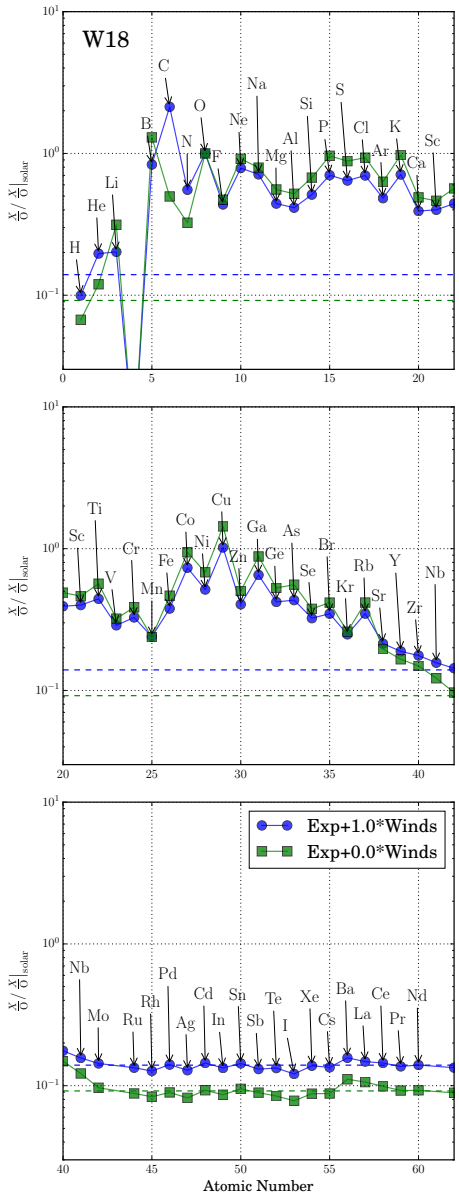

Figure 3.20: Integrated nucleosynthesis of the elements for all stars considered (9 – 120 $M_{\odot}$) using the W18 central engine. The results have been normalized to oxygen and the dashed line show net production occurring for production factors bigger than 0.14, if winds are included, 0.092 if they are not. The displacement of the overall normalization is due to the production of oxygen itself in winds. While individual isotopes may be affected (Fig. 3.21), no net nucleosynthesis occurs for elements above Z = 40.

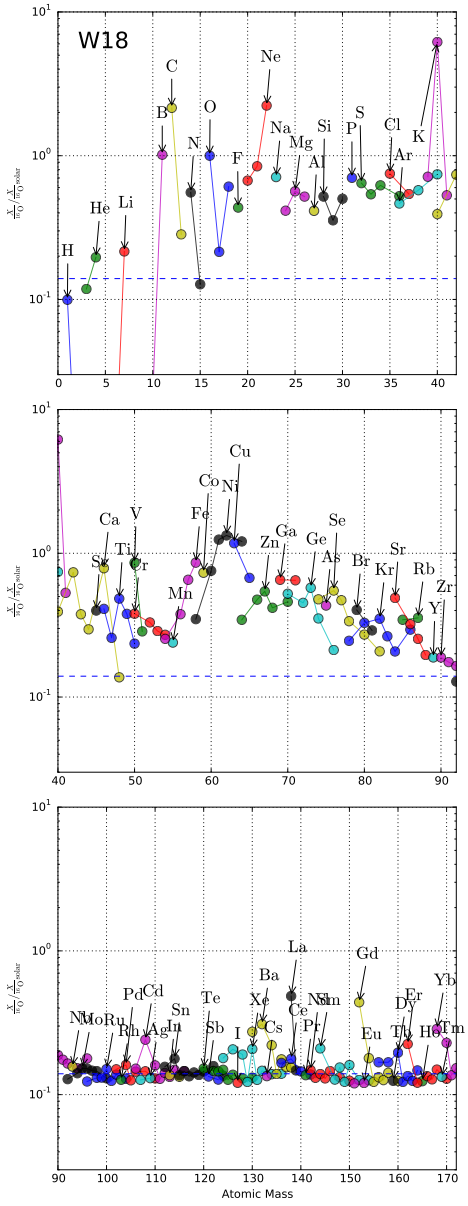

Figure 3.21: The same yields as in Fig. 3.20 for the W18 central engine including the wind, but now given for the individual isotopes of each element.

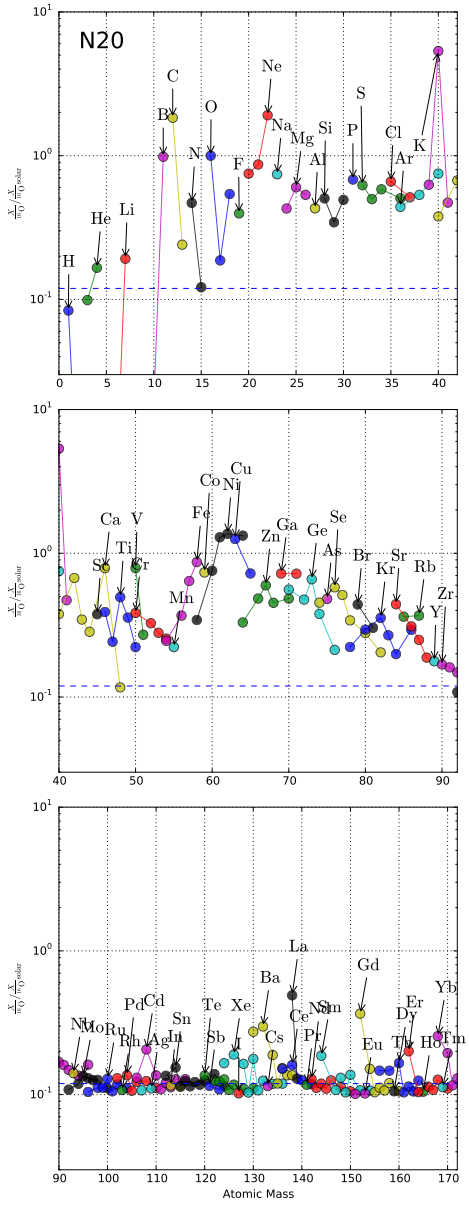

Figure 3.22: Similar to Fig. 3.21, this figure gives results using the N20 central engine instead of W18. There are no significant differences.

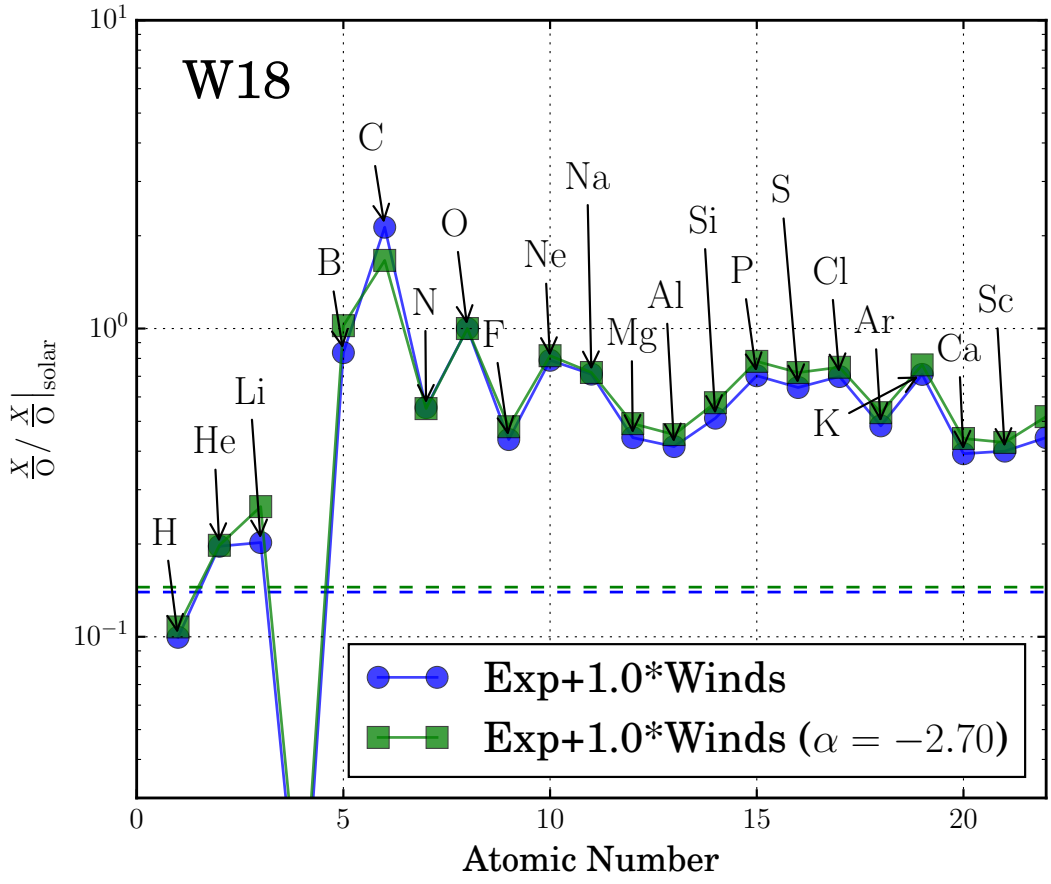

Figure 3.23: Similar to Fig. 3.20, but using a steeper mass dependence for the IMF. Here the results of using a Salpeter IMF with a power-law dependence of −2.35 are compared to those obtained using a slope of −2.7. The dashed lines here indicate net production for both ensembles at 0.14.

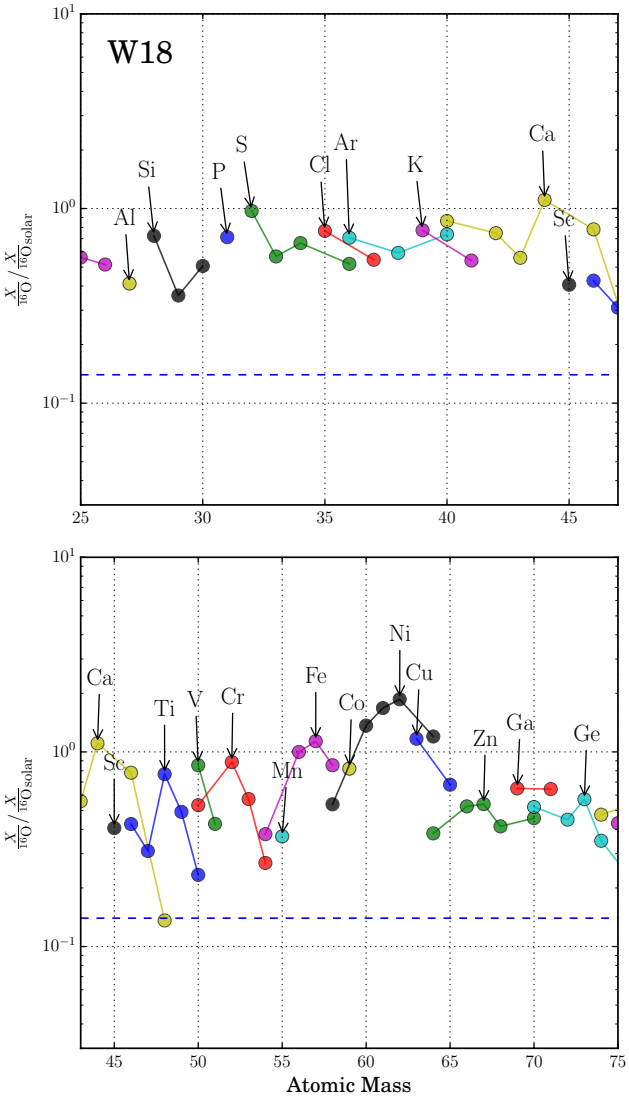

Figure 3.24: Similar to Fig. 3.21, this figure includes contributions from all 9–120 $M_\odot$ supernovae and their winds, but also an additional component from SN Ia. Added to the average yield in Fig. 3.21 is that of a typical sub-Chandrasekhar mass SN Ia (Woosley and Kasen, 2011) with a sufficient quantity of iron to make its solar abundance relative to oxygen. Not only does this variety of SN Ia make iron, but also raises the production of ^{44}Ca to its full solar value and increases the abundances of Si, S, Ar, and Ca so that they are closer to solar. Note, however, the underproduction of Mn/Fe. The dashed line for net production here is at 0.14.

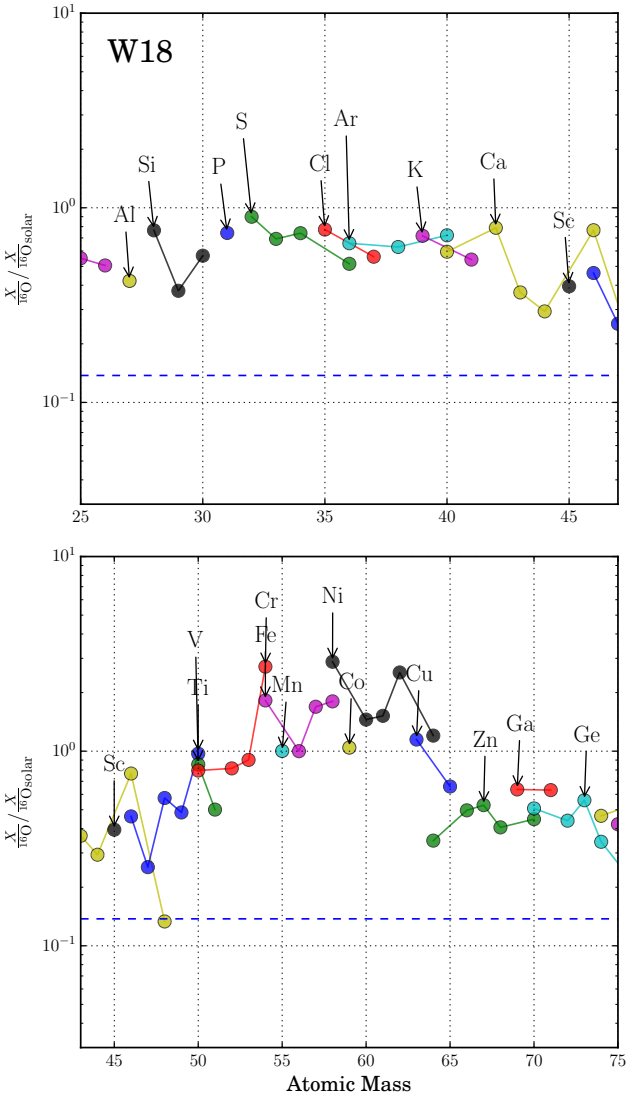

Figure 3.25: Similar to Fig. 3.24, but including the yields of a Chandrasekhar mass model for SN Ia (Nomoto's W7) rather than the sub-Chandrasekhar model. The dashed line for net production here is at 0.14. Manganese is much improved, but ^{44}Ca is lost

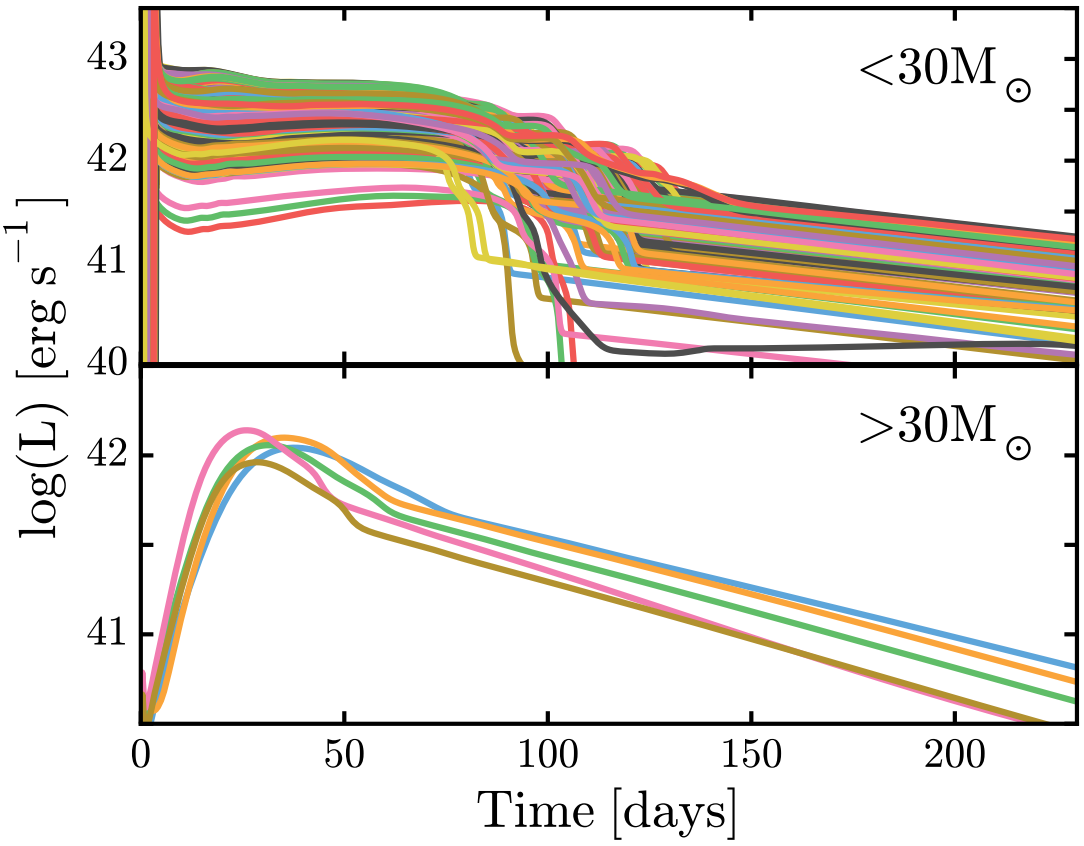

Figure 3.26: For each successful explosion calculation, the bolometric light curve was followed for 230 days. Lighter models (top) that retained a good fraction of their envelopes were SN IIp, while heavier models (bottom) which lost most or all of their envelopes were SN Ib or Ic. Both panels show all models that were successfully exploded by Z9.6, W18 and N20 calibrators.

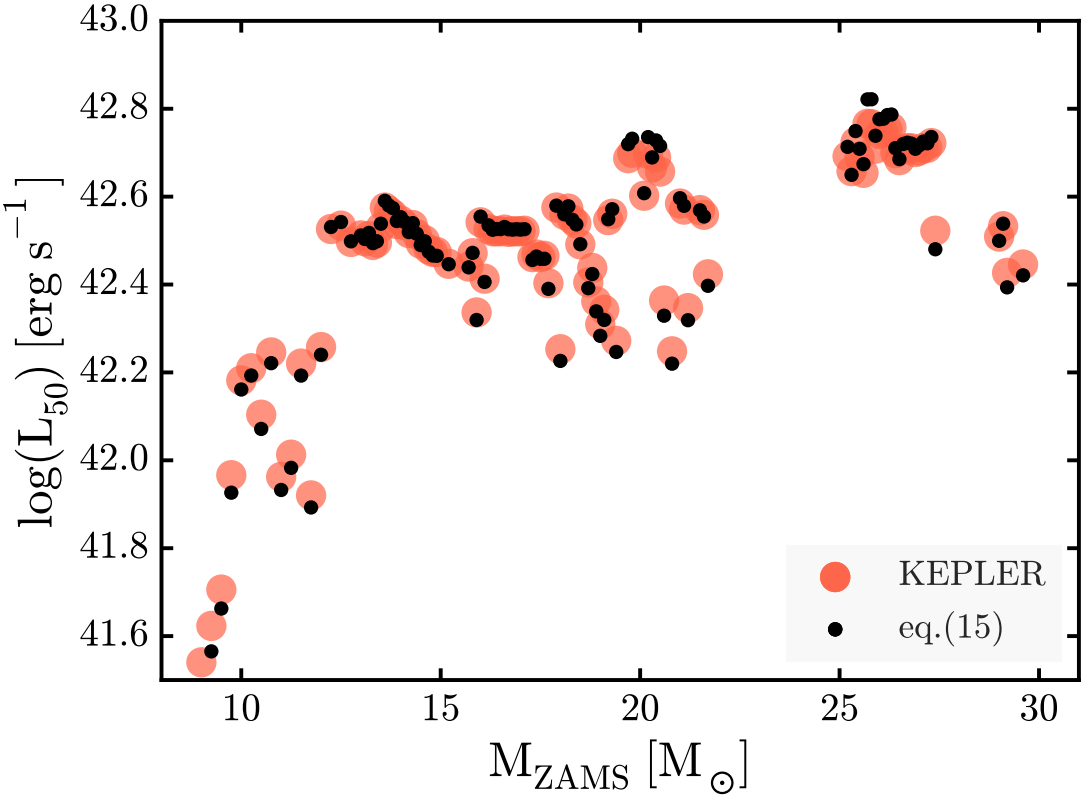

Figure 3.27: Plateau luminosities 50 days post-breakout for the successfully exploded models of the Z9.6 and N20 series (red circles) are compared with eq. (3.14) (black circles). The agreement is striking. Results for the W18 series are not shown, but are very similar to those of N20.

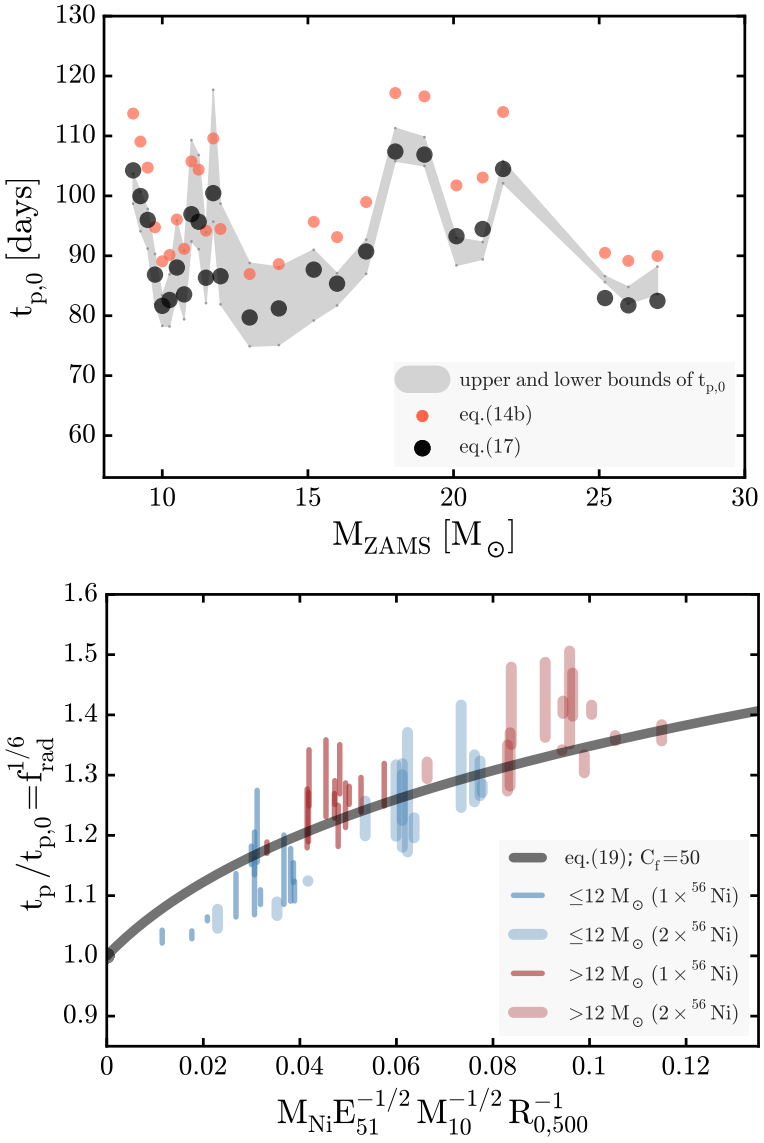

Figure 3.28: Top: the plateau durations from a set of 26 models calculated assuming no radioactive decay are shown in comparison with Popov's unmodified scaling law (eq. (3.13)) and a renormalized version. The upper and lower bounds on $t_{p,0}$ from the models (see text) give the gray shaded region. The eq. (3.13) with $C_t = 96$ days systematically overestimates the measured durations by about to 10%. The same scaling normalized to C_t=88 days produces better agreement. Bottom: the effect of radioactivity on the plateau duration is shown from the same set of models that included no radioactivity ($t_{p,0}$), with the default calculated yields of ^{56}Ni (t_p), and twice that value (t_p). Models from progenitors with initial mass larger than about 12 $M_\odot$ follow the correction term derived in eq. (3.18) reasonably well, but smaller models are overestimated. The fit is improved when the constant in the brackets of eq. (3.18) C_f is 50, i.e. the black curve is: $(1+50 M_{Ni} E_{51}^{-1/2} M_{10}^{-1/2} R_{0,500}^{-1})^{1/6}$.

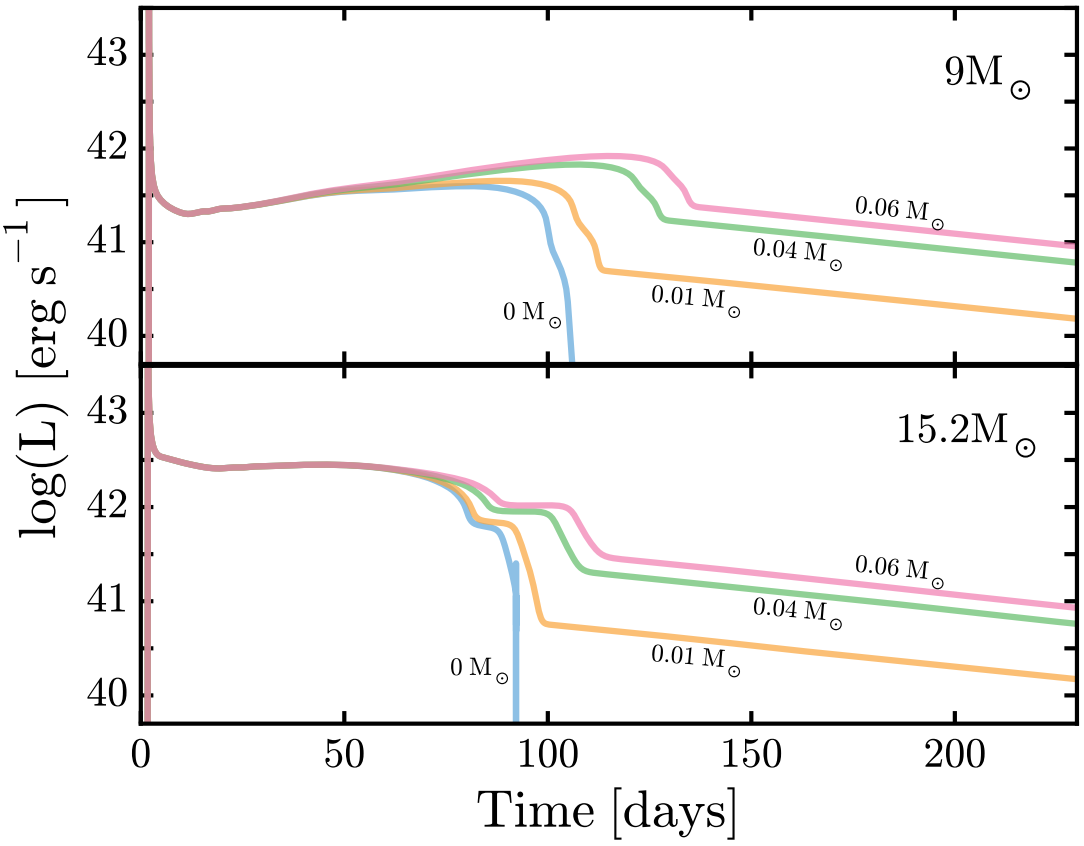

Figure 3.29: The light curves due to various amounts of nickel masses are shown for the 9.0 $M_\odot$ model of the Z9.6 series (top) and the 15.2 $M_\odot$ model from the N20 series. The KEPLER model gave 0.004 $M_\odot$nickel for the 9.0 $M_\odot$ model and 0.070 $M_\odot$ for the 15.2 $M_\odot$ model. Energy generation from the decay of these masses were multiplied by a constant to simulate the production of various amounts of ^{56}Ni and the resulting curves are shown. ^{56}Ni masses of more than 0.01 $M_\odot$ for the 9.0 $M_\odot$ model are unlikely, but shown for comparison.

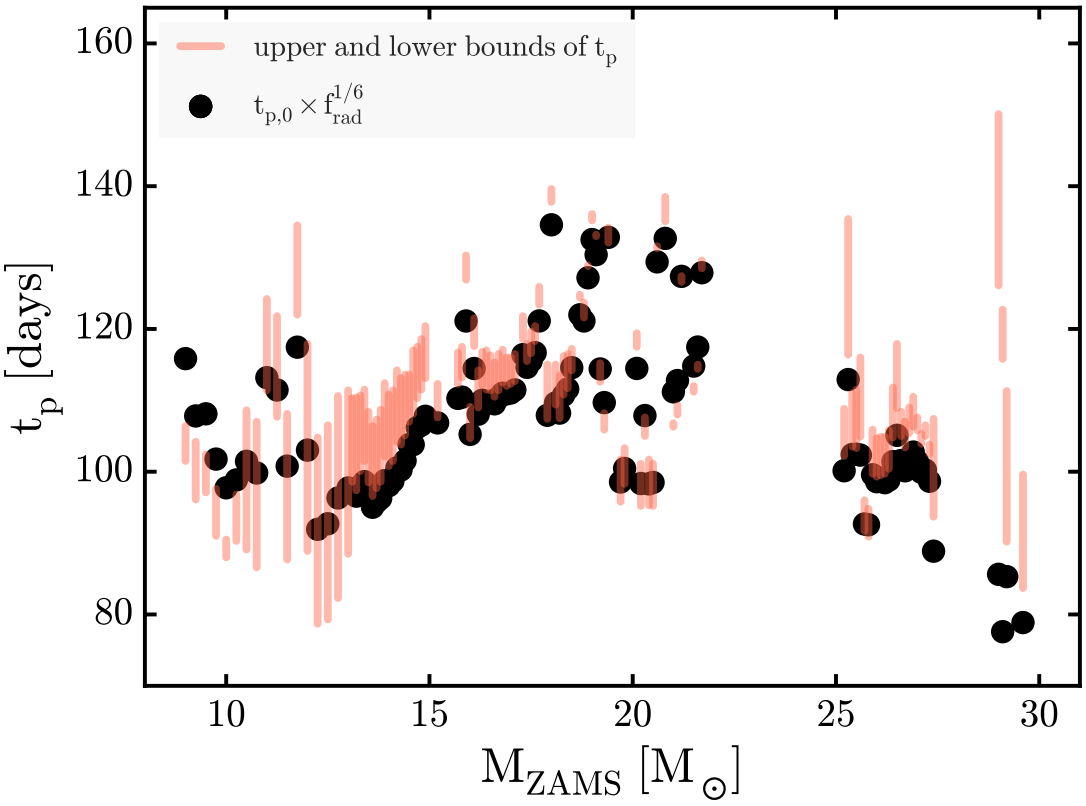

Figure 3.30: The scaling laws that showed good agreement in Fig. 3.28 are now compared against the standard explosion models with their ^{56}Ni included. The models used are from the Z9.6 and N20 series. A red vertical bar represents a range of possible plateau durations calculated from the models assuming that 1) the photospheric radius had receded to 50% of its maximum value (lower bound); or 2) the whole star had recombined (upper bound). Black points result from multiplying eq. (3.13) with $C_t = 88$ by the correction term, eq. (3.18), with $C_f = 50$.

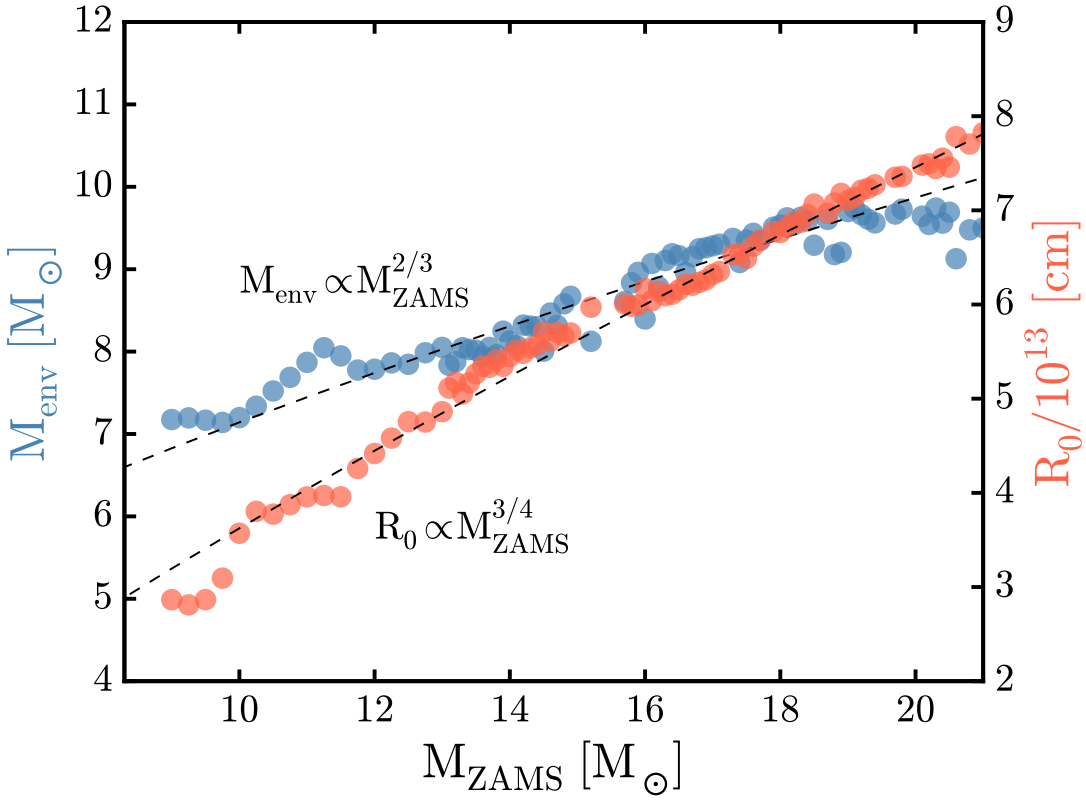

Figure 3.31: The scaling of the envelope mass and radius with the initial mass for progenitors below 21 $M_\odot$. The radius scales as $M_{ZAMS}^{3/4}$, while the envelope mass scales approximately as $M_{ZAMS}^{2/3}$. The envelope mass peaks near 20 $M_\odot$ and begins to decline at higher mass due to mass loss, so these scalings cannot be used outside the range shown.

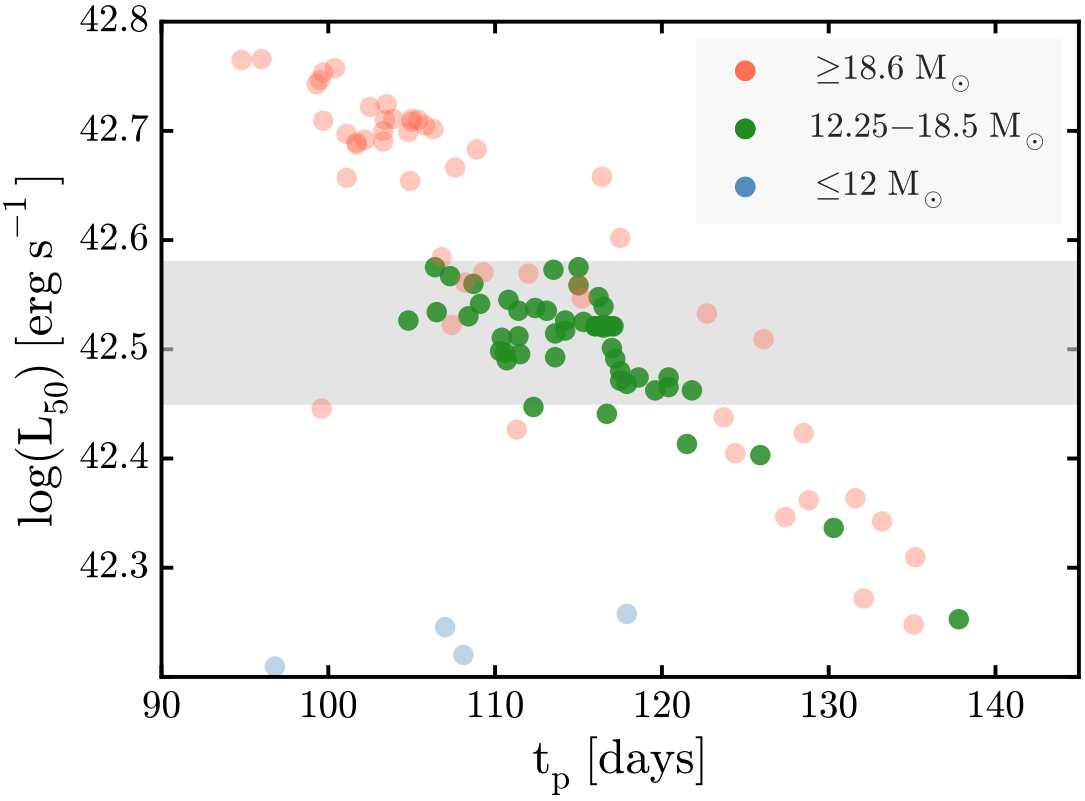

Figure 3.32: The correlation between the plateau luminosities and durations is shown for the exploded models based on the Z9.6 and N20 engines. The plateau duration here is an upper bound, the starting time of the radioactive tail when the full star has recombined. Green points, which represent 35% of all supernovae, show a strong clustering. Above log L_{50} = 42.3 erg s^{-1}, the luminosity is clearly anti-correlated with the plateau duration. The low mass models from series Z9.6 all have luminosities well below the gray box, and some of them have log L_{50} below 42.2 erg s^{-1} and fall on the plotted grid.

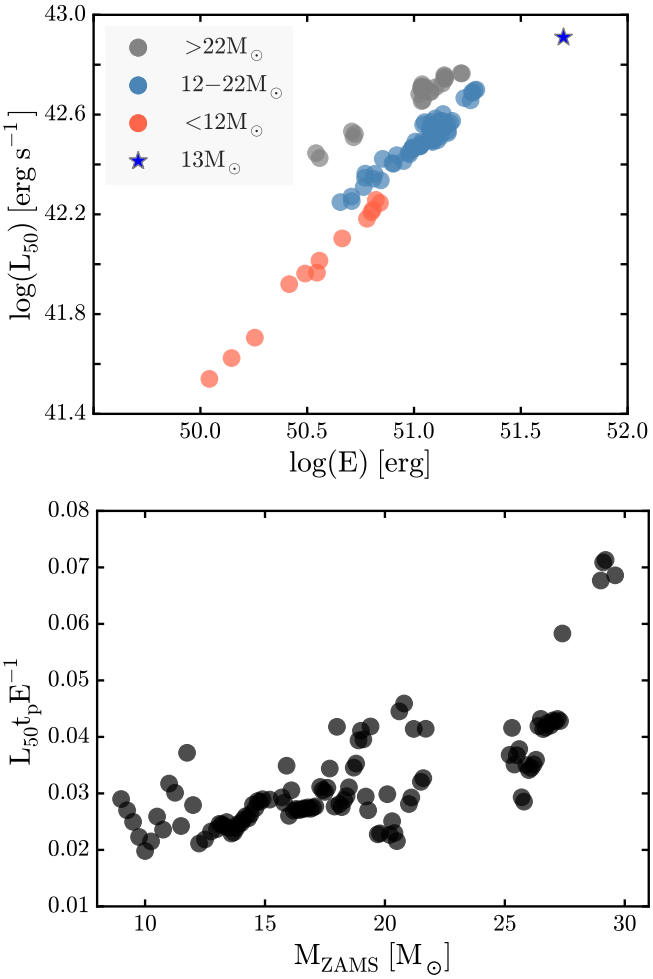

Figure 3.33: Top: the correlation between plateau luminosities at 50 days and the explosion energies for Z9.6 and N20 engines. The 13 $M_\odot$ model from the N20 engine has been re-calculated with the explosion energy scaled up to 5×10^{51} ergs and is plotted as a single blue star. Explosions from stars smaller than 22 $M_\odot$, which are most supernovae, show a strong positive correlation of luminosity with energy. Bottom: the ratio of $L_{50}t_p$ and explosion energy is shown as a function of initial progenitor mass. Integration of the light curve shows that $L_{50}t_p$ is an accurate proxy for the total radiated energy. The typical SN IIp supernova radiates 2-4% of its explosion energy as light.

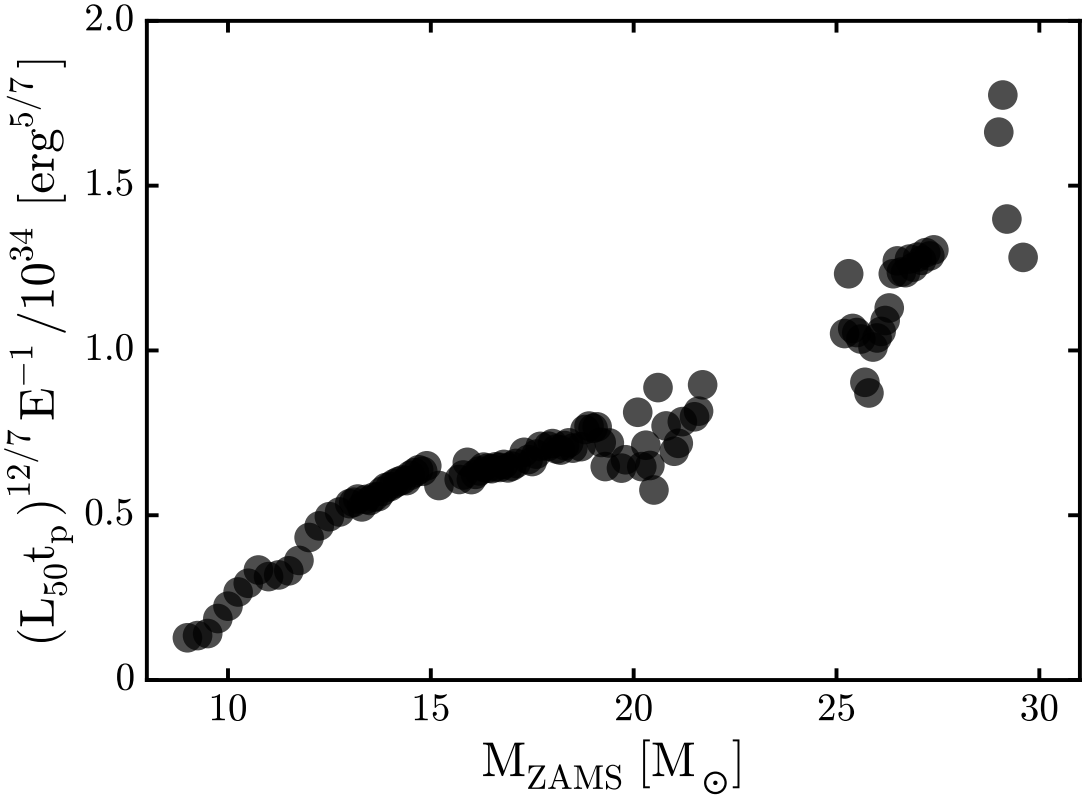

Figure 3.34: The quantity $(L_{50}t_p)^{12/7}E^{-1}$ is plotted against the ZAMS mass of the progenitor shown for all exploded models of Z9.6 and N20 engines. This correlation allows an approximate determination of the progenitor mass given measurements of plateau luminosity and duration along with an explosion energy estimated from Fig. 3.33.

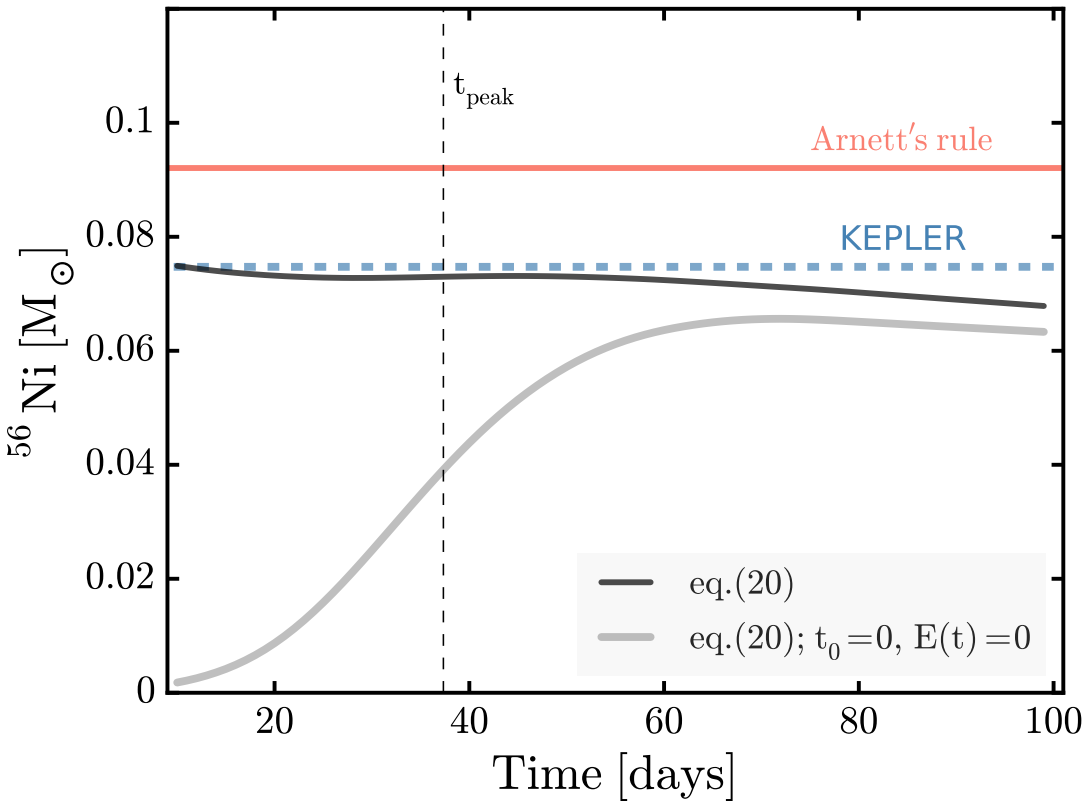

Figure 3.35: Estimates of the ^{56}Ni mass for the 80 $M_\odot$ progenitor exploded using the N20 engine. The KEPLER calculation synthesized 0.074 $M_\odot$ of ^{56}Ni. The energy conservation argument described in eq. (3.19) closely agrees with this value until late times when the leakage of gamma rays becomes significant. The special case of this argument presented in Katz *et al.* (2013) for type Ia light curves, underestimates the nickel mass, but works better than the Arnett's rule.

Chapter 4

The Most Luminous Supernovae

4.1 Introduction

In this chapter we shift gears and explore the limiting cases of peak luminosity and radiated energy, considering several scenarios often invoked for their interpretation. This work was largely motivated by the recent observations that revealed a stunning diversity of extremely luminous supernovae, seemingly increasing in radiant energy without bound. This includes the recently discovered ultra-luminous supernova (ULSN) ASSASN-15lh (SN2015L) (Dong *et al.*, 2016), though its interpretation still remain controversia (Brown *et al.*, 2016).

We consider scenarios powered by colliding shells, pair-instability supernovae, and newly-born magnetars (e.g. Gal-Yam, 2012; Quimby *et al.*, 2011). Each of these energy sources will give different results when occurring in a stripped core of helium or carbon and oxygen (Type I) or a supergiant (Type II), and both cases are considered. All calculations of explosions and light curves use `KEPLER`, and employ presupernova models that have been published

previously (presented in chapter 4).

The more extreme case of "relativistic supernovae" - either supernovae with relativistic jets or the explosion of super-massive stars that collapse because of general relativistic instability (Fuller *et al.*, 1986; Chen *et al.*, 2014) is not considered here. These are rare events with their own distinguishing characteristics.

4.2 Prompt Explosions and Pair-Instability

Any explosive energy that deposits before the ejecta significantly expands will suffer severe adiabatic degradation that will prevent the supernova from being particularly bright. An upper bound for prompt energy deposition in a purely neutrino-powered explosion is $\sim 2-3\times10^{51}$ erg (Fryer and Kalogera, 2001; Ugliano *et al.*, 2012; Pejcha and Thompson, 2015; Ertl *et al.*, 2016), which is capable of explaining common supernovae (Sukhbold *et al.*, 2016), but not the more luminous ones. In a red, or worse, blue supergiant, the expansion from an initial stellar radius of, at most, 10^{14} cm, to a few times 10^{15} cm, where recombination occurs, degrades the total electromagnetic energy available to $\lesssim 10^{50}$ erg. Even in the most extreme hypothetical case, where a substantial fraction of a neutron star binding energy, $\sim 10^{53}$ erg, deposits instantly, the light curve is limited to a peak brightness of approximately 10^{44} erg s^{-1} (neglecting the very brief phase of shock break out).

This can be demonstrated analytically and numerically. Adopting the expression for plateau luminosity and duration from Popov (1993) and Kasen and Woosley (2009), as calibrated to numerical models by Sukhbold *et al.* (2016), Type II supernovae have a luminosity on

their plateaus of

$$L_p = 8.5 \times 10^{43}\ R_{0,500}^{2/3} M_{env,10}^{-1/2} E_{53}^{5/6}\ \mathrm{erg\ s^{-1}}, \tag{4.1}$$

where $R_{0,500}$ is the progenitor radius in 500 $R_\odot$, $M_{env,10}$ is the envelope mass in 10 $M_\odot$, and $E_{53} \lesssim 1$ is the prompt explosion energy in units of 10^{53} erg. The approximate duration of the plateau, ignoring the effects of radioactivity, is given by

$$\tau_p = 41\ E_{53}^{-1/6} M_{10}^{1/2} R_{0,500}^{1/6}\ \mathrm{days}. \tag{4.2}$$

This plateau duration is significantly shorter than common supernovae due to the much higher energies considered.

These relations compare favorably with a model for a 15 $M_\odot$ explosion calculated with an assumed explosion energy of 0.5×10^{53} erg (Fig. 4.1). Here the red supergiant pre-supernova stellar model from Woosley *et al.* (2007) had a radius of 830 $R_\odot$ and an envelope mass, 8.5 $M_\odot$. The estimated luminosity on the plateau from eq. (4.1) is 6.7×10^{43} erg s^{-1} and duration from eq. (4.2) is 46 days. The corresponding KEPLER model in Fig. 4.1 had a duration of ~ 45 days and a luminosity at day 25 of 6.6×10^{43} erg s^{-1}. The total energy emitted is approximately $L_p \tau_p$, or $3 \times 10^{50} E_{53}^{2/3} R_{0,500}^{5/6}$ erg.

Similar limits apply to pair-instability supernovae (PISN) in red supergiant progenitors. Again, maximum explosion energies are $\lesssim 10^{53}$ erg (Heger and Woosley, 2002). For the most extreme, rarest case, $M_{10} \approx 20$, $R_{0,500} \approx 5$ and $E_{53} \approx 1$, eq. (4.1) and eq. (4.2) imply plateau luminosities near 5×10^{43} erg s^{-1} for about 200 days. These values are consistent with

the KEPLER models given in Scannapieco *et al.* (2005). The total radiated energy is 1×10^{51} erg. Most of the radioactivity decays during the plateau. Since the decay energy is substantially less than the explosion energy, the modification of the light curve during its bright plateau is not appreciable.

We conclude that ULSN must be energized by a power source that deposits its energy well after the original explosion. The known delayed energy sources are radioactivity, colliding winds, and pulsars.

4.3 Radioactivity

The most prolific sources of ^{56}Ni are PISN. The rarest, most massive PISN produces, at most, 50 $M_\odot$ of ^{56}Ni in an explosion with a final kinetic energy of 9×10^{52} erg (Heger and Woosley, 2002). This large production only occurs for the the most massive helium cores ($\sim$130 $M_\odot$), which very nearly collapse to black holes. The total energy available from the decay of large amount of ^{56}Ni is substantial,

$$E_{dec} \approx 2.4 \times 10^{51} \left(\frac{M_{Ni}}{50 M_\odot} \right) (3e^{-t/\tau_{Co}} + e^{-t/\tau_{Ni}}) \text{ erg}, \tag{4.3}$$

where M_{Ni} is the ^{56}Ni mass in $M_\odot$, and τ_{Co} = 111 d and τ_{Ni} = 8.7 d are mean lives of ^{56}Co and ^{56}Ni. For a nickel mass of $\sim$50 $M_\odot$ the total energy is nearly 10^{52} erg. Most of this energy is lost during the adiabatic expansion to peak, however.

For a star that has lost its hydrogen envelope, an approximate estimate when the PISN light curve peaks is given by equating the effective diffusion timescale, t_d, to age. This gives a

time of peak luminosity, t_p, of

$$\begin{aligned} t_p &= \left(\frac{3\kappa}{4\pi c}\right)^{1/2} \left(\frac{M_{ej}^3}{2E_{exp}}\right)^{1/4} \\ &\sim 177 \left(\frac{M_{ej}}{130 M_\odot}\right)^{3/4} \left(\frac{E_{exp}}{10^{53}\text{erg}}\right)^{-1/4} \text{ days,} \end{aligned} \tag{4.4}$$

where M_{ej} is the ejecta mass in $M_\odot$ and E_{exp} is the explosion energy in erg. Considering the similarity of high velocity and iron-rich composition to Type Ia supernovae, an opacity $\kappa \approx 0.1$ cm^2 g^{-1} is assumed. Arnett's Rule (Arnett, 1979) then implies a maximum luminosity of

$$L_p \approx 8 \times 10^{44} \left(\frac{M_{Ni}}{50 M_\odot}\right) e^{-t_p/\tau_{Co}} \text{ erg s}^{-1}. \tag{4.5}$$

Only the luminosity due to the decay of ^{56}Co is included here, since for $t \sim t_p$, most of ^{56}Ni will have already decayed. For the fiducial values of t_p and M_{Ni}, the peak luminosity is then roughly 1.5×10^{44} erg s^{-1}, which compares favourably with models in which the hydrodynamics and radiation transport are treated carefully (Kasen *et al.*, 2011; Kozyreva and Blinnikov, 2015) and with the analytic models of (Chatzopoulos *et al.*, 2013).

Assuming that the total emitted energy by a Type I supernova is

$$E_{rad} \approx \frac{1}{2} L_p t_p + E_{dec}(t_p), \tag{4.6}$$

and using the fiducial values, the approximate upper bound on the total luminous energy in a PISN-Type I is 2.6×10^{51} erg, about one quarter of the total decay energy.

4.4 Colliding Shells

4.4.1 Generic Models

Observations show that a substantial fraction of ULSN, especially those of Type IIn, are brightened by circumstellar interaction (e.g. Kiewe *et al.*, 2012). In some cases this interaction can be extremely luminous (Smith *et al.*, 2010, 2011a). The necessary mass loss is often attributed to prior outbursts of the star as a luminous blue variable (LBV; e.g. Smith *et al.*, 2011b) or a pulsational-pair-instability supernova (PPISN, Woosley *et al.*, 2007), though other possibilities, e.g. common envelope (Chevalier, 2012), are sometimes invoked.

The luminosity of colliding shells is limited by their differential speeds, their masses, and the radii at which they collide. If the collision happens at too small a radius where the ejecta is still very optically thick, colliding shells become another variant of "prompt explosions" (§ 4.2). On the other hand, if the collision happens at too large a radius, the resulting transient has a longer time scale, lower luminosity, and may not emit chiefly in the optical (Chevalier and Irwin, 2012). In practice, these constraints limit the radius where the shells collide and produce a bright optical transient to roughly 10^{15} - 10^{16} cm. A similar range of radii is obtained by multiplying typical collision speeds, $\sim 5{,}000$ km s^{-1}, by the duration of an ULSN, ~ 100 days.

Chevalier and Irwin (2012) give a maximal "cooling luminosity" for colliding shells in which most of the dissipated energy goes into light (see also Smith *et al.*, 2010, eq. 1),

$$L \lesssim 2\pi r^2 \rho v_{shock}^3 = 0.5 \frac{\dot{M}}{v_{wind}} v_{shock}^3 \tag{4.7}$$

where $\dot{M}$ is the pre-explosive mass loss rate with speed v_{wind}, and v_{shock} is the shock speed of the explosive ejecta impacting that "wind". Narrow lines in the spectra of Type IIn supernovae, including some very luminous ones (Kiewe *et al.*, 2012), imply pre-explosion wind speeds of a few hundred to 1000 km s^{-1}. At those speeds, and given that the light curve is generated at $r \sim 10^{15} - 10^{16}$ cm, the relevant time for the mass loss is a few years before the final explosion. The velocity of the shock is $v_{shock} \approx \sqrt{2E/M}$, where E is the explosion energy of mass M. Here we normalize it to 10^9 cm s^{-1} as in Chevalier and Irwin (2012), though it implies a very energetic explosion. The luminosity from the collision is then

$$L \approx 3.1 \times 10^{44} \frac{\dot{M}_{-1}}{v_{wind,7}} v^3_{shock,9} \text{ erg s}^{-1}, \tag{4.8}$$

where $\dot{M}_{-1}$ is the mass loss rate a few years before the explosion normalized to 0.1 $M_\odot$ per year, $v_{wind,7}$ is in 10^2 km s^{-1} and $v_{shock,9}$ is in units of 10^4 km s^{-1}. Typical values for the outbursts that produce very bright bright Type IIn supernovae are $\dot{M}_{-1} = 1$, $v_{wind,7} = 1$ to 10, and $v_{shock,9} = 0.5$ (Kiewe *et al.*, 2012) implying peak luminosities near 5×10^{43} erg s^{-1}. The large ejection in η-Carina in the 1840's ejected 12 $M_\odot$ moving at $v_{wind,7}$ up to 6.5 (Smith, 2008).

It is the mass of the shell into which a supernova of given energy plows that matters most (van Marle *et al.*, 2010). We are unaware of any models other than PPISN (§ 4.4.2 or 10 $M_\odot$ stars (Woosley and Heger, 2015b) that eject solar masses of material just years before dying. If a generous upper limit of 10 $M_\odot$ between 10^{15} and 10^{16} cm ($M_{10} = 1$) is adopted, $\dot{M}_{-1}/v_{wind,7}$ is $\lesssim 3 M_{10} R_{16}^{-1}$ where R_{16} is the outer edge of the interaction region in 10^{16} cm units. For a shock speed $v_{shock,9} = 0.5$ and an event duration of 100 days, $R_{16} \sim 0.5$. The

maximum luminosity is then $10^{45} v_{shock,9}^{3} M_{10} R_{16}^{-1}$ erg s^{-1} $\approx 3 \times 10^{44}$ erg s^{-1}. More generally the maximum luminosity is L = $10^{45} \tau_{SN,100}^{-1} M_{10} v_{shock,9}^{2}$ erg s^{-1} where $\tau_{SN,100}$ is the duration of the brightest part of the light curve. This limit is sufficient to accommodate all ULSN that maybe powered by collisions and is consistent with the theoretical results of van Marle *et al.* (2010).

It might be possible to raise this limit by invoking slightly greater shock speeds or shell masses. The former requires extremely energetic supernovae though. Accelerating a shell of 10 $M_{\odot}$ to 10^{9} cm s^{-1} requires an explosion energy of at least 10^{52} erg and 100% conversion efficiency. This is considerably more than neutrinos can provide and already indicates a source that is, at heart, rotationally powered. Yet it may be that having high mass loss rates removes sufficient angular momentum to inhibit the formation of rapidly rotating iron cores. Even energetic PISN do not develop speeds of 10,000 km s^{-1} in a significant part of their mass. Moreover, PISN are burning carbon radiatively in their centers the last few years of their life and, except for PPISN (§ 4.4.2), experience no obvious instability that would lead to the impulsive ejection of 10 $M_{\odot}$.

With considerable uncertainty, we thus adopt an upper limit for colliding shells of 3×10^{44} erg s^{-1} and a total radiated energy of $\tau_{SN} L \sim 3 \times 10^{51}$ erg. For bare helium cores which are not PPISN and clearly not LBVs, the values are likely to be much smaller because of the smaller shell masses, but existing models, do not allow a specific estimate.

4.4.2 Pulsational-pair instability supernovae

The most luminous colliding shell models with definite predictions for their luminosity are PPISN (Woosley *et al.*, 2007; Yoshida *et al.*, 2016). For a narrow range of masses

corresponding to stars with 50 - 55 $M_\odot$ helium cores, a supergiant star, red or blue, will eject its hydrogen envelope at speeds $\sim$ 1000 km s^{-1}, and a year or so later eject one or more very energetic shells that smash into it (Woosley and Heger, 2015a). The source of the energy is the thermonuclear burning of carbon and oxygen. For lighter helium cores, low energy shells are ejected in rapid succession before the envelope has expanded to 10^{15} cm. The collision energy is adiabatically degraded and the resulting supernova is not especially luminous (Woosley 2016, in prep.). For heavier cores, the pulses are too infrequent and produce collisions outside of 10^{16} cm that last much longer than one hundred days.

In the narrow helium-core mass range of 50 - 55 $M_\odot$ though, one or more pulses occurring a year or so after the one that ejects the envelope, eject additional shells carrying a energy of up to 1×10^{51} erg (Woosley and Heger, 2015a). Radiating all this energy over a 10^7 s interval gives a luminosity that can approach 10^{44} erg s^{-1} (Woosley *et al.*, 2007).

For helium cores lacking any hydrogen envelope the luminosities are less because of the lack of a massive low velocity reservoir to turn kinetic energy into light. Typical peak luminosities for Type I PPISN are thus near 3×10^{43} erg s^{-1}, and the light curve can be more highly structured (Woosley and Heger, 2015a).

4.5 Magnetars

With some tuning, the energy deposited by a young magnetar in the ejecta of a supernova can significantly brighten its light curve (Maeda *et al.*, 2007; Woosley, 2010; Kasen and Bildsten, 2010). The model has been successfully applied to numerous observations of Type Ic

ULSN (e.g. Inserra *et al.*, 2013; Nicholl *et al.*, 2013; Howell *et al.*, 2013) and magnetars seem a natural consequence of collapse of rapidly rotating cores (e.g. Mösta *et al.*, 2015).

The rotational kinetic energy of a magnetar with a period $P_{ms} = P/ms$ is approximately $E_m \approx 2 \times 10^{52} P_{ms}^{-2}$ erg, where $E_{m,max} \approx 4$ times10^{52} erg is the rotational energy for an initial period of $\sim$0.7 ms. Usually this period is restricted to $>$ 1ms, because of rotational instabilities that lead to copious gravitational radiation. However, Metzger *et al.* (2015) have recently discussed the possibility that the limiting rotational kinetic energy could exceed 10^{53} erg, depending on the neutron star mass and the equation of state and here we adopt that value as an upper bound. This energy reservoir can be tapped through vacuum dipole emission, which is approximately $E_m/t_m \approx 10^{49} B_{15}^2 P_{ms}^{-4}$ erg s^{-1}, where $B_{15} = B/10^{15}$ G is the dipole field strength at the equator, and $t_m = 2 \times 10^3 P_{ms}^2 B_{15}^{-2}$ s is the magnetar spin-down timescale. A magnetic dipole moment B(10km)^3 is adopted, and an angle of $\pi/6$ between the magnetic and rotational axes has been assumed. Combining these relations, one obtains the temporal evolution of the rotational energy and magnetar luminosity as $E_m(t) = E_{m,0} t_m/(t_m + t)$ and $L_m(t) = E_{m,0} t_m/(t_m + t)^2$.

The peak luminosity can be estimated using the diffusion equation and ignoring the radiative losses in the first law of thermodynamics (Kasen and Bildsten, 2010):

$$L_p = \frac{E_{m,0}}{t_d} \left[\xi \ln\left(1 + \frac{1}{\xi}\right) - \frac{\xi}{1+\xi} \right], \tag{4.9}$$

where $\xi = t_m/t_d$ is the ratio of spin-down to effective diffusion timescales. The term inside square brackets has a maximum at $\xi \approx 1/2$, obtained by solving $d(L_p t_d/E_{m,0})/d\xi = 0$. This implies an optimal field strength for maximizing the peak luminosity is:

$$B_{15}\Big|_{L_{p,max}} \simeq 66 P_{ms,0} t_d^{-1/2}. \tag{4.10}$$

That is, for a given combination of $P_{ms,0}$ and ejecta parameters - M_{ej}, E_{sn}, κ, the brightest possible peak luminosity is obtained for this field strength.

The maximum peak luminosity is then $L_{p,max} \simeq E_m/10t_m$. For the limiting initial spin of $P_{ms,0} = 0.7$ms the corresponding field strength is $B \approx 4 \times 10^{13}$ G (for $\kappa = 0.1$ cm^2 g^{-1}, $M_{ej} = 3.5$ $M_\odot$ and $E_{SN} = 1.2 \times 10^{51}$ erg), and the limiting peak luminosity is $L_{p,max} \approx 2 \times 10^{46}$ erg s^{-1}. Here $E_m \gg E_{SN}$, therefore unless one invokes even lower κ, M_{ej} and much larger E_m, any transient with brighter observed luminosity will be hard to explain by the magnetar model (Fig. 4.2).

Using a version of Arnett's Rule (Inserra *et al.*, 2013, e.g.), $L_m(t_p) = L_p$, the time for L_p is $t_p = (E_m t_m L_p^{-1})^{1/2} - t_m$. For the maximal luminosity, the corresponding peak time is then $t_{p,max} \simeq 2.2 t_m$. This can be used to estimate the limiting radiated energy in the same way as in eq. (4.6) to find that:

$$E_{rad,max} \simeq 0.4 E_{m,0}. \tag{4.11}$$

Any observation with a total radiated energy of $E_{rad} > 4 \times 10^{52}$ erg will be nearly impossible to explain by the magnetar model. A more conventional value and one that fits ASASSN-151h (Fig. 4.2), is 2×10^{52} erg. This is within a factor of two of the limiting magnetar kinetic energy inferred for gamma-ray bursts by Mazzali *et al.* (2014).

To illustrate these limits, a series of magnetar-powered models based upon exploding

CO cores (from Sukhbold and Woosley, 2014) was calculated to find a best fit to the light curve of ASASSN-15lh. In each case, soon after bounce, the magnetar deposited its energy in the inner ejecta at a rate given by the vacuum dipole spin-down rate. The top panel of Fig. 4.2 shows the best fitting model, which employs a magnetar with an initial period of 0.7 ms and magnetic field strength of 2×10^{13} G, illuminating the ejecta in the explosion of a 14 $M_\odot$ CO core ($M_{ej} \approx 11.2 M_\odot$).

These magnetar parameters agree well with the previously published fits, but the ejecta masses are different. An ejecta mass of 15 $M_\odot$ was obtained by Dai *et al.* (2016), as they used simple semi-analytical models, which ignored all dynamical effects and deviate from hydrodynamic calculations most when $E_m \gg E_{sn}$. An ejecta mass of only 3 $M_\odot$ was used in Metzger *et al.* (2015), as they applied the same simple semi-analytical model for the early release of the data spanning only ∼60 days. That fit would not work for the later data shown in Fig. 4.2, and the ejecta would become optically thin at an early time. Bersten *et al.* (2016) limited their models to small He-cores (8 $M_\odot$), and their model does not fit the broad peak of ASASSN-15lh well.

Also shown in the top panel is the light curve from the limiting case of a magnetar with $P_{ms} = 0.7$, $B = 4 \times 10^{13}$ G powering only 3.5 $M_\odot$ ejecta (from $5 M_\odot$ CO core). This model reaches $\sim 7 \times 10^{45}$ erg s^{-1}, but the peak is much narrower and it becomes optically thin within a month.

Magnetars can also illuminate bright, long lasting Type II supernovae. The bottom panel of Fig. 4.2, shows the same magnetar that was applied for the fit to ASASSN-15lh, now embedded inside the remnant of a 15 $M_\odot$ red supergiant progenitor. Because the ejecta mass

is much larger, the light curve is fainter and much broader. The ejecta stays optically thick for nearly 4 months. Much as radioactive decay extends the plateau duration by causing ionization, magnetar-deposited energy also significantly extends the optically thick period.

4.6 Summary and Conclusions

Table 4.1 summarizes the maximum luminosity and total luminous energy for the models considered. Given the various approximations made, the numbers are probably accurate to a factor of two in most cases except for shell "collisions" where definitive models are lacking (§ 4.4.1). In all but the magnetar-powered models, the peak luminosities are a few times 10^{44} erg s^{-1} and peak integrated powers are near 10^{51} erg. This is gratifying since most "superluminous supernovae" are within those bounds (e.g. Nicholl *et al.*, 2015).

For point-like explosions, which includes PISN of Type II, the prompt energy injection is typically degraded by a factor of ~ 100 by adiabatic expansion, so even obtaining 10^{51} erg of light requires an explosion that strains the limits of both neutron star binding energy (core-collapse supernovae) and thermonuclear energy (PISN). The upper bound for PISN-Type I is also well determined by both analytic scaling rues and numerical models.

For supernovae whose light comes from colliding shells, the constraints are less accurate due to lack of knowledge about the masses of the shells involved and the supernova explosion energies in cases where large impulsive mass loss occurs just before the star dies. The limit in the table assumes shock speeds less than 5000 km s^{-1} and shell masses less than 10 $M_\odot$. Estimates for PPISN are more precise because the mass of the helium core needed to

make luminous optical supernovae is highly constrained. In order that the duration of the pulses be years and not months or centuries, the helium core mass need to be in the range 50 - 55 $M_{\odot}$ and that restricts the energy of the secondary pulses and supernova.

Magnetars are a special case. The limits come from using a simple dipole formula in a situation where it has not been observationally tested and assuming what some would regard as a high limiting rotational energy for neutron stars. Rotation can tap an energy reservoir almost as great as the binding energy of the neutron star and deposit it over an arbitrarily long time scale - depending on the choice of magnetic field strength. Thus the optical efficiency for converting rotational energy to light can be (forced to be) very high.

It is interesting though that the upper bounds for magnetar-powered light curves are so high. This implies a possible observable diagnostic. Supernovae that substantially exceed 3×10^{44} erg s^{-1} for an extended period and which have total luminous powers far above 3×10^{51} erg should be considered strong candidates for containing an embedded magnetar. Similarly, "supernovae" that exceed the generous limits for magnetar power given in Table 4.1 may not be supernovae at all.

ASASSN-15lh (Dong *et al.*, 2016) is an interesting case in this regard. Fig. 4.2 shows that it can, barely, be accommodated by a magnetar model and Table 4.1 says it must be a magnetar, if it is a supernova. At the time of writing of this thesis, new data have been published on this object revealing the late time rebrightening in UV (Brown *et al.*, 2016), which casts more confusion to the origin of this fascinating event. This implies that simple magnetar powering of the ejecta is not sufficient to fully explain the light curve, instead one would need to invoke late time ionization break out as suggested by Metzger *et al.* (2014), or invoke a hybrid scenario

involving collision of shells along with magnetar injection (Chatzopoulos *et al.*, 2016).

Table 4.1: Limiting Peak Luminosities and Radiated Energies

	model	L_p [erg s^{-1}]	E_{rad} [erg]
Type II	prompt	1×10^{44}	3×10^{50}
	PISN	5×10^{43}	1×10^{51}
	collisions	3×10^{44}	3×10^{51}
	PPISN	1×10^{44}	1×10^{51}
	magnetar	1×10^{45}	9×10^{51}
Type I	PISN	2×10^{44}	3×10^{51}
	PPISN	3×10^{43}	1×10^{51}
	magnetar	2×10^{46}	4×10^{52}

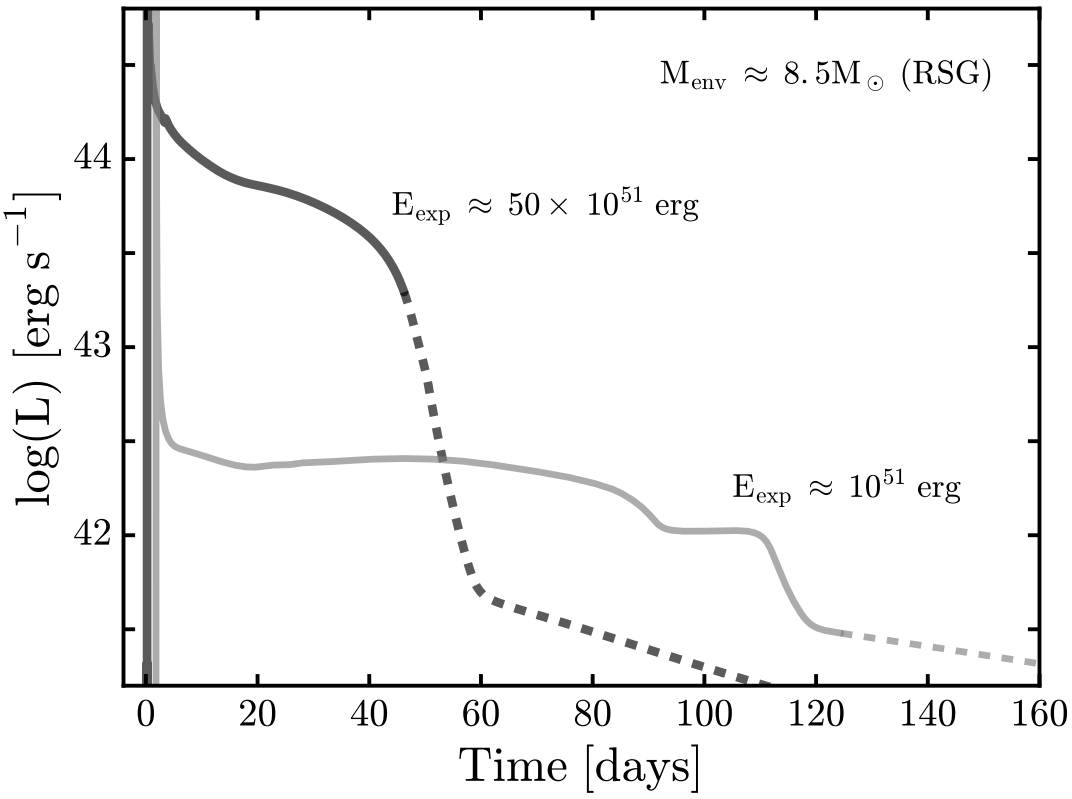

Figure 4.1: Bolometric light curves for a 15 $M_\odot$ supergiant exploded with two different values of prompt energy deposition. One with $E_{exp} = 10^{51}$ erg, is typical of common Type IIp supernovae; the other with $E_{exp} = 50 \times 10^{51}$ erg is near the upper bound of what any prompt, point explosion might provide. Even for this extreme case, the plateau luminosity does not exceed $\sim 10^{44}$ erg s^{-1}. The curves are dashed when the ejecta become optically thin and the blackbody representation of their emission becomes questionable. The presupernova star, originally 15 $M_\odot$ at birth, had a mass of 12.6 $M_\odot$, of which 8.5 $M_\odot$ was in the hydrogen envelope, and a radius of $R_{0,500} \sim 1.7$. The luminosity at shock break out in the more energetic model peaked at 1.5×10^{47} erg s^{-1}, but only lasted for about 100 seconds.

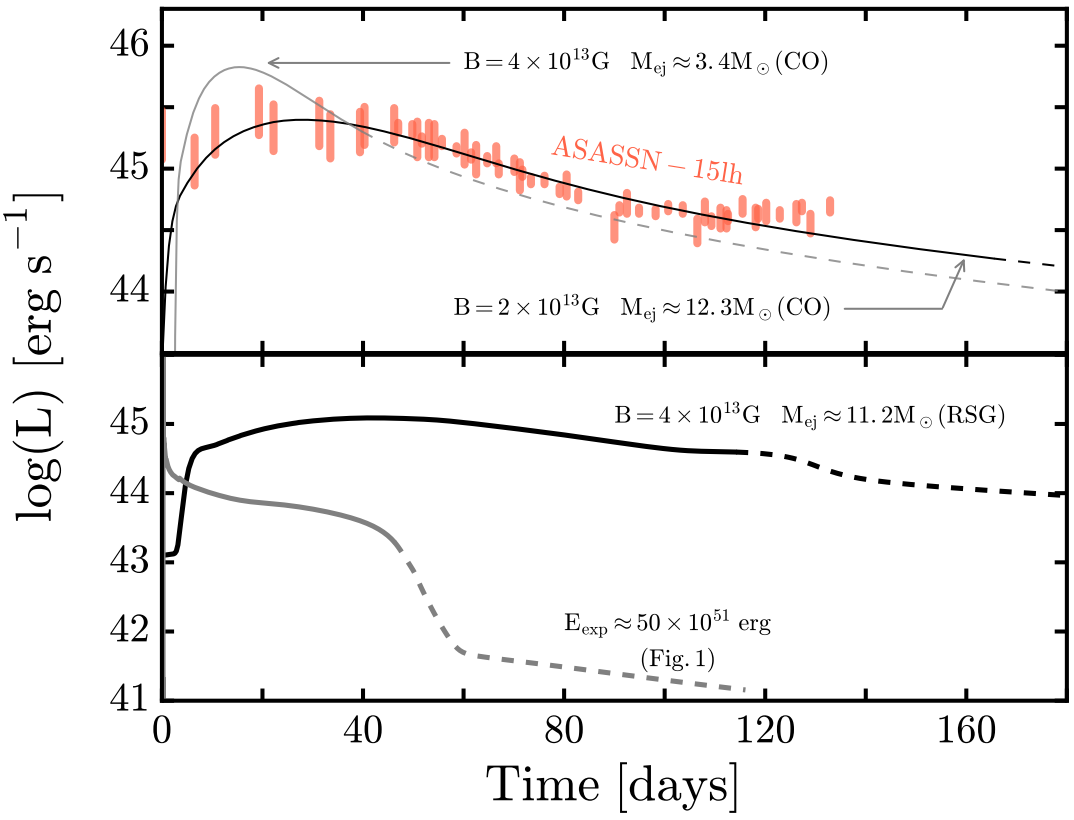

Figure 4.2: Top: The luminous transient ASASSN-15lh compared with a magnetar model in which the initial rotational energy was 5×10^{52} erg. Similar magnetars embedded in a less ejecta will give slightly brighter light curves. Bottom: The same magnetar used in the top panel for fitting ASASSN-15lh is embedded in the ejecta of a massive red supergiant progenitor. The light curve is dimmer than the Type I case, but substantially brighter than the prompt explosion case shown in Fig. 4.1. The dashed curve marks the transition to nebular phase.

Bibliography

Arcones, A.; Janka, H.-T. and Scheck, L. Nucleosynthesis-relevant conditions in neutrino-driven supernova outflows. I. Spherically symmetric hydrodynamic simulations. A&A **467**, 1227 (2007).

Arnett, W. D. On the theory of Type I supernovae. ApJ **230**, L37 (1979).

Arnett, W. D. Type I supernovae. I - Analytic solutions for the early part of the light curve. ApJ **253**, 785 (1982).

Arnett, W. D.; Bahcall, J. N.; Kirshner, R. P. and Woosley, S. E. Supernova 1987A. ARA&A **27**, 629 (1989).

Barkat, Z. Late stages of stellar evolution. In Bludman, S. A.; Mochkovitch, R. and Zinn-Justin, J., eds., *Supernovae* (1994), p. 31.

Bennett, M. E.; Hirschi, R.; Pignatari, M.; Diehl, S.; Fryer, C.; Herwig, F.; Hungerford, A.; Nomoto, K.; Rockefeller, G.; Timmes, F. X. and Wiescher, M. The effect of ^{12}C +^{12}C rate uncertainties on the evolution and nucleosynthesis of massive stars. MNRAS **420**, 3047 (2012).

Bersten, M. C.; Benvenuto, O. G.; Orellana, M. and Nomoto, K. The Unusual Super-luminous Supernovae SN 2011kl and ASASSN-15lh. ApJ **817**, L8 (2016).

Biello, J. A. *Layer formation in semiconvection*. Ph.D. thesis, THE UNIVERSITY OF CHICAGO (2001).

Bouchet, P.; Phillips, M. M.; Suntzeff, N. B.; Gouiffes, C.; Hanuschik, R. W. and Wooden, D. H. The Bolometric Lightcurve of Supernova 1987A - Part Two - Results from Visible and Infrared Spectrophotometry. A&A **245**, 490 (1991).

Brown, J. M. and Woosley, S. E. Nucleosynthetic Constraints on the Mass of the Heaviest Supernovae. ApJ **769**, 99 (2013).

Brown, P. J.; Yang, Y.; Cooke, J.; Olaes, M.; Quimby, R. M.; Baade, D.; Gehrels, N.; Hoeflich, P.; Maund, J.; Mould, J.; Patat, F.; Wang, L. and Wheeler, J. C. ASASSN-15lh: A Superluminous Ultraviolet Rebrightening Observed by Swift and Hubble. *ArXiv e-prints* (2016).

Buchmann, L. New Stellar Reaction Rate for 12C(alpha , gamma) 16O. ApJ **468**, L127 (1996).

Buchmann, L. Errata to New Stellar Reaction Rate for 12C(alpha , gamma) 16O. ApJ **479**, L153 (1997).

Burbidge, E. M.; Burbidge, G. R.; Fowler, W. A. and Hoyle, F. Synthesis of the Elements in Stars. *Reviews of Modern Physics* **29**, 547 (1957).

Burrows, A. Colloquium: Perspectives on core-collapse supernova theory. *Reviews of Modern Physics* **85**, 245 (2013).

Burrows, A. and Lattimer, J. M. Neutrinos from SN 1987A. ApJ **318**, L63 (1987).

Cayrel, R.; Depagne, E.; Spite, M.; Hill, V.; Spite, F.; François, P.; Plez, B.; Beers, T.; Primas, F.; Andersen, J.; Barbuy, B.; Bonifacio, P.; Molaro, P. and Nordström, B. First stars V - Abundance patterns from C to Zn and supernova yields in the early Galaxy. A&A **416**, 1117 (2004).

Chabrier, G. Galactic Stellar and Substellar Initial Mass Function. PASP **115**, 763 (2003).

Chatzopoulos, E.; Wheeler, J. C.; Vinko, J.; Horvath, Z. L. and Nagy, A. Analytical Light Curve Models of Superluminous Supernovae: χ^2-minimization of Parameter Fits. ApJ **773**, 76 (2013).

Chatzopoulos, E.; Wheeler, J. C.; Vinko, J.; Nagy, A. P.; Wiggins, B. K. and Even, W. P. Extreme Supernova Models for the Superluminous Transient ASASSN-15lh. *ArXiv e-prints* (2016).

Chen, K.-J.; Heger, A.; Woosley, S.; Almgren, A.; Whalen, D. J. and Johnson, J. L. The General Relativistic Instability Supernova of a Supermassive Population III Star. ApJ **790**, 162 (2014).

Chen, K.-J.; Woosley, S. E. and Sukhbold, T. Magnetar-Powered Supernovae in Two Dimensions. I. Superluminous Supernovae. *ArXiv e-prints* (2016).

Chevalier, R. A. Common Envelope Evolution Leading to Supernovae with Dense Interaction. ApJ **752**, L2 (2012).

Chevalier, R. A. and Irwin, C. M. X-Rays from Supernova Shocks in Dense Mass Loss. ApJ **747**, L17 (2012).

Chieffi, A. and Limongi, M. Pre-supernova Evolution of Rotating Solar Metallicity Stars in the Mass Range 13-120 M $_{Ł}$ and their Explosive Yields. ApJ **764**, 21 (2013).

Chugai, N. N. and Utrobin, V. P. Does the energy of type IIP supernovae depend on the stellar mass? *Astronomy Letters* **40**, 291 (2014).

Cooperstein, J.; Bethe, H. A. and Brown, G. E. Shock propagation in supernovae: Concept of net ram pressure. *Nuclear Physics A* **429**, 527 (1984).

Costa, V.; Pumo, M. L.; Bonanno, A. and Zappalà, R. A. The s-process weak component: uncertainties due to convective overshooting. A&A **447**, 641 (2006).

Couch, S. M. On the Impact of Three Dimensions in Simulations of Neutrino-driven Core-collapse Supernova Explosions. ApJ **775**, 35 (2013).

Crowther, P. A.; Lennon, D. J. and Walborn, N. R. Physical parameters and wind properties of galactic early B supergiants. A&A **446**, 279 (2006).

Dai, Z. G.; Wang, S. Q.; Wang, J. S.; Wang, L. J. and Yu, Y. W. The Most Luminous Supernova ASASSN-15lh: Signature of a Newborn Rapidly Rotating Strange Quark Star. ApJ **817**, 132 (2016).

Dessart, L.; Hillier, D. J.; Li, C. and Woosley, S. On the nature of supernovae Ib and Ic. MNRAS **424**, 2139 (2012).

Dessart, L.; Hillier, D. J.; Livne, E.; Yoon, S.-C.; Woosley, S.; Waldman, R. and Langer, N. Core-collapse explosions of Wolf-Rayet stars and the connection to Type IIb/Ib/Ic supernovae. MNRAS **414**, 2985 (2011).

Dessart, L.; Hillier, D. J.; Woosley, S.; Livne, E.; Waldman, R.; Yoon, S.-C. and Langer, N. Radiative-transfer models for supernovae IIb/Ib/Ic from binary-star progenitors. MNRAS **453**, 2189 (2015).

Dong, S.; Shappee, B. J.; Prieto, J. L.; Jha, S. W.; Stanek, K. Z.; Holoien, T. W.-S.; Kochanek, C. S.; Thompson, T. A.; Morrell, N.; Thompson, I. B.; Basu, U.; Beacom, J. F.; Bersier, D.; Brimacombe, J.; Brown, J. S.; Bufano, F.; Chen, P.; Conseil, E.; Danilet, A. B.; Falco, E.; Grupe, D.; Kiyota, S.; Masi, G.; Nicholls, B.; Olivares E., F.; Pignata, G.; Pojmanski, G.; Simonian, G. V.; Szczygiel, D. M. and Woźniak, P. R. ASASSN-15lh: A highly superluminous supernova. *Science* **351**, 257 (2016).

Eastman, R. G.; Schmidt, B. P. and Kirshner, R. The Atmospheres of Type II Supernovae and the Expanding Photosphere Method. ApJ **466**, 911 (1996).

El Eid, M. F.; Meyer, B. S. and The, L.-S. Evolution of Massive Stars Up to the End of Central Oxygen Burning. ApJ **611**, 452 (2004).

Eldridge, J. J.; Fraser, M.; Smartt, S. J.; Maund, J. R. and Crockett, R. M. The death of massive stars - II. Observational constraints on the progenitors of Type Ibc supernovae. MNRAS **436**, 774 (2013).

Ensman, L. M. and Woosley, S. E. Explosions in Wolf-Rayet stars and Type Ib supernovae. I - Light curves. ApJ **333**, 754 (1988).

Ertl, T.; Janka, H.-T.; Woosley, S. E.; Sukhbold, T. and Ugliano, M. A Two-parameter Criterion for Classifying the Explodability of Massive Stars by the Neutrino-driven Mechanism. ApJ **818**, 124 (2016).

Faulkner, J. Low-Mass Red Giants as Binary Stars without Angular Momentum. In Podsiadlowski, P.; Rappaport, S.; King, A. R.; D'Antona, F. and Burderi, L., eds., *Evolution of Binary and Multiple Star Systems* (2001), vol. 229 of *Astronomical Society of the Pacific Conference Series*, p. 3.

Faulkner, J. *Red giants: then and now*, pp. 149–226 (2005).

Fischer, T.; Whitehouse, S. C.; Mezzacappa, A.; Thielemann, F.-K. and Liebendörfer, M. Protoneutron star evolution and the neutrino-driven wind in general relativistic neutrino radiation hydrodynamics simulations. A&A **517**, A80 (2010).

Foglizzo, T.; Kazeroni, R.; Guilet, J.; Masset, F.; González, M.; Krueger, B. K.; Novak, J.; Oertel, M.; Margueron, J.; Faure, J.; Martin, N.; Blottiau, P.; Peres, B. and Durand, G. The Explosion Mechanism of Core-Collapse Supernovae: Progress in Supernova Theory and Experiments. PASA **32**, e009 (2015).

Fransson, C. and Kozma, C. Radioactivities and nucleosynthesis in SN 1987A. New A Rev. **46**, 487 (2002).

Fröhlich, C.; Martínez-Pinedo, G.; Liebendörfer, M.; Thielemann, F.-K.; Bravo, E.; Hix, W. R.; Langanke, K. and Zinner, N. T. Neutrino-Induced Nucleosynthesis of A>64 Nuclei: The νp Process. *Physical Review Letters* **96**, 142502 (2006).

Fryer, C. L. Mass Limits For Black Hole Formation. ApJ **522**, 413 (1999).

Fryer, C. L. and Kalogera, V. Theoretical Black Hole Mass Distributions. ApJ **554**, 548 (2001).

Fuller, G. M.; Woosley, S. E. and Weaver, T. A. The evolution of radiation-dominated stars. I - Nonrotating supermassive stars. ApJ **307**, 675 (1986).

Gal-Yam, A. Luminous Supernovae. *Science* **337**, 927 (2012).

Hamuy, M. Observed and Physical Properties of Core-Collapse Supernovae. ApJ **582**, 905 (2003).

Hanke, F.; Marek, A.; Müller, B. and Janka, H.-T. Is Strong SASI Activity the Key to Successful Neutrino-driven Supernova Explosions? ApJ **755**, 138 (2012).

Heger, A. and Langer, N. Presupernova Evolution of Rotating Massive Stars. II. Evolution of the Surface Properties. ApJ **544**, 1016 (2000).

Heger, A.; Langer, N. and Woosley, S. E. Presupernova Evolution of Rotating Massive Stars. I. Numerical Method and Evolution of the Internal Stellar Structure. ApJ **528**, 368 (2000).

Heger, A. and Woosley, S. E. The Nucleosynthetic Signature of Population III. ApJ **567**, 532 (2002).

Heger, A. and Woosley, S. E. Nucleosynthesis and Evolution of Massive Metal-free Stars. ApJ **724**, 341 (2010).

Heger, A.; Woosley, S. E. and Spruit, H. C. Presupernova Evolution of Differentially Rotating Massive Stars Including Magnetic Fields. ApJ **626**, 350 (2005).

Herwig, F. The evolution of AGB stars with convective overshoot. A&A **360**, 952 (2000).

Higdon, J. C. and Lingenfelter, R. E. The Superbubble Origin of ^{22}Ne in Cosmic Rays. ApJ **590**, 822 (2003).

Hirschi, R.; Meynet, G. and Maeder, A. Stellar evolution with rotation. XII. Pre-supernova models. A&A **425**, 649 (2004).

Hoffman, R. D.; Woosley, S. E.; Fuller, G. M. and Meyer, B. S. Production of the Light p-Process Nuclei in Neutrino-driven Winds. ApJ **460**, 478 (1996).

Howell, D. A.; Kasen, D.; Lidman, C.; Sullivan, M.; Conley, A.; Astier, P.; Balland, C.; Carlberg, R. G.; Fouchez, D.; Guy, J.; Hardin, D.; Pain, R.; Palanque-Delabrouille, N.; Perrett, K.; Pritchet, C. J.; Regnault, N.; Rich, J. and Ruhlmann-Kleider, V. Two Superluminous Supernovae from the Early Universe Discovered by the Supernova Legacy Survey. ApJ **779**, 98 (2013).

Humphreys, R. M. and McElroy, D. B. The initial mass function for massive stars in the Galaxy and the Magellanic Clouds. ApJ **284**, 565 (1984).

Iglesias, C. A. and Rogers, F. J. Updated Opal Opacities. ApJ **464**, 943 (1996).

Inserra, C.; Smartt, S. J.; Jerkstrand, A.; Valenti, S.; Fraser, M.; Wright, D.; Smith, K.; Chen, T.-W.; Kotak, R.; Pastorello, A.; Nicholl, M.; Bresolin, F.; Kudritzki, R. P.; Benetti, S.; Botticella, M. T.; Burgett, W. S.; Chambers, K. C.; Ergon, M.; Flewelling, H.; Fynbo, J. P. U.; Geier, S.; Hodapp, K. W.; Howell, D. A.; Huber, M.; Kaiser, N.; Leloudas, G.; Magill, L.; Magnier, E. A.; McCrum, M. G.; Metcalfe, N.; Price, P. A.; Rest, A.; Sollerman, J.; Sweeney, W.; Taddia, F.; Taubenberger, S.; Tonry, J. L.; Wainscoat, R. J.; Waters, C. and Young, D. Super-luminous Type Ic Supernovae: Catching a Magnetar by the Tail. ApJ **770**, 128 (2013).

Israel, M. H.; Binns, W. R.; Christian, E. R. and Cummings, A. C. Observation of 60Fe in the Galactic Cosmic Rays. *Proc. 34th International Cosmic Ray Conference (The Hague), Proceedings of Science* **1**, 394 (2015).

Iwamoto, K.; Brachwitz, F.; Nomoto, K.; Kishimoto, N.; Umeda, H.; Hix, W. R. and Thielemann, F.-K. Nucleosynthesis in Chandrasekhar Mass Models for Type IA Supernovae and Constraints on Progenitor Systems and Burning-Front Propagation. ApJS **125**, 439 (1999).

Janka, H.-T. Explosion Mechanisms of Core-Collapse Supernovae. *Annual Review of Nuclear and Particle Science* **62**, 407 (2012).

Janka, H.-T.; Hanke, F.; Hüdepohl, L.; Marek, A.; Müller, B. and Obergaulinger, M. Core-collapse supernovae: Reflections and directions. *Progress of Theoretical and Experimental Physics* **2012**, 01A309 (2012).

Janka, H.-T. and Mueller, E. Neutrino heating, convection, and the mechanism of Type-II supernova explosions. A&A **306**, 167 (1996).

Janka, H.-T.; Müller, B.; Kitaura, F. S. and Buras, R. Dynamics of shock propagation and nucleosynthesis conditions in O-Ne-Mg core supernovae. A&A **485**, 199 (2008).

Jerkstrand, A.; Timmes, F. X.; Magkotsios, G.; Sim, S. A.; Fransson, C.; Spyromilio, J.; Müller, B.; Heger, A.; Sollerman, J. and Smartt, S. J. Constraints on Explosive Silicon Burning in Core-collapse Supernovae from Measured Ni/Fe Ratios. ApJ **807**, 110 (2015).

Käppeler, F.; Gallino, R.; Bisterzo, S. and Aoki, W. The s process: Nuclear physics, stellar models, and observations. *Reviews of Modern Physics* **83**, 157 (2011).

Kasen, D. and Bildsten, L. Supernova Light Curves Powered by Young Magnetars. ApJ **717**, 245 (2010).

Kasen, D. and Woosley, S. E. Type II Supernovae: Model Light Curves and Standard Candle Relationships. ApJ **703**, 2205 (2009).

Kasen, D.; Woosley, S. E. and Heger, A. Pair Instability Supernovae: Light Curves, Spectra, and Shock Breakout. ApJ **734**, 102 (2011).

Katz, B.; Kushnir, D. and Dong, S. An exact integral relation between the Ni56 mass and the bolometric light curve of a type Ia supernova. *ArXiv e-prints* (2013).

Kiewe, M.; Gal-Yam, A.; Arcavi, I.; Leonard, D. C.; Emilio Enriquez, J.; Cenko, S. B.; Fox, D. B.; Moon, D.-S.; Sand, D. J.; Soderberg, A. M. and CCCP, T. Caltech Core-Collapse Project (CCCP) Observations of Type IIn Supernovae: Typical Properties and Implications for Their Progenitor Stars. ApJ **744**, 10 (2012).

Kitaura, F. S.; Janka, H.-T. and Hillebrandt, W. Explosions of O-Ne-Mg cores, the Crab supernova, and subluminous type II-P supernovae. A&A **450**, 345 (2006).

Kochanek, C. S. Failed Supernovae Explain the Compact Remnant Mass Function. ApJ **785**, 28 (2014).

Kochanek, C. S. Constraints on core collapse from the black hole mass function. MNRAS **446**, 1213 (2015).

Kozyreva, A. and Blinnikov, S. Can pair-instability supernova models match the observations of superluminous supernovae? MNRAS **454**, 4357 (2015).

Kushnir, D. The progenitors of core-collapse supernovae suggest thermonuclear origin for the explosions. *ArXiv e-prints* (2015).

Langer, N. Helium enrichment in massive early type stars. A&A **265**, L17 (1992).

Langer, N.; El Eid, M. F. and Baraffe, I. Blue supergiant supernova progenitors. A&A **224**, L17 (1989).

Langer, N.; Fricke, K. J. and Sugimoto, D. Semiconvective diffusion and energy transport. A&A **126**, 207 (1983).

Lattimer, J. M. The Nuclear Equation of State and Neutron Star Masses. *Annual Review of Nuclear and Particle Science* **62**, 485 (2012).

Lattimer, J. M. and Prakash, M. Neutron Star Structure and the Equation of State. ApJ **550**, 426 (2001).

Li, W.; Chornock, R.; Leaman, J.; Filippenko, A. V.; Poznanski, D.; Wang, X.; Ganeshalingam, M. and Mannucci, F. Nearby supernova rates from the Lick Observatory Supernova Search - III. The rate-size relation, and the rates as a function of galaxy Hubble type and colour. MNRAS **412**, 1473 (2011).

Liebendörfer, M. A Simple Parameterization of the Consequences of Deleptonization for Simulations of Stellar Core Collapse. ApJ **633**, 1042 (2005).

Limongi, M. and Chieffi, A. Nucleosynthesis of ^{60}Fe in massive stars. New A Rev. **50**, 474 (2006a).

Limongi, M. and Chieffi, A. The Nucleosynthesis of ^{26}Al and ^{60}Fe in Solar Metallicity Stars Extending in Mass from 11 to 120 M_{solar}: The Hydrostatic and Explosive Contributions. ApJ **647**, 483 (2006b).

Lodders, K. Solar System Abundances and Condensation Temperatures of the Elements. ApJ **591**, 1220 (2003).

Longland, R.; Iliadis, C. and Karakas, A. I. Reaction rates for the s-process neutron source ^{22}Ne + α. Phys. Rev. C **85**, 065809 (2012).

Lovegrove, E. and Woosley, S. E. Very Low Energy Supernovae from Neutrino Mass Loss. ApJ **769**, 109 (2013).

Lovegrove, E. and Woosley, S. E. XXX XXX XXX. *in preparation for* ApJ (2015).

Maeda, K.; Tanaka, M.; Nomoto, K.; Tominaga, N.; Kawabata, K.; Mazzali, P. A.; Umeda, H.; Suzuki, T. and Hattori, T. The Unique Type Ib Supernova 2005bf at Nebular Phases: A Possible Birth Event of a Strongly Magnetized Neutron Star. ApJ **666**, 1069 (2007).

Maeder, A. Evidences for a bifurcation in massive star evolution. The ON-blue stragglers. A&A **178**, 159 (1987).

Maeder, A. Stellar yields as a function of initial metallicity and mass limit for black hole formation. A&A **264**, 105 (1992).

Mazzali, P. A.; McFadyen, A. I.; Woosley, S. E.; Pian, E. and Tanaka, M. An upper limit to the energy of gamma-ray bursts indicates that GRBs/SNe are powered by magnetars. MNRAS **443**, 67 (2014).

Meakin, C. A. and Arnett, D. Turbulent Convection in Stellar Interiors. I. Hydrodynamic Simulation. ApJ **667**, 448 (2007).

Meakin, C. A.; Sukhbold, T. and Arnett, W. D. Presupernova structure of massive stars. Ap&SS **336**, 123 (2011).

Melson, T.; Janka, H.-T. and Marek, A. Neutrino-driven Supernova of a Low-mass Iron-core Progenitor Boosted by Three-dimensional Turbulent Convection. ApJ **801**, L24 (2015).

Menon, A. and Heger, A. The Quest for BlueSuperGiants: Binary Merger Model for the Evolution of the Progenitor of SN1987A. *in preparation for* ApJ (2016).

Metzger, B. D.; Margalit, B.; Kasen, D. and Quataert, E. The diversity of transients from magnetar birth in core collapse supernovae. MNRAS **454**, 3311 (2015).

Metzger, B. D.; Vurm, I.; Hascoët, R. and Beloborodov, A. M. Ionization break-out from millisecond pulsar wind nebulae: an X-ray probe of the origin of superluminous supernovae. MNRAS **437**, 703 (2014).

Meynet, G. and Arnould, M. Synthesis of ^{19}F in the He-burning zones of massive stars. In Kaeppeler, F. and Wisshak, K., eds., *Nuclei in the Cosmos 2* (1993), pp. 503–508.

Mösta, P.; Ott, C. D.; Radice, D.; Roberts, L. F.; Schnetter, E. and Haas, R. A large-scale dynamo and magnetoturbulence in rapidly rotating core-collapse supernovae. Nature **528**, 376 (2015).

Mueller, E. Nuclear-reaction networks and stellar evolution codes - The coupling of composition changes and energy release in explosive nuclear burning. A&A **162**, 103 (1986).

Müller, B. The dynamics of neutrino-driven supernova explosions after shock revival in 2D and 3D. MNRAS **453**, 287 (2015).

Nadezhin, D. K. Some secondary indications of gravitational collapse. Ap&SS **69**, 115 (1980).

Nicholl, M.; Smartt, S. J.; Jerkstrand, A.; Inserra, C.; McCrum, M.; Kotak, R.; Fraser, M.; Wright, D.; Chen, T.-W.; Smith, K.; Young, D. R.; Sim, S. A.; Valenti, S.; Howell, D. A.; Bresolin, F.; Kudritzki, R. P.; Tonry, J. L.; Huber, M. E.; Rest, A.; Pastorello, A.; Tomasella, L.; Cappellaro, E.; Benetti, S.; Mattila, S.; Kankare, E.; Kangas, T.; Leloudas, G.; Sollerman, J.; Taddia, F.; Berger, E.; Chornock, R.; Narayan, G.; Stubbs, C. W.; Foley, R. J.; Lunnan, R.; Soderberg, A.; Sanders, N.; Milisavljevic, D.; Margutti, R.; Kirshner, R. P.; Elias-Rosa, N.; Morales-Garoffolo, A.; Taubenberger, S.; Botticella, M. T.; Gezari, S.; Urata, Y.; Rodney,

S.; Riess, A. G.; Scolnic, D.; Wood-Vasey, W. M.; Burgett, W. S.; Chambers, K.; Flewelling, H. A.; Magnier, E. A.; Kaiser, N.; Metcalfe, N.; Morgan, J.; Price, P. A.; Sweeney, W. and Waters, C. Slowly fading super-luminous supernovae that are not pair-instability explosions. Nature **502**, 346 (2013).

Nicholl, M.; Smartt, S. J.; Jerkstrand, A.; Inserra, C.; Sim, S. A.; Chen, T.-W.; Benetti, S.; Fraser, M.; Gal-Yam, A.; Kankare, E.; Maguire, K.; Smith, K.; Sullivan, M.; Valenti, S.; Young, D. R.; Baltay, C.; Bauer, F. E.; Baumont, S.; Bersier, D.; Botticella, M.-T.; Childress, M.; Dennefeld, M.; Della Valle, M.; Elias-Rosa, N.; Feindt, U.; Galbany, L.; Hadjiyska, E.; Le Guillou, L.; Leloudas, G.; Mazzali, P.; McKinnon, R.; Polshaw, J.; Rabinowitz, D.; Rostami, S.; Scalzo, R.; Schmidt, B. P.; Schulze, S.; Sollerman, J.; Taddia, F. and Yuan, F. On the diversity of superluminous supernovae: ejected mass as the dominant factor. MNRAS **452**, 3869 (2015).

Nieuwenhuijzen, H. and de Jager, C. Parametrization of stellar rates of mass loss as functions of the fundamental stellar parameters M, L, and R. A&A **231**, 134 (1990).

Nomoto, K. Evolution of 8-10 solar mass stars toward electron capture supernovae. II - Collapse of an O + NE + MG core. ApJ **322**, 206 (1987).

Nomoto, K. and Hashimoto, M. Presupernova evolution of massive stars. Phys. Rep. **163**, 13 (1988).

Nomoto, K.; Kobayashi, C. and Tominaga, N. Nucleosynthesis in Stars and the Chemical Enrichment of Galaxies. ARA&A **51**, 457 (2013).

Nomoto, K.; Sugimoto, D.; Sparks, W. M.; Fesen, R. A.; Gull, T. R. and Miyaji, S. The Crab Nebula's progenitor. Nature **299**, 803 (1982).

O'Connor, E. and Ott, C. D. Black Hole Formation in Failing Core-Collapse Supernovae. ApJ **730**, 70 (2011).

O'Connor, E. and Ott, C. D. The Progenitor Dependence of the Pre-explosion Neutrino Emission in Core-collapse Supernovae. ApJ **762**, 126 (2013).

Ozel, F. and Freire, P. Masses, Radii, and Equation of State of Neutron Stars. *ArXiv e-prints* (2016).

Özel, F.; Psaltis, D.; Narayan, R. and Santos Villarreal, A. On the Mass Distribution and Birth Masses of Neutron Stars. ApJ **757**, 55 (2012).

Paxton, B.; Bildsten, L.; Dotter, A.; Herwig, F.; Lesaffre, P. and Timmes, F. Modules for Experiments in Stellar Astrophysics (MESA). ApJS **192**, 3 (2011).

Paxton, B.; Cantiello, M.; Arras, P.; Bildsten, L.; Brown, E. F.; Dotter, A.; Mankovich, C.; Montgomery, M. H.; Stello, D.; Timmes, F. X. and Townsend, R. Modules for Experiments in Stellar Astrophysics (MESA): Planets, Oscillations, Rotation, and Massive Stars. ApJS **208**, 4 (2013).

Paxton, B.; Marchant, P.; Schwab, J.; Bauer, E. B.; Bildsten, L.; Cantiello, M.; Dessart, L.; Farmer, R.; Hu, H.; Langer, N.; Townsend, R. H. D.; Townsley, D. M. and Timmes, F. X. Modules for Experiments in Stellar Astrophysics (MESA): Binaries, Pulsations, and Explosions. ApJS **220**, 15 (2015).

Pejcha, O. and Thompson, T. A. The Landscape of the Neutrino Mechanism of Core-collapse Supernovae: Neutron Star and Black Hole Mass Functions, Explosion Energies, and Nickel Yields. ApJ **801**, 90 (2015).

Pignatari, M.; Hirschi, R.; Wiescher, M.; Gallino, R.; Bennett, M.; Beard, M.; Fryer, C.; Herwig, F.; Rockefeller, G. and Timmes, F. X. The ^{12}C + ^{12}C Reaction and the Impact on Nucleosynthesis in Massive Stars. ApJ **762**, 31 (2013).

Poelarends, A. J. T.; Herwig, F.; Langer, N. and Heger, A. The Supernova Channel of Super-AGB Stars. ApJ **675**, 614-625 (2008).

Popov, D. V. An analytical model for the plateau stage of Type II supernovae. ApJ **414**, 712 (1993).

Poznanski, D. An emerging coherent picture of red supergiant supernova explosions. MNRAS **436**, 3224 (2013).

Quimby, R. M.; Kulkarni, S. R.; Kasliwal, M. M.; Gal-Yam, A.; Arcavi, I.; Sullivan, M.; Nugent, P.; Thomas, R.; Howell, D. A.; Nakar, E.; Bildsten, L.; Theissen, C.; Law, N. M.; Dekany, R.; Rahmer, G.; Hale, D.; Smith, R.; Ofek, E. O.; Zolkower, J.; Velur, V.; Walters, R.; Henning, J.; Bui, K.; McKenna, D.; Poznanski, D.; Cenko, S. B. and Levitan, D. Hydrogen-poor superluminous stellar explosions. Nature **474**, 487 (2011).

Rauscher, T.; Heger, A.; Hoffman, R. D. and Woosley, S. E. Nucleosynthesis in Massive Stars with Improved Nuclear and Stellar Physics. ApJ **576**, 323 (2002).

Saio, H.; Nomoto, K. and Kato, M. Nitrogen and helium enhancement in the progenitor of supernova 1987A. Nature **334**, 508 (1988).

Salpeter, E. E. The Luminosity Function and Stellar Evolution. ApJ **121**, 161 (1955).

Scalo, J. M. The stellar initial mass function. Fund. Cosmic Phys. **11**, 1 (1986).

Scannapieco, E.; Madau, P.; Woosley, S.; Heger, A. and Ferrara, A. The Detectability of Pair-Production Supernovae at z $<\tilde{}$ 6. ApJ **633**, 1031 (2005).

Scheck, L.; Kifonidis, K.; Janka, H.-T. and Müller, E. Multidimensional supernova simulations with approximative neutrino transport. I. Neutron star kicks and the anisotropy of neutrino-driven explosions in two spatial dimensions. A&A **457**, 963 (2006).

Schürmann, D.; Gialanella, L.; Kunz, R. and Strieder, F. The astrophysical S factor of ^{12}C(α,γ)^{16}O at stellar energy. *Physics Letters B* **711**, 35 (2012).

Schwab, J.; Podsiadlowski, P. and Rappaport, S. Further Evidence for the Bimodal Distribution of Neutron-star Masses. ApJ **719**, 722 (2010).

Seitenzahl, I. R.; Cescutti, G.; Röpke, F. K.; Ruiter, A. J. and Pakmor, R. Solar abundance of manganese: a case for near Chandrasekhar-mass Type Ia supernova progenitors. A&A **559**, L5 (2013a).

Seitenzahl, I. R.; Ciaraldi-Schoolmann, F.; Röpke, F. K.; Fink, M.; Hillebrandt, W.; Kromer, M.; Pakmor, R.; Ruiter, A. J.; Sim, S. A. and Taubenberger, S. Three-dimensional delayed-detonation models with nucleosynthesis for Type Ia supernovae. MNRAS **429**, 1156 (2013b).

Shigeyama, T.; Nomoto, K. and Hashimoto, M. Hydrodynamical models and the light curve of Supernova 1987A in the Large Magellanic Cloud. A&A **196**, 141 (1988).

Shiode, J. H. and Quataert, E. Setting the Stage for Circumstellar Interaction in Core-Collapse Supernovae. II. Wave-driven Mass Loss in Supernova Progenitors. ApJ **780**, 96 (2014).

Sieverding, A.; Huther, L.; Langanke, K.; Martínez-Pinedo, G. and Heger, A. Neutrino Nucleosynthesis of radioactive nuclei in supernovae. *ArXiv e-prints* (2015).

Smartt, S. J. Progenitors of Core-Collapse Supernovae. ARA&A **47**, 63 (2009).

Smartt, S. J. Observational Constraints on the Progenitors of Core-Collapse Supernovae: The Case for Missing High-Mass Stars. PASA **32**, e016 (2015).

Smith, N. Discovery of a Nearby Twin of SN 1987A's Nebula around the Luminous Blue Variable HD 168625: Was Sk -69 202 an LBV? AJ **133**, 1034 (2007).

Smith, N. A blast wave from the 1843 eruption of η Carinae. Nature **455**, 201 (2008).

Smith, N. The Crab nebula and the class of Type IIn-P supernovae caused by sub-energetic electron-capture explosions. MNRAS **434**, 102 (2013).

Smith, N. and Arnett, W. D. Preparing for an Explosion: Hydrodynamic Instabilities and Turbulence in Presupernovae. ApJ **785**, 82 (2014).

Smith, N.; Chornock, R.; Silverman, J. M.; Filippenko, A. V. and Foley, R. J. Spectral Evolution of the Extraordinary Type IIn Supernova 2006gy. ApJ **709**, 856 (2010).

Smith, N.; Li, W.; Miller, A. A.; Silverman, J. M.; Filippenko, A. V.; Cuillandre, J.-C.; Cooper, M. C.; Matheson, T. and Van Dyk, S. D. A Massive Progenitor of the Luminous Type IIn Supernova 2010jl. ApJ **732**, 63 (2011a).

Smith, N.; Li, W.; Silverman, J. M.; Ganeshalingam, M. and Filippenko, A. V. Luminous blue variable eruptions and related transients: diversity of progenitors and outburst properties. MNRAS **415**, 773 (2011b).

Spiro, S.; Pastorello, A.; Pumo, M. L.; Zampieri, L.; Turatto, M.; Smartt, S. J.; Benetti, S.; Cappellaro, E.; Valenti, S.; Agnoletto, I.; Altavilla, G.; Aoki, T.; Brocato, E.; Corsini, E. M.; Di Cianno, A.; Elias-Rosa, N.; Hamuy, M.; Enya, K.; Fiaschi, M.; Folatelli, G.; Desidera, S.; Harutyunyan, A.; Howell, D. A.; Kawka, A.; Kobayashi, Y.; Leibundgut, B.; Minezaki, T.; Navasardyan, H.; Nomoto, K.; Mattila, S.; Pietrinferni, A.; Pignata, G.; Raimondo, G.; Salvo, M.; Schmidt, B. P.; Sollerman, J.; Spyromilio, J.; Taubenberger, S.; Valentini, G.; Vennes, S. and Yoshii, Y. Low luminosity Type II supernovae - II. Pointing towards moderate mass precursors. MNRAS **439**, 2873 (2014).

Spruit, H. C. Semiconvection: theory. A&A **552**, A76 (2013).

Steiner, A. W.; Hempel, M. and Fischer, T. Core-collapse Supernova Equations of State Based on Neutron Star Observations. ApJ **774**, 17 (2013).

Sukhbold, T.; Ertl, T.; Woosley, S. E.; Brown, J. M. and Janka, H.-T. Core-collapse Supernovae from 9 to 120 Solar Masses Based on Neutrino-powered Explosions. ApJ **821**, 38 (2016).

Sukhbold, T. and Woosley, S. E. The Compactness of Presupernova Stellar Cores. ApJ **783**, 10 (2014).

Sukhbold, T. and Woosley, S. E. The Most Luminous Supernovae. ApJ **820**, L38 (2016).

Suntzeff, N. B.; Phillips, M. M.; Elias, J. H.; Walker, A. R. and Depoy, D. L. The energy sources powering the late-time bolometric evolution of SN 1987A. ApJ **384**, L33 (1992).

Thielemann, F.-K.; Nomoto, K. and Hashimoto, M.-A. Core-Collapse Supernovae and Their Ejecta. ApJ **460**, 408 (1996).

Timmes, F. X.; Woosley, S. E.; Hartmann, D. H.; Hoffman, R. D.; Weaver, T. A. and Matteucci, F. 26Al and 60Fe from Supernova Explosions. ApJ **449**, 204 (1995a).

Timmes, F. X.; Woosley, S. E. and Weaver, T. A. Galactic chemical evolution: Hydrogen through zinc. ApJS **98**, 617 (1995b).

Timmes, F. X.; Woosley, S. E. and Weaver, T. A. The Neutron Star and Black Hole Initial Mass Function. ApJ **457**, 834 (1996).

Tominaga, N.; Blinnikov, S. I. and Nomoto, K. Supernova Explosions of Super-asymptotic Giant Branch Stars: Multicolor Light Curves of Electron-capture Supernovae. ApJ **771**, L12 (2013).

Tur, C.; Heger, A. and Austin, S. M. On the Sensitivity of Massive Star Nucleosynthesis and Evolution to Solar Abundances and to Uncertainties in Helium-Burning Reaction Rates. ApJ **671**, 821 (2007).

Ugliano, M.; Janka, H.-T.; Marek, A. and Arcones, A. Progenitor-explosion Connection and Remnant Birth Masses for Neutrino-driven Supernovae of Iron-core Progenitors. ApJ **757**, 69 (2012).

Utrobin, V. P. Supernova 1987A: The Envelope Mass and the Explosion Energy. *Astronomy Letters* **31**, 806 (2005).

Utrobin, V. P. and Chugai, N. N. Supernova 2000cb: high-energy version of SN 1987A. A&A **532**, A100 (2011).

Utrobin, V. P.; Wongwathanarat, A.; Janka, H.-T. and Müller, E. Supernova 1987A: neutrino-driven explosions in three dimensions and light curves. A&A **581**, A40 (2015).

Valenti, S.; Fraser, M.; Benetti, S.; Pignata, G.; Sollerman, J.; Inserra, C.; Cappellaro, E.; Pastorello, A.; Smartt, S. J.; Ergon, M.; Botticella, M. T.; Brimacombe, J.; Bufano, F.; Crockett, M.; Eder, I.; Fugazza, D.; Haislip, J. B.; Hamuy, M.; Harutyunyan, A.; Ivarsen, K. M.; Kankare, E.; Kotak, R.; Lacluyze, A. P.; Magill, L.; Mattila, S.; Maza, J.; Mazzali, P. A.; Reichart, D. E.; Taubenberger, S.; Turatto, M. and Zampieri, L. SN 2009jf: a slow-evolving stripped-envelope core-collapse supernova. MNRAS **416**, 3138 (2011).

van Marle, A. J.; Smith, N.; Owocki, S. P. and van Veelen, B. Numerical models of collisions between core-collapse supernovae and circumstellar shells. MNRAS **407**, 2305 (2010).

Viallet, M.; Meakin, C.; Arnett, D. and Mocák, M. Turbulent Convection in Stellar Interiors. III. Mean-field Analysis and Stratification Effects. ApJ **769**, 1 (2013).

Vinkó, J.; Takáts, K.; Szalai, T.; Marion, G. H.; Wheeler, J. C.; Sárneczky, K.; Garnavich, P. M.; Kelemen, J.; Klagyivik, P.; Pál, A.; Szalai, N. and Vida, K. Improved distance determination to M 51 from supernovae 2011dh and 2005cs. A&A **540**, A93 (2012).

Walborn, N. R.; Lasker, B. M.; Laidler, V. G. and Chu, Y.-H. The composite image of Sanduleak -69 deg 202, candidate precursor to supernova 1987 A in the Large Magellanic Cloud. ApJ **321**, L41 (1987).

Wanajo, S.; Janka, H.-T. and Kubono, S. Uncertainties in the νp-process: Supernova Dynamics Versus Nuclear Physics. ApJ **729**, 46 (2011a).

Wanajo, S.; Janka, H.-T. and Müller, B. Electron-capture Supernovae as The Origin of Elements Beyond Iron. ApJ **726**, L15 (2011b).

Wanajo, S.; Janka, H.-T.; Müller, B. and Heger, A. . *in preparation for* ApJ (2016).

Wanajo, S.; Janka, H.-T.; Müller, B. and Kubono, S. Proton vs. neutron captures in the neutrino winds of core-collapse supernovae. *Journal of Physics Conference Series* **312**, 042008 (2011c).

Wanajo, S.; Nomoto, K.; Janka, H.-T.; Kitaura, F. S. and Müller, B. Nucleosynthesis in Electron Capture Supernovae of Asymptotic Giant Branch Stars. ApJ **695**, 208 (2009).

Wang, W.; Harris, M. J.; Diehl, R.; Halloin, H.; Cordier, B.; Strong, A. W.; Kretschmer, K.; Knödlseder, J.; Jean, P.; Lichti, G. G.; Roques, J. P.; Schanne, S.; von Kienlin, A.; Weidenspointner, G. and Wunderer, C. SPI observations of the diffuse ^{60}Fe emission in the Galaxy. A&A **469**, 1005 (2007).

Weaver, T. A. and Woosley, S. E. Evolution and explosion of massive stars. In Ehlers, J.; Perry, J. J. and Walker, M., eds., *Ninth Texas Symposium on Relativistic Astrophysics* (1980), vol. 336 of *Annals of the New York Academy of Sciences*, pp. 335–357.

Weaver, T. A. and Woosley, S. E. Nucleosynthesis in massive stars and the $^{12}C(\alpha, \gamma)^{16}O$ reaction rate. Phys. Rep. **227**, 65 (1993).

Weaver, T. A.; Zimmerman, G. B. and Woosley, S. E. Presupernova evolution of massive stars. ApJ **225**, 1021 (1978).

Wellstein, S. and Langer, N. Implications of massive close binaries for black hole formation and supernovae. A&A **350**, 148 (1999).

West, C.; Heger, A. and Austin, S. M. The Impact of Helium-burning Reaction Rates on Massive Star Evolution and Nucleosynthesis. ApJ **769**, 2 (2013).

Wiktorowicz, G.; Belczynski, K. and Maccarone, T. Black hole X-ray transients: The formation puzzle. In *Binary Systems, their Evolution and Environments* (2014), p. 37.

Wood, T. S.; Garaud, P. and Stellmach, S. A New Model for Mixing by Double-diffusive Convection (Semi-convection). II. The Transport of Heat and Composition through Layers. ApJ **768**, 157 (2013).

Woosley, S. E. SN 1987A - After the peak. ApJ **330**, 218 (1988).

Woosley, S. E. Bright Supernovae from Magnetar Birth. ApJ **719**, L204 (2010).

Woosley, S. E.; Blinnikov, S. and Heger, A. Pulsational pair instability as an explanation for the most luminous supernovae. Nature **450**, 390 (2007).

Woosley, S. E.; Hartmann, D. H.; Hoffman, R. D. and Haxton, W. C. The nu-process. ApJ **356**, 272 (1990).

Woosley, S. E. and Heger, A. The Progenitor Stars of Gamma-Ray Bursts. ApJ **637**, 914 (2006).

Woosley, S. E. and Heger, A. The Deaths of Very Massive Stars. In Vink, J. S., ed., *Very Massive Stars in the Local Universe* (2015a), vol. 412 of *Astrophysics and Space Science Library*, p. 199.

Woosley, S. E. and Heger, A. The Remarkable Deaths of 9-11 Solar Mass Stars. ApJ **810**, 34 (2015b).

Woosley, S. E.; Heger, A. and Weaver, T. A. The evolution and explosion of massive stars. *Reviews of Modern Physics* **74**, 1015 (2002).

Woosley, S. E. and Kasen, D. Sub-Chandrasekhar Mass Models for Supernovae. ApJ **734**, 38 (2011).

Woosley, S. E.; Langer, N. and Weaver, T. A. The evolution of massive stars including mass loss - Presupernova models and explosion. ApJ **411**, 823 (1993).

Woosley, S. E.; Langer, N. and Weaver, T. A. The Presupernova Evolution and Explosion of Helium Stars That Experience Mass Loss. ApJ **448**, 315 (1995).

Woosley, S. E. and Weaver, T. A. Presupernova models: sensitivity to convective algorithm and Coulomb corrections. Phys. Rep. **163**, 79 (1988).

Yamaguchi, H.; Badenes, C.; Foster, A. R.; Bravo, E.; Williams, B. J.; Maeda, K.; Nobukawa, M.; Eriksen, K. A.; Brickhouse, N. S.; Petre, R. and Koyama, K. A Chandrasekhar Mass Progenitor for the Type Ia Supernova Remnant 3C 397 from the Enhanced Abundances of Nickel and Manganese. ApJ **801**, L31 (2015).

Yang, H. and Chevalier, R. A. Evolution of the Crab Nebula in a Low Energy Supernova. ApJ **806**, 153 (2015).

Yoon, S.-C.; Langer, N. and Norman, C. Single star progenitors of long gamma-ray bursts. I. Model grids and redshift dependent GRB rate. A&A **460**, 199 (2006).

Yoshida, T.; Umeda, H.; Maeda, K. and Ishii, T. Mass ejection by pulsational pair instability in very massive stars and implications for luminous supernovae. MNRAS **457**, 351 (2016).

Zaussinger, F. and Spruit, H. C. Semiconvection: numerical simulations. A&A **554**, A119 (2013).

Zhang, W.; Woosley, S. E. and Heger, A. Fallback and Black Hole Production in Massive Stars. ApJ **679**, 639-654 (2008).